Determining Timescales and Paleoenvironments of Quaternary Human Evolution Using Stable and Radiogenic Isotopes

By

Elizabeth Niespolo

A dissertation submitted in partial satisfaction of the

requirements for the degree of

Doctor of Philosophy

in

Earth & Planetary Science

In the

Graduate Division

of the

University of California, Berkeley

Committee in charge:

Professor Paul R. Renne, Chair
Professor Kurt M. Cuffey
Professor Todd E. Dawson
Dr. Warren D. Sharp

Summer 2019

Abstract

Determining Timescales and Paleoenvironments of Quaternary Human Evolution Using Stable and Radiogenic Isotopes

by

Elizabeth Niespolo

Doctor of Philosophy in Earth & Planetary Science

University of California, Berkeley

Professor Paul R. Renne, Chair

Assessing the covariance of human biological and cultural evolution with major climate fluctuations requires independent, precise, and accurate chronologies documenting environmental change in association with rare fossils and archaeology. This thesis aims to improve and diversify geochronological tools and associated paleoenvironmental characterization of paleoanthropological sequences using two of the most precise and accurate chronometers applicable in the Quaternary Period, $^{40}Ar/^{39}Ar$ and U-Series (i.e., ^{230}Th) geochronology, combined with light stable isotopes, to reconstruct timescales and terrestrial paleoenvironments at paleoanthropological sites.

The first chapter refines the age of the Alder Creek sanidine (ACs) fluence monitor which is frequently utilized to determine $^{40}Ar/^{39}Ar$ ages of volcanic rocks in association with hominid fossil-bearing and archaeological deposits in eastern Africa. The age of ACs is significantly different if anchored by astronomical tuning (t_{ACs} = 1.1848 ± 0.0006 Ma, σ) than if anchored solely by constraints from radioactive decay (t_{ACs} = 1.1891 ± 0.0008 Ma), possibly due to 1) leads and lags in the deposition of astronomically tuned sequences, 2) inaccuracy of decay constants, and/or 3) assumptions inherent to each dating method. The second chapter outlines the use of C, N, and O stable isotopes of ostrich eggshells to reconstruct local paleoenvironments at African archaeological sites. Combined with novel ^{230}Th burial dating of ostrich eggshells, these may provide precisely dated paleoenvironmental records for sites up to ~ 500 ka. The light stable isotope composition of ostrich eggshells from two eastern African archaeological sites ~50 – 4 ka, which include diachronous occurrences of the Middle to Later Stone Age transition, suggest a mosaic of local environments through time and space that is not apparent from global or regional paleoenvironmental records. In the third chapter, I apply ^{230}Th dating to coral abrader artifacts from a stratified archaeological sequence at Tangatatau Rockshelter, Mangaia (Cook Islands). I compare the results with a recent Bayesian ^{14}C chronology for the site and develop screening criteria to identify reliable ^{230}Th dates from buried contexts at other sites in an effort to develop more precise ways of dating Polynesian expansion. Precise ^{230}Th dates from coral abraders support early Polynesian arrival to Mangaia (1011.6 ± 5.8 CE) and the arrival of the sweet potato (*Ipomoea batatas*) to no later than 1361–1466 CE, indicating that trans-Pacific voyaging had introduced this South American native plant to the Cook Islands by that time. The techniques used in this thesis demonstrate the power of integrative research in isotope geochemistry to address questions about geological processes and human evolution.

Table of Contents

TABLE OF CONTENTS ..... **I**

LIST OF FIGURES ..... **III**

LIST OF TABLES ..... **V**

ACKNOWLEDGEMENTS ..... **VI**

INTRODUCTION **1**

CHAPTER 1: INTERCALIBRATION AND AGE OF THE ALDER CREEK SANIDINE $^{40}AR/^{39}AR$ STANDARD **5**

ABSTRACT 5
1: INTRODUCTION 5
2: METHODS 8
2.1: Samples *8*
2.2: Sample preparation *9*
2.3: Irradiation *11*
2.4: Analytical procedures *13*
3: RESULTS 17
3.1: R values *17*
3.2: Comparison with previous data *20*
3.3: Age of ACs *22*
3.4: Recoil? *24*
3.5: Application to the Matuyama-Brunhes Boundary (MBB) *24*
4: CONCLUSIONS 25

CHAPTER 2: CARBON, NITROGEN, AND OXYGEN ISOTOPES OF OSTRICH EGGSHELLS PROVIDE SITE-SCALE PLEISTOCENE-HOLOCENE PALEOENVIRONMENTAL RECORDS FOR EASTERN AFRICAN ARCHAEOLOGICAL SITES **26**

ABSTRACT 26
1: INTRODUCTION 26
2: BACKGROUND 28
2.1: Stable isotopes of ostrich eggshells as paleoenvironmental proxies *28*
2.2 Context of eastern African sites Lukenya Hill and Kisese II *31*
3: METHODS 41
3.1: Stable Isotopes *41*
3.2: Chronology and Age Modeling *41*
4: RESULTS FROM ANCIENT OES 45
4.1: Carbon Isotopes *50*
4.2: Nitrogen Isotopes *52*
4.3: Oxygen Isotopes *52*
5: DISCUSSION 55
5.1: Relations among isotope proxies *55*
5.2: Comparison between the OES isotope records at Lukenya Hill and Kisese II *62*
5.3: Localized expression of regional paleoclimate events *63*
5.5: Comparison to other regional paleoclimate records *66*
5.6: Possible Drivers of Diverse Local Paleoenvironments *67*
5.7: Summary *68*
6: CONCLUSIONS 68

CHAPTER 3: ^{230}TH DATING OF CORAL ABRADERS FROM STRATIFIED DEPOSITS AT TANGATATAU ROCKSHELTER, MANGAIA, COOK ISLANDS: IMPLICATIONS FOR BUILDING PRECISE CHRONOLOGIES IN POLYNESIA **70**

ABSTRACT 70

1: Introduction 70
1.1: Mangaia Island and MAN-44 excavations at Tangatatau Rockshelter *73*
2: Samples and Methods 77
3: Results 80
3.1: Overview *80*
3.2: Pleistocene corals *80*
3.3: Identifying reliable coral ^{230}Th dates *82*
3.4: Laser ablation ICP-MS *95*
3.5: Suitability of Porites versus Acropora for ^{230}Th dating *95*
3.6: Modified screening criteria for ^{230}Th dating of corals from buried contexts *96*
3.7: Stratigraphic relations of Holocene coral abrader ^{230}Th dates and ^{14}C model ages *97*
4: Discussion 98
4.1: Archaeological Implications of ^{230}Th chronology at MAN-44 ..... *98*
5. Conclusions 100

CONCLUSION 102

BIBLIOGRAPHY 103

APPENDIX A: SUPPLEMENTARY FIGURES FOR CHAPTER 1 121

APPENDIX B: SUPPLEMENTARY MATERIALS FOR CHAPTER 2 131

B.1: Background: Formation of eggshell and preservation of OES structures in deep time 131
B.2: Methods: Sample Preparation Protocol 131
B.3: Results: Protocol testing on Modern OES 132
B.4: Discussion: assessing modeled $\Delta^{18}O_{FOLIARH2O}$ values 133
B.5: Supplementary Figures and Tables for Chapter 2 134
B.6: References 138

APPENDIX C: SUPPLEMENTARY MATERIALS FOR CHAPTER 3 140

C.1: Methods 140
C.1.1: Sample preparation *140*
C.1.2: Aridus/Solutions methods *140*
C.1.3: LA-ICP-MS methods *141*
C.1.4: XRD methods *142*
C.2: Supplementary Figures and Tables for Chapter 3 143
C.3: References 158

List of Figures

Figure 1.1. Disc maps for each of the 18.54-mm aluminum irradiation discs……...……..……..… 12

Figure 1.2 Compilation of R_{FCs}^{ACs} values from previous publications and this work..…….... 19

Figure 2.1 Map of modern physiognomic vegetation showing locations of the Lukenya Hill and Kisese II rockshelters and nearby lakes……...…….….... 33

Figure 2.2 Selected ostrich eggshell fragments from Kisese II……..……..…… 35

Figure 2.3 Plot of $\delta^{13}C$ values of total organic fraction (TOF) versus inorganic fraction (calcite) of modern and ancient ostrich eggshells ...…….... 43

Figure 2.4 Observed carbon isotope fractionation in ancient OES versus age…...…..……. 44

Figure 2.5 The C, N, and O isotopic compositions of OES from Lukenya Hill and corresponding proxy variables through time …….... 48

Figure 2.6 The C, N, and O isotopic compositions of OES from Kisese II and corresponding proxy variables through time …….. 49

Figure 2.7 Mean annual precipitation (MAP) versus $\delta^{15}N$ values of modern ostrich eggshell from South Africa and emu eggshell from Australia …….……...……..... 51

Figure 2.8 Comparisons of each isotope system from OES results…….……. 57

Figure 2.9 Comparison of model $\delta^{18}O$ values…….……..... 61

Figure 2.10 Summary of wet intervals over the last ~50 ka from the sites discussed as compared to proximal lakes……..…….…. 65

Figure 3.1 Maps of central Eastern Polynesia showing Mangaia Island with the location of Tangatatau Rockshelter ……..... 72

Figure 3.2 Replicate analyses of four *Acropora* coral abraders from MAN-44……..……..... 81

Figure 3.3 Summary of ^{14}C age model and ^{230}Th dates from MAN-44…….....……..…... 83

Figure 3.4 Back-calculated $(^{234}U/^{238}U)_0$ for Holocene coral abraders from MAN-44, Mangaia.…..... 84

Figure 3.5 Back-calculated $(^{234}U/^{238}U)_0$ for Holocene coral abraders at MAN-44, Mangaia..... 86

Figure 3.6 Effects of alteration to calcite on Th and U isotopic ratios of Holocene corals.....….. 89

Figure 3.7 *Acropora* coral abrader MAN-44-U-Th#-7..……..…. 90

Figure 3.8 *Acropora* coral abrader MAN-44-U-Th#-6 ……..……..… 91

Figure 3.9 Spatial variation of [U] and $^{232}Th/^{238}U$ values in pristine and altered corals determined via laser ablation ……. 93

Figure A.1 F-values of all samples included in the weighted mean F-value for each pit from irradiation 450PRA……...……... 119

Figure A.2 F-values for samples from irradiation 452A……..……..... 120

Figure A.3 F-values for samples from irradiation 449…….…..... 121

Figure A.4 F-values for samples from irradiation 424 …….…... 121

Figure A.5 F-values for Mes4 and FCs samples from irradiation 424……..…..... 122

Figure A.6 Age results for FCs analyses on Noblesse …...…….. 122 – 124

Figure A.7 Age results for ACs analyses on Noblesse …….....… 125 – 127

Figure B.1 Petrographic thin sections of three ostrich eggshells in cross-polarized transmitted light 134

Figure B.2 Isotopic composition of the total organic fraction (TOF) in modern OES fragments from the same egg ……..... 135

Figure C.1 *Acropora* coral abrader MAN-44-U-Th#-1 ……..... 144
Figure C.2 *Acropora* coral abrader MAN-44-U-Th#-5…….....… 144
Figure C.3 *Acropora* coral abrader MAN-44-U-Th#-9…….....……..... 145
Figure C.4 *Acropora* coral abrader MAN-44-U-Th#-16…….....…..…..... 146
Figure C.5 *Porites* coral abrader MAN-44-U-Th#-22 …….....……..... 147
Figure C.6 *Porites* coral abrader MAN-44-U-Th#-24 …….....……..... 147
Figure C.7 Solution re-analyses of selected coral abraders…….....…… 148
Figure C.8 Apparent ^{230}Th ages, U concentrations, and (^{234}U/^{238}U) ratios of Pleistocene coral abraders from MAN-44 …….....…… 149
Figure C.9 XRD diffractograms for standards with known mixtures of aragonite and calcite..... 150
Figure C.10 X-Ray Diffractograms from selected samples from MAN-44…….....….... 151
Figure C.11 [U] and ^{232}Th/^{238}U from LA-ICP-MS traverses of MAN-44-U-Th#-1 ....….....…… 152
Figure C.12. [U] and ^{232}Th/^{238}U from LA-ICP-MS traverses of MAN-44-U-Th#-4 ….....……... 153
Figure C.13 [U] and ^{232}Th/^{238}U from LA-ICP-MS traverses of MAN-44-U-Th#-5 …….....……. 154
Figure C.14 [U] and ^{232}Th/^{238}U from LA-ICP-MS traverses of MAN-44-U-Th#-7 …….....……. 155
Figure C.15 [U] and ^{232}Th/^{238}U from LA-ICP-MS traverses of MAN-44-U-Th#-8….....….....…. 156
Figure C.16 [U] and ^{232}Th/^{238}U from LA-ICP-MS traverses of MAN-44-U-Th#-11….....…..… 157

List of Tables

Table 1.1 Summary of R_{FCs}^{ACs} from published data 7
Table 1.2 Size fractions and irradiation times for each disc..... 10
Table 1.3 Weighted mean F-values of individual pits from all irradiations in this study..... 15
Table 1.4 *R* values from co-irradiated samples in irradiations 450PRA, 452A, and 449, and calculated *R* values from irradiation 424 16
Table 1.5 Matrix of intralaboratory weighted mean R values for all iterations of the four samples evaluated..... 18
Table 1.6 Interlaboratory values of R_{FCs}^{ACs} obtained by different methods..... 21
Table 1.7 Summary of ages for ACs..... 23
Table 2.1 List of stable isotope terms and proxy definitions..... 29
Table 2.2 Lukenya Hill isotope data and re-calibrated ^{14}C ages..... 37
Table 2.3 Isotope data for Kisese II..... 40
Table 3.1 Highest Posterior Density (HPD) estimates for Bayesian calibration model parameters in the main excavation block of MAN-44 74
Table 3.2 Coral abraders analyzed in this study with their stratigraphic information..... 75
Table 3.3 Summary of ^{230}Th dates of Holocene coral abraders from site MAN-44 listed by stratigraphic zone..... 78
Table 3.4 ^{230}Th ages for Pleistocene coral abraders from MAN-44, Mangaia..... 79
Table 3.5 General characteristics of the spatial distribution of U and Th in samples analyzed by laser ablation ICP-MS..... 94
Table B.1 Extraction protocol tests on modern OES fragments from the same egg..... 136
Table C.1 Comparison of faraday with ion counter measurements after normalizing to CRM-145 standard..... 143

Supplementary File 1.1 (digital) Data table for all $^{40}Ar/^{39}Ar$ measurements
Supplementary File 2.1 (digital) Data table for all isotope measurements of ostrich eggshells
Supplementary File 3.1 (digital) Data table for all U-series solution measurements, laser ablation measurements, and XRD results for corals from MAN-44, Mangaia

Acknowledgements

There is a lot I am grateful to have learned and done at Berkeley and there are many people to thank for these opportunities. I thank Paul Renne for serving as chair of my dissertation in addition to serving on my exam committee, being my first project advisor, and for his exceptional advising these past five years. I thank Warren Sharp for serving as my second project advisor, exam and dissertation committee member, and for his invaluable advising throughout the years at Berkeley. I thank Michael Manga for serving as chair of my qualifying exam committee, for always being available to converse about science or otherwise, and for being an excellent teacher of geodynamics. I also thank M. Manga for being the first geology professor to give me a chance at research, despite my lack of geology background at the time. I thank Kurt Cuffey for serving on my qualifying exam and dissertation committees, and I appreciate Kurt's insights and constructive criticism in formative moments of my Ph.D. I thank Todd Dawson for serving on my qualifying exam and dissertation committees, for his most enjoyable course in stable isotope ecology, and for providing a space to share ideas in his classroom.

I thank my co-authors on the manuscripts that comprise the chapters of this thesis for granting permission to use and reproduce the material from a publication of which he/she was co-author as part of my dissertation at UC Berkeley: Paul R. Renne, Daniel Rutte, Alan L. Deino, Warren D. Sharp, Christian A. Tryon, J. Tyler Faith, Jason Lewis, Kathryn Ranhorn, Stefania Mambelli, Melanie J. Miller, Todd E. Dawson, and Patrick V. Kirch. I thank Elsevier permission to permit the inclusion of published material in a thesis or dissertation. Funding for this research has been provided by a UC Berkeley Fellowship, The Leakey Foundation, NSF BCS-1727085, BCS-1521133, EAR-1322017, and the Ann and Gordon Getty Foundation.

Because each chapter in this thesis comes from a manuscript that has been published or that is in review, I thank all those who helped improve those manuscripts. This includes researchers who provided analytical services such as J. Attard for XRD analyses and Paula Reimer at the University of Belfast ^{14}Chrono Centre for ^{14}C analyses, the workers from excavation teams who recovered many of the samples I studied in this thesis, students in the IsoTopics classes who discussed ideas with me, Renne group members, U Lab group members, and the anonymous reviewers who improved those manuscripts that are already published. I also am grateful to my colleagues in archaeology who acquired other sources of funding and permits to excavate and retrieve samples that I was able to study.

While this dissertation is certainly representative of the research I conducted in my Ph.D. program, I was fortunate to have many opportunities to become involved in additional diverse projects. For this reason, I have many people to thank for giving me these opportunities. First, I am thankful to Paul Renne and Warren Sharp for inviting me to participate in so many incredible projects across the globe. I am thankful for the collaborators who took me under their wing in the field, including Biagio Giaccio, Eleonora Regattieri, Giovanni Zanchetta, Paolo Galli, and Sebastien Nomade in the Fucino Basin of Italy, and Simon Armitage, Christopher Henshilwood, Karen Van Niekerk, and Graham Avery in South Africa. I am thankful to Courtney Sprain for taking me as her field assistant to the Hell Creek in Montana and teaching me paleomagnetic sampling techniques. I especially would like to thank the Middle Awash research team for inviting me into a project unlike any other, and for the chance to see how world class paleoanthropology research is conducted. Thanks goes to Berhane Asfaw, Yonas Beyene, Yonatan Sahle, and the Middle Awash field crew, of whom there are too many to name, but

thanks to Ahmed Elema, Lad, and the Afar people for teaching me about life in the Afar. I thank Marianne Brasil for her friendship and feel lucky to have met a most excellent future collaborator. I particularly thank Giday Woldegabriel for his mentorship in the field, and Tim White, from whom it has been a privilege to learn about paleoanthropology and all aspects of field science. I thank Tim for the opportunity to come to the Middle Awash and for being a mentor to me both at Berkeley and in the field. I am a better field scientist than I could have hoped to become, thanks to what I learned in the Middle Awash.

I learned a lot in the classroom at Berkeley and thank the professors who were generous with their time while I was their student. I have been fortunate to feel as though I had many places on campus where I felt a sense of belonging beyond the Earth & Planetary Science Department. I am grateful to Todd and Stefania Mambelli who helped some of my ideas about stable isotope ecology blossom into research projects. I also thank Stefania, Melanie Miller, and Wenbo Yang for assistance in the stable isotope lab. I thank the Human Evolution Research Center, particularly Leslea Hlusko, Tim White, Marianne Brasil, and Joshua Carlson, for including me in seminars and other events.

The Berkeley Geochronology Center (BGC) has become a home for me, and it is in large part due to the people there. I thank Tim Becker for his training, help, and patience in the noble gas lab, Al Deino and Roland Mundil for discussion of data, Abed (Abdur-Rahim) Jaouni and Aileen (Chihiro) Ishida for sample preparation assistance, Nicholas Fylstra, Christina Polito, and Brian Jones for their assistance and training in the uranium lab, Lisa Smeenk for assistance with paleomagnetic samples, and to the personnel at BGC, namely Françoise Spaulding-Keller and Tania Borostyan. I have met my future colleagues and made friends at BGC, and I am thankful for the time I spent with all of the students and postdocs who have come through the lab in my 5 years there, especially Courtney Sprain, Isabel Fendley, Andrew Tholt, Daniel Rutte, C. Brenhin Keller, Alyssa Abbey, Neil Griffis, Matthew Fox, and Chelsea Willett. I am grateful to all the BGC scientists for their kindness and availability to discuss science or elsewise at the coffee pot. I thank the graduate students and postdocs in the Earth & Planetary Science Department for the collaboration, comradery, and inspiration through the years, as well as the staff in the department for their help with administrative tasks. I am grateful to my students who made teaching a pleasure to do, and I am particularly grateful to Luis Erick Aguirre-Palafox and Kimberly Vargas who went from being excellent students of petrology to invaluable lab assistants at BGC.

I was also at Berkeley as an undergraduate and some of my professors in this stage of life helped guide me with their advice and experience. I thank Marc Davis and James Graham in the UC Berkeley Astronomy department for cultivating my interest in astronomy, despite my resistance to learn to code at the time. I thank Kim Shelton and Ted Peña in the UC Berkeley Classics department for training me in excavation techniques and archival collections study, and for showing me the magic of field-based science. As a master's student at CSU Long Beach, I was welcomed into the Geology Department by Gregory Holk even though I had a lot of catching up to do. His decision to put faith in me, when no other geology program would take the risk, represents a turning point in my academic path. I send my deepest gratitude to Greg for being an excellent M.S. advisor and for helping me break into the field. I am grateful for his mentorship, as well as the mentorship of Hector Neff, Carl Lipo, Richard Behl, and Stan Finney. I thank Carl for teaching me about archaeology both in the classroom and the lab. I particularly want to thank Hector for taking me to the field in Mexico, for the enriching personal and scientific experiences I gained from those field seasons, and for the opportunities to do research in archaeological science.

This work is the outcome of multidisciplinary, collaborative efforts in the field and the lab. Without collaborators in paleontology, biology, archaeology, geology, and geochemistry, I would not have learned so much about the many facets of Earth Science that drive my research. None of this would have been possible without the professional support and collaborative web of my advisors, Paul Renne and Warren Sharp. I cannot express in words how their influence has changed my life, the way I think, and who I have become professionally. Paul and Warren have given me unbridled freedom to explore scientific questions, and their faith in my abilities has catapulted me to opportunities far beyond what I could have dreamt. Each has shown me the power of producing consistently excellent and transparent results, and the importance of cautious, thoughtful interpretation. Paul has given me every opportunity to thrive as a student. This includes sending me to every workshop under the time-telling sun (special thanks to Frits Hilgen, Sietske Batenberg, and Diederik Liebrand for their incredible workshop in Sicily on cyclostratigraphy), showing me how to be a good and effective teacher of petrology, introducing me to the geochronology community, providing me with the strongest foundation of data analysis I could have, and for patiently explaining the nuts and bolts of noble gas measurements and data interpretation. Warren has been the most thoughtful advisor at every step of my program and gave me room to explore new avenues of research. I am extremely thankful for Warren's incredible dedication of time to me, from hours-long weekly meetings to careful editing of manuscripts, for teaching me how to write a proposal, to process and dissect complicated data, and for sharing the thrilling experience of discovery with me in developing new dating applications. I thank both Paul and Warren for leading by example and showing me what it looks like to run a lab and be an outstanding P.I. with the utmost integrity and care. I am forever grateful for their guidance and mentorship and I consider it an honor and a privilege to learn from them.

I will always be thankful that I had the chance to return to the East Bay, where I grew up, to complete my Ph.D. at Berkeley. Beyond my professional life, I have many loved ones who supported me through this long academic road. I thank my father and sister for being proud of me. I am thankful for the personal support of my closest friends, especially Kate, Caroline, Maja, Brielle, Dana, Taylor, and Mollie. My mother Laura is the best role model I could hope to have. I am forever grateful for her love, sacrifices, support, strength, and advice that helped me become the person I am today. I want to finally thank my fiancée Devin who has been with me through all of my graduate school adventures – he continued to support my dreams when I was figuring out my plans, when I started a master's program, and again when I committed to the Ph.D. at Berkeley. His unwavering support, love, compassion, and sense of humor have helped me enjoy each day of these years in graduate school. The journey would not have been so pleasant without Devin, and I am grateful to him as we move on to the next phase of my academic career together.

Introduction

The co-occurrence of major climate fluctuations with the evolution and diversification of the human lineage starting ~6 million years ago (Ma) has inspired researchers to assess whether climate events correlated with or caused changes in human biological and cultural evolution. Beyond interpretations that biological evolution such as speciation events may have been driven by climate changes (e.g., DeMenocal, 2011; Grove and Burke, 2015; Potts, 1998; Vrba, 1985), adaptations by hominids[1] including *H. sapiens* have been posited to be driven or mediated by climate, such as advancements in material culture (e.g., Jones and Stewart, 2016; Potts et al., 2018; Ziegler et al., 2013) and geographic range expansion out of Africa (e.g., Tierney et al., 2017; Timmermann and Friedrich, 2016). After the development of modern human behaviors characterizing the Middle Stone Age as early as ~320 thousand years ago (ka) (Deino et al., 2018), when humans appear to adapt to more diverse environments and later successfully disperse out of Africa, interrogators begin to flip the question of cause and effect between climate and human evolution, to ask how humans may have instead unintentionally modified, impacted, and eventually purposefully manipulated their environments. In assessing the consequences of environmental modification, correlative extinctions of other fauna have led to debates on whether human arrival into new territories may have caused ecosystem shifts, extirpations, extinctions, and even ecological collapse (Cooper et al., 2015; Diamond, 2005; Miller et al., 2016; Pires et al., 2015).

The timing, tempo, and sequence of these climatic, biological, and cultural changes, and how they are geologically recorded, are crucial to test hypotheses on the covariance of human evolutionary and environmental change. Yet, highly resolved, far-field climate records (e.g., marine, ice cores) frequently referenced in this context may lack the ability to address localized paleoenvironmental change relevant to the small spatial scales and coarser temporal resolution documented by the paleoanthropological record. Necessary but not sufficient conditions to hypothesize causal webs linking climate, human evolution, and associated extinctions include the need for independent, precise, and accurate chronologies documenting environmental change in association with rare fossils and archaeology.

This research integrates high-precision geochronology and stable isotope proxy-records within the context of human biological and cultural evolution. Here, I utilize 40-argon/39-argon ($^{40}Ar/^{39}Ar$) and uranium-series (U-series) geochronology in tandem with light stable isotopes to analyze a diverse array of terrestrial depositional environments and time ranges characterizing when and in what environmental context humans evolved, innovated, and expanded our geographic range within and outside of Africa. Each chapter outlines the use of one of these applications and then provides a case study addressing geological and paleoanthropological questions in the Quaternary Period. The following chapters provide a foundation for refining and improving the quality (e.g., precision, accuracy, applicability) of geochronometers and isotope proxy-records so that their application to human evolutionary and other geologic records are better characterized, utilized, and applied. Because each chapter focuses on the application of one of these three techniques, a brief introduction to each technique is warranted.

In Chapter 1, I refine the age of Alder Creek sanidine, a widely used mineral standard employed in Quaternary applications of $^{40}Ar/^{39}Ar$ geochronology. The $^{40}Ar/^{39}Ar$ dating

[1] For clarity, the term "hominid" is defined here to include all taxa on the human lineage after the last common ancestor between chimpanzees and humans.

technique derives from the potassium-argon (K-Ar) technique, in which radioactive ^{40}K decays by electron capture to ^{40}Ar (Aldrich and Nier, 1948). However, because of the diverse geochemical behavior of K, a large ion lithophile, and its daughter product Ar, an inert noble gas, these two elements must be measured under different conditions in a mass spectrometer. Thus, to measure and calculate ages from the K-Ar technique, two separate samples must be analyzed, one for its K content and isotope composition, and one for its Ar isotope composition. However, subtly different physical and chemical properties and different analytical procedures may affect the precision and accuracy of a resulting age calculation derived from two independent measurements. Instead, the $^{40}Ar/^{39}Ar$ dating technique allows measurement of all parameters necessary to calculate an age in a single aliquot of sample (Dickin, 1995; McDougall and Harrison, 1999; Merrihue and Turner, 1966). This is possible by converting the less abundant, stable isotope of ^{39}K into ^{39}Ar by neutron capture in a nuclear reactor. This technique is most frequently applied to volcanic rocks, including basalts and ash fall deposits called tephra or tuffs. The most precise and accurate approaches typically analyze a K-rich feldspar, such as volcanic sanidine, and use laser step-heating or total fusion of single- to multi-grain aliquots. Sanidine is uniquely effective for dating eruptive episodes because it is not only an abundant K-rich mineral frequently found in alkalic tuffs (also called tephra), but it also forms late in the magma crystallization process just prior to eruption. Sanidine-dated tephra are particularly useful in geological and paleoanthropological applications because they represent a geologically "instantaneous" event of an explosive volcanic eruption. Tephra are deposited as a blanket of ash that can cover a landscape for ~ km to up to ~10^3 km in the case of large eruptions (e.g., Albert et al., 2019; Giaccio et al., 2017; Mark et al., 2017). These isochronous tephra deposits become interbedded with sedimentary sequences hosting fossils and archaeology, which if dated by the $^{40}Ar/^{39}Ar$ method, provide chronostratigraphic anchors for intercalated fossiliferous sediments. This approach has been a bulwark for determining the ages of fossils in the eastern African rift valleys where volcanic activity has persisted since before the earliest evidence of hominids in the rift valleys (e.g., Renne et al., 1999; WoldeGabriel et al., 2001).

Mineral standards are required in the $^{40}Ar/^{39}Ar$ technique, because they allow characterization of the nuclear reactions produced from high-energy neutron flux in the nuclear reactor. Irradiating standards with minerals from lithologic units of unknown age allow nuclear fluence parameters to be extrapolated to samples of unknown age. Standards thus must have well-defined ages in order to determine neutron fluence parameters precisely and accurately. In Chapter 1, I outline an approach to determining the age of Alder Creek sanidine by co-irradiating it with other standards whose ages have been determined by K-Ar and other approaches and using a simple metric to relate the ages of any two samples. The refined age of the Alder Creek standard is not only now applied to various paleoanthropological records (Deino et al., 2018, 2019; E.M. Niespolo et al., 2018a), but it also has implications for its independent comparison of $^{40}Ar/^{39}Ar$ ages to other widely used chronometers such as U-Pb and astronomical tuning.

In Chapter 2, I review and suggest novel light stable isotope paleoenvironmental proxy records using ostrich eggshells recovered from paleoanthropological sites in Africa. Unlike radioactive isotopes like K and U, stable isotopes do not decay with time. Stable isotope studies are based on comparisons of the ratios of the lighter versus heavier isotopes of the same element in a natural sample compared to the relative abundances of two isotopes in an isotopically well-characterized and homogeneous material (also called a standard). Because isotope offsets relative to natural abundances on earth, or fractionation, are process-related, fractionation between two stable isotopes can be measured to learn about geological, physical, chemical, and biological

processes in the past. Light stable isotope ratios are particularly impacted by kinetic effects because of the larger relative mass difference between two isotopes of the same element. There are many interpretations of the light stable isotope compositions of terrestrial and extraterrestrial materials which depend on the processes affecting each isotope system (Sharp, 2007). The stable isotopic composition of biologically produced materials, such as biominerals and organic compounds, are impacted by both physical and biological processes causing fractionation due to equilibrium and disequilibrium effects such as kinetic and exchange reactions (Fry, 2006). Biological processes impacting the stable isotope composition of animal tissues in many cases relate to the local environment and/or diet of the plant or animal (e.g., Ambrose and DeNiro, 1986; Dawson et al., 2002; DeNiro and Epstein, 1981; Koch, 1998; Levin et al., 2006).

Chapter 2 describes how the C, N, and O isotopic composition of the calcite and organic fraction of ostrich eggshells relate to the ostrich diet, mean annual precipitation, and evapotranspiration, respectively. With internal reliability criteria, these proxy systems can be applied to archaeologically recovered ostrich eggshells and used for paleoenvironmental reconstruction. As an example of these applications, I discuss the paleonvironmental proxy records using a ~50-4 ka record of ostrich eggshell $\delta^{13}C$, $\delta^{15}N$, and $\delta^{18}O$ values from archaeological sites recording the Middle to Later Stone Age (MSA/LSA) transition at Lukenya Hill (Kenya) and Kisese II (Tanzania). This archaeological transition defines an advancement in human behaviors exhibited by advances in material culture (Faith et al., 2013; Klein, 2008; McBrearty and Brooks, 2000; Tryon and Faith, 2013), and the interval coincides with the timing of the successful radiation of *H. sapiens sapiens* from Africa (e.g., Akazawa et al., 2002; Henn et al., 2018). Pairing these approaches with a newly developed application of dating ostrich eggshells with $^{230}Th/U$ burial dating (E.M. Niespolo et al., 2018b, 2017, Sharp et al., 2015, n.d.) these proxies have the potential to reconstruct precisely dated paleoenvironmental records on timescales of $\sim 10^6$ years and in geographic regions beyond the African continent prior to extirpation of the ostrich (*S. camelus*) in Eurasia.

In Chapter 3, I outline the application of ^{230}Th dating of coral artifacts from Eastern Polynesia, the final and most isolated extent of human geographic range expansion on Earth starting ~ 1 ka. ^{230}Th (also called $^{230}Th/U$ or U-series) dating relies on the long-lived parent isotope ^{238}U which decays into a series of radiogenic daughter isotopes until it becomes the stable daughter ^{206}Pb (Bourdon et al., 2003; Dickin, 1995). Certain intermediate radiogenic isotopes, ^{234}U and ^{230}Th, have significantly long half-lives such that their simultaneous production and decay with respect to the parent isotopes can serve as an independent chronometer with respect to the U-Pb decay system. This technique can be readily applied from the latest Holocene ($\sim 10^1$ a) to the Middle Pleistocene (up to ~750 ka in ideal samples). U-series dating has been an especially useful tool for dating carbonates because oxidized U (UO_2) dissolved in aqueous solutions readily substitutes for the calcium ion (Ca^{2+}) in the carbonate structure ($CaCO_3$). Carbonates precipitate in Ca-saturated solutions in both marine and terrestrial environments, and so the U-series technique is widely applied to carbonates (e.g., calcite, aragonite) such as travertine, corals, pedogenic carbonates, and speleothems (Edwards et al., 2003; Henderson and Anderson, 2003; Richards and Dorale, 2003). While corals in marine contexts have provided a rich history of paleoceanographic change that can be precisely dated by U-series (e.g., Cheng et al., 2000; Edwards et al., 2003), chapter 3 focuses on the application of ^{230}Th dating coral artifacts derived from MAN-44, a carefully excavated Holocene archaeological site at Tangatatau rockshelter on the island of Mangaia, Eastern Polynesia. MAN-44 hosts numerous coral artifacts once used as abrading tools to make mother-of-pearl fish

hooks. I establish internal reliability criteria based on the U-series isotopic data, mineralogy, and geochemical distribution of U and Th in coral samples and compare the results to a Bayesian ^{14}C chronology for the site. The most extreme examples of environmental manipulation are claimed to have caused negative faunal and environmental impacts on not only native species but also on the pre-industrial human populations themselves. A popular example of this comes from the interpretations of the Polynesian archaeological record of Rapa Nui, where some suggest environmental ecosystem collapse drove human population decline (Diamond, 2005), while other current research suggests environmental modification was done to sustain populations during eastern Polynesian expansion (Hunt and Lipo, 2012; Kirch et al., 2017a). Site MAN-44 has been an early example of sustainable environmental modification in Polynesian prehistory (Diamond, 2017; Kirch et al., 2017a). The results of ^{230}Th coral dates at MAN-44 imply an earlier arrival to Mangaia than previously determined by ^{14}C dating alone and still consistent with Mangaian settlement pre-dating colonization of the more isolated Pacific Islands further east. ^{230}Th coral dates provide the temporal framework to demonstrate early evidence of return voyages from South America, with implications for refining the understanding of Polynesian expansion across eastern Polynesia prior to European contact.

These techniques are all unique in their execution and application, but integrated together, they provide a powerful tool kit to understanding the timing, tempo, and environmental context of human evolution and adaptation.

Chapter 1: Intercalibration and age of the Alder Creek sanidine $^{40}Ar/^{39}Ar$ standard

Abstract

The accuracy of $^{40}Ar/^{39}Ar$ geochronology relies in large part on precise and accurate calibration of the ages and K-Ar isotopic compositions of standards. A widely used standard for Quaternary samples, the ~1.2 Ma Alder Creek sanidine (ACs), has published ages spanning a range of ~2%. New measurements of ACs co-irradiated with the Fish Canyon sanidine (FCs) standard and sanidines from astronomically dated Miocene tuffs in Crete and Morocco yield results that enable both (i) a direct calibration of ACs relative to FCs, and (ii) stepwise calibrations between these two standards employing the Miocene intermediaries. Results are summarized by the parameter R_{FCs}^{ACs}, defined as the ratio of ($^{40}Ar^*/^{39}Ar_K$) of ACs to FCs, which embodies the fundamental age relationship between these standards that is independent of systematic variables such as decay constants or absolute ages of standards. Our new measurements, executed using three mass spectrometers and various irradiation and analytical protocols, yield a weighted mean $R_{FCs}^{ACs} = 0.041702 \pm 0.000014$ (σ). This result can be combined with previously published determinations of *R* values for ACs relative to the Miocene tuffs and to FCs to yield a recommended interlaboratory value of $R_{FCs}^{ACs} = 0.041707 \pm 0.000011$. The weighted-mean age of ACs using this interlaboratory value, based on astronomically-calibrated ages of FCs and the Miocene intermediary sanidines, is $t_{ACs} = 1.1848 \pm 0.0006$ Ma (± 0.05%). Applying this result to the most precise published $^{40}Ar/^{39}Ar$ data for the Matuyama-Brunhes geomagnetic polarity reversal yields $t_{MBB} = 780.1 \pm 0.8$ ka. In addition, these new data for ACs support previous conclusions that U-Pb zircon ages from the Alder Creek rhyolite incorporate ~13 ka of pre-eruptive residence time.

1: Introduction

The $^{40}Ar/^{39}Ar$ technique is one of the most powerful dating methods available given its potential for high-precision ages and its broad applicability in a multitude of geological settings. However, the accuracy of the technique is limited by our knowledge of the true age and K-Ar isotopic composition of standards (neutron fluence monitors) used to determine the $^{40}Ar^*/^{40}K$ ratios of unknowns through neutron activation analysis. Accuracy concerns are especially critical in the late Neogene, where $^{40}Ar/^{39}Ar$ ages are evaluated against comparably precise constraints from independent dating methods such as orbital tuning, ^{14}C, or U-series.

Good analytical practice in $^{40}Ar/^{39}Ar$ dating dictates that the ages of standards should be as close as possible to the ages of samples being dated in order to minimize mass spectrometric biases potentially imposed by divergent ion beam intensities and their ratios. Accordingly, Turrin et al. (1994) proposed sanidine from the early Pleistocene Alder Creek rhyolite in the Napa-Sonoma volcanic province of northern California as a Quaternary (*sensu lato*) $^{40}Ar/^{39}Ar$ standard. This sanidine (ACs) was proposed in part because the lava was emplaced during the Cobb Mountain geomagnetic polarity event, which can in principle be dated independently by

orbital tuning methods. Turrin et al. (1994) obtained an age of 1.186 ±0.006[2] Ma for this sanidine, based on an age of 27.84 Ma for the neutron fluence monitor used, sanidine from the Fish Canyon Tuff of Colorado (FCs). Renne et al. (1998) reported an age of 1.194 ±0.007 Ma using 28.02 Ma for FCs, identical to the value reported by Turrin et al. (1994) when recalculated to the same age for FCs. A subsequent study (Nomade et al., 2005) of sanidine from a recollected sample yielded an age of 1.193 ±0.001 Ma also using 28.02 Ma as the age of FCs, indistinguishable from the prior two results.

More recently, several ages for ACs relative to FCs have been published by Coble et al. (2011), McDougall et al. (2012), Phillips and Matchan (2013), Rivera et al. (2013) and Jicha et al. (2016) that are distinct from the previous results as summarized by Nomade et al. (2005). Part of this inconsistency is due to different ages ascribed to the FCs standard upon which these ages are based; this is mainly because ^{40}Ar* concentrations in K-Ar dated primary ('first-principals' standards calibrated through separate K and Ar measurements) standards weren't well known enough to resolve interlaboratory differences between calibrations of FCs. To isolate the effects of different calibrations versus analytical variability, we focus herein on Ar isotope systematics rather than computed ages. A simple metric for the age relationship between any two samples, which is independent of irradiation time or age assumed for the anchoring standard (in this case, FCs), is the *R*-value introduced by Renne et al. (1998):

$$R_{FCs}^{ACs} = \frac{\left(e^{\lambda t_{ACs}} - 1\right)}{\left(e^{\lambda t_{FCs}} - 1\right)} \equiv \frac{\left({}^{40}Ar*/{}^{39}Ar_K\right)_{ACs}}{\left({}^{40}Ar*/{}^{39}Ar_K\right)_{FCs}} \tag{1.1}$$

where λ is the total ^{40}K decay constant, ${}^{40}Ar*$ is the proportion of ^{40}Ar that is radiogenic, and ${}^{39}Ar_K$ is the proportion of ^{39}Ar that is produced from potassium during neutron activation. *R*, which relates the age of ACs to that of FCs, may be determined either from corrected mass spectrometric data or from reported ages. For convenience, we define a parameter *F* as:

$$F \equiv {}^{40}Ar*/{}^{39}Ar_K \tag{1.2}$$

such that

$$R_{FCs}^{ACs} = \frac{F_{ACs}}{F_{FCs}} \tag{1.3}$$

[2]All uncertainties in this paper are stated at the level of σ.

Publication	R	± (abs.)	± (%)
Turrin et al. (1994)	0.04229	0.00021	0.50%
Renne et al. (1998)	0.04229	0.00006	0.14%
Nomade et al. (2005)	0.04230	0.00006	0.14%
Coble et al. (2011)	0.04180	0.00021	0.50%
McDougall et al. (2012)	0.04189	0.0006	1.43%
Rivera et al. (2013)	0.04175	0.00003	0.07%
Phillips & Matchan (2013)	0.04169	0.00002	0.04%
Singer (2014)	0.04185	0.00011	0.27%
Jicha et al. (2016)	0.04176	0.00004	0.09%

Table 1.1: Summary of R_{FCs}^{ACs} from published data. These reflect excess scatter yielding an imprecise and potentially inaccurate calibration of ACs.

Table 1.1 shows a summary of *R* for the published ACs to FCs data. The population of *R* exhibits excess scatter about the weighted mean (0.041787 ± 0.000014), as indicated by a mean square of weighted deviates (MSWD, equivalent to the reduced chi-squared statistic) of 39.9. This indicates that the observed scatter is more than expected by the stated analytical uncertainties of the data (the data are 'overdispersed').

A contributing factor to the overdispersion may be the underestimation of error introduced in attempting to measure co-irradiated samples of ACs and FCs with $^{40}Ar/^{39}Ar$ ratios differing by a factor of ~24, which requires inevitable compromises in irradiation times and attendant differences in the behavior of ion beams, particularly of ^{40}Ar and ^{39}Ar. In order to mitigate these difficulties, part of this study is designed to calibrate the ACs standard with a sample intermediate in age between ACs and FCs, allowing the R_{FCs}^{ACs} value to be determined stepwise using the relationship

$$R_{FCs}^{ACs} = R_{X}^{ACs} \cdot R_{FCs}^{X} \tag{1.4}$$

For this purpose, sample "X" can be completely arbitrary provided it is intermediate in age between ACs and FCs and yields reproducible Ar isotope data. Ideally, it should be similar in chemical composition to ACs and FCs to minimize differences in irradiation-induced interference corrections; i.e., a sanidine is most suitable.

For this study, ACs and FCs were co-irradiated and analyzed with sanidines from an ignimbrite of the Messâdit section, Melilla basin, Morocco (Mes4) and sanidine from the A1 distal fallout tephra of the Faneromeni section at Sitia, Crete, Greece (A1). These tuffs have independent orbitally tuned ages of 6.791 ±0.005 Ma and 6.943 ±0.0025 Ma, respectively (Kuiper et al., 2008; Rivera et al., 2011). The Messâdit sanidine was previously analyzed by Kuiper et al. (2008) and serves in large part as basis for an orbitally tuned age of 28.201 ±0.023 Ma for FCs. The A1 sanidine was used by Kuiper et al. (2004) and Rivera et al. (2011) to determine ages of 28.21 ±0.04 and 28.172 ±0.014 Ma, respectively, for FCs. Thus, in addition to serving as intermediaries in the stepwise intercalibration of ACs and FCs, independent orbitally tuned ages can be determined for ACs through Mes4 and A1. The calibration of ACs using astronomically tuned standards instead of primary standards minimizes the introduction of uncertainty from decay constants into the final age calculation for young Cenozoic samples (Kuiper et al, 2008). By varying grain size, irradiation time and degassing schedule (i.e., step-heating versus total fusion), and employing multi- as well as single-collector mass spectrometry, we test for the possible effects of recoil, varying ion-beam behavior, and detector intercalibration.

In addition to the stepwise intercalibration of ACs with FCs through the two intermediaries (Mes4 and A1), new direct ACs/FCs intercalibration data are presented for comparison. As shown below, these various approaches yield consistent results.

2: Methods

2.1: Samples

ACs (ACs-2) The Alder Creek sanidine (ACs) was obtained from the same sample (ACs-2) of the Alder Creek rhyolite analyzed by Nomade et al. (2005) from Cobb Mountain, California (N38°48'6.1", W122°45'05.4"). Phenocrystic sanidine prepared from this sample has been widely distributed to $^{40}Ar/^{39}Ar$ community worldwide. The Alder Creek rhyolite was erupted during the Cobb Mountain geomagnetic polarity subchron, whose age has been estimated by orbital tuning of marine sediments between 1.173 to 1.185 Ma (Horng et al., 2002) and 1.190 to 1.215 Ma (Channell et al., 2002; Shackleton et al., 1990).

Mes4 (ME00-2) Phenocrystic sanidine from sample ME00-2 (N35°21'5.48", W3°1'26.93") is from an ignimbrite in the Messâdit section of Kuiper et al. (2008), and it is equivalent to sample Mes4 of that study. The tuff occurs near the base of the sequence and is ~5m thick, distinctly thicker than any other tuff in the section. The sample analyzed on MAP 1 and a MAP215-50 instrument dubbed "Nexus" was collected by P.R.R. accompanied by K. Kuiper in 2000. A second sample (analyzed on the Noblesse) was collected in 2001 by A.L.D., accompanied by K. Kuiper.

A1 (FAN-1) Sample FAN-1 (N35°13'19.57", E26° 3'59.00") is phenocrystic sanidine from the dacitic-rhyolitic A1 tephra as identified in the Faneromeni marine sapropel cyclostratigraphic section on Crete (FAN-1; Kuiper et al., 2004; Rivera et al., 2013, 2011), collected by A.L.D. accompanied by K. Kuiper in 1999.

FCs The sample of Fish Canyon Tuff was collected in 1998 (N 37°36.646', W 106°42.331') by A.L.D. and C. Swisher. 264 kg of rock were collected and sent to M. Villeneuve at the Geological Survey of Canada for sanidine separation.

2.2: Sample preparation

All samples were crushed, sieved, and washed in distilled water in an ultrasonic bath. Sanidine was separated using a Frantz Isodynamic magnetic separator and heavy liquids. The sanidine concentrates were cleaned with dilute hydrofluoric acid in an ultrasonic bath for 5 minutes to remove adhering groundmass, and finally handpicked to purity. Size fractions used in the various experiments are listed in Table 1.2.

Irradiation			Size fractions (μm)			
Number	Time (h)	Layout	ACs	Mes4	A1	FCs
450PRA	4 h	mixed pits	841-1410	595-841, 841-1410	-	-
424	10 h	separate pits	600-700	500-600	500-600	300-350
452A	3 h	mixed pits	700 – 840	500-600	-	400-500
449	3 h	mixed pits	700-840	-	-	350-400

Table 1.2. Size fractions and irradiation times for each disc. See Figure 1 for disk configurations and sample arrangements.

2.3: Irradiation

Samples were irradiated in the Cd-lined, in-core CLICIT facility of the Oregon State University TRIGA reactor. Irradiation times are given in Table 1.2. Figure 1.1 shows the layout of the samples in the high-purity Al discs used as sample containers. In three irradiations (450PRA, 452A, and 449) the samples were mixed within individual pits and in one irradiation (424) the samples were irradiated in separate pits. Irradiation 424 contained ACs, FCs, Mes4, and A1 all in separate pits equidistant from the disc center. Planar regressions were fit to the FCs data to determine comparable *F* values of FCs in pits containing ACs, Mes4, or A1. In irradiation 450PRA, the horizontal (within disc) fluence variations were monitored with additional ACs samples allowing assessment of maximal gradients over mixed pits and to evaluate fluence variation between separate pits.

The approximate radiogenic ^{40}Ar concentration ratio of ~6 between ACs and Mes4/A1 and of ~4 between Mes4/A1 and FCs allowed a reasonable compromise in irradiation time. Contrasting with an approximate ^{40}Ar concentration difference of ~24 between ACs and FCs. This highlights the advantage of the intermediate intercalibration step using *R* values in avoiding under- or over-irradiation of one of the samples. We chose irradiation times of 3-4 h—optimized for ACs, Mes4 and A1—for irradiations 450PRA, 452A and 449 and a more FCs-optimized irradiation time of 10 h for irradiation 424. In addition, in irradiation 450PRA the grain sizes of Mes4 and ACs were paired in pits with the intent to yield similarly sized ion beams of ^{40}Ar or ^{39}Ar depending on the size fraction of ACs loaded with Mes4. For equivalently sized samples, ^{39}Ar ion beams after irradiation are similar, while the combination of ACs with a smaller Mes4 fraction yields similarly sized ^{40}Ar ion beams.

Interference corrections were based on the following nucleogenic production ratios (Renne et al., 2015): $(^{40}Ar/^{39}Ar)_K = (7.30 \pm 0.92) \times 10^{-4}$; $(^{37}Ar/^{39}Ar)_K = (2.24 \pm 0.16) \times 10^{-4}$; $(^{38}Ar/^{39}Ar)_K = (1.196 \pm 0.013) \times 10^{-2}$; $(^{39}Ar/^{37}Ar)_{Ca} = (7.02 \pm 0.12) \times 10^{-4}$; $(^{36}Ar/^{37}Ar)_{Ca} = (2.702 \pm 0.004) \times 10^{-2}$; $^{36}Cl/^{38}Cl = (2.628 \pm 0.002) \times 10^{2}$.

To evaluate fluence gradients over the Al discs, the two distinct irradiation geometries used require separate treatment (Figure 1.1). In irradiations 449, 450PRA, and 452A, the various samples were irradiated in mixed pits with depths of 2–3.3 mm and diameters of 3.2–5.3 mm. Filling height of irradiation pits was similar, excluding influence by axial fluence gradients (i.e., variation in flux in the vertical direction of the stacked discs). Assuming equal distribution of grains in the pits, no absolute correction for horizontal fluence gradients need be made when comparing average F values of different samples in one pit. However, given the finite spatial extent of the pits, the fluence gradient adds to the variance of the F values within each pit. Rutte et al. (2015) showed that the three-dimensional variation of neutron fluence in a reactor core is expected to be the result of superposing inverse-square and exponential decay functions. However, over the small extent of the irradiation discs a planar fit is a good first order approximation with residuals of <0.3%, and mostly <0.1%. The computed gradients over individual pits are 0.04% (n=4; 449a), 0.15% (n=9; 450PRA), and 0.01% (n=2; 452A). Thus, within-pit horizontal fluence gradients may explain up to 0.15% of the variance of *F* values and therefore some excess dispersion in F values (MSWD >1). In irradiation 424, *F* values of FCs distributed over the disc were used to fit a planar function, representing horizontal variation in neutron fluence (n = 4; 0.21 %/cm, residuals 0.024%). We normalized all results of this disc, allowing comparison of F values of individual pits to FCs.

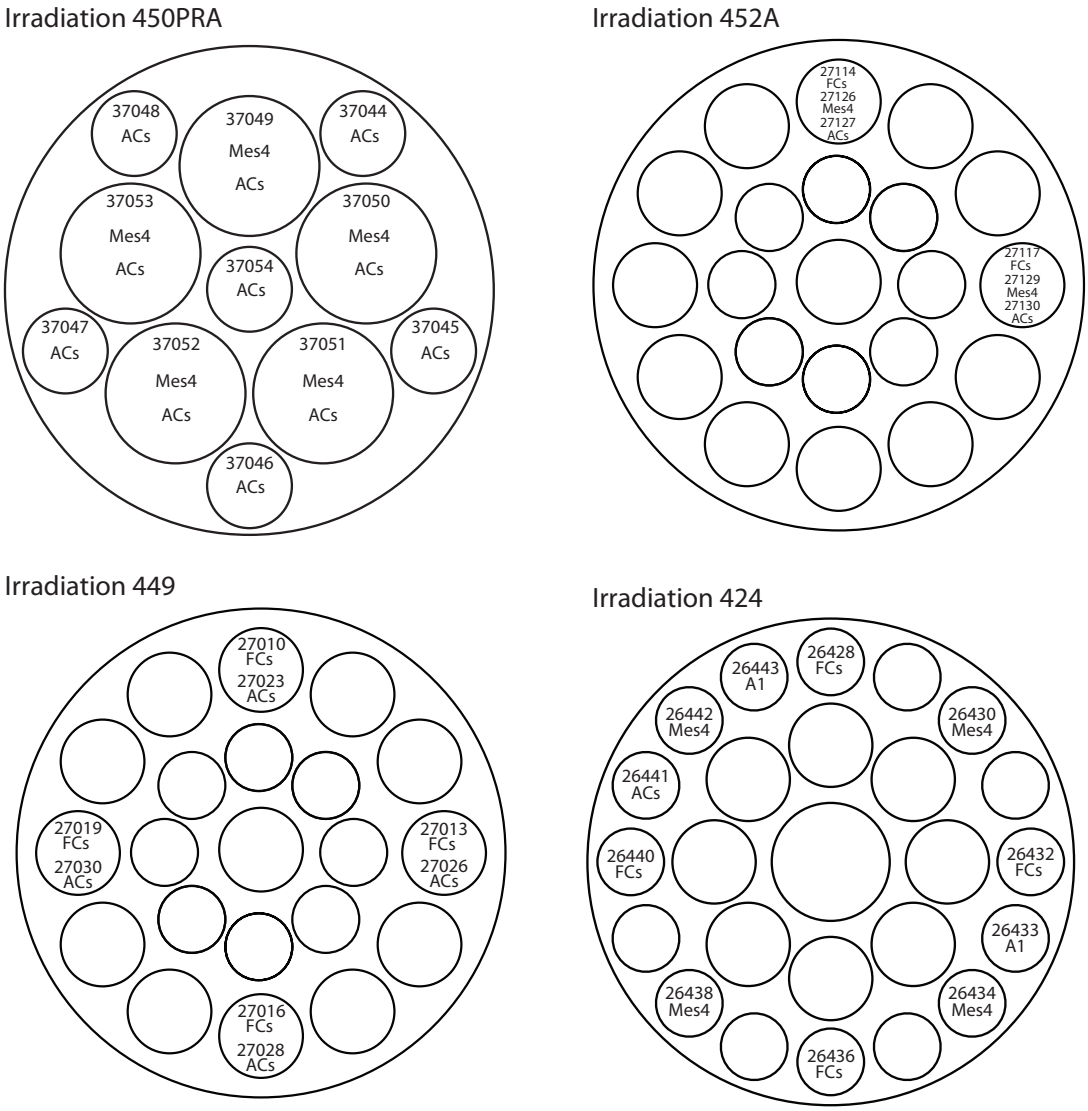

Figure 1.1. Disc maps for each of the 18.54-mm aluminum irradiation discs. ACs and Mes4 samples in irradiation 450PRA have the same lab ID numbers and were distinguished during analysis by $^{40}Ar^*/^{39}Ar_K$.

2.4: Analytical procedures

All analyses were conducted at the Berkeley Geochronology Center (BGC) on three mass spectrometers dubbed Nexus, MAP 1, and Noblesse.

2.4.1: Nexus and MAP 1

Irradiation 450PRA consisted of an eleven pit 18.54-mm aluminum disc irradiated for 4 hours. The five large pits of the disc were loaded with an even mixture of ACs and Mes4 in order to eliminate uncertainties in the neutron fluence between pits. Six additional small pits contained only ACs in order to provide additional control of neutron fluence across the disc area. Two large pits from this irradiation were analyzed on MAP1, a MAP 215-C mass spectrometer. Three large pits of mixed ACs and Mes4 as well as the six pits containing only ACs from irradiation 450PRA were analyzed on Nexus. Both MAP instruments have Nier-type ion sources and analog electron multiplier detectors.

Single grains from the large pits of mixed ACs/Mes4 underwent total laser fusion from a CO2 laser at 8 watts of power. ACs samples from small pits were measured by laser fusion analyses of 3-grain aliquots that were used only in the evaluation of fluence gradients and not in any calculations of R values.

For each sample, blank, and air pipette, fifteen cycles at 8-35 integrations per cycle were measured for each Ar isotope using peak hopping by magnetic field switching on a single detector. Evolved gases were cooled to ca. -100 to -130 °C using a cryotrap and exposed to a ca. 450 °C hot getter to remove reactive gases.

For each large pit of ACs/Mes4, a mean blank correction was determined using background isotopic measurements analyzed between each single-grain analysis. Blanks between sample measurements were stationary over time, and mean values and their standard deviations were used to correct the data for unknowns and air pipettes. For Nexus runs, blanks were 3-4 × 10^{-17}, 5-15 × 10^{-19}, and 7-8 × 10^{-19} moles for ^{40}Ar, ^{39}Ar and ^{36}Ar, respectively. For MAP 1 runs, blanks were 1-2 × 10^{-16}, 1-2 × 10^{-18}, and 2-3 × 10^{-19} moles for ^{40}Ar, ^{39}Ar and ^{36}Ar, respectively.

Mass discrimination was determined based on automated analyses of air pipettes between every five single grain analyses (plus intercalated blanks) using air pipette data based on a power law correction (Renne et al., 2009) and the atmospheric values of Lee et al. (2006); values of 1.0099 to 1.0104 and 1.0126 per Dalton were determined for Nexus and MAP 1, respectively.

2.4.2: Noblesse

Samples analyzed on the *Noblesse* multicollector mass spectrometer were irradiated in three separate batches. Irradiations 449 and 452A contained pits loaded with crystals of more than one sample: 449 had four pits with both ACs and FCs standards, and 452A had four pits loaded with both of these as well as with Mes4. Irradiations 449 and 452A, like 450PRA, allow direct comparison of *F*-values for evaluation of *R* without necessarily accounting for differences in neutron fluence.

The samples analyzed using the *Noblesse* multicollector instrument were degassed by incremental heating on a dedicated extraction line. Quasi-uniform heating of each sample (a single grain of sanidine) was achieved via illumination with a CO_2 laser fitted with a beam-shaping lens to generate a flat energy profile of adjustable diameter, typically 2 mm at the target

distance. Individual grains of sanidine were heated for ~30 seconds at progressively increasing power levels (0.9–8 watts) until fusion was achieved; typically 3-10 steps were employed for ACs, Mes4, and A1, and 4–13 steps for FCs. Evolved gas was exposed for several minutes to an approximately -130°C cryotrap to remove H_20, and to a GP-50 SAES getter to remove reactive gases.

Ar isotopic measurements were performed on a *Noblesse* 5-collector sector-magnet mass spectrometer, configured with one axial Faraday detector and four off-axis, symmetrically arrayed ETP ion counters. Prior to inlet of sample gas from the extraction line for determination of Ar isotopic composition, a 3% aliquot of the extraction line volume was measured on the mass spectrometer within a short (~7 s) interval. On the basis of this brief measurement, adjustments were made as necessary to the sample abundance by pumping away a calibrated fraction of the gas to evacuated ballast volumes. The goal of this procedure was to restrict the signal level of ^{40}Ar on the ion counters to less than ~500 kcps across all experiments, corresponding to a maximum ^{40}Ar of ~6×10^{-15} moles. Typically, volume splitting was unnecessary, given careful adjustment of the step-heating schedule. Subsequent to this test protocol, the remainder of the sample gas was inlet to the mass spectrometer and five Ar isotopes measured over a period of ~800 seconds. The isotopic measurement process involved simultaneous measurement of ^{40}Ar, ^{37}Ar, and ^{36}Ar on separate ion counters, alternating with peak hopping to position ^{38}Ar and ^{39}Ar on the same ion counter as ^{40}Ar. All signals were normalized to the ^{40}Ar ion counter. ^{36}Ar signal normalization was achieved through periodic measurement of the $^{40}Ar/^{36}Ar$ ratio of air argon (Lee et al., 2006) inlet from an air-reservoir pipetting system. Ar abundance from air aliquots experiments was closely matched to the unknowns, yielding 2.3×10^{-15} moles ^{40}Ar. ^{37}Ar and ^{38}Ar signal normalizations were achieved through periodic measurement of ^{40}Ar from a static gas sample on relevant detectors in a systematic round-robin peak-hopping procedure.

Procedural blanks, matching sample gas extractions precisely but without firing the laser, were run every four analyses and typically yielded ~6×10^{-17}, 4×10^{-19}, and 4×10^{-19} moles of ^{40}Ar, ^{39}Ar, and ^{36}Ar, respectively. Blanks preceding air pipette measurements were tailored specifically to mimic an actual air pipette extraction, with the exception that the inner pipette valve leading to the air reservoir was not opened. The Noblesse has sufficiently high resolution to distinguish an almost entirely hydrocarbon free shoulder at mass 36, where the measurement for ^{36}Ar is made. For further details of the analytical procedures refer to Deino et al. (2010).

Irradiation	Pit #	Lab ID	Sample	Wtd. Mean F	± (abs.)	± (%)	Number of grains included (excluded)[a]
450PRA	6	37049	ACs	0.61929	0.00045	0.074	28 (1)
			Mes4	3.5532	0.0011	0.032	30 (2)
	7	37050	ACs	0.61972	0.00043	0.069	22 (2)
			Mes4	3.5653	0.0008	0.022	23 (0)
	8	37051	ACs	0.62072	0.00052	0.084	30 (0)
			Mes4	3.5622	0.0010	0.029	32 (1)
	9	37052	ACs	0.62315	0.00074	0.12	30 (0)
			Mes4	3.5798	0.0016	0.044	26 (3)
	10	37053	ACs	0.62453	0.00073	0.12	25 (0)
			Mes4	3.5882	0.0012	0.033	26 (0)
424	13	26441	ACs	0.25263	0.00029	0.11	14 (1)
	3	26430	Mes4	1.45013	0.00072	0.050	12 (1)
	7	26434	Mes4	1.44807	0.00064	0.044	13 (2)
	11	26438	Mes4	1.45128	0.00063	0.043	14 (0)
	15	26442	Mes4	1.45161	0.00068	0.047	14 (0)
	6	26433	A1	1.47732	0.00082	0.056	15 (0)
	16	26443	A1	1.48139	0.00094	0.063	17 (0)
	1	26428	FCs	6.0471	0.0024	0.039	11 (0)
	5	26432	FCs	6.0443	0.0026	0.043	10 (0)
	9	26436	FCs	6.0433	0.0021	0.035	10 (0)
	13	26440	FCs	6.0515	0.0025	0.041	10 (0)
449	1	27023	ACs	0.8583	0.0010	0.11	7 (1)
		27010	FCs	20.646	0.012	0.058	6 (0)
	4	27026	ACs	0.86083	0.00085	0.10	11 (0)
		27013	FCs	20.6600	0.0092	0.044	7 (0)
	7	27028	ACs	0.86173	0.00091	0.11	10 (0)
		27016	FCs	20.6288	0.0087	0.042	7 (0)
	10	27030	ACs	0.85600	0.00079	0.09	9 (1)
		27019	FCs	20.6289	0.0088	0.043	6 (0)
452A	1	27127	ACs	0.83806	0.00088	0.10	11 (1)
		27126	Mes4	4.8128	0.0022	0.046	10 (0)
		27114	FCs	20.0787	0.0069	0.034	9 (0)
	4	27130	ACs	0.83671	0.00088	0.10	9 (0)
		27129	Mes4	4.8072	0.0023	0.048	10 (0)
		27117	FCs	20.0738	0.0064	0.032	9 (0)

[a] Filtered with a normalized median absolute deviation (nMAD) threshold of 3

Table 1.3. Weighted mean F-values of individual pits from all irradiations in this study.

Lab ID	R_{Mes4}^{ACs}	± (abs.)	± (%)	Irradiation
37049	0.174292	0.000140	0.080372	450PRA
37050	0.173821	0.000126	0.072562	450PRA
37051	0.174253	0.000154	0.088388	450PRA
37052	0.174074	0.000220	0.126425	450PRA
37053	0.174051	0.000213	0.122101	450PRA
27127/27126	0.174232	0.000319	0.183017	452A
27130/27129	0.174152	0.000430	0.247127	452A
(R_{FCs}^{ACs}) / ( )	0.174193	0.000289	0.165648	424
Lab ID	R_{FCs}^{Mes4}	**± (abs.)**	**± (%)**	**Irradiation**
27126/27114	0.239551	0.000177	0.073805	452A
27129/27117	0.239339	0.000159	0.066558	452A
Irr. 424	0.239694	0.000089	0.037166	424
Lab ID	R_{FCs}^{ACs}	**± (abs.)**	**± (%)**	**Irradiation**
27127/27114	0.041737	0.000070	0.167476	452A
27130/27117	0.041682	0.000099	0.237995	452A
27023/27010	0.041546	0.000050	0.121312	449
27026/27013	0.041671	0.000045	0.107029	449
27028/27016	0.041773	0.000044	0.104135	449
27030/27019	0.041672	0.000042	0.100786	449
26441	0.041753	0.000067	0.161425	424
Calculated	0.041655	0.000035	0.083354	R_{Mes4}^{ACs} (450PRA) × (Kuiper et al., 2008)

Irradiation 424 individual pit R values vs. FCs

Lab ID	R_{FCs}^{unk}	± (abs)	± (%)	Sample ID "*Unk*"
26430	0.239658	0.000214	0.089085	Mes4
26433	0.244508	0.000251	0.102614	A1
26434	0.239524	0.000145	0.060662	Mes4
26438	0.239932	0.000194	0.080648	Mes4
26441	0.041753	0.000067	0.160948	ACs
26442	0.239779	0.000183	0.076154	Mes4
26443	0.244866	0.000252	0.102954	A1

Table 1.4. *R* values from co-irradiated samples in irradiations 450PRA, 452A, and 449, and calculated *R* values from irradiation 424. Under R_{FCs}^{Mes4} the four pits of Mes4 in irradiation 424 are given as a weighted mean *R* value (details in text).

3: Results

3.1: R values

Results in terms of inverse variance weighted mean *F* values for each sample in each irradiation position are shown in Table 1.3 and Supplementary Figures 1.1-1.5. For all of the *Noblesse* data, which were analyzed by incremental heating, the integrated results were used for the most appropriate comparison with total fusion results from Nexus and MAP-1. Step heating data are provided as individual steps in the supplementary tables. 13 of 85 step heating results of FCs (Supplementary Figure 6) are identified as clearly rising after the first step; 5 of these had integrated ages above the mean and 8 of them had ages below the mean. However, using the same nMAD = 3 filter as used for calculating weighted mean *F* values, calculation of integrated ages shows no significant affect to the weighted mean age of FCs for these spectra. While some recent studies (e.g., Jicha et al., 2016; Phillips and Matchan, 2013) have suggested that FCs is a non-ideal standard due to variations in age spectra, our data reveal little evidence to question the suitability of FCs as a standard for high-precision $^{40}Ar/^{39}Ar$ geochronology based on total gas measurements. Likewise, our step heating results for ACs produce consistent flat age spectra and a well-constrained distribution of total gas ages (MSWD = 1.94) for 71 out of 72 analyses (Supplementary Figure 7), unlike that indicated by Jicha et al. (2016). Step heating results for Mes4 and A1 can also be found as Supplementary Figures 8-9. For irradiations 449 (FCs and ACs), 450PRA (ACs and Mes4) and 452A (ACs, Mes4, and FCs), the samples were co-irradiated in the same disc position and the corresponding *R*-values for each position are shown in Table 1.4. For irradiation 424 (ACs, Mes4, A1, and FCs) each sample was irradiated in a separate pit and the *R*-values between each of the samples was determined by interpolation. For the determination of *F* values for each position we used an nMAD > 3 (normalized median absolute deviation from the median) criterion to define outliers which were then excluded from further calculations; on this basis 16 of 533 analyses were excluded. *R* values were then computed from the appropriate *F* values per Equation (1.3).

Determinations of *R* values relating the various samples are presented in matrix form as shown in Table 1.5. The *R* matrix provides a summary of intralaboratory weighted mean *R* values between any two standards. The column header indicates the numerator of the *R* value and the row header indicates the denominator. These R values may be used to integrate these data with previous and future data sets. Our seven new direct measurements of R_{FCs}^{ACs} (weighted mean R_{FCs}^{ACs} = 0.041689 ± 0.000020) are consistent with values obtained using Mes4 or A1 as intermediaries (weighted means R_{FCs}^{ACs} = 0.041714 ± 0.000020 and 0.041753 ± 0.000080, respectively). We take the weighted mean (R_{FCs}^{ACs} = 0.041702 ± 0.000014, 0.033%) of these three determinations as the best estimate of our intralaboratory value.

R_{row}^{column}	**ACs**	**Mes4**	**A1**	**FCs**
ACs	1	5.743859 ± 0.002195 (± 0.038%)	5.860311 ± 0.010375 (± 0.177%)	23.993239 ± 0.009950 (± 0.041%)
Mes4	0.174099 ± 0.000067 (± 0.038%)	1	1.020825 ± 0.000833 (± 0.082%)	4.173618 ± 0.001240 (± 0.030%)
A1	0.170639 ± 0.000302 (± 0.177%)	0.979600 ± 0.000800 (± 0.082%)	1	4.086868 ± 0.002970 (± 0.073%)
FCs	0.041678 ± 0.000017 (± 0.041%)	0.239600 ± 0.000071 (± 0.030%)	0.244686 ± 0.000178 (± 0.073%)	1

Table 1.5. Matrix of intralaboratory weighted mean R values for all iterations of the four samples evaluated.

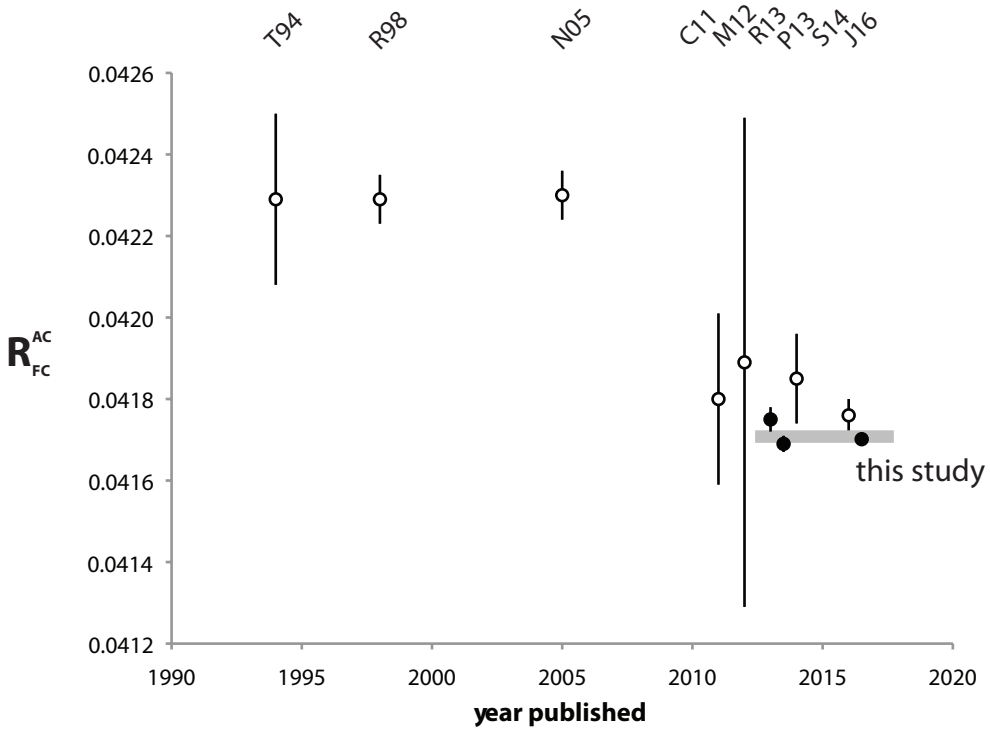

Figure 1.2. Compilation of R_{FCs}^{ACs} values from previous publications and this work. Abbrevations are for:T94: Turrin et al. (1994); R98: Renne et al. (1998); N05: Nomade et al. (2005); C11: Coble et al. (2011); M12: McDougall et al. (2012); R13: Rivera et al. (2013); P13: Phillips & Matchan (2013); S14: Singer et al. (2014); J16: Jicha et al. (2016). Solid circles identify R_{FCs}^{ACs} that were incorporated into the weighted mean interlaboratory R_{FCs}^{ACs} represented by the shaded gray bar (see text for justification).

3.2: Comparison with previous data

Our direct determination of R_{FCs}^{ACs} can be compared with previous results shown in Table 1.1 (Figure 1.2). Results differ significantly from pre-2006 studies (Nomade et al., 2005; Renne et al., 1998; Turrin et al., 1994), all of which were conducted at BGC. Several factors render our new data superior to those of the previous studies: (1) The spatial density of neutron fluence monitoring is much higher, including many co-irradiations in the same pit; (2) Choice of grain sizes and irradiation durations to optimize ^{39}Ar and ^{40}Ar ion beams and their ratios; (3) Use of 15 cycles of peak-hopping (versus 7-10 cycles in the previous studies) on the single-collector (MAP) instruments provides more accurate constraints on the intercepts of ion beam intensity versus time, particularly for ^{36}Ar; (4) More integrations per cycle were employed for ^{36}Ar and ^{39}Ar for the MAP data, further enhancing the accuracy of ion beam intercepts. Hence, pre-2006 results are excluded based on our well-informed confidence in the superiority of the new data. The results of Coble et al. (2011), McDougall et al. (2012), and Singer (2014) are relatively imprecise and compatible with a large range of values; hence these are excluded. We attempted to include the data of Jicha et al. (2016), obtained from the same preparation of ACs as ours, by computing total gas results for their incrementally-heated ACs samples. The uncertainties we calculate from their data are larger than reported. The MSWD calculated for R_{FCs}^{ACs} from total gas results of Jicha et al. (2016) (computed from incremental heating data) is 31.4, much larger than the value of 6.41 determined from their single step fusion results. Our own total gas results for R_{FCs}^{ACs}, obtained with an identically configured mass spectrometer, are significantly less scattered with an MSWD value of 2.03. We suspect that Jicha et al. (2016) underestimated contributions from background or interference corrections resulting in spuriously high precision and resultant overdispersion of their data. For these reasons, we exclude the results of Jicha et al. (2016) from our interlaboratory compilation despite their reported R_{FCs}^{ACs} being indistinguishable from our own. Our new results can be most appropriately be compared with Rivera et al. (2013) and Phillips and Matchan (2013). We note that the latter study used 2-3 grains of ACs for their step-heating analyses (D. Phillips, written communication, 2014), in contrast to all other data considered here which are based on analysis of single crystals. The weighted mean R_{FCs}^{ACs} of these three sets of experiments is 0.041702 ± 0.000011 (0.026%).

A stepwise determination of R_{FCs}^{ACs} may be calculated using Mes4 as an intermediary. Our eight independent measurements of R_{Mes4}^{ACs} are the first of which we are aware and these form a coherent data set with a weighted mean of 0.174099 ± 0.000067 (0.038%). Our three new measurements of R_{FCs}^{Mes4} compare reasonably well with those of Kuiper et al. (2008), and accordingly we combine our data with the latter to yield an interlaboratory value of 0.239555 ± 0.000066 (0.027%). The corresponding stepwise value of $R_{FCs}^{ACs} = R_{Mes4}^{ACs} \cdot R_{FCs}^{Mes4}$ is 0.041706 ± 0.000020 (0.047%).

Method	R_{FCs}^{ACs}	±σ	±σ (%)
Direct	0.041702	0.000011	0.03%
Via Mes4	0.041706	0.000020	0.05%
Via A1	0.041753	0.000038	0.09%
Weighted Mean	**0.041707**	**0.000011**	**0.03%**

Table 1.6. Interlaboratory values of R_{FCs}^{ACs} obtained by different methods.

A second stepwise determination of R_{FCs}^{ACs} is calculated using A1 as an intermediary. Our data yield a value of 0.041753 ± 0.000080 (0.191%), which may be compared with a value of 0.041753 ± 0.000043 (0.104%) determined from the data of Rivera et al. (2011) and Rivera et al. (2013). The interlaboratory weighted mean of both results gives R_{FCs}^{ACs} = 0.041753 ± 0.000038 (0.091%).

The three distinct approaches to determining R_{FCs}^{ACs} using interlaboratory data as discussed above are summarized in Table 1.6. As shown, these result in a weighted mean R_{FCs}^{ACs} = 0.041707 ± 0.000011 (0.026%), which we recommend as an interlaboratory value.

3.3: Age of ACs

In the foregoing we have derived interlaboratory values for the intercalibration of ACs with several other standards. These values are based on analysis in three different laboratories, using five different mass spectrometers (three multicollector and two single collector) employing a variety of analytical protocols. We turn now to the issue of the age of the ACs standard.

3.3.1 Age based on astrochronology of Mes4

Using our results for R_{Mes4}^{ACs}, the astrochronologic age of 6.791 ± 0.005 Ma (Kuiper et al., 2008), the ^{40}K total decay constant of 5.463 ± 0.107 × 10^{-10} a^{-1} (Min et al., 2000), Equations 5 and 6 of Renne et al. (1998) yield

$$t_{ACs} = \frac{1}{5.463\times10^{-10}a^{-1}} ln\left|\left(e^{(5.463\times10^{-10}a^{-1})(6.791\times10^{6}a)} - 1\right)(0.174099) + 1\right| \quad (1.5)$$

= 1.1841 ± 0.00098 Ma

3.3.2 Age based on astrochronology of A1

Our results for R_{A1}^{ACs} combined with the R_{A1}^{ACs} value in Table 1 of Rivera et al. (2013) (0.170462 ± 0.000313) yield a weighted mean value of 0.17055 ± 0.00022 (0.127%). Substituting this value and the astrochronologic age of 6.943 ±0.0025 Ma for the A1 tephra into the above Equation (1.5) yields an independent astronomical age (t_{ACs} = 1.1860 ± 0.0016 Ma) that is indistinguishable from that based on Mes4 (although less precise because *R* was less well determined).

Method	Age of ACs (Ma)	± σ (Ma)	± σ (%)
Via FCs*	1.1849	0.0009	0.08%
Via Mes4	1.1841	0.0010	0.08%
Via A1	1.1860	0.0016	0.13%
Astronomical	**1.1848**	**0.0006**	**0.05%**
Optimization	**1.1891**	**0.0008**	**0.07%**

*Based on all Messâdit section tuning data of Kuiper et al., 2008

Table 1.7. Summary of ages for ACs. Astronomical result shows the weighted mean of three ages via FCs, Mes4, and A1 calibrations above. Optimization result shows the age of ACs using the weighted mean interlaboratory R_{FCs}^{ACs} in the optimization calibration (Renne et al., 2011).

3.3.3: Ages based on intercalibration with FCs

Using our preferred interlaboratory value of $R_{FCs}^{ACs} = 0.041707 \pm 0.000011$ (Table 1.6), we can calculate an astronomical age for ACs based on the astronomical calibration of FCs from Messâdit (Kuiper et al., 2008). This is not strictly independent of the foregoing results based on Mes4, because data from Mes4 were included in that calibration. Using the astrochronological age of 28.201 ± 0.022 Ma for FCs (Kuiper et al., 2008), using the uncertainty which neglects contribution from the decay constant, and applying Equation (1.5) with appropriate substitutions, yields $t_{ACs} = 1.1849 \pm 0.0009$ Ma, in excellent agreement with the other two astronomically-calibrated ages. Although these three ages are not strictly independent, we take the weighted mean $t_{ACs} = 1.1848 \pm 0.0006$ Ma (0.052%) as the best representation of all available astronomical constraints on the age of ACs.

A fundamentally different approach uses the so-called optimization calibration of (Renne et al., 2011), which is based on an optimal fit to ^{40}K disintegration data, K and Ar isotopic data for the FCs standard, and pairs of ^{40}Ar/^{39}Ar and ^{238}U-^{206}Pb data representing a partial normalization to the ^{238}U decay constant. Using our preferred interlaboratory value of R_{FCs}^{ACs} as above applied to the calibration of Renne et al. (2011) yields $t_{ACs} = 1.1891 \pm 0.0008$ Ma, which is distinct at 95% confidence from the Mes4 and FCs based astronomically calibrated ages outlined above, but not from the less precisely determined age based on A1. However, all of these ages (Table 1.7) are younger than the younger mode of ^{238}U-^{206}Pb zircon ages (1.1978 ± 0.0023 Ma) inferred by Rivera et al. (2013) for the Alder Creek rhyolite based on the likelihood of pre-eruptive residence time of zircons in silicic magmas (Simon et al., 2008).

3.4: Recoil?

The data from irradiation 450PRA, wherein two different size fractions of Mes4 were coirradiated with a single size fraction of ACs, can be used to evaluate the possibility of age bias due to differential ^{39}Ar recoil effects (Hall, 2014). The ratio of ^{39}Ar ion beams for ACs relative to Mes4 for the two positions with larger Mes4 grains is ~0.68, whereas for the three positions with smaller Mes4 grains the average ratio is ~1.60. *R* shows no correlation with the relative ^{39}Ar ion beams, from which we conclude that any bias due to differential ^{39}Ar recoil effects is negligible owing to the close match in grain sizes. Hence the fractional ^{39}Ar recoil loss from each sample is comparable, and the effect on the computed *R* values is negligible as the fraction retained is the same in the *F* values comprising the numerator and the denominator.

3.5: Application to the Matuyama-Brunhes Boundary (MBB)

As the most recent non-excursional geomagnetic polarity reversal, the Matuyama/Brunhes boundary (MBB) is arguably the single most referenced magnetostratigraphic marker in Quaternary chronostratigraphic studies. Estimates of the age of the MBB span >20 ka (Singer, 2014). The most precise datum available for the age of the MBB is from the Sulmona paleolake of central Italy (Sagnotti et al., 2014), where the MBB is tightly bracketed by ^{40}Ar/^{39}Ar dates on sanidine from intercalated tephras, and was dated to 786.1 ± 0.8

ka based on the ACs age calibration of Nomade et al. (2005) and the decay constants of Steiger and Jäger (1977) This age corresponds to a value of $R_{ACs}^{MBB} = 0.65830 \pm 0.00067$, which combined with our values of R_{Mes4}^{ACs} and R_{A1}^{ACs} yields indistinguishable ages of 779.6 ± 1.0 ka and 780.8 ± 1.3 ka for astronomical ages based on Mes4 and A1, respectively. These two independent calibrations yield a weighted mean age for the MBB of 780.1 ± 0.8 ka. The optimization calibration (Renne et al., 2011) of ACs applied to the MBB yields an age of 782.8 ± 1.0 ka, indistinguishable from either of the independent astronomical ages or their weighted mean mainly due to the relatively large uncertainty in R_{ACs}^{MBB}. All of these results are significantly older than the age of 773.1 ± 0.4 ka for the MBB inferred by Channell et al. (2010) based on correlation of marine oxygen isotope records to an orbitally tuned ice-volume model. While this discrepancy may have important implications for paleoceanography and/or geomagnetic field behavior, such issues are beyond the scope of this paper.

4: Conclusions

Our new $^{40}Ar/^{39}Ar$ measurements of the ACs standard relative to the widely-used FCs standard, directly as well as through an intermediate step using two astronomically dated sanidines (Mes4 and A1), enable determination of R_{FCs}^{ACs} that is consistent with other recent measurements of this parameter, yielding an interlaboratory value with relative uncertainty of 0.026%. The resulting improvement in interlaboratory consistency is reassuring, but does not completely resolve the issue of absolute calibration as the weighted mean astronomical age (1.1848 ± 0.0006 Ma) differs significantly (by 0.36%) from the optimization calibrated age (1.1891 ± 0.0008 Ma).

Application of the interlaboratory data to the most precise $^{40}Ar/^{39}Ar$ data for the age of the Matuyama-Brunhes boundary (Sagnotti et al., 2014) yields ages for the boundary of 780.1 ± 0.8 ka (weighted mean astronomical age) and 782.8 ± 1.0 ka (optimization age) which are indistinguishable at the 95% confidence level. Both of these ages are distinctly older than that ascribed to the MBB by Channell et al. (2010).

Our results compared with the ^{238}U-^{206}Pb zircon data (Rivera et al., 2013) indicate that zircons from the Alder Creek rhyolite record 13 ± 2 (based on the astronomical age of ACs) or 9 ± 2 ka (based on the optimization age of ACs) of pre-eruptive magma residence time. This conclusion agrees with that of Rivera et al. (2013), and it is noteworthy because it indicates that even the youngest mode of zircon U-Pb ages pre-dates eruption by a resolvable interval (assuming that the $^{40}Ar/^{39}Ar$ system accurately records the time of eruption). In this case the bias is small compared with some other examples (Simon et al., 2008; Wotzlaw et al., 2014) but it raises the question of what distinct petrologic event, if any, is recorded by zircon U-Pb ages in cases wherein a well-defined and geochemically distinct youngest age mode is present. If such modes represent the integrated history of zircon crystallization (Ickert et al., 2015), then they may cluster well but still be biased by tens or hundreds of ka relative to the eruption age.

Re-printed with permission from: Niespolo, E.M., Rutte, D., Deino, A.L., & Renne, P.R., 2017, Intercalibration and age of the Alder Creek sanidine $^{40}Ar/^{39}Ar$ standard. Quaternary Geochronology, v. 39, 205 – 213, doi: 10.1016/j.quageo.2016.09.004

Chapter 2: Carbon, nitrogen, and oxygen isotopes of ostrich eggshells provide site-scale Pleistocene-Holocene paleoenvironmental records for eastern African archaeological sites

Abstract

Quantitative, well-dated, local paleoenvironmental records are necessary to 1) evaluate localized responses to regional to global-scale climate change and 2) test hypotheses regarding the covariance of environment and human biological and cultural evolution. Ostrich eggshell (OES) fragments are common in African archaeological sequences, are amenable to ^{14}C and $^{230}Th/U$ dating, and their stable carbon ($\delta^{13}C$) and nitrogen ($\delta^{15}N$) isotopic compositions track local vegetation and mean annual precipitation, respectively. We review previous interpretations of the stable isotopic composition of OES, apply a novel calibration to estimate paleo- mean annual precipitation (PMAP) from $\delta^{15}N$ values, and show that oxygen isotopes ($\delta^{18}O$ values) record evapotranspiration if other components of the water cycle are constrained. The stable isotopic compositions of the organic fraction of OES, extracted using a digestion protocol presented in this study, remain unaltered at least to ~50 ka, indicating potential to examine even older OES. We present a ~50-4 ka record of OES $\delta^{13}C$, $\delta^{15}N$, and $\delta^{18}O$ values from archaeological sites recording the Middle to Later Stone Age (MSA/LSA) transition at Lukenya Hill (Kenya) and Kisese II (Tanzania). At Lukenya Hill, PMAP increased progressively over time from driest conditions ~50 – 31.2 ka (~390 ± 90 mm/yr) to wettest conditions ~6.9 – 3.7 ka (~790 ± 100 mm/yr), despite consistent mixed to C_4-dominated flora suggested from dietary $\delta^{13}C$ values. Conditions were consistently more mesic at Kisese II: driest conditions occur ~46 – 44 ka (~610 ± 125 mm/yr) and wettest conditions ~35.9 – 34.3 ka and ~ 23.7 – 21.2 ka (~750 ± 25 and 45 mm/yr, respectively) with consistently mixed to C_3-dominated flora. Relative increases in C_4 flora correlate with lower PMAP at Kisese II. $\delta^{18}O$ values do not covary with the $\delta^{13}C$ or $\delta^{15}N$ values equivalently at the two localities, but can be interpreted as a proxy for evapotranspiration, which is controlled by temperature, relative humidity, and/or photosynthetic pathway. These proxies indicate changes in paleoenvironment throughout records at both sites, including during the MSA/LSA transition, but changes at each locality contrast with each other. This is likely explained by local ecological and climatological effects that are not resolved by regional-scale paleoclimate records.

1: Introduction

Archaeological and climate records are discontinuous spatially and/or temporally, particularly in eastern Africa (Blome et al., 2012), which today is characterized by diverse rainfall regimes that differ spatially in both amount and seasonal distribution. This, combined with a highly variable bedrock geology and topography, has created a heterogenous patchwork of local environments that can vary across scales of 10^1-10^3 km (e.g., Adams et al., 1996; Lind and Morrison, 1974; Shorrocks, 2007; White, 1983). Proxy records from ice, marine, and lake cores are commonly used to assess possible relations between climatic and human behavioral change (e.g., Jones and Brian A Stewart, 2016; Tierney et al., 2017; Timmermann and Friedrich, 2016; Ziegler et al., 2013). However, these records are generally remote from continental deposits

holding archaeological materials, do not resolve environmental change at scales directly relevant to archaeological sites and their occupants, and are difficult to correlate with archaeological sequences due to insufficiently precise chronological controls on one or both records. The extent to which the present pattern of intra-regional environmental variability can be extended into the past is unknown, but comparison of long-term data from eastern African lacustrine records ≥ 100 km from equatorial paleoanthropological sites has suggested contrasting persistent trends towards either increased aridity (Owen et al., 2018) or a progressively wetter climate (Johnson et al., 2016) throughout the Late Pleistocene. Thus, it is unclear how eastern African lacustrine climate records representing large scale (i.e., >100's km^2) changes correspond to habitat-scale (i.e., < 100's km^2) environmental changes in eastern Africa, the latter which more closely approximates spatial scales experienced by human groups in the past. Furthermore, Middle Stone Age (MSA) sites are spatially unevenly distributed across different biogeographic zones (Tryon and Faith, 2013), and detailed study of individual MSA archaeological sites as well as multi-site analyses have indicated that there may be variable habitat-scale responses to larger scale climate change (Ambrose, 2001; Blome et al., 2012). While the analysis of archaeologically recovered faunal assemblages and local sedimentology are among the most robust records of *qualitative* local environmental change (e.g., wet v. dry) corresponding with archaeological records, there are few ways to assess *quantitative* changes (e.g., precipitation amount) in past environments directly from the archaeological record.

In contrast, paleoenvironmental information obtained directly from archaeological sequences obviates such problems of relevance and correlation, allowing more robust tests of hypotheses regarding the covariance of climate and human behavioral change. Given such variability at the regional as well as the continental scale throughout the Late Pleistocene (Blome et al., 2012), our study of possible environmental drivers for archaeological change begins at the archaeological site as an initial step that must precede comparisons to other records from different depositional basins. Well-preserved ostrich eggshell fragments from excavations can characterize the local paleoenvironment because their carbon and nitrogen stable isotope compositions provide quantitative proxies for vegetation type and mean annual precipitation (MAP), respectively (Johnson et al., 1998; Von Schirnding et al., 1982). Below, we discuss ostrich eggshell oxygen isotopes, how they may relate to local environmental variables, and present a model to estimate evapotranspiration (related to temperature, relative humidity, and plant photosynthetic pathway).

When stratigraphically associated with other archaeological materials, ancient ostrich eggshell can be used to characterize past local environments at geographic and temporal scales directly relevant to human subsistence. This work aims to construct and connect local scale paleoenvironmental records to larger (regional, global) scale records. By applying established and novel interpretations of the stable isotope compositions of ostrich eggshells (OES), we characterize local paleoenvironments of archaeological rockshelter localities in eastern Africa, at Lukenya Hill sites GvJm 22 and GvJm 16 (Kenya) and Kisese II (Tanzania), recording ~50 ka of human subsistence. The last 50 ka include various climatic and archaeological changes such as the Last Glacial Maximum and the African Humid Period, as well as the Middle Stone Age to Later Stone Age (MSA/LSA) archaeological transition. Using carbon, nitrogen and oxygen stable isotope compositions in ostrich eggshell, shown here to retain primary compositions to at least ~50 ka, we evaluate the fidelity of each isotopic record ($\delta^{13}C$, $\delta^{15}N$, and $\delta^{18}O$ values). We then compare the three isotope records integrated at and across the sites which are separated by only by ~300 m elevation, 3° latitude, and 350 km distance, in the context of other

archaeological data. We then assess isotopic signatures of major climate events recorded in the local paleoenvironmental records from Kisese II and Lukenya Hill, we compare them to lacustrine records >100 km away, and we discuss possible dynamic mechanisms responsible for inferred paleoenvironmental changes. The isotopic proxies for past vegetation, precipitation, and evapotranspiration allow us to directly examine if local environmental characteristics were similar or distinct at the two sites during the MSA/LSA transition, whether environments were characterized by extreme or rapid changes during or leading up to the MSA/LSA transition, or if characteristic regional climate changes are recorded at the sites in ostrich eggshell stable isotopes.

2: Background

2.1: Stable isotopes of ostrich eggshells as paleoenvironmental proxies

Ostrich (*Struthio camelus)* eggshell fragments accumulate at archaeological sites through human use, transport, and discard. Ostrich eggs can serve as a nutritious food source, and ethnographic and Late Pleistocene-Holocene examples demonstrate additional uses of the shells as canteens (sometimes decorated with incisions) and as raw material for the production of beads (e.g., Henshilwood et al., 2014; Texier et al., 2013; Wilmsen, 2015). As a result, eggshells are frequently found in archaeological deposits. Because ostriches are broadly unselective feeders, the isotopic compositions of their eggshells reflect local environmental parameters where they obtain their food (Milton et al., 1994). The carbon (C), nitrogen (N), and oxygen (O) isotopic compositions of ostrich eggshells are determined by the local paleoenvironment because the home range of daily food sources of ostriches is ~85 km^2 (Milton et al., 1994; Williams et al., 1993). This is within the geographic range of transport of MSA obsidian tools (e.g., Blegen, 2017; Tryon and Faith, 2013), is within the home ranges expected for equatorial foragers (Kelly, 2013), and thus it can be broadly equated to the home or interaction range for Late Pleistocene eastern African groups when eggshells are retrieved from archaeological deposits.

Ostriches lay eggs annually over a period of ~2 weeks (Leuthold, 1976; Moreau, 1950; Sinclair, 1978). Even in regions with bimodal rainfall, such as around Kisese II and Lukenya Hill, all but one modern subspecies of ostrich (*S. camelus molybdophanes*) lay eggs in only one breeding season per year, typically a few months after the long rainy season (March – May; Leuthold, 1976). Eggshells rapidly form in < 24 hours (Nys et al., 2004, 1999) and their stable isotope composition reflects a snapshot of the ostrich diet of the prior ~3 – 5 days (Johnson et al., 1998). Because OES are stable under modern storage conditions, archival materials recovered from historical excavations are also suitable for light stable isotope analyses and geochronology. While isotopic analyses of animal dentitions (and more rarely bones) found at archaeological or paleontological sites may be used to reconstruct past hominid[3] environments, OES offer an important advantage over these systems because they can be directly dated by both AMS ^{14}C and $^{230}Th/U$ burial dating (Bird et al., 2003; E.M. Niespolo et al., 2018c; Sharp et al., 2016, n.d.), rather than estimated from bounding strata. Below we outline previous efforts to understand each isotope paleoenvironmental proxy. A list of commonly used terms, with reference to these proxy records and those proposed here, is provided in table 2.1.

[3]For clarity, the term "hominid" is defined here to include all taxa on the human lineage after the last common ancestor between chimpanzees and humans.

Term	Definition	Units
R	ratio of rare to common isotope; e.g., $^{18}O/^{16}O$	none
δ	$1000 \times \left(\frac{R_{Sample} - R_{Standard}}{R_{Standard}}\right)$ - 1	‰
$\alpha_{A\text{-}B}$	R_A/R_B	none
$\Delta_{A\text{-}B}$	$\delta_A\text{-}\delta_B \approx 10^3 \ln \alpha_{A\text{-}B}$	‰
$\Delta^{13}C_{calcite\text{-}TOF}$	$\delta^{13}C_{calcite} - \delta^{13}C_{TOF} = 15 \pm 2$	‰
$\delta^{13}C_{diet}$	$\delta^{13}C_{calcite}$ - 16.2	‰
f_{C4}	fraction of C_4 plants consumed	none
PMAP	paleo-mean annual precipitation, using equation 2.4	mm/year
$\alpha_{bodyH2O\text{-}calcite}$	1.0379 ± 0.002	none
$\delta^{18}O_{bodyH2O}$	calculated from $\alpha_{bodyH2O\text{-}calcite}$ and $\delta^{18}O_{calcite}$	‰
$\delta^{18}O_{foliarH2O}$ model 1	solve for $\delta^{18}O_{foliarH2O}$ using calculated ostrich $\delta^{18}O_{bodyH2O}$ and equation 2.5; result derived from $\delta^{18}O_{calcite}$	‰
$\delta^{18}O_{foliarH2O}$ model 2	foliar water $\delta^{18}O$ value calculated from ostrich $\delta^{13}C_{diet}$, f_{C4}, and estimated $\delta^{18}O$ values for cellulose from C_3 and C_4 plants; calculate $\delta^{18}O_{foliarH2O}$ using equation 2.8; result derived from $\delta^{13}C_{calcite}$	‰

Table 2.1: List of stable isotope terms and proxy definitions.

2.1.1: Carbon isotopes in ostrich eggshell

Controlled feeding experiments demonstrated that $\delta^{13}C$ values in OES reflect dietary (plant) $\delta^{13}C$ values offset by biological fractionation (i.e., the trophic effect; Ambrose and DeNiro, 1986; DeNiro and Epstein, 1981; Vogel, 1983) in both the calcite and total organic fraction (TOF) of the eggshell:

$$\Delta^{13}C_{calcite\text{-}diet} = \delta^{13}C_{calcite} - \delta^{13}C_{diet} = +16.2 \pm 0.5‰ \quad (2.1)$$

and

$$\Delta^{13}C_{TOF\text{-}diet} = \delta^{13}C_{TOF} - \delta^{13}C_{diet} = +1.5 \pm 0.8‰ \quad (2.2)$$

as determined by analyses of OES from South African wild ostriches (Johnson et al., 1998; Von Schirnding et al., 1982). Observations of wild ostriches have shown they are opportunistic water-conserving herbivores that feed almost entirely on green plants within their home range with a slight dietary preference for C_3 plants (e.g., leafy plants better adapted to cooler and/or wetter climates), but they generally sample the ambient vegetation in correspondence with the abundance of available plant groups (Milton et al., 1994; Williams et al., 1993). These equations allow us to calculate the $\delta^{13}C_{diet}$ of ostriches from either the calcite or TOF $\delta^{13}C$ values. In modern OES, the difference between the $\delta^{13}C$ values of eggshell calcite and TOF reflect a constant biological fractionation about $\Delta^{13}C_{calcite\text{-}TOF} = 14.7‰$ (Johnson et al., 1998). Those authors suggested that this relation should also apply in well-preserved ancient eggshells and is a necessary condition for inferring that primary C and N isotope values have been retained by ancient OES. Accordingly, Johnson et al. (1998) recommended an acceptance criterion of:

$$\Delta^{13}C_{calcite\text{-}TOF} = 15 \pm 2‰ \quad (2.3).$$

2.1.2: Nitrogen isotopes in ostrich eggshell

Ostriches obtain nitrogen primarily from consumed green plant material (i.e., leaves), and so the $\delta^{15}N$ values of OES are higher relative to foliar $\delta^{15}N$ values due to the trophic effect (Ambrose and DeNiro, 1986; DeNiro and Epstein, 1981). Plants take up nitrogen from the soil with negligible fractionation, especially in N- limited systems frequently found in semi-arid to arid climates (Högberg, 1997); therefore their foliar $\delta^{15}N$ values should mainly reflect the N isotopic composition of soil sources. Soil $\delta^{15}N$ values increase with decreasing MAP (Amundson et al., 2003), due to water availability effects on soil N dynamics and trophic effects (Högberg, 1997). Previous work has demonstrated strong linear inverse relationships between foliar $\delta^{15}N$ values and mean annual precipitation (MAP; e.g., Austin and Sala, 1999; Craine et al., 2009). Because ostriches derive their nitrogen from leaves, OES $\delta^{15}N$ values should preserve this inverse relationship with MAP and record rainfall from the most recent rainy season when leaves grew last (e.g., Johnson et al., 1998), with some time-averaged component depending on the timescales and proportion of N storage in a plant. Most areas inhabited by ostriches experience seasonal long rains rather than year-round rainfall (i.e., a winter or summer rainfall season); hence, most rain for the year occurs in the season preceding egg-laying, so $\delta^{15}N$ values from

seasonally-laid eggs should closely reflect MAP, or perhaps slightly underestimate it, if there is a second short rainy season not represented due to seasonal egg-laying patterns.

2.1.3: Oxygen isotopes in ostrich eggshell

In well-constrained cases, oxygen isotopes of biomineral carbonates can serve as proxies for aridity, as is the case with tooth enamel carbonate from evaporation-sensitive fauna (Levin et al., 2006), and the ^{17}O composition of eggshell and teeth (Passey et al., 2014). Similarly, Miller and Fogel (2016) have proposed a quantitative aridity proxy using $\delta^{18}O$ values of emu (*Dromaius novaehollandiae*) eggshell, considering that emus are obligate drinkers and their $\delta^{18}O$ values will mainly record the $\delta^{18}O$ values of evaporatively enriched standing water bodies. Other studies have interpreted $\delta^{18}O$ values of OES as a qualitative monitor of changing aridity (Lee-Thorp and Ecker, 2015; Roberts et al., 2016).

2.1.4: Preservation of primary stable isotope compositions

Preservation of primary eggshell composition is required to interpret stable isotope records from ancient OES, and because ostrich eggshell is composed almost entirely of low-Mg calcite, it is stable in soil environments in semi-arid to arid climates. Organics represent ~1-3 wt.% of OES comprised mainly of proteins (70%) and polysaccharides (30%) which vary compositionally throughout the eggshell (Feng et al., 2001; Mikhailov, 1997; Nys et al., 1999, and references therein; Von Schirnding et al., 1982). We will refer to the organic component in terms of the total organic fraction (TOF) in OES. Ratite eggshell calcite structures are shown to preserve for ~10^6 years, including primary isotopic $\delta^{13}C$ values, under appropriate environmental conditions (e.g., Segalen et al., 2002; Ségalen and Lee-Thorp, 2009; Stern et al., 1994). Amino acids racemize over this timescale and serve as the basis for amino acid racemization dating, but because they are sensitive to temperature, the preservation of primary, diagenetically unaltered organic material is on the order of ~10^5 years in warmer climates (Brooks et al., 1990) – a sufficiently long time range to analyze organics from Middle- to Late Pleistocene-Holocene OES in Africa. OES from Equus Cave (South Africa) retained the expected $\Delta^{13}C_{calcite\text{-}TOF}$ for up to 17 ka (Johnson et al., 1997), and Newsome et al. (2011) presented $\delta^{15}N$ values of eggshells from emu and the extinct *Genyornis newtonii* as old as ~130 ka. If additional processes such as burning (altering the isotopic composition of TOF, e.g., Miller et al., 2016) or deposition under unsuitable conditions for calcite stability have altered the eggshell composition, $\Delta^{13}C_{calcite\text{-}TOF}$ would fall outside of its natural variability and these samples would not be suitable to interpret the isotopic composition of the TOF.

2.2 Context of eastern African sites Lukenya Hill and Kisese II

2.2.1: Contextualizing the MSA/LSA transition

Paleoenvironmental records retrieved from precisely dated archaeological sequences reveal the diverse array of ecosystems available to humans in the Middle and Later Stone Age (Tryon and Faith, 2013). The shift from Middle Stone Age (MSA) to Later Stone Age (MSA) technologies represents a fundamental change in the Late Pleistocene African archaeological record and it often plays an important role in understanding the origin and dispersal of modern

humans (*Homo sapiens*). This is because (1) genetic and fossil data support an African origin for our species, possibly in eastern Africa, with a key interval of several out-of-Africa dispersals occurring 40-60 ka based on the inferred age of a genetic bottleneck among non-African populations (Henn et al., 2018; Mallick et al., 2016), (2) the earliest LSA assemblages in eastern Africa date to 40-60 ka (Ambrose, 1998; Gliganic et al., 2012; Ranhorn and Tryon, 2018), and (3) early Eurasian Upper Paleolithic assemblages associated with fossil *H. sapiens* share broad technological similarities to early LSA ones, particularly in the production of smaller, blade and bladelet-based assemblages and greater use of ochre colorants and items of personal adornment (Klein, 2008). Why the MSA/LSA transition occurred remains poorly understood, although it is clear that the timing of transition varies between sites across Africa, from as early as 60 ka (Gliganic et al., 2012), to perhaps as late as the Holocene (Tribolo et al., 2017). The diachronous nature of the MSA/LSA transition may be related to multiple inter-related phenomena, including (1) local innovations in response to changes in the immediate environment, (2) the presence of larger and more dense human populations on increasingly crowded landscapes, (3) the spread of new ideas through existing social networks, or (4) population dispersals across Africa prior to and coincident with out-of-Africa expansions (Tryon, n.d.; Tryon and Faith, 2016).

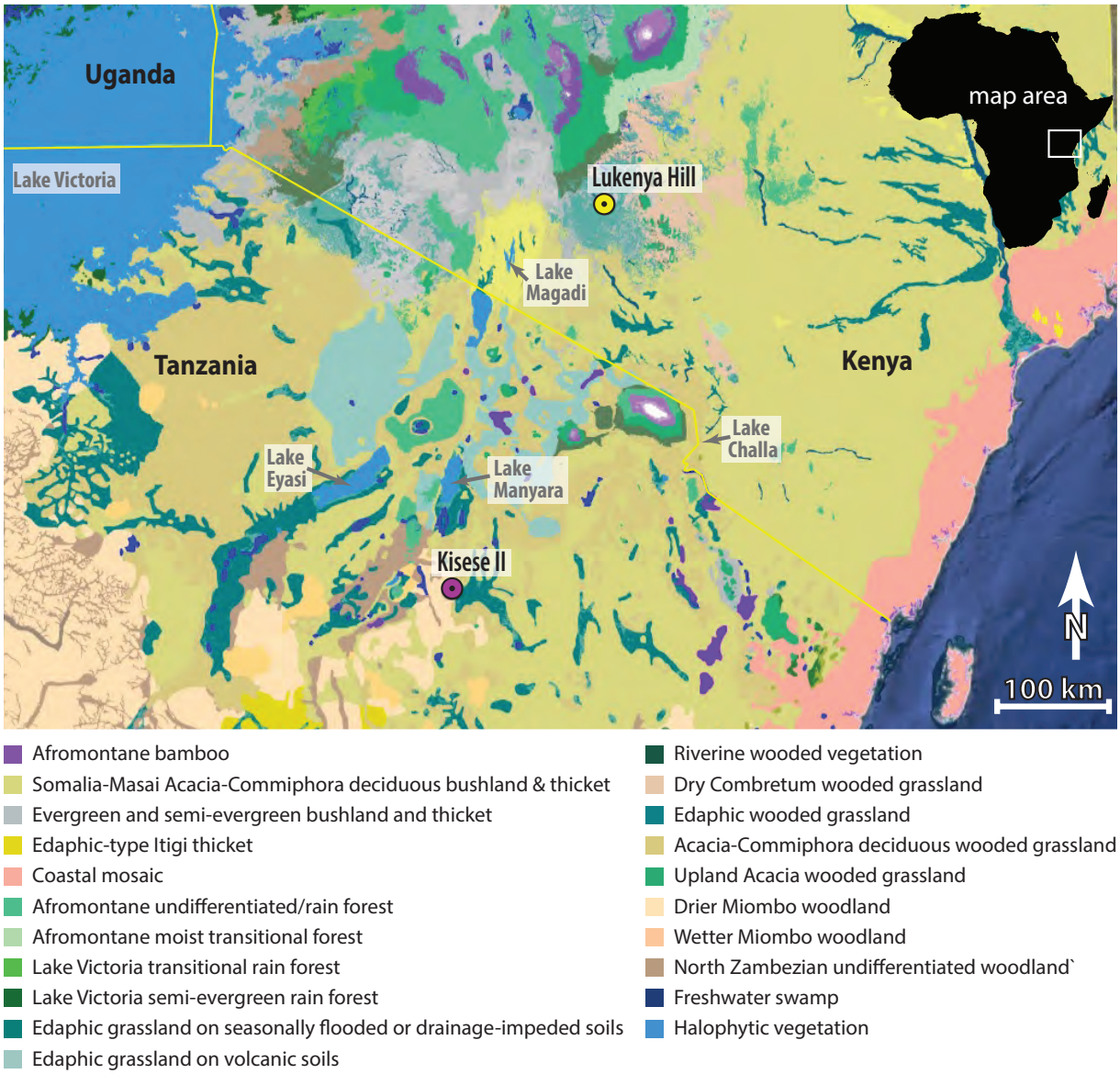

Figure 2.1: Map of modern physiognomic vegetation (after Van Bruegel et al., 2015) showing locations of the Lukenya Hill and Kisese II rockshelters and nearby lakes. Lukenya Hill is surrounded by an extensive edaphic grassland but is within 100 km (typical range of ostriches) of other diverse vegetation, while Kisese II is immediately surrounded by diverse vegetation. Vegetation map after Van Breugel et al, 2015; map constructed using Google Earth.

2.2.1: Eggshell samples

Ostrich eggshells from two sites at Lukenya Hill (Kenya) and one at Kisese II (Tanzania) were studied (figure 2.1; van Breugel et al., 2015). The majority of the Lukenya Hill (1° 28' 12.00"S, 37° 0' 0.00"E) samples came from site GvJm 22, and two came from site GvJm 16 (~500 m from GvJm 22), two of many rockshelter sites on an inselberg of Precambrian gneiss East of the Kenyan Rift Valley. All samples were drawn from collections stored at the National Museums of Kenya, Nairobi. ^{14}C-dated OES and other lines of evidence indicate that the Lukenya Hill localities record human activities from > 46 ka until the early 20th century (Gramly, 1976; Tryon et al., 2015). At site GvJm 22, the MSA/LSA transition has been conservatively estimated between ~46-26 ka, with the low temporal resolution a result of the ~45 ka radiocarbon (^{14}C) limit and the relatively coarse excavation methods. The MSA/LSA transition is recognized here by a shift from Levallois to blade and bladelet lithic production, the more frequent use of grinding stones, and the presence of ostrich eggshell beads (Tryon et al., 2015), with a partial human calvaria (KNM-LH-1) dated to ~23 ka (Tryon et al., 2015). OES beads, fragments, or worked pieces are relatively rare at site GvJm 22 (n = 16).

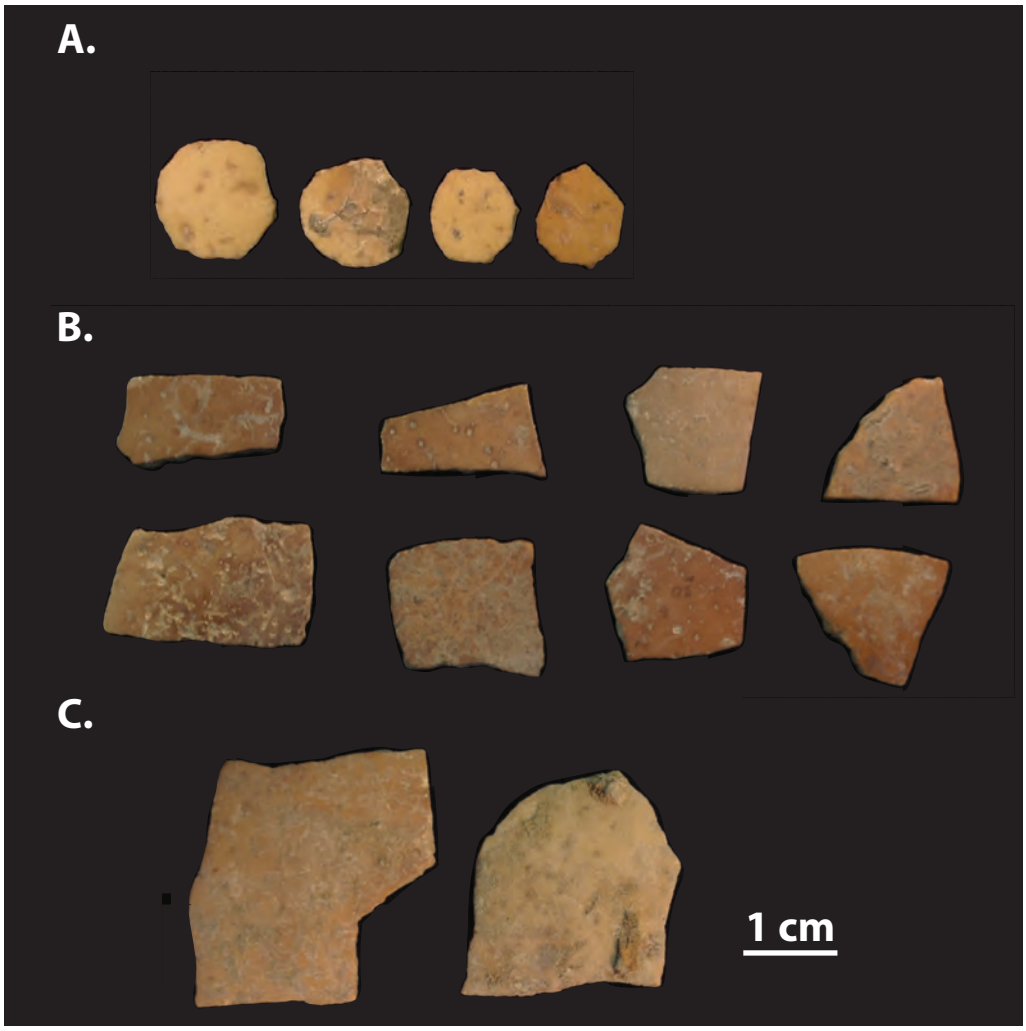

Figure 2.2: Selected ostrich eggshell fragments from Kisese II. A. Bead blanks from Spit VI; B. fragments from Spit X; C. fragments from Spit XIII. The 1-cm scale bar applies to every sample.

Kisese II is an archaeological painted rockshelter site among the UNESCO World Heritage Kondoa Rock-Art Sites (4° 25' 15.00"S, 35° 50' 0.00"E). Excavated in 1956 (Inskeep, 1962; Tryon et al., 2019, 2018), it contains artifacts representative of the MSA/LSA transition including OES beads, ochre, blades, and backed points, as well as much younger red-and-white paintings of humans, animals and geometric figures (Tryon et al., 2018). Twenty-five AMS ^{14}C dates and four conventional ^{14}C dates of OES allowed each horizontally excavated level (or "spit") to be constrained with maximum and minimum ages; the site ranges in age from >46 to 4 ka, with the MSA/LSA transition estimated to have begun ~36 – 34 ka (Tryon et al., 2018). Kisese II preserves > 5,000 complete beads or fragments related to their manufacture (Tryon et al., 2018); the OES studied here are mostly unworked fragments and some partial bead blanks (figure 2.2) from the archived collections stored at the National Museum of Tanzania.

2.2.2: Local environments

The two localities are characterized today by different local ecosystems and rainfall amounts, but similar temperatures. The persistence of grazer-dominated faunas from the GvJm 22 rockshelter at Lukenya Hill suggest that the MSA/LSA transition occurred despite minimal changes in the local environment (Marean, 1992; Tryon et al., 2015; Robinson, 2017), whereas fauna from Kisese II suggest more diverse ecosystems (Tryon et al., 2019). Today, these two localities are characterized by relatively different local environments and rainfall amounts, despite similar annual rainfall patterns and temperatures. Northern Tanzania as well as the highland regions of central Kenya, where the sites are located, receive rainfall in two phases, as short events October – December and longer, more intense events March – May (McSweeney et al., 2012a; McSweeney et al., 2012b). The diverse modern vegetation distribution surrounding the localities are shown in figure 2.1 (van Breugel et al., 2015). Situated on the high plains above the Athi-Kapiti Plain east of the Kenyan Rift Valley at ~1750 mASL, Lukenya Hill has a modern mean annual temperature (MAT) of ~20 – 24° C and MAP of ~630 mm/year (McSweeney et al., 2012a). Vegetation surrounding Lukenya Hill includes edaphic-wooded to upland acacia-wooded grassland (van Breugel et al., 2015). Kisese II is located at ~1460 mASL, ~200 m below the escarpment of the Irangi Hills East of the Gregory rift valley in Tanzania, with a modern MAT of ~21 – 23° C and MAP of ~850-1,020 mm/year (Mcsweeney et al., 2012b; Tryon et al., 2018). Woodlands in the Irangi Hills, wooded and edaphic grasslands at the base of the escarpment, and dry bushland further east, surround Kisese II (van Breugel et al., 2015), and the site lies at the margin of the *miombo* woodlands characteristic of south-central Africa.

In other studies, these localities have been determined to straddle a climatic boundary between regions defined as those that "show persistent climatic similarities through time" by Blome et al. (2012). However, these regions are not defined by equivalently rich paleoclimate data sets. Kisese II is found within the region defined by Blome et al. (2012) as tropical Africa (1° S – 19° S boundaries in eastern Africa) which is defined by 19 terrestrial climate records and 5 marine records, while Lukenya Hill is found within the region defined as eastern Africa, defined by only 3 terrestrial climate records and no marine records. Hence, OES stable isotope records also provide an opportunity to more densely populate terrestrial climate records in these sparsely sampled regions and better define the boundaries of climatically distinct regions which include numerous archaeological sites hosting OES, such as in eastern Africa.

Lukenya Hill Sample ID	Trench	Total Organic Fraction (VNIST 1577b)				Calcite Fraction		Geochronology	
		% N	$\delta^{15}N$ (‰)	% C	$\delta^{13}C_{org}$ (‰)	$\delta^{13}C_{calcite}$ (VPDB, ‰)	$\delta^{18}O$ (VSMOW, ‰)	^{14}C Lab ID	calBP (95.4%)
110-120	A	8.65	6.3	43.81	-22.4	-7.39	34.02	UBA-24889	3,867 - 3,693
120-130A	B	12.93	5.4	48.03	-22.0	-7.25	35.49	UBA-24877	4,814 - 4,444
160-170	B	4.10	*4.5*	43.40	-22.5	-6.25	35.96	UBA-24887	4,782 - 4,416
150-160	B	11.12	7.1	42.10	-21.0	-6.07	34.74	UBA-24879	4,861 - 4,630
120-130A	Test Pit					-7.84	35.16	UBA-23927	5,276 - 4,871
105-110	C	9.41	7.3	37.95	-16.0	-3.20	34.70	UBA-24888	6,879 - 6,669
98.50-98.45A*	Test Pit	8.71	6.6	36.07	-22.5	-6.85	37.54	UBA-24894	12,703 - 12,178
98.45-98.40B*	Test Pit	7.43	*5.7*	38.90	-23.0	-9.51	29.09	UBA-24893	13,710 - 13,403
120-130B	A	4.61	9.7	48.62	-22.2	-7.37	37.85	UBA-24885	15,350 - 14,933
120-130C	A	7.14	9.3	58.31	-22.2	-7.37	38.89	UBA-24886	15,565 - 15,119
130-140A	Test Pit					-1.59	39.97	UBA-23928	15,591 - 15,157
140-150A	A	6.09	*8.9*	49.82	-23.1	-6.68	37.05	UBA-24881	15,691 - 15,239
120-130A	A	4.33	8.4	34.04	-22.5	-4.69	37.33	UBA-24884	15,771 - 15,283
140-150C	A	10.04	9.2	49.62	-21.9	-6.49	38.49	UBA-24883	18,830 - 18,422
140-150B	A	5.37	*9.0*	53.63	-23.0	-6.40	36.19	UBA-24882	22,155 - 21,565
140-150B	Test Pit			44.52	-24.4	-4.04	36.66	UBA-23933	23,888 - 23,180
130-140C	Test Pit	6.97	8.0	54.27	-22.8	-4.12	36.56	UBA-23930	23,924 - 23,226
130-140B	Test Pit	5.34	9.2	49.32	-23.1	-4.15	36.28	UBA-23929	23,996 - 23,355
190-Breccia	A	7.22	7.8	36.05	-20.7	-3.12	36.07	UBA-24890	26,319 - 25,777
170-180	B	5.40	*8.8*	38.99	-23.0	-7.26	34.29	UBA-24878	32,583 - 31,194
140-150C	Test Pit	6.70	10.8	48.34	-21.4	-5.03	37.27	UBA-23934; AA 102890	32,792 - 31,247
130-140A	B	4.07	*10.3*	28.49	-20.8	-4.07	34.34	UBA-24880	38,498 - 35,974
140-150D	Test Pit	8.14	11.1	49.94	-22.2	-7.12	34.78	UBA-23935; AA102889	39,002 - 36,103
140-150A	Test Pit	3.32	10.0	42.28	-21.9	-3.46	36.35	UBA-23932	50,003 - 45,201

Table 2.2: Lukenya Hill isotope data and re-calibrated ^{14}C ages (after Tryon et al., 2015). All ages but one (140-150A) were calibrated using a mixed calibration between southern and northern hemisphere calibrations (SHCal and IntCal13; Hogg et al., 2013; Reimer et al., 2013), determined using the OxCal software (Bronk-Ramsey 2001; 2016). Italicized samples have uncertainty of ±0.4‰ on $\delta^{15}N$ rather than usual ±0.2‰. Empty cells indicate samples were too small or not analyzed. Lines separate groups of samples averaged to evaluate mean and standard deviation of a number of OES over discrete time intervals defined by the OES ^{14}C ages. Samples with an asterisk (*) came from GvJm16, a nearby rock shelter sequence, and these dates are presented here for the first time.

Kisese II Sample ID	Spit	Total Organic Fraction (VNIST1577b)				Calcite Fraction		Geochronology			
		% N	δ ^{15}N (‰)	% C	δ ^{13}C (‰)	δ^{13}C (‰ VPDB)	δ^{18}O (‰ VSMOW)	UBA-No.	calBP (95.4%)	maximum age (ka)	minimum age (ka)
KII II-B	II					-7.77	35.13	UBA-27430	4,230 – 3,990	4.23	3.99
KII I-B	I	1.97	6.8	7.26	-20.0	-4.57	36.60	UBA-27428	4,380 – 4,090	4.38	4.09
2017KII-I-A	I	14.19	7.4	50.22	-19.3	*-4.49*	34.36			4.4	4.1
2017KII-I-B	I	14.15	7.0	50.90	-22.5	*-9.13*	*31.11*			4.4	4.1
2017KII-Ib-A	Ib	13.01	8.0	52.86	-22.1	*-8.38*	*30.90*			4.4	4.1
KII I-A	I	9.04	6.4	31.72	-19.1	-4.87	34.76	UBA-27427	4,410 – 4,160	4.41	4.16
KII V-B	V	8.66	5.9	35.35	-22.7	-9.66	33.33	UBA-27434	10,650 – 10,300	10.65	10.3
2017KII-II-A	II	13.21	6.6	51.00	-20.9	*-7.30*	*29.60*			18.1	4.2
2017KII-II-B	II	10.06	8.0	55.97	-22.8	*-9.04*	*29.28*			18.1	4.2
2017KII-II-C	II	9.06	5.7	58.91	-24.1	*-8.77*	*32.83*			18.1	4.2
KII III-B	III	5.89	9.2	24.27	-19.0	-4.01	35.51	UBA-27432	17,230 – 16,720	17.23	16.72
2017KII-III-A	III	13.05	6.9	50.15	-21.9	*-7.67*	*32.53*			17.5	16.7
2017KII-III-B	III	9.47	4.9	52.16	-23.3	*-8.55*	*30.63*			17.5	16.7
KII III-A	III	1.91	7.5	9.20	-22.2	-6.01	34.84	UBA-27431	17,550 – 17,140	17.55	17.14
2017KII-IV-B	IV	9.63		48.14	-22.7	*-8.36*	*33.31*			18.4	17.4
2017KII-IV-A	IV	10.82	11.1	48.18	-21.7	*-9.72*	*34.38*			18.4	17.4
KII II-A	II	5.91	7.1	41.22	-22.7	-6.13	34.59	UBA-27429	18,190 – 17,840	18.19	17.84
2017KII-V-A	V	12.91	6.1	52.63	-21.2	*-8.72*	*33.86*	UBA-34477	18,250 – 17,900	18.25	17.9
2017KII-V-B	V	8.69	3.4	51.39	-24.1	*-8.73*	*30.95*			18.8	17.9
2017KII-V-C	V	11.89	8.9	49.09	-21.1	*-7.39*	*34.80*			18.8	17.9
KII V-A	V	9.30	8.3	36.84	-15.1	-0.63	34.89	UBA-27433	18,810 – 18,510	18.81	18.51
KII XXI-A	XXI	4.08	7.9	17.65	-22.2	-7.26	36.91	UBA-27441	19,230 – 18,890	19.23	18.89
2017KII-VI-A	VI	13.05	5.4	52.18	-21.6	*-8.00*	*31.72*			22.7	17.9
2017KII-VI-B	VI	11.15	7.6	51.17	-17.5	*-2.28*	*33.89*			22.7	17.9
2017KII-VI-C	VI	10.57	6.5	43.12	-20.6	*-3.55*	*34.69*			22.7	17.9
2017KII-VI-D	VI	11.27	8.6	50.82	-16.6	*-1.82*	*31.71*			22.7	17.9
2017KII-VII-B	VII	9.66	7.3	53.86	-19.7	*-3.18*	*34.49*			22.7	17.9
2017KII-VII-C	VII	7.38	7.4	63.44	-21.8	-7.05	33.08			22.7	17.9

Kisese II Sample ID	Spit	Total Organic Fraction (VNIST1577b)				Calcite Fraction		Geochronology			
		% N	$\delta^{15}N$ (‰)	% C	$\delta^{13}C$ (‰)	$\delta^{13}C$ (‰ VPDB)	$\delta^{18}O$ (‰ VSMOW)	UBA-No.	calBP (95.4%)	maximum age (ka)	minimum age (ka)
2017KII-VIII-A	VIII	12.22	6.0	50.76	-21.3	-5.87	36.53			22.7	17.9
2017KII-VIII-B	VIII	12.27	7.4	52.06	-21.4	-7.57	33.03			22.7	17.9
2017KII-VIII-C	VIII	11.08	6.7	48.23	-21.5	-7.07	35.29			22.7	17.9
2017KII-VIII-D	VIII	12.23	7.3	49.16	-17.9	-2.35	38.24			22.7	17.9
2017KII-IX-A	IX	10.60	8.1	43.70	-19.6	-4.60	33.97			22.7	21.2
2017KII-IX-B	IX	6.44	6.7	35.16	-22.6	-6.20	37.41			22.7	21.2
2017KII-IX-C	IX	8.65	4.9	58.94	-21.9	-6.53	36.75			22.7	21.2
2017KII-IX-D	IX	3.20	5.7	13.04	-18.5	-6.95	35.99			22.7	21.2
2017KII-X-B	X	3.99	4.8	30.63	-22.5	-5.53	36.95			23.7	23.1
2017KII-X-C	X	9.63	5.1	61.02	-22.7	-8.14	36.56			23.7	23.1
2017KII-X-D	X	7.33	5.7	54.11	-23.5	-8.26	34.09			23.7	23.1
2017KII-X-E	X	6.89	4.3	42.07	-24.2	-8.52	33.95			23.7	23.1
2017KII-X-F	X	7.38	7.0	28.55	-19.4	-7.20	33.27			23.7	23.1
2017KII-X-G	X	9.59	8.1	60.41	-22.6	-8.44	35.46			23.7	23.1
2017KII-X-H	X	6.41	7.4	37.83	-22.6	-6.52	35.75			23.7	23.1
2017KII-X-A	X	5.99	5.3	38.43	-23.3	-7.59	36.50	UBA-34479	23,680 – 23,130	23.68	23.21
KII XII-B	XII	5.55	6.6	23.53	-21.8	-7.25	35.43	UBA-27436	34,580 – 33,720	34.58	33.72
2017KII-XII-A	XII	9.62	5.2	42.47	-22.0	-7.65	35.17			35.1	33.7
2017KII-XII-B	XII	8.74	6.0	43.48	-23.2	-9.83	33.66			35.1	33.7
KII XII-A	XII	7.34	6.8	33.76	-23.0	-9.45	34.62	UBA-27435	35,050 – 34,050	35.05	34.05
2017KII-XI-A	XI	6.67	6.1	42.95	-21.7	-7.45	34.37	UBA-34480	35,140 – 34,250	35.1	34.3
2017KII-XI-B	XI	7.43	6.3	32.52	-18.6	-3.55	35.65			35.1	34.3
2017KII-XI-D	XI	5.73	4.8	43.20	-20.4	-4.00	35.28			35.1	34.3
2017KII-XI-F	XI	10.55	7.1	52.21	-17.1	-2.37	32.30			35.1	34.3
2017KII-XI-G	XI	9.07	5.9	41.60	-19.7	-5.32	33.85			35.1	34.3
2017KII-XI-H	XI	11.43	5.9	58.02	-22.2	-9.50	32.60			35.1	34.3
2017KII-XI-C	XI	7.19	7.5	68.55	-23.0	-6.84	35.65			35.1	34.3
2017KII-XI-E	XI	8.92	5.6	37.53	-21.7	-7.30	35.76			35.1	34.3
KII XV-A	XV	3.29	7.2	19.42	-21.5	-5.91	33.07	UBA-27437	35,470 – 34,270	35.47	34.27

Kisese II Sample ID	Spit	Total Organic Fraction (VNIST1577b)				Calcite Fraction		Geochronology			
		% N	$\delta^{15}N$ (‰)	% C	$\delta^{13}C$ (‰)	$\delta^{13}C$ (‰ VPDB)	$\delta^{18}O$ (‰ VSMOW)	UBA-No.	calBP (95.4%)	maximum age (ka)	minimum age (ka)
2017KII-XV-A	XV	2.81	6.9	13.17	-19.8	-9.85	30.77			35.9	34.3
2017KII-XV-B	XV	3.62	6.3	16.68	-21.8	-6.82	31.98			35.9	34.3
KII XV-B	XV	3.42	4.3	18.75	-22.6	-7.78	34.89	UBA-27438	35,850 – 34,660	35.85	34.66
2017KII-XIV-D	XIV	1.65		5.62	-22.5	-5.65	35.08			39.9	33
2017KII-XIV-A	XIV	3.61	6.0	15.67	-21.3	-7.38	34.99			39.9	33
2017KII-XIV-B	XIV	2.90	7.6	12.12	-19.5	-8.96	31.28			39.9	33
2017KII-XIII-A	XIII	1.77	7.3	8.30	-16.9	-3.77	34.13			39.9	33.7
2017KII-XIII-B	XIII	3.29	6.3	14.26	-20.7	-7.23	36.69			39.9	33.7
2017KII-XVI-A	XVI	4.15	8.9	18.46	-20.9	-5.84	34.30			39.6	34.3
2.07KII-XVI-B	XVI	2.33	6.5	16.68	-21.1	-6.48	34.14			39.6	34.3
2017KII-XVII-A	XVII	1.08	7.5	5.02	-18.8	-7.04	32.39			39.6	34.3
2017KII-XVII-B	XVII	2.00	8.6	9.51	-17.4	-2.66	35.15			39.6	34.3
2017KII-XVII-C	XVII	1.51	6.8	10.33	-16.5	-4.84	33.31			39.6	34.3
KII XIX-A	XIX	1.89	6.2	10.32	-22.6	-7.41	32.50	UBA-27439	38,600 – 36,600	38.6	36.6
2017KII-XVIII-B	XVIII	4.24	6.2	19.18	-21.9	-5.56	39.65	UBA-34481	39,590 – 38,340	39.6	38.3
2017KII-VII-A	VII	9.04	11.4	49.17	-19.4	*-6.90*	*32.77*	UBA-34478	42,790 – 41,730	42.79	41.73
2017KII-XX-B	XX	2.04	8.3	18.72	-22.1	-8.20	28.76			46.2	42.7
2017KII-XX-C	XX	2.59	8.7	20.87	-23.1	-7.87	30.11			46.2	42.7
2017KII-XX-D	XX	1.11	9.0	6.98	-18.6	-3.90	33.93			46.2	42.7
2017KII-XX-E	XX	1.95	6.1	15.42	-22.6	-6.18	32.98			46.2	42.7
2017KII-XX-F	XX	1.05	7.2	7.25	-22.1					46.2	42.7
2017KII-XXI-B	XXI	1.78	9.4	15.48	-19.9	-2.68	37.16			46.8	42.7
2017KII-XXI-C	XXI	1.68	6.6	13.50	-22.0					46.8	42.7
2017KII-XXI-D	XXI	1.39	8.9	12.22	-20.2	-7.03	32.85			46.8	42.7
KII XIX-B	XIX	4.03	6.4	25.71	-21.2	-4.93	32.02	UBA-27440	46,710 – 42,990	46.71	42.99
KII XXI-B	XXI	3.94	6.2	27.34	-20.9	-5.69	33.18	UBA-27442	46,850 – 43,120	46.85	43.12

Table 2.3: Isotope data for Kisese II. Italicized samples have 1σ analytical precision $\delta^{13}C_{calcite}$ = 0.1‰ analytical precision, $\delta^{18}O_{calcite}$ = 0.057‰; all others are $\delta^{13}C_{calcite}$ = 0.05‰ and $\delta^{18}O_{calcite}$ = 0.046‰. Ages and age ranges are after Tryon et al. (2018).

3: Methods

3.1: Stable Isotopes

OES samples were prepared for stable isotope analyses with a novel protocol designed to optimize yields of TOF and obtain reproduceable results on fragments from the same eggshell (see Appendix B; Niespolo et al., 2015). All tests were completed on fragments from the same farmed modern ostrich eggshell (Solvang, CA). Briefly, we tested several acid strengths and acidification sequences on 15 OES fragments from a modern egg for isotope analysis based on continuous flow isotope ratio mass spectrometry. The protocol requires sample sizes of ~300 mg and consequently larger acid volumes to completely dissolve the calcite fraction and retain sufficient TOF for online analysis. A few of the modern OES test samples were also rinsed with 0.1N NaOH; these results indicated NaOH degraded the TOF resulting in altered isotopic compositions. Further discussion of our findings and complete protocol is presented in Appendix B. The N and C isotopic compositions of our modern OES fragments should be similar given that they all derive from the same egg. We measured an average $\delta^{15}N$ value = 7.0 ± 0.5‰ and average $\delta^{13}C$ = -24.0 ± 0.4‰ (n = 11; Appendix B). Thus, ancient OES stable isotope compositions should be reproducible at these levels of precision if multiple fragments came from the same egg. Eggs deriving from different ostriches from a number of different years should demonstrate a more diverse sampling of the plants on the landscape than the highly reproducible results of multiple fragments from the same egg.

Isotopic analyses were completed in the UC Berkeley Center for Stable Isotope Biogeochemistry (CA, U.S.A.). $\delta^{13}C$ and $\delta^{18}O$ values of the prepared calcite fraction of OES were analyzed using a MultiCarb system in line with a GV IsoPrime mass spectrometer in dual inlet mode. Calcite standards were NBS 19 (limestone) along with two internal lab standards; calcite data is reported relative to Vienna Pee Dee Belemnite (VPDB; Hut, 1987) and $\delta^{18}O$ values are re-calculated according to Vienna Standard Mean Ocean Water (VSMOW; Coplen, 1996). Run precision for Lukenya Hill $\delta^{13}C$ and $\delta^{18}O$ values are 0.019‰ and 0.036‰ based on within-run reproducibility of standards (table 2.2; all errors 1σ), respectively. Kisese II samples whose Sample ID does not begin with "2017" are reported according to the within-run precision of 0.026‰ and 0.06‰ (table 2.3, $\delta^{13}C$ and $\delta^{18}O$ values, respectively). Sample IDs beginning with "2017" are reported according to their precision in the supplementary data (0.05 to 0.1‰ for $\delta^{13}C$ and 0.046 to 0.057‰ for $\delta^{18}O$). Long-term precisions of $\delta^{13}C$ and $\delta^{18}O$ values are respectively 0.05‰ and 0.07‰. Total organic fraction (TOF) of OES was analyzed using a CHNOS Elemental Analyzer interfaced to an IsoPrime 100 mass spectrometer. Raw data were calibrated using laboratory standards NIST 1577b (bovine liver) and NIST 1547 (peach). Run precision is ±0.1‰ and ±0.2‰ for $\delta^{13}C$ and $\delta^{15}N$, respectively, except where specified otherwise in the supplementary data. For both calcite and TOF analyses, standards were added throughout the run for raw data corrections and to measure accuracy and precision. Statistical analyses on data sets were performed in R (R Core Team, 2018).

3.2: Chronology and Age Modeling

Our analyses of OES from Lukenya Hill and Kisese II are based on legacy collections from excavations conducted in the 1950s-1970s (cf. Gramly, 1976; Inskeep, 1962; Tryon et al., 2019, 2018, 2015) that used horizontal excavation units cross-cutting dipping sedimentary

deposits. This resulted in the admixture of formerly discrete depositional units, which combined with limited data on the horizontal distribution of material at each site, reduces the resolution of our understanding of the archaeological record.

However, the chronology of our analyzed OES fragments is much better than that of the excavated associated lithic or faunal material because much of our analyzed sample is directly dated by the ^{14}C method. Each OES analyzed from Lukenya Hill has been ^{14}C-dated to obviate any ambiguity of chronostratigraphic placement (Tryon et al., 2015), including two unpublished dates on OES from GvJm 16 (table 2.2). For consistency, we report the ^{14}C dates for OES from Lukenya Hill (table 2.2) using a mixture of the southern and northern hemisphere calibration curves (Hogg et al., 2013; Reimer et al., 2013) to accommodate the samples being from near-equatorial regions, following the method of (Tryon et al., 2018) and using the OxCal software (Bronk-Ramsey, 2001; Bronk Ramsey, 2016). Sample 140-150A is calibrated after Cheng et al. (2018) because it is older than the limit of ^{14}C calibrations available in OxCal; for explanation, see Sharp et al. (n.d.). Seven of the OES from GvJm 22 also have reliable uranium-thorium ($^{230}Th/U$) burial ages (Sharp et al., 2015, n.d.). Therefore, each OES from Lukenya Hill has a stable isotope composition that can be precisely placed in time. At Kisese II, 29 OES were ^{14}C-dated to estimate age ranges for each horizontally excavated unit (Tryon et al., 2018) and are reported in table 2.3 using the same mixed calibration curve. It was impractical to date every OES from Kisese II ($n = 87$)*;* therefore, the ages of some OES fragments not directly ^{14}C dated are bounded by the age range of the excavated spit that contained them as given in Tryon et al. (2018) and provided in table 2.3.

In an effort to smooth out variation introduced by feeding habits of individual birds and interannual variations in vegetation and rainfall, we evaluate multiple OES per time interval (range of n for $\delta^{15}N$ = [3,11], median $n = 4$; range of n for $\delta^{13}C$, $\delta^{18}O$ = [3,12], median $n = 5$) and compare means and standard deviations (σ) of contemporaneous OES proxies between sites. We take the average isotopic compositions of 2-5 OES at Lukenya Hill in groups according to their ^{14}C ages. At Kisese II, some spits overlap with others in age. We have thus divided these overlapping spits into age ranges that accommodate the highest temporal resolution possible and still include at least 4 OES fragments per binned interval. Even at coarse chronological resolution, mean isotope values in each system overlap at 1σ between groups with overlapping time intervals. However, lacking precise and continuous chronological resolution, more robust statistical methods to integrate stable isotope results through time (such as moving average approaches) were not justifiable and resulted in either truncated, overly smoothed models (for large n in the moving average, or large smoothing parameters) or inaccurate moving average results from integration of temporally disparate data. To visualize how each isotope system changes through time at Kisese II, we use linear interpolation of mean values from age bins for each isotope system, but with expanded uncertainties in intervals with less precise chronology (for example, from 18.1 – 4.2 ka, uncertainties reflect the sum of uncertainties of overlapping bins).

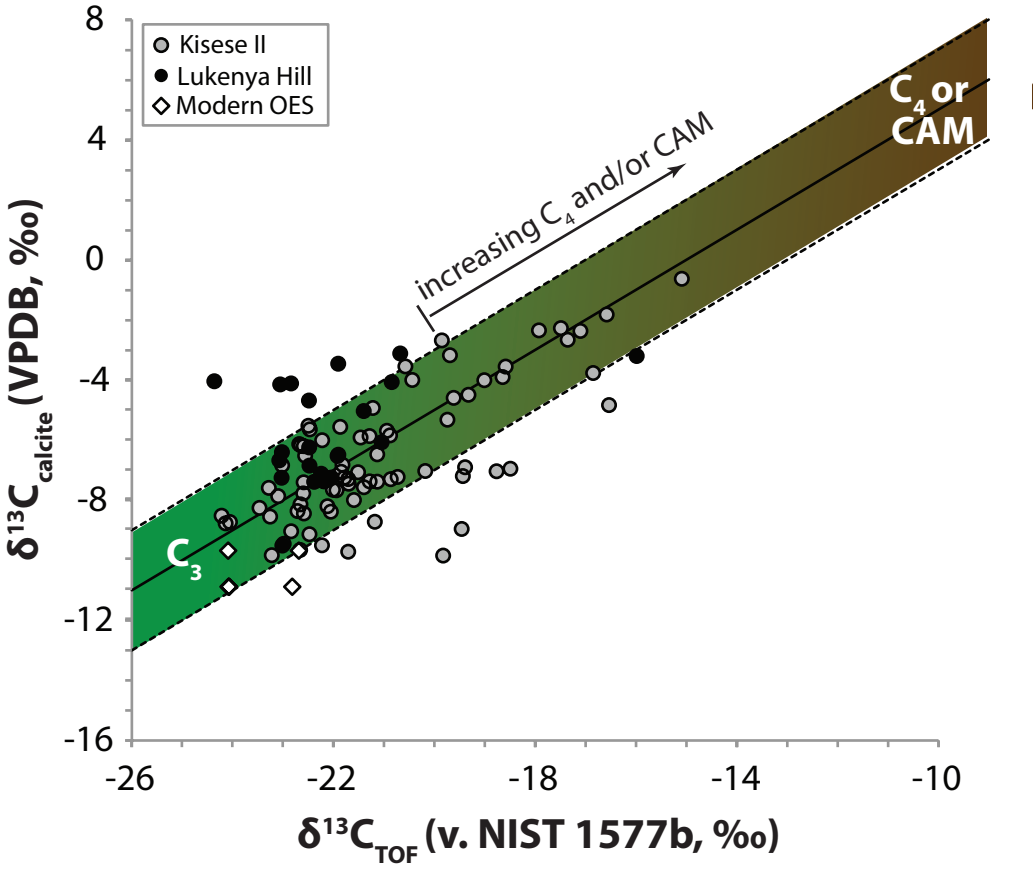

Figure 2.3: Plot of $\delta^{13}C$ values of total organic fraction (TOF) versus inorganic fraction (calcite) of modern and ancient ostrich eggshells (from this study). Boxes show compositions expected for diets consisting of 100% C_3 and 100% C_4 plants. The endmember for C_4 and/or CAM plants in the diet is referred in the text as the C_4 component of the diet. Solid line with dashed uncertainties (after Johnson et al., 1998) shows the consistent fractionation observed between TOF and calcite in modern eggshells regardless of diet. Ancient eggshells plotting within the dashed lines preserve pristine carbon isotope fractionation, and by inference, primary $\delta^{15}N$ values.

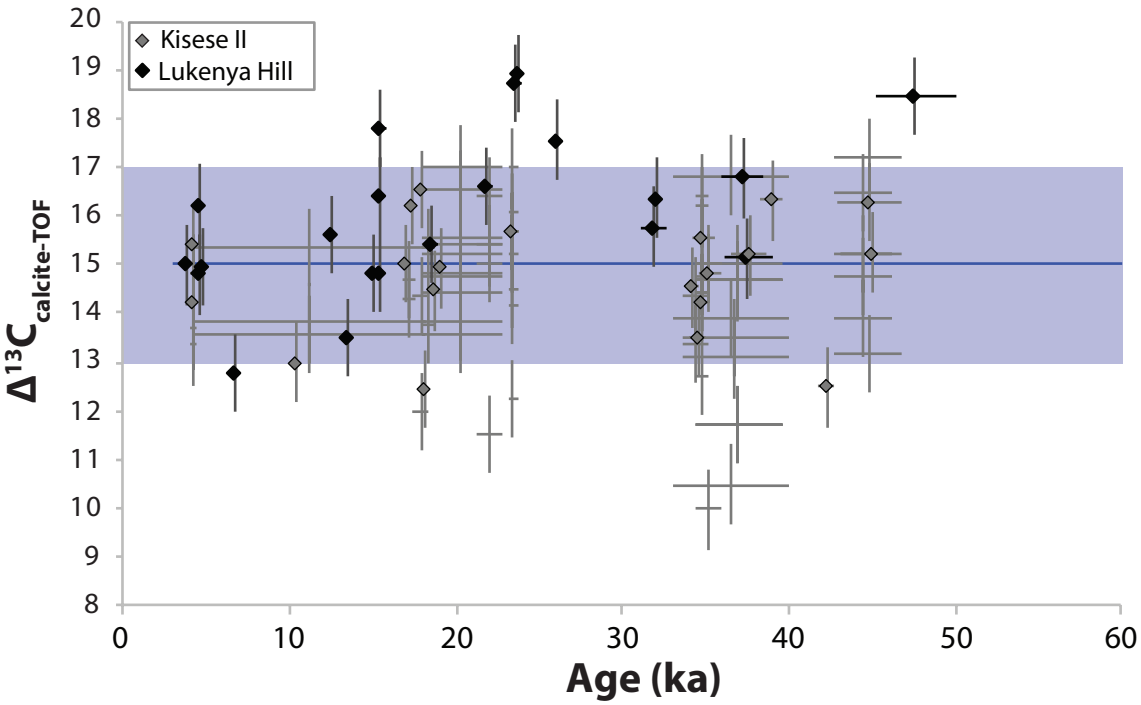

Figure 2.4: Observed carbon isotope fractionation ($\Delta^{13}C_{calcite\text{-}TOF}$ = 15 ± 2‰) in ancient OES versus age. Ages are from Tryon et al. (2015) and Tryon et al. (2018). All Lukenya Hill and some Kisese II eggshells were directly dated via ^{14}C (highlighted with diamond symbols) while ages of the remaining Kisese II samples were estimated from dated samples in the same excavation level or 'spit'; crosses whose x-axis length is indicative of the age range estimate for the spit of origin. Most samples show fractionation within the expected range. Those that do not are poorly correlated with age, suggesting diagenesis is controlled by other factors.

4: Results from Ancient OES

All samples with both TOF and calcite isotopic analyses are first assessed by calculating $\Delta^{13}C_{calcite\text{-}TOF}$ (figure 2.3, after equation 2.3, Johnson et al., 1998). As calcite is highly stable compared to organics in semi-arid to arid climates, deviation from the $\Delta^{13}C_{calcite\text{-}TOF}$ value was interpreted as degradation or alteration of the primary isotopic composition of TOF. The samples that did not satisfy the range of well-preserved $\Delta^{13}C_{calcite\text{-}TOF}$ were only further evaluated here in terms of calcite isotopic composition (C, O). Twenty-three OES calcite samples were analyzed from Lukenya Hill, 21 of which yielded sufficient material for online analysis of TOF. Fifteen out of 21 OES from Lukenya Hill show the expected $\Delta^{13}C_{calcite\text{-}TOF}$ (figure 2.3). Eighty-four of 87 samples analyzed from Kisese II were large enough to yield sufficient TOF for analysis; 73 of 84 samples reproduced the expected $\Delta^{13}C_{calcite\text{-}TOF}$ (figure 2.3). There is no apparent relationship between sample age and failure to produce this fractionation value (figure 2.4), indicating that age does not govern isotopic preservation of TOF and the technique indeed should be applicable on timescales similar to those of preservation of amino acids in eggshells, (~10^5-10^6 years; e.g., Brooks et al., 1990; Demarchi et al., 2016). The samples too small to produce sufficient TOF for isotopic analysis were still large enough to produce calcite $\delta^{13}C$ and $\delta^{18}O$ values. All isotope data, and C and N compositions from the TOF of 110 OES fragments collected from the archaeological sites are found in Tables 2.2 and 2.3 and all individual OES calculated proxy values can be found in the supplementary data. Tables 2.4 and 2.5 provide the average isotopic values for each time interval at Lukenya Hill and Kisese II, respectively, and the inferred average proxy values for each system. Figure 2.5 provides the measured $\delta^{13}C$, $\delta^{15}N$, and $\delta^{18}O$ values, as well as the calculated individual and mean $\delta^{13}C$ values of the ostrich diet, corresponding PMAP, and foliar $\delta^{18}O$ values, as a function of time, at Lukenya Hill. Figure 2.6 shows the same information for Kisese II. Below we summarize the results of each isotope system at both sites through time.

Age range from (ka)	Age range to (ka)	Mean $\delta^{13}C$ (VPDB, ‰)	Mean $\delta^{13}C_{diet}$ (‰)	± (1σ)	Mean $\delta^{15}N$ (VNIST1577b, ‰)	± (1σ)	Mean PMAP (mm/yr)	± (1σ)	Mean $\delta^{18}O$ (VSMOW) (‰)	± (1σ)	Model 1 mean $\delta^{18}O_{folia\ rH2O}$	± (1σ)	Model 2 mean $\delta^{18}O_{folia\ rH2O}$	± (1σ)	*n*
6.9	3.7	-6.3	-22.5	1.7	5.8	1.1	790	103	35.0	0.7	3.9	0.5	2.0	0.8	4 (N); 4 (C/O)
13.7	12.2	-8.2	-24.4	1.9	6.1	0.6	761	55	33.3	6.0	2.7	4.1	1.1	0.9	2 (N); 5 (C/O)
18.8	14.9	-5.7	-21.9	2.2	9.2	0.3	482	28	38.3	1.1	6.1	0.7	2.4	1.1	5 (N); 7 (C/O)
26.3	21.6	-4.4	-20.6	1.2	ND	ND	ND	ND	36.4	0.2	4.8	0.2	3.0	0.6	4 (C/O)
50.0	31.2	-5.4	-21.6	1.7	10.3	1.0	391	94	35.4	1.3	4.1	0.9	2.5	0.9	3 (N); 5 (C/O)

Table 2.4: Mean isotope values and proxies for Lukenya Hill. ^{14}C ages were used to constrain each interval of time represented.

Age range from (ka)	Age range to (ka)	Mean $\delta^{13}C$ (VPDB, ‰)	Mean $\delta^{13}C_{diet}$ (‰)	± (1σ)	Mean $\delta^{15}N$ (VNIST1577b, ‰)	± (1σ)	Mean PMAP (mm/yr)	± (1σ)	Mean $\delta^{18}O$ (VSMOW) (‰)	± (1σ)	Model 1 mean $\delta^{18}O_{foliarH2O}$	± (1σ)	Model 2 mean $\delta^{18}O_{foliarH2O}$	± (1σ)	*n*
4.4	4.0	-6.5	-22.7	2.1	7.1	0.6	674	54	33.8	2.3	3.0	1.6	1.9	1.1	5
10.7	10.3	-9.7	-25.9	0.9	5.9	0.2	779	*100*	33.3	1.0	2.7	1.0	0.4	1.0	1
18.1	4.2	-8.4	-24.6	0.9	6.8	1.2	705	105	30.6	2.0	0.8	1.3	1.0	0.5	3
17.6	16.7	-6.6	-22.8	2.0	7.1	1.8	671	158	33.4	2.2	2.7	1.5	1.9	1.0	3
19.2	17.4	-7.1	-23.3	2.8	7.1	2.2	674	195	34.2	1.7	3.3	1.2	1.7	1.4	4 N; 6 C/O
22.7	17.9	-4.9	-21.1	2.5	7.0	0.9	681	81	34.3	2.1	3.3	1.4	2.8	1.2	10
22.7	21.2	-6.1	-22.3	1.0	6.6	1.6	723	143	36.0	1.5	4.5	1.0	2.2	0.5	3 N; 4 C/O
23.7	23.1	-7.5	-23.7	1.1	5.8	1.4	788	128	35.3	1.4	4.1	0.9	1.4	0.5	5 N; 8 C/O
35.1	33.7	-6.7	-22.9	2.4	6.2	0.8	758	73	34.5	1.2	3.5	0.8	1.9	1.2	11 N; 12 C/O
35.9	34.3	-7.6	-23.8	1.7	5.9	1.5	779	134	32.7	1.7	2.3	1.2	1.4	0.8	3 N; 4 C/O
39.9	33.0	-6.6	-22.8	2.0	6.5	0.7	729	60	34.4	2.0	3.5	1.4	1.9	1.0	3 N; 75C/O
39.6	34.3	-5.7	-21.9	1.6	7.3	1.3	658	121	34.5	2.5	3.5	1.7	2.4	0.8	5 N; 7 C/O
46.9	41.7	-5.9	-22.1	1.8	7.6	1.3	626	122	32.6	2.4	2.2	1.6	2.2	0.9	7 N; 11 C; 9 O

Table 2.5: Mean isotope and proxy values through time at Kisese II. Italicized error on PMAP value is an arbitrary imposed error due to only one sample in this interval; errors are standard deviation of the mean value. ^{14}C ages and suggested age ranges after Tryon et al. (2018) were used to constrain each interval of time represented.

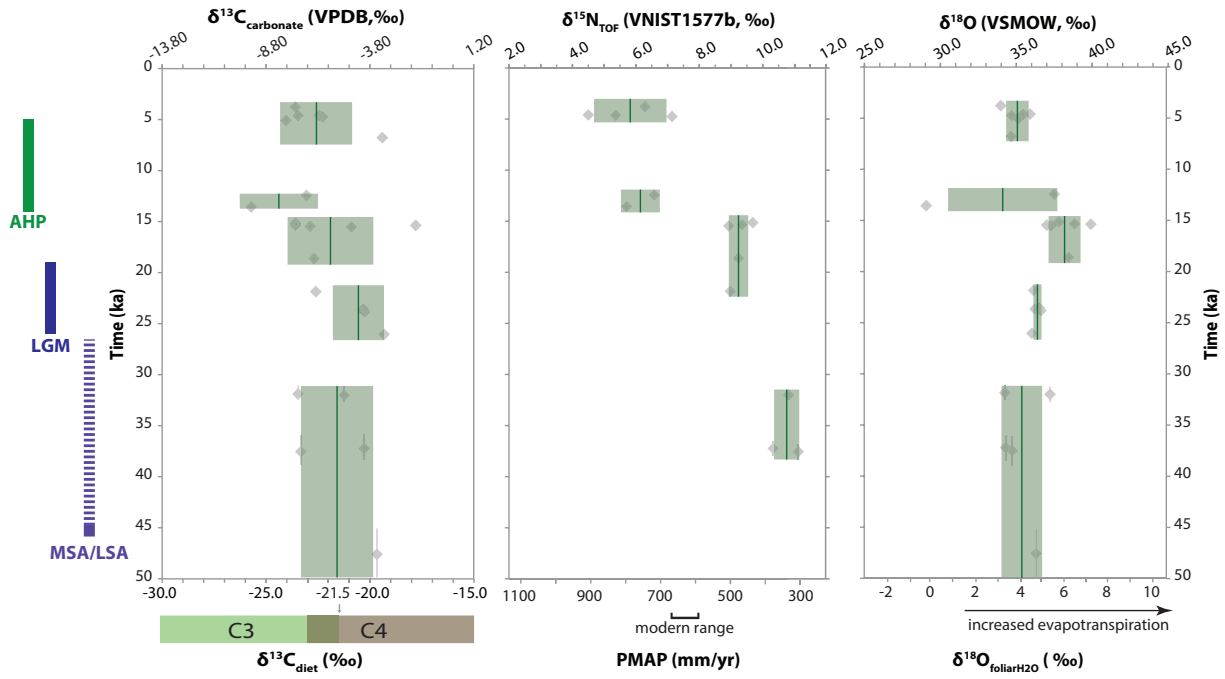

Figure 2.5: The C, N, and O isotopic compositions of OES from Lukenya Hill and corresponding proxy variables through time. Each OES from Lukenya Hill was ^{14}C-dated. Green boxes show mean and standard deviation for grouped data. Calculated paleo- mean annual precipitation (PMAP) progressively increases through time from ~38 to 4 ka and correlates with a modest shift toward more C_3-rich diet. The MSA/LSA transition at Lukenya Hill, from c. >46 – 26 ka, occurs during the period with the lowest inferred mean PMAP in our record. $\delta^{18}O$ values do not co-vary consistently with C and N isotopes.

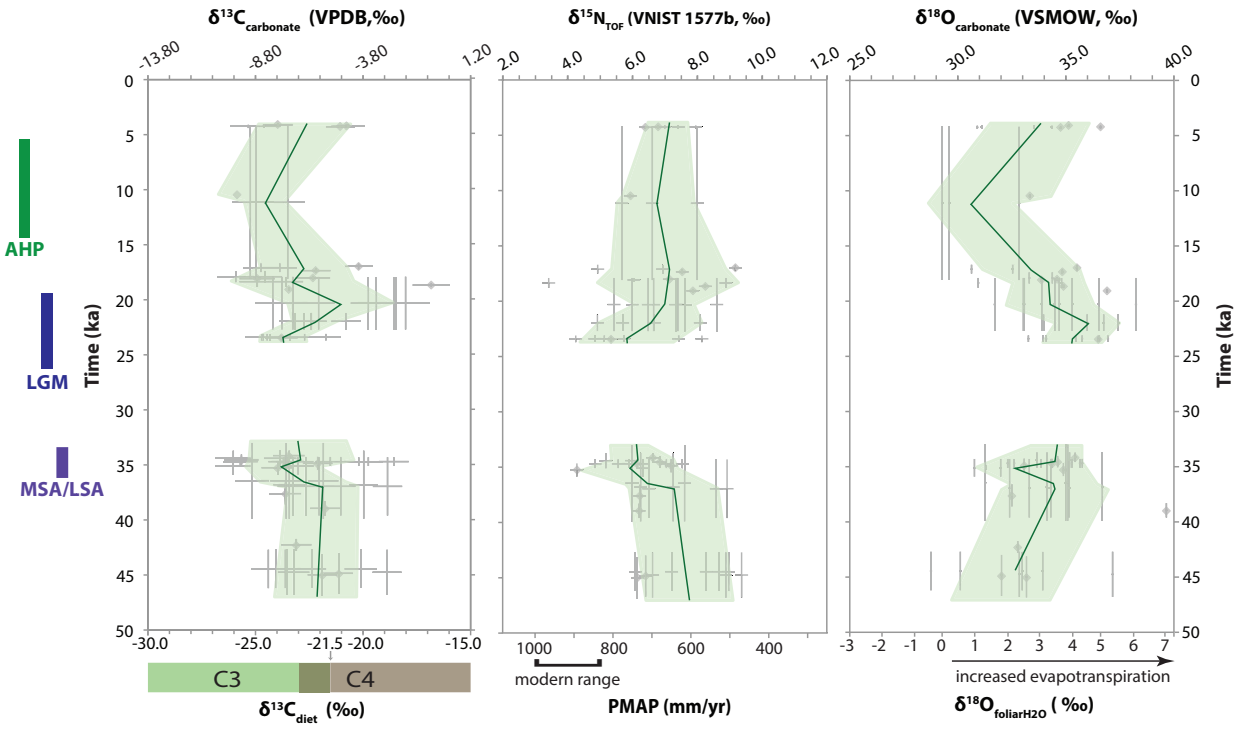

Figure 2.6: The C, N, and O isotopic compositions of OES from Kisese II and corresponding proxy variables through time. Grouping of mean values is explained in the text. Individual analyses (gray crosses) are averaged over discrete time intervals to show trends through time (green bars). Trends reveal co-occurring shifts in vegetation and precipitation up to ~50 ka. Dietary $\delta^{13}C$ values (left) trend toward more C_3-rich vegetation during periods with higher rainfall (center panel) and correspond with increased evapotranspiration (right). There are broadly oscillating trends in mean proxy values over time, with peak PMAP occurring at ~22 ka and ~36-34 ka, approximately coincident with the onset of the MSA/LSA transition (36-34 ka) at Kisese II.

4.1: Carbon Isotopes

We calculate the proportion of C_3 versus C_4 and/or CAM plants from the $\delta^{13}C$ values of ancient OES based on a simple two end-member linear mixing model (figure 2.3), taking an average value for each end-member ($\delta^{13}C_{C3}$ = -28.5‰, Kohn, 2010; $\delta^{13}C_{C4}$= -13‰, e.g., Ehleringer and Cerling, 2002). In a study compiling modern global $\delta^{13}C$ values of C_3 plants, Kohn (2010) suggests the maximum $\delta^{13}C$ = -23‰ for C_3 plants, as values greater than this are restricted to places with MAP < 10mm/year and some settings with the genus *Pinus,* which is native only to northern African circum-Mediterranean regions prior to historical introduction to South Africa in the 17th century (e.g., Moran et al., 2000). Accordingly, we apply a cutoff $\delta^{13}C$ value = -21.5‰ to evaluate the presence/absence of C_4 plants on the landscape; this conservatively accounts for a ~1.5‰ decrease in the average $\delta^{13}C$ of atmospheric CO_2 from post-industrial plants sampled by these modern studies due to the Suess Effect (e.g., Farquhar et al., 1989; Keeling, 1979; Keeling et al., 2017).

Crassulacean acid metabolism (CAM) plants may also be present in these environments and subsequently in ostrich diets (e.g., Williams et al., 1993). CAM plants in Africa broadly overlap in carbon isotope composition with C_4 plants more than with C_3, perhaps associated with higher abundance of obligate CAM flora (Cornwell et al., 2018, 2016). Because they may be isotopically indistinguishable from C_3 and C_4 plants, we cannot infer their presence on the landscape directly, as CAM plants do not have hard parts (e.g., phytoliths) that are preserved in the geologic record. However, given there is no evidence in the modern landscape or faunal records that CAM is/was predominant on the landscape near these localities (Marean, 1992, 1991; Robinson, 2017; Tryon et al., 2019; van Breugel et al., 2015), we will refer to plant dietary $\delta^{13}C$ values that may be isotopically ascribed to C_4 or CAM as the "C_4" endmember.

At Lukenya Hill, calcite $\delta^{13}C$ values range from -1.6‰ to -9.5‰, corresponding to a range of calculated diet $\delta^{13}C$ values varying from -17.8‰ to -25.7‰ (table 2.2 and supplementary data). These imply ostriches were consuming diverse diets, with between 8 – 60% contributions of C_4 plants (mean = 33 ± 12% C_4 diet). Ten of 23 OES produced dietary $\delta^{13}C$ values greater than -21.5‰, indicating a C_4-dominant diet in nearly half the samples. Mean dietary $\delta^{13}C$ values (table 2.4) range from -20.6 ± 1.2‰ to -24.4 ± 2.2‰, indicative of mixed to C_4-rich diets in different time intervals.

At Kisese II, calcite and TOF $\delta^{13}C$ values correspond to a range of dietary $\delta^{13}C$ values between -16.8‰ and -26.1‰ (table 2.3 and supplementary data), reflecting 6 – 66% C_4 dietary contribution (mean C_4 contribution = 28 ± 13.7%), similar to the Lukenya Hill OES samples. Twenty-one of 87 OES produced dietary $\delta^{13}C$ values greater than -21.5‰, indicating a C_4-rich diet in fewer than one-quarter of the samples. At Kisese II, mean values of $\delta^{13}C_{diet}$ through time reflect a mixed C_3-C_4 diet to a C_3-rich diet (table 2.5), particularly just before and after the temporal hiatus (~33.0 – 23.7 ka; figure 2.6).

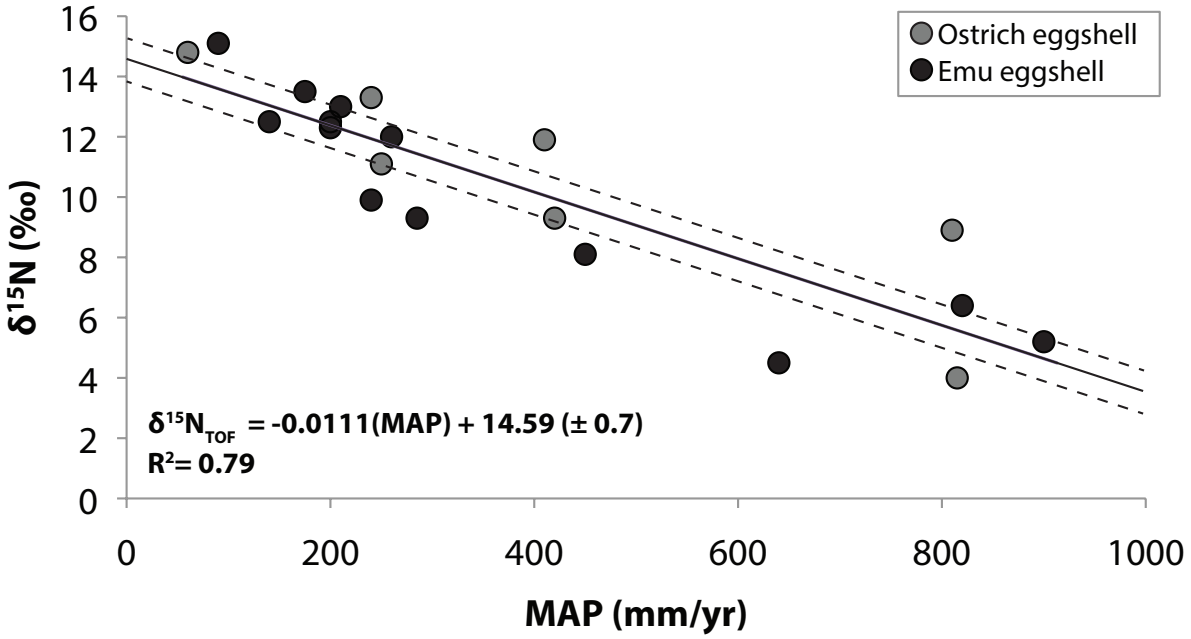

Figure 2.7: Mean annual precipitation (MAP) versus $\delta^{15}N$ values of modern ostrich eggshell from South Africa (from Johnson et al., 1998) and emu eggshell from Australia (Newsome et al., 2011). Solid line is least squares best fit and dashed lines are 66.7% confidence interval.

4.2: Nitrogen Isotopes

Previous studies have shown that the N isotopic composition of eggshell of wild South African ostrich and Australian emu are inversely related to MAP in their native habitats (Johnson et al., 1998; Newsome et al., 2011). Figure 2.7 shows that modern eggshell $\delta^{15}N$ values of both species plotted versus contemporary MAP are well fitted by a single linear regression (Pearson correlation coefficient $R^2 = 0.79$, p-value $= 1.8 \times 10^{-7}$):

$$\delta^{15}N = -0.01 \times (PMAP) + 14.59 \quad (2.4)$$

That is, a single inverse relation between $\delta^{15}N$ values and MAP is observed in modern studies of distinct ratite species on different continents. This relation is likely valid because both ratites are mostly herbivorous feeders, inhabit semi-arid to arid climates, and occupy similar niches in their respective food webs, leading to similar trophic effects expressed in the N isotopic compositions of their eggshells. Since foliar N is found to be inversely related to MAP globally (Craine et al., 2009), we expect similar relationships between $\delta^{15}N$ values of ratite eggshells and MAP to apply wherever ratite feeding habits are similar. Accordingly, we infer that we can estimate PMAP at Lukenya Hill and Kisese II using the inverse relation in figure 2.7.

Pristine $\delta^{15}N$ values of OES from Lukenya Hill range from 4.5‰ to 11.1‰, which correspond to PMAP values of ~900 to 310 mm/year, respectively, using Equation 2.4 (after figure 2.7). Mean $\delta^{15}N$ values become progressively less positive through time, corresponding with a progressive increase in PMAP over the temporal ranges represented. The lowest mean PMAP (386 ± 85 mm/yr) occurs 37.6 – 31.2 ka, and the highest mean PMAP (790 ± 103 mm/yr) occurs from 6.9 – 3.8 ka, higher than modern MAP at Lukenya Hill (~630 mm/year; McSweeney et al., 2012a).

$\delta^{15}N$ values from Kisese II range from 3.4 to 9.2‰, corresponding to PMAP from ~1010 to 490 mm/yr, respectively. In contrast to the progressive increase in PMAP at Lukenya Hill, the $\delta^{15}N$ values of OES from Kisese II indicate changing rainfall throughout the record that subtly oscillates between relatively drier and wetter periods. The wettest periods are just before and after the depositional hiatus (mean PMAP = 727 ± 46 mm/yr from 39.6 – 34.4 ka, n = 22; 765 ± 32 mm/yr from 23.7 – 21.2 ka, n = 9). Both of these wetter intervals appear drier than present conditions near Kisese II, estimated at 850 – 1050 mm/year (Mcsweeney et al., 2012b). The driest periods are at the beginning of the record (mean PMAP = 646 ± 110 mm/yr from 46.8 – 41.7 ka, n = 9) and in the most recent interval of our record in the Holocene (mean PMAP = 674 ± 54 mm/yr from 4.4. – 4.1 ka, n = 5). These dry intervals are still significantly wetter than the drier intervals at Lukenya Hill.

4.3: Oxygen Isotopes

We can estimate fluxes to the O isotopic composition of ostrich eggshell to quantify environmental signals influencing the $\delta^{18}O$ values of eggshell calcite. The oxygen isotopic composition of OES calcite varies due to 1) temperature of formation, 2) kinetic and equilibrium effects associated with biomineralization, and 3) the $\delta^{18}O$ value of body water (hereafter, $\delta^{18}O_{bodyH20}$). $\delta^{18}O_{bodyH20}$ values depend on 4) atmospheric oxygen incorporated during respiration and digestion, 5) consumed waters, and 6) water lost via excretion or evaporation during

respiration and thermoregulation (Koch, 1998; Luz et al., 1984). Ostriches are warm-blooded animals with stable body temperatures at c. 39º C (Crawford and Schmidt-Nielsen, 1967; Eagle et al., 2015), and since eggshells mineralize very rapidly, temperature and equilibrium effects can be considered constant across the biomineralization process and should not be reflected in changes in OES $\delta^{18}O$ values. Atmospheric oxygen $\delta^{18}O$ is roughly constant (~+24‰, VSMOW; Luz and Barkan, 2011) and its enrichment in ^{18}O (known as the Dole Effect) will result in consistently more positive values of OES calcite $\delta^{18}O$ values. However, respiration and thermoregulation are non-constant and vary greatly with ambient temperature (Schmidt-Nielsen et al., 1969) given that ostriches do not have sweat glands and require increased respiration to thermoregulate. Unless the $\delta^{18}O$ value of atmospheric O_2 changed significantly in the past, and since there is constant fractionation between cellulose and foliar $\delta^{18}O$ values (e.g., Sternberg, 1989), we would expect the majority of changes in the $\delta^{18}O$ value of body water used during OES mineralization to derive from changes in $\delta^{18}O$ of consumed water, or foliar $\delta^{18}O$ (hereafter $\delta^{18}O_{foliarH2O}$).

4.3.1: Towards a measure of past evapotranspiration

Like other animals deemed "evaporation-sensitive" (e.g., Levin et al., 2006), as non-obligate drinkers, ostriches derive most of their water from plant-leaf water, and therefore we propose that $\delta^{18}O$ values in OES calcite should primarily reflect the oxygen isotopic composition of leaves. $\delta^{18}O$ values of plant leaf water are controlled by the isotopic composition of meteoric water which is modified by soil evaporation and transpiration (predominantly controlled by vapor pressure difference (i.e. relative humidity) and temperature; (Barbour et al., 2004; Kahmen et al., 2011; Roden and Ehleringer, 1999). These altogether result in higher $\delta^{18}O$ values of plant leaf water and derived cellulose than their sources, as described by Kahmen et al. (2011). Since foliar $\delta^{18}O$ values derived from a consistent meteoric water source will vary depending on photosynthetic pathway and ambient climatic variables (Epstein et al., 1977; Sternberg et al., 1984), relative variations of foliar $\delta^{18}O$ values through time should reflect relative changes in net evapotranspiration, whether driven by temperature, humidity, and/or physiological responses in the plant (e.g., Dawson et al., 2002).

Passey et al. (2014) constrained the fractionation factor (α) between ostrich body water and eggshell calcite ($\alpha_{calcite\text{-}bodyH2O} = 1.0379 \pm 0.002$; Passey et al., 2014). We can use this to back-calculate the $\delta^{18}O$ values of body water from our $\delta^{18}O$ values of OES ($\delta^{18}O_{bodyH2O}$, supplementary data), and then quantify relative components contributing to body water using mass balance to determine $\delta^{18}O_{foliarH2O}$ values. A model by Kohn (1996) relates $\delta^{18}O$ values of biomineral apatite in obligate-drinking herbivorous birds and other fauna, providing estimates for the weighted contributions for each of the variables described above. Modifying this model for non-obligate drinkers like ostriches, the largest source of oxygen to the diet is from foliar water (57%), with other contributions from atmospheric oxygen due to respiration and thermoregulation (~30%), leaf cellulose oxygen (~9%), and oxygen from water vapor in air (4%, all after Kohn, 1996). These can be simplified to a linear relationship between body water and source water, namely foliar water (hereafter $\delta^{18}O_{foliarH2O}$):

$$\delta^{18}O_{bodyH2O} = A + B * \delta^{18}O_{foliarH2O} \quad (2.5)$$

For herbivorous birds, A and B are 5.83‰ and 0.71, respectively (Kohn, 1996). Calculated $\delta^{18}O_{foliarH2O}$ values for each ancient OES $\delta^{18}O$ value in our study were determined by calculating $\delta^{18}O_{bodyH2O}$ and then solving Equation 2.5 for $\delta^{18}O_{foliarH2O}$ (supplementary data). Resultant $\delta^{18}O_{foliarH2O}$ values from these calculations will be referred to as derived from "model 1".

We can model the $\delta^{18}O$ value of foliar water from OES stable isotopes another way, by using a model for the mean oxygen isotopic compositions of cellulose and leaf water in C_3 and C_4 plants in tropical semi-arid to arid climates (Sternberg et al., 1984). Sternberg et al. (1984) showed that measured $\delta^{18}O$ values of cellulose from C_3 and C_4 plants in hot semi-arid climates have a ~10‰ difference between C_3 and C_4 plant cellulose $\delta^{18}O$ values. This relation can be used to estimate cellulose $\delta^{18}O$ values in tropical arid climates if the fraction of C_3 versus C_4 plants is known. Using our calculated dietary $\delta^{13}C$ values from measured OES $\delta^{13}C$ values, we can determine the fraction *f* of C_3 versus C_4 (i.e. non-C_3) plants in the diet using mass balance using the same linear two endmember mixing model (Section 2.1.1). For example, the fraction of C_4 plants in the diet can be determined:

$$f_{C4} = (\delta^{13}C_{diet} - \delta^{13}C_{C3}) \div (\delta^{13}C_{C4} - \delta^{13}C_{C3}) \quad (2.6)$$

Using average cellulose $\delta^{18}O$ values in C_3 and C_4 plants (Sternberg et al., 1984), we can calculate the $\delta^{18}O$ of cellulose derived from the ostrich diet directly:

$$\delta^{18}O_{cellulose} = (1 - f_{C4}) \times \delta^{18}O_{C3} + f_{C4} \times \delta^{18}O_{C4} \quad (2.7)$$

Then, we can calculate a $\delta^{18}O_{foliarH2O}$ value by using the relationship between oxygen isotopic compositions of leaf water and cellulose (e.g., Sternberg, 1989):

$$\delta^{18}O_{foliarH2O} \sim \delta^{18}O_{cellulose} - 27‰ \quad (2.8)$$

These derived $\delta^{18}O_{foliarH2O}$ values hereafter will be referred to as derived from "model 2" and can be found in the supplementary data. In both models, lower $\delta^{18}O$ values should correspond with a decrease in the isotopic fractionation associated with evapotranspiration and higher $\delta^{18}O$ values correspond with higher modeled $\delta^{18}O_{foliarH2O}$ values and therefore increased evapotranspiration.

4.3.2: $\delta^{18}O$ values as an evapotranspiration proxy at each locality

The ranges of $\delta^{18}O$ values are broadly similar at the two localities. The $\delta^{18}O$ values of OES calcite at Lukenya Hill vary between 29.1 and 40.0‰ (table 2.2), with subtle shifts in mean values through time (table 2.4 and figure 2.5). The highest mean $\delta^{18}O$ value occurs from 18.8 – 14.9 ka (mean $\delta^{18}O = 38.3 \pm 1.1$, $n = 7$), corresponding with high evapotranspiration. The lowest mean $\delta^{18}O$ values occur at the beginning and end of the record (35.0 ± 0.7‰ from 6.9 – 3.7 ka, $n = 4$, and 35.4 ± 1.3‰, from 50 – 31.2 ka, $n = 5$), corresponding with low evapotranspiration. Standard deviations are of similar magnitude as those in the mean $\delta^{13}C$ values, from 0.3‰ to up to 3.6‰ – this high endmember σ corresponds to the interval with only two samples.

At Kisese II, $\delta^{18}O$ values range [28.8, 39.7‰] (table 2.3 and figure 2.6). Minima in mean $\delta^{18}O$ values = 32.6 ± 2.4‰ and occur early in the record (~46.9 – 41.7 ka), corresponding with minima in evapotranspiration (table 2.5). Maximum mean $\delta^{18}O$ values = 35.6 ± 1.4‰ from (~23.7 – 21.2 ka), just after the hiatus in data, and they correspond with increased

evapotranspiration. Uncertainties on the mean $\delta^{18}O$ values at Kisese II range from $\sigma = 1.2$ to 2.5‰; these are somewhat larger than at Lukenya Hill (Kisese II *n* ranges from 3 to 12).

5: Discussion

The isotopic variation of each element studied in OES allows us to assess the relations between the three proxies and compare them to other regional-scale lacustrine proxy records. OES isotope proxy records are discussed 1) relative to each element, including the utility of the foliar $\delta^{18}O$ models; 2) between localities, contextualized by co-occurring faunal and material culture records, such as the MSA/LSA transition; 3) in terms of the expression of well-known climate events recorded in other records; and 4) compared to regional paleoclimate records. We then evaluate which potential dynamic processes may be recorded by the isotope proxy records.

5.1: Relations among isotope proxies

5.1.1: Correlations between the three isotope systems

If each isotope system is interpreted as an independent paleoenvironmental proxy, the three isotope systems should not vary systematically with respect to each other. If proxies are intertwined, we may observe some systematic relationships between isotope systems. Figure 2.8 presents all the isotope data in two-dimensional plots to allow assessment of such relationships. Statistical assessments of isotope sets are presented in tables 2.6 and 2.7 as symmetric matrices. Pearson product-moment correlation coefficients (R) indicate small linear correlations between each isotope system (table 2.6) and a non-parametric rank correlation test, Kendall's tau correlation coefficient (τ), also indicates weak correlation between the three systems (table 2.7).

In both cases, the weakest correlations are between $\delta^{15}N$ and $\delta^{18}O$ values ($R^2 = 0.016$, $p > 0.05$; $\tau = 0.074$, $p > 0.05$), with p-values indicating that there is no statistically significant correlation between the two systems. The strongest correlations are between $\delta^{13}C$ and $\delta^{18}O$ values ($R^2 = 0.149$, $p < 0.05$; $\tau = 0.265$, $p < 0.05$); correlations between $\delta^{15}N$ and $\delta^{13}C$ values are weak ($R^2 = 0.071$, $p < 0.05$; $\tau = 0.221$, $p < 0.05$), but both correlation pairs are statistically significant.

While there may not be strong correlations between any two isotope variables, we can speculate how each proxy record may affect the others considering the biological, climatological, and physiological processes impacting the isotope signatures. For example, $\delta^{15}N$ values may weakly co-vary with $\delta^{13}C$ values if plants adapted to drier climates, such as C_4 plants, become predominant during intervals with low PMAP. We may expect $\delta^{15}N$ values to co-vary with $\delta^{18}O$ values, if precipitation is coupled with relative humidity. From these data, samples with estimated PMAP < 500 mm/yr also all have $\delta^{18}O$ values > 34‰ (figure 2.8), implying there may be a relationship between lower PMAP and higher $\delta^{18}O$ values, possibly due to coupling of low precipitation and decreased relative humidity. A possible cause for subtle correlation between $\delta^{13}C$ and $\delta^{18}O$ values may be the relation between how plants using different photosynthetic pathways are adapted to different environments. C_4 plants are better adapted to environments with high temperatures, low humidity and low pCO_2 (Ehleringer et al., 1997), so we may observe increases in C_4 plants from the dietary $\delta^{13}C$ values co-varying with increased $\delta^{18}O$ values. The broader range of O isotopic signatures may also be attributed to the physiological response of C_3 plants to increased temperatures and decreased humidity, when C_3 plants may shut down

photosynthesis resulting in enrichment in ^{18}O (e.g., Sternberg et al., 1984). More negative $\delta^{13}C_{diet}$ values in the data set (~ -27 to -22‰) have $\delta^{18}O$ values ~ 28 to 38 ‰, and less negative $\delta^{13}C_{diet}$ (~ -22 to -15‰) have more restricted, elevated $\delta^{18}O$ values (~ 33 to 40‰). While there is some overlap in the range of $\delta^{18}O$ values, these ranges in $\delta^{13}C_{diet}$ broadly correspond with C_3 versus C_4 plant types, suggesting that plant photosynthetic pathway may be subtly varying with the $\delta^{18}O$ values of OES. In cases of mixed C_3 - C_4 diets, there are overlapping ranges of $\delta^{18}O$ values. This corroborates the findings of (Faith, 2018) who interprets the $\delta^{18}O$ aridity index from faunal tooth enamel as being affected by different paleodiets. It appears that $\delta^{18}O$ values are responding to more than a single climatic/physiological variable, which may include precipitation amount, humidity (e.g., vapor pressure difference at the leaf surface), temperature, and plant photosynthetic pathway.

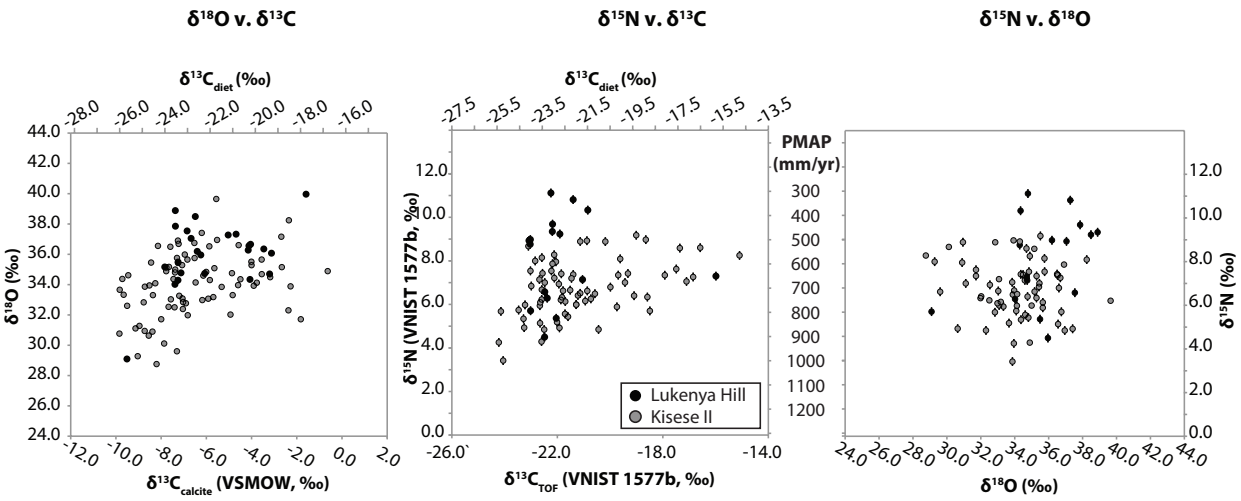

Figure 2.8: Comparisons of each isotope system from OES results. There is a subtle positive correlation between $\delta^{18}O$ and $\delta^{13}C$ values (Pearson $R^2 = 0.15$).

Pearson's R [R^2] (p-value)	$\delta^{13}C$	$\delta^{15}N$	$\delta^{18}O$
$\delta^{13}C$	1	0.267 [0.071] (0.00747)	0.386 [0.149] (4.861e-05)
$\delta^{15}N$	0.267 [0.071] (0.00747)	1	0.127 [0.016] (0.2105)
$\delta^{18}O$	0.386 [0.149] (4.861e-05)	0.127 [0.016] (0.2105)	1

Table 2.6: Pearson's correlation coefficients (R) with p-value in parentheses. Values are presented as a symmetric matrix. Null hypothesis is that there is no correlation between the variables in the row versus the column.

Kendall's τ (p-value)	$\delta^{13}C$	$\delta^{15}N$	$\delta^{18}O$
$\delta^{13}C$	1	0.221 (0.00129)	0.265 (6.229e-05)
$\delta^{15}N$	0.221 (0.00129)	1	0.074 (0.2803)
$\delta^{18}O$	0.265 (6.229e-05)	0.074 (0.2803)	1

Table 2.7: Kendall's correlation coefficients (τ) with p-value in parentheses. Values are presented as a symmetric matrix. Null hypothesis is that there is no correlation between the variables in the row versus the column.

5.1.2: Assessing the foliar $\delta^{18}O$ models

$\delta^{18}O$ values from OES have been typically challenging to interpret but have been taken as a qualitative aridity proxy in previous work (e.g., Lee-Thorp and Ecker, 2015; Roberts et al., 2016). However, with the addition of the PMAP proxy from $\delta^{15}N$ values, we now have a direct quantitative proxy for precipitation to elucidate wet versus dry time intervals. This has caused us to question the previously applied qualitative $\delta^{18}O$ aridity proxy; here we have shown that $\delta^{18}O$ values do not have any statistically significant correlation with $\delta^{15}N$ (and hence with PMAP), and we would expect a significant negative correlation if aridity were inversely related to precipitation. Instead, we propose that evapotranspiration, described by foliar water $\delta^{18}O$ values, is a more appropriate proxy derived from OES oxygen isotopes. Two models for $\delta^{18}O_{foliarH2O}$ values were computed here using different components of the observed data sets to assess uncertainties in each model. Figure 2.9 compares the two models described in section 4.3.1: model 1 calculates $\delta^{18}O_{foliarH2O}$ values using Kohn's model (1996), calculated $\delta^{18}O_{bodyH2O}$ based on measured $\delta^{18}O$ values from OES calcite and the fractionation factor $\alpha_{calcite\text{-}bodyH2O}$ (Passey et al., 2014), and Equation 2.5, and model 2 calculates $\delta^{18}O_{foliarH2O}$ values using our calculated dietary $\delta^{13}C$ values, approximated $\delta^{18}O_{cellulose}$ for C_3 and C_4 plants (after Sternberg et al., 1984), and Equation 2.8. A systematic offset between modeled $\delta^{18}O_{foliarH2O}$ values was observed (figure 2.9). The range of $\delta^{18}O_{foliarH2O}$ values for model 1 versus model 2 are [-0.4‰, 7.0‰] and [0.3‰, 4.9‰], respectively. Individual foliar water $\delta^{18}O$ values calculated for each sample differ between the models by as little as 0.1‰ to as much as 4.6‰ (supplementary data).

It may be that model 1 produces systematically elevated values with respect to model 2 due to explicit evaluation of other contributors to the oxygen isotopic composition of biominerals (such as atmospheric O_2 and respiration, which are not considered in model 2). Larger differences in the two model results may imply a greater contribution of other biological effects after foliar water consumption that would result in enrichment in ^{18}O, such as increased respiration and/or thermoregulation. With little primary data to compare to the $\delta^{18}O_{foliarH2O}$ proxy values, we compare the results of each model to those produced by a model of modern foliar water $\delta^{18}O$ values in Eastern Africa based on biophysical models of plant leaf isotope fractionation and local point precipitation isotope and climate data (West et al., 2008). The range of calculated values from both models presented here broadly reflect values modeled by West et al. (2008) for equatorial and high-altitude Eastern African regions and tropical central/western African regions (range $\delta^{18}O_{foliarH2O}$ ~1 – 10‰; West et al., 2008: figure 1). Our model $\delta^{18}O_{foliarH2O}$ values appear credible, given they are not far from expected values determined in such published isoscape models.

To evaluate the $\delta^{18}O$ proxy for evapotranspiration, figures 2.5 and 2.6 present OES $\delta^{18}O$ values on the upper x-axis calculated $\delta^{18}O_{foliarH2O}$ values on the lower x-axis using the approach of our model 1, as this calculation derives directly from the $\delta^{18}O$ values of OES calcite. This allows the discussion of $\delta^{18}O_{foliarH2O}$ values to remain independent with respect to the dietary $\delta^{13}C$ values, which contribute to the calculation of $\delta^{18}O_{foliarH2O}$ values in model 2. Further discussion of the two model results, and their strengths and weaknesses, can be found in the Supplementary Materials.

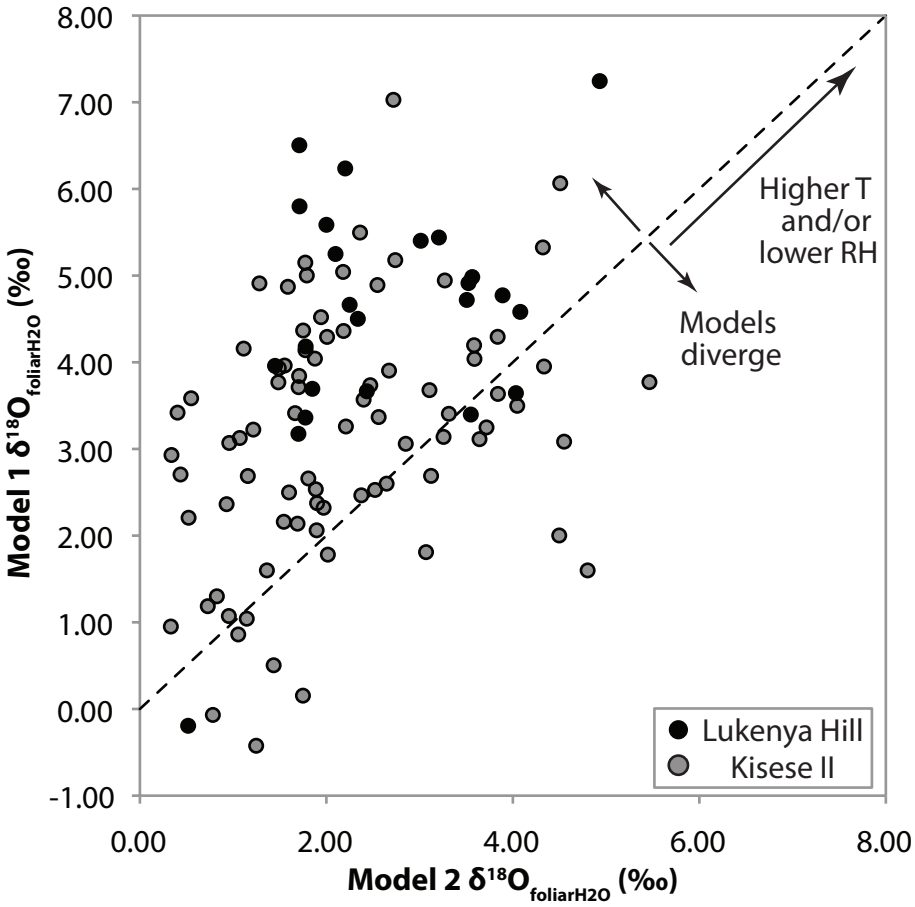

Figure 2.9: Comparison of model $\delta^{18}O$ values. X-axis provides values calculated from model 2, and y-axis provides values are from model 1. Points near the 1:1 line (dashed) demonstrate better agreement between models; values in the more positive direction of either axis indicate higher temperatures (T) and/or lower relative humidity (RH).

5.2: Comparison between the OES isotope records at Lukenya Hill and Kisese II

We can compare the $\delta^{13}C_{diet}$ values from OES to the faunal records to evaluate if they show similar indications of C_3 and C_4 plants on the landscape. We can compare the paleoenvironmental proxy data between sites through the ~50 ka interval, particularly with respect to archaeological change, such as the during the MSA/LSA transition at each site.

At Lukenya Hill, individual $\delta^{13}C_{diet}$ values vary subtly through time, but mean values indicate a mixed to dominantly C_4 plant contribution to the diet in most intervals. The highest mean values correspond with diets rich in C_4 plants during earlier intervals, and later intervals are characterized by relative increases in C_3 plants. Faunal analyses at Lukenya Hill indicate a predominantly C_4-rich landscape throughout the ~50 ka interval, though several arid adapted taxa (e.g., *Equus grevyi* and *Oryx beisa*) disappear at the onset of the Holocene as (Marean, 1992, 1991; Robinson, 2017). This is largely consistent with the OES $\delta^{13}C$ values, although the faunal record does not change significantly in the early Holocene to represent more C_3 browsers, suggesting perhaps a bias in representation of grazers in the archaeological record here (e.g., if people preferentially foraged for large game in the grassy plains below the inselberg). At Kisese II, mean values subtly oscillate between mixed and C_3-dominant diets: lowest mean $\delta^{13}C$ values, indicative of C_3-dominant diets, occur ~35.9 – 34.3 ka and 23.7 – 23.1 ka. Faunal analyses from Kisese II are challenging to interpret due to the incompleteness of the collection today (Tryon et al., 2019), but they indicate diverse grassland and wooded ecosystems in contrast to the abundant grazers of Lukenya Hill. This is largely in agreement with the OES dietary $\delta^{13}C$ values.

Unlike the carbon isotopes, mean values in nitrogen isotopic compositions at the two sites show distinct absolute values in PMAP and different trends through time (figures 2.5 & 2.6). Precipitation gradually increases through time at Lukenya Hill from an arid to semi-arid climate, while at Kisese II, precipitation patterns oscillate between wet and dry but remain within the range of semi-arid to possibly temperate climates. The two records share some common characteristics, for example, minimum mean PMAP values occur at the earliest intervals, even if they differ significantly in their magnitudes. Individual minimum OES $\delta^{15}N$ values infer similar maximum values in PMAP at the two sites, greater than ~900 mm/yr (OES with $\delta^{15}N$ values < 4.6‰); these are found in the wettest intervals at both localities. Integrating these observations, the $\delta^{15}N$ values indicate that: 1) As is the case today, in the past Kisese II had generally higher precipitation than Lukenya Hill. This implies a stable degree of relative difference between the sites. However, the nature of temporal variation differs at each site; that is, 2) there is a modest oscillatory precipitation pattern at Kisese II while PMAP at Lukenya Hill steadily increases through time to a maximum in the later Holocene that is wetter than it is today.

At Lukenya Hill, highest mean $\delta^{18}O_{foliarH2O}$ values occur in both models between ~26.3 – 21.6 ka and 18.8 – 14.9 ka, implying increased evapotranspiration during intervals of intermediate PMAP and a C_4-rich ostrich diet (figure 2.5). Because C_4 plants are better adapted to arid environments and are relatively abundant there, this may imply that high $\delta^{18}O_{foliarH2O}$ values at Lukenya Hill are responding to changes in temperature and/or physiological adaptation of C_4 plants to arid climates.

At Kisese II, mean $\delta^{18}O_{foliarH2O}$ values are higher in intervals with higher PMAP and more C_3 plants in the diet, indicating wetter, more C_3-rich intervals are characterized by higher evapotranspiration (figure 2.6). The trend of higher PMAP and concomitant evapotranspiration may imply a temperature control on $\delta^{18}O_{foliarH2O}$ values, and thus increased temperatures

indicated by high mean $\delta^{18}O_{foliarH2O}$ values, if precipitation and relative humidity are coupled. This relationship is apparent from ~35.1 – 33.7 ka and ~23.7 – 21.2 ka. If precipitation and relative humidity are in fact coupled, intervals with lower $\delta^{18}O_{foliarH2O}$ values may similarly reflect lower temperatures or physiological adaptation of C_4 plants to a more arid climate. For example, from ~46.9 – 41.7 ka and from ~17.6 ka on into the Holocene, $\delta^{18}O_{foliarH2O}$ values are lower when there is variably mixed to predominant C_3 plants in the diet and intermediate mean PMAP values; this would imply cooler temperatures in these intervals.

Both sites host archaeological evidence of the MSA/LSA transition occurring at different times. The OES stable isotope proxies indicate variable and distinct trends in the paleoenvironments of Kisese II and Lukenya Hill through time, including during the MSA/LSA transitions (figures 2.5 and 2.6). For example, precipitation at the two sites contrast most during their respective MSA/LSA transitions. Several spits overlap in time with the MSA/LSA transition at Kisese II. At Kisese II, a maximum in PMAP occurs during the onset of the MSA/LSA transition along with high evapotranspiration is observed in this interval as well. Mean $\delta^{18}O_{foliarH2O}$ values are higher during the MSA/LSA transition, when there is higher rainfall amount and diet is dominated by C_3 plants. This implies that times of higher PMAP and increased C_3 vegetation correspond with times of higher net evapotranspiration. If evapotranspiration is governed by temperature, relative humidity, and paleodiet, these high $\delta^{18}O$ values may be due to higher temperatures. If evapotranspiration is increased during periods of high PMAP (such as during the MSA/LSA transition), there may be increased rainfall but perhaps also higher temperatures.

Vegetation was consistently more arid-adapted at Lukenya Hill than at Kisese II, where $\delta^{13}C$ values indicate a mixed diet, including during the MSA/LSA transition. At Lukenya Hill, the highest mean $\delta^{18}O$ values of plant leaf waters occur during the MSA/LSA transition, when the mean PMAP is lowest and there is relatively abundant C_4 plants. Hence, the MSA/LSA transition is characterized by low rainfall, high temperature and/or aridity, and a relatively high C_4 plant composition relative to other periods here and at Kisese II.

5.3: Localized expression of regional paleoclimate events

The OES isotope records also provide a framework to examine the climate at each site during well-resolved larger scale climate events. We address two well-known climate intervals, the Last Glacial Maximum and the African Humid Period, which are well-resolved in eastern African lacustrine and other climate records.

5.3.1: The Last Glacial Maximum (~26 – 19 ka)

The Last Glacial Maximum (LGM, ~26 – 19 ka; Clark et al., 2009) is defined by large Northern Hemisphere ice sheets resulting in drier and cooler climates in eastern Africa (Johnson, 2017). If OES isotope proxies are responding to this larger-scale climate event, we may expect to find higher proportions of C_4 plants in the diet, lower PMAP, and/or increased evapotranspiration (if humidity is coupled with precipitation).

The fraction of C_4 plants in ostrich diets increases at both sites during the LGM relative to prior intervals. Four of five OES from Lukenya Hill during the LGM have $\delta^{13}C_{diet} > -21.5‰$, which may indicate more arid-adapted plants there, but $\delta^{13}C_{diet}$ values at this locality are generally more abundant in C_4 plants throughout the ~46 ka interval. At Lukenya Hill, PMAP is

gradually increasing during the LGM but still relatively low compared to the Holocene intervals. Since the LGM thus does not appear to impact the vegetation at Lukenya Hill, and given other records implicate cooler climates during the LGM, high $\delta^{18}O_{foliarH2O}$ values are likely a sign of increased aridity.

At Kisese II, 11 out of 26 OES reflect some dietary contribution from C_4 plants during the LGM, with relative increases in $\delta^{13}C_{diet}$ values through the LGM (figure 2.6). This shift in vegetation may reflect an increase in aridity, temperature, or an ecological response to lower pCO_2 during the LGM (Petit et al., 1999): because C_4 plants function better than C_3 plants in low pCO_2 regimes, they may expand their abundance and/or range in such climates (e.g., Ehleringer et al., 1997). At Kisese II, one of two maxima in PMAP occur at the beginning of the LGM, so if precipitation and relative humidity are coupled here, high $\delta^{18}O$ values of plant leaf waters combined with a relative increase in C_4 plants in this interval corroborate an adaptive ecological response of increased C_4 vegetation due to lower pCO_2, during the LGM.

5.3.2 The African Humid Period (~14 – 5 ka)

The African Humid Period (AHP, ~14 – 5 ka; (Demenocal et al., 2000; Shanahan et al., 2015) is defined by a period of higher rainfall across circum-Saharan Africa, when the Sahara also supported vegetative and lacustrine ecosystems. At Lukenya Hill, OES dated 13.7 to 12.2 ka indicate a relatively mixed diet compared to all other periods with C_4-rich diets. This suggests that C_3 plants may have been relatively more abundant in the early Holocene at Lukenya Hill, consistent with an ecological response to increased rainfall associated with the onset of the AHP. Peak mean PMAP values at Lukenya Hill in the Holocene are greater than modern MAP (~630 mm/year), implying the environment has become drier since the Early- to Middle Holocene. Our OES $\delta^{15}N$ results at Lukenya Hill are consistent with increased precipitation during the African Humid Period and support other evidence that the AHP was wetter than it is today (Shanahan et al., 2015). Low mean $\delta^{18}O$ values occur during the AHP, corresponding with the trends in increasing PMAP into the AHP and a progressively increasing contribution of C_3 plants. Decreases in temperature and/or aridity are associated with increased rainfall periods here during the AHP.

At Kisese II, three of six OES from 4.4 – 4.1 ka reflect some C_4 contribution (mean $\delta^{13}C_{diet}$ = -22.5 ± 2.3‰). Although only one in five in the preceding interval (18.1 – 4.2) ka indicate a C_4 contribution, this interval is poorly constrained in time. Nevertheless, there appears to have been mixed availability of both C_3 and C_4 plants just after the AHP, particularly 4.4 – 4.1 ka. Precipitation at Kisese II does not increase to its maximum mean PMAP during the African Humid Period like it does at Lukenya Hill, but considering uncertainties on the mean values, some intervals during the AHP are indistinguishable from the maximum mean values in PMAP observed earlier in the record there. At Kisese II, lowest mean $\delta^{18}O$ values of plant leaf water occur during the Holocene when there is modest PMAP. If $\delta^{18}O_{foliarH2O}$ is mainly controlled by temperature at this site, low values would imply cooler temperatures during and after the AHP. The Kisese II OES isotope record does not implicate a strong signal of the AHP as is apparent at Lukenya Hill.

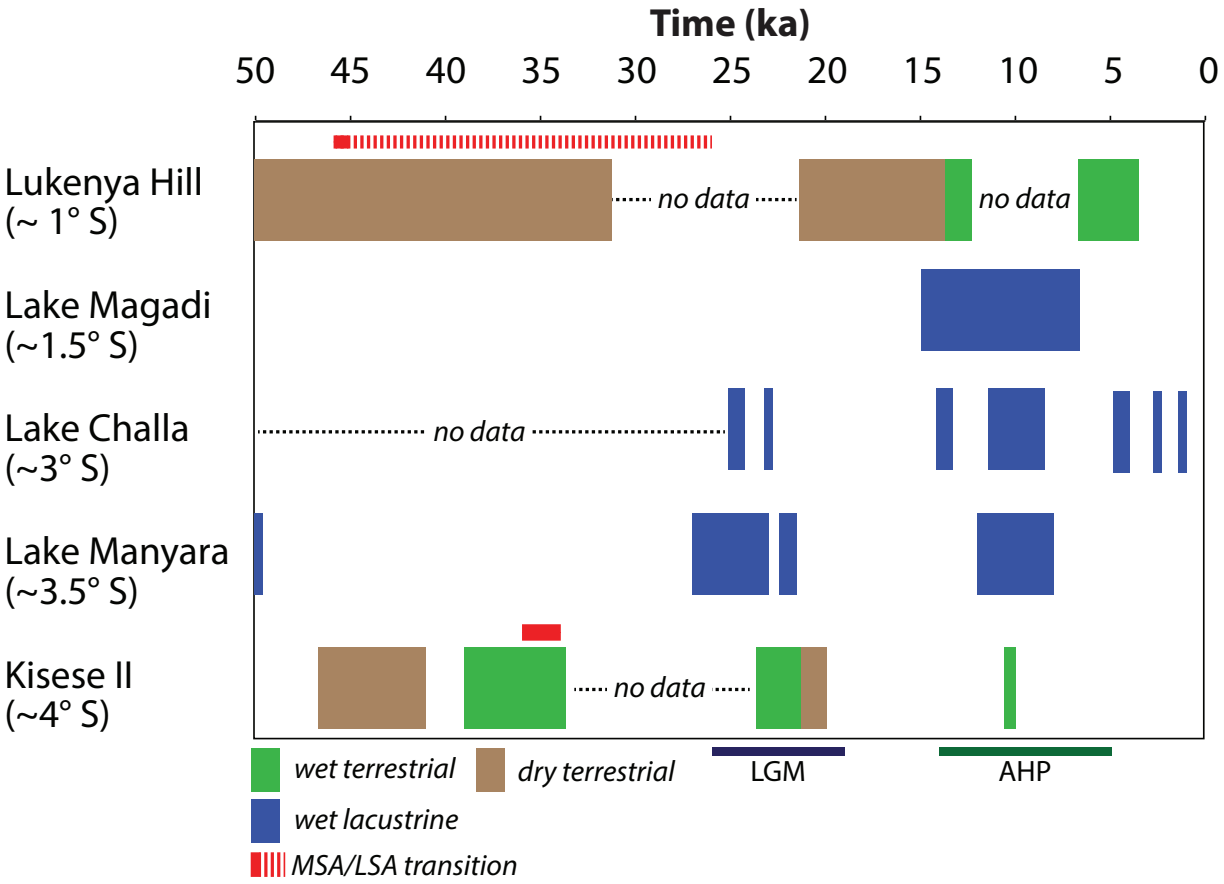

Figure 2.10: Summary of wet intervals over the last ~50 ka from the sites discussed as compared to proximal lakes. Qualitative indicators of wet intervals are indicated from proxies from lake records near Kisese II and Lukenya Hill compared to wet and dry intervals at the sites indicated from the $\delta^{15}N$ PMAP proxy. The MSA/LSA transition at each locality is also highlighted (red bars) along with the Last Glacial Maximum (LGM) and the African Humid Period (AHP). Qualitative proxies from each lacustrine record define wetter intervals relative to their respective proxy records; un-marked intervals from the lacustrine records are absent of evidence favoring wet climates. The proxy records come from the following published literature: Lake Magadi (Owen et al., 2019, 2018); Lake Challa (Verschuren et al., 2009); Lake Manyara (Bachofer et al., 2018; Casanova and Hillaire-Marcel, 1992).

5.5: Comparison to other regional paleoclimate records

With the three isotope systems at Kisese II and Lukenya Hill, we can clarify how local environmental changes compare with regional records. Examining records from nearby lacustrine sequences, there appear to be some agreements and other contradictions.

The OES stable isotope records at Kisese II and Lukenya Hill clearly record one or more of the "humid" intervals evidenced in the proximal lacustrine records but the locality and proximal lacustrine records do not agree in all intervals. Figure 2.10 summarizes wet and dry intervals defined by PMAP at Lukenya Hill and Kisese II compared to qualitative proxy indicators for wet intervals from lacustrine records nearest to the sites. Lake Magadi and Lake Manyara are similarly out of phase and in particular show contrasting responses to the LGM (Casanova and Hillaire-Marcel, 1992; Owen et al., 2019, 2018). However, the Lake Magadi record demonstrates progressive aridification following the LGM until the AHP, indicated by increases in local, woodland, and afromontane pollen (Owen et al., 2019). This is unlike the nearby Lukenya Hill OES isotope record which becomes progressively wetter through time up to the AHP. Nearby Kisese II, Lake Manyara records lake level transgressions just before and through the LGM, and again at the onset of the Holocene, identifying these as "humid" periods (Bachofer et al., 2018; Casanova and Hillaire-Marcel, 1992). The OES isotope record at Kisese II agrees with part of the Lake Manyara record – particularly regarding the wetter LGM – but not entirely, with respect to the Holocene. Furthermore, Lake Manyara shows no evidence of a wetter interval from ~39 – 34 ka, as is indicated by the PMAP and vegetation proxies at Kisese II. The Lake Challa record has the most in common with the Kisese II PMAP record, indicative of a wet LGM and a drier mid-Holocene (during the AHP), which is attributed to changes in the intensity of the African monsoon (Tierney et al., 2011b; Verschuren et al., 2009). Lake Eyasi, while proximal to Kisese II, hosts nearby archaeology and fossils which have been recently dated to ~115 ka, contesting previous ages of ~35 ka (Domínguez-Rodrigo et al., 2007), making this record difficult to reconcile chronologically with our data; hence, it has not been included in our comparisons.

Farther afield, At Lake Malawi farther South of Kisese II, proxies indicate variation between wooded grasslands and woodlands over the last ~50 ka with progressive increases in wetness and temperatures, particularly by the LGM (Johnson et al., 2016). This again agrees with a wetter LGM but differs with respect to precipitation trends through time relative to the Kisese II PMAP proxy record. The presence of an AHP signal at Lukenya Hill also agrees with the conclusions of Shanahan et al. (2015), that the AHP terminated later with decreasing latitudes into the Southern Hemisphere. This agrees with a record farther south from the Congo Fan (~5.5° S; Schefuß et al., 2005). Yet, the Congo Fan record is closer in latitude to Kisese II (4.42° S), where the paleo-MAP record calculated from the $\delta^{15}N$ values there not only reflects different trends and precipitation amounts through time than at Lukenya Hill, they also do not reflect a relatively wet interval during the AHP.

OES stable isotope data suggest that Lukenya Hill (~ 1° S) and Kisese II (~ 4° S) straddle an important boundary in Late Pleistocene climate systems that serve to emphasize the importance of local-scale reconstructions for comparison with hominid behavioral change preserved in the archaeological record. Blome et al (2012) divide eastern Africa from tropical Africa at about ~ 1° S latitude, based on among various local paleoclimatic and paleoenvironmental archives on either side of this latitude. Differences in the local

paleoenvironmental records at Lukenya Hill and Kisese II corroborate diverse climate regimes across this ~ 1° S boundary, but they also imply that general trends in a regionally wetting or drying climate apparent in lacustrine records do not necessarily apply at the habitat scale precisely.

5.6: Possible Drivers of Diverse Local Paleoenvironments

The contrasting relationships between the three isotopes at each locality imply that precipitation, humidity, and temperature may not co-vary with vegetation in the same way in each place. Differences in humidity, temperature, and/or precipitation could be controlled by the same dynamic variables at the two localities, but their relative geographic positions may result in absolute differences in the coupling of these climate variables. For example, PMAP trends at Lukenya Hill may follow trends associated with the African monsoon (e.g., Shanahan et al., 2015), as indicated by the presence of an AHP maximum in rainfall. PMAP at Kisese II was oscillatory and may be associated with glacial and interglacial cycles, but additional temporally highly resolved data, particularly in the depositional hiatus, would be needed to assess this carefully. Tierney et al. (2011a) propose that contributing rainfall from different sources, such as the Atlantic and Indian Oceans, may contribute to the increase in net rainfall during the AHP. Since a wetter AHP is only seen at one of the two localities studied here (Lukenya Hill), PMAP there may partly reflect different geographic sources of precipitation between low southern hemisphere and equatorial latitudes. If this is the case, this would in turn affect the bulk meteoric water $\delta^{18}O$ values if multiple water sources contribute to foliar water $\delta^{18}O$ at one site but not at another site. However, changes in sea surface temperatures over the Indian Ocean can also affect rainfall amount over the localities of interest (e.g., Shanahan et al., 2015). Eastern African equatorial meteoric waters derive mainly from the Indian ocean via the Somali (and more locally, the Turkana) Jet(s), whose trajectories are strongly influenced by the steep altitudinal gradients characterizing the eastern African highlands (Nicholson, 2017, and references therein). Differences in atmospheric pressure controlled by the strength of the Turkana Jet may lead to variation in wind patterns and precipitation over these two localities and possibly differences in humidity and/or air temperatures not related to different precipitation sources. Hence, it isn't necessary to invoke multiple sources of precipitation to result in different rainfall intensities over small distances.

Alternatively, different or shifting dynamic mechanisms may be responsible for diverse climates at each locality. For example, the Intertropical Convergence Zone (ITCZ)[4] might undergo secular latitudinal shifts through time (e.g., Blome et al., 2012) and control un-correlated precipitation changes at both sites. Lake Challa records indicate that at equatorial latitudes, the ITCZ may experience shifts in mean annual position over orbital timescales which can lead to compression of the tropical convective zone (Verschuren et al., 2009). This may lead to different dynamic processes governing rainfall over a range of near-equatorial latitudes, such as the ITCZ, and its position relative to the Turkana Low Level Jet (e.g., Hartman, 2018; Nicholson, 2016, 2017). This may explain the distinct relationships between precipitation and climatic variables controlling evapotranspiration (humidity and/or temperature) differences in rainfall amount, and differing rainfall and vegetation trends through time.

[4] The ITCZ is defined here as the location of maximum rainfall over land on the continents.

5.7: Summary

Blome et al. (2012) speculated that hominid "populations in equatorial and eastern Africa may have been buffered from the extremes of climate change by locally steep altitudinal and rainfall gradients" (Blome et al., 2012: 563). However, spatially dense data sets are still lacking to reconstruct the mosaic of paleoenvironments potentially available to hominids at any given time. For example, if the variability of environments were correlated with human innovation such as the transition to the Later Stone Age, we would expect the paleoenvironments to differ during the MSA/LSA transition relative to preceding intervals. But, subtle consistent environmental variability appears to be the norm rather than the exception at both localities: at any point in the last ~50 ka, Lukenya Hill and Kisese II were environmentally different and transitioning to different environments over ~ multi-ka timescales (the temporal resolution at which we can assess most climate and archaeological records of interest). For example, the Lukenya Hill OES isotopic record shows evidence of a dry, C_4-rich, moderately arid and/or warm environment during the MSA/LSA transition; then the record indicates increased precipitation and a modest increase in C_3 vegetation during the AHP, corroborating wetter climates into the Holocene despite low precipitation in the LGM. In contrast, the wettest intervals at Kisese II coincide with the LGM and the 36-34 ka interval coincident with the onset of the MSA/LSA transition there, with no suggestion of a relatively more humid period during the Holocene. If the environments at these two localities were always different from one another and were also always changing through time at this temporal resolution, the time-transgressive MSA/LSA transition occurring in different paleoclimates across a distance < 350 km, cannot be explained as an adaptive response to absolute differences or similarities in environments, a specific environmental change, or to the tempo of such of changes. This implies that the spread of LSA technologies is in response to other, non-environmental causes. The diverse and unique paleoenvironments through space and time at Kisese II and Lukenya Hill highlight the need for localized, precisely and accurately dated, paleoenvironmental records in order to assess possible correlations between human evolution and innovation and environmental change.

6: Conclusions

Analyses of ostrich eggshell fragments from the Lukenya Hill and Kisese II sequences, brought to these sites by humans, allow reconstruction of past local environments directly relevant to human subsistence. Modern calibrations on ratite eggshells have provided a basis to interpret the isotopic compositions of carbon and nitrogen in OES as proxies for paleo-vegetation and PMAP, and we propose a model to interpret the oxygen isotopic composition of OES as a novel proxy for evapotranspiration. Trends indicated by $\delta^{13}C$, $\delta^{15}N$ and $\delta^{18}O$ values of ostrich eggshell complement other proxy records that highlight large-scale changes in climate, such as the identification of the African Humid Period at Lukenya Hill, the Last Glacial Maximum at Kisese II, and time-transgressive variations in precipitation with latitude. But, the isotopic composition of OES may reveal changes in local climate more relevant to human subsistence in a given locale than those typically determined from regional scale proxy records. This is exemplified here by the apparent differences in the OES isotope proxies compared to proximal lacustrine records, and in the coupling of temperature and/or relative humidity (inferred from $\delta^{18}O$ values) compared to the changes in rainfall or vegetation (derived from $\delta^{15}N$ or $\delta^{13}C$ values, respectively) at the two localities. Different dynamic processes may be responsible for the

diverse paleoenvironments across equatorial latitudes, or site position relative to a process that undergoes secular shifts, such as the ITCZ, which may lead to variation in the strength of local climatological controls such as the Turkana Jet. Other frequently used paleoclimate proxy records, such as ocean or lake cores, may not capture such mesoscopic variability in climate as is possible with the isotope systems of OES.

The integrated three-isotope approach applied at two eastern African archaeological localities demonstrates variable localized paleoenvironments from ~50 ka onward, where environmental change (changing precipitation, vegetation, and temperature and/or relative humidity) is the norm rather than the exception, and shows that environmental change is not restricted to the respective MSA/LSA transitions. Populating the landscape with highly resolved local OES isotope records from archaeological sites could allow more direct assessment of the relationship between environmental and archaeological change at a greater spatial scale. The results from Kisese II and Lukenya Hill also mark the first published use of stable isotopes in the organic fraction of ostrich eggshells at eastern African archaeological sites, which provides a quantitative proxy for local paleo-precipitation. These data derive from significantly older eggshells than previously studied African archaeological OES assemblages, demonstrating the potential to apply these methods to other African sites well into the Late Pleistocene. With the abundance of OES at archaeological sites across the African continent and beyond, and recent development of ^{230}Th/U burial dating of ostrich eggshell, there is potential to build site-specific, precisely dated, three-isotope paleoenvironmental records up to ~10 times the ~45 ka limit of ^{14}C dating.

Chapter 3: ^{230}Th dating of coral abraders from stratified deposits at Tangatatau Rockshelter, Mangaia, Cook Islands: Implications for building precise chronologies in Polynesia

Abstract

Polynesian archaeology has relied primarily on ^{14}C dating to establish the timing and tempo of human colonization of the eastern Pacific, ensuing cultural development, and human-environmental interactions. Despite advancements in ^{14}C dating including accelerator mass spectrometry, selection of short-lived plant remains to avoid in-built age, and the use of Bayesian models to refine ^{14}C-based chronologies, large uncertainties introduced during calibration to calendar ages can severely limit the resolution of ^{14}C dates in this context. ^{230}Th dating of coral abraders, a common artifact in many Polynesian archaeological sequences, can potentially provide much more precise dates. We report 25 ^{230}Th dates for *Acropora* and *Porites* coral abraders from a well-studied, stratified archaeological sequence at Tangatatau Rockshelter, Mangaia (site MAN-44, Cook Islands), develop screening criteria to identify reliable ^{230}Th dates from buried contexts, and compare the results with a recent Bayesian ^{14}C chronology for the site. Visual characteristics (gray color, microcrystalline sugary texture) can aid identifying altered corals before analysis but are non-diagnostic of the suitability of samples for dating. Some corals that were fully remineralized to calcite preserved suitable U and Th isotopic compositions and produced ages in agreement with ^{14}C and pristine aragonitic coral ^{230}Th dates, suggesting that unlike subaerially exposed corals, buried corals may be susceptible to mineral alteration without perturbing the U-series isotopic systematics, possibly due to burial under reducing conditions. In general, corals with reliable ^{230}Th dates preserve initial (^{234}U/^{238}U) ratios in equilibrium with seawater and have (^{230}Th/^{232}Th) ratios > 10. Reliable dates at MAN-44 cluster within layers, preserve stratigraphic order, and agree with the previous ^{14}C chronology. Precise ^{230}Th dates (median ± 7.4 yr, all errors 2σ) from coral abraders support early Polynesian arrival on Mangaia (by 1011.6 ± 5.8 CE) and the arrival of the sweet potato (*Ipomoea batatas*) no later than 1361–1466 CE, indicating that trans-Pacific voyaging had introduced this South American native plant to the Cook Islands by the mid-15th century. With suitable samples, ^{230}Th dating of corals from stratified sequences has great potential for developing refined chronologies for Polynesian and other Pacific archaeological sites.

1: Introduction

Precise and accurate chronologies are essential to understanding the sequence and tempo of the geographic range expansion and environmental effects of human populations across the Pacific. However, problems inherent to the technique most widely applied to Pacific Island archaeology, ^{14}C geochronology, make this technique insufficient to clarify existing debates. For example, despite enhanced sample selection criteria and advancements in AMS ^{14}C dating, debate over the timing of Polynesian settlement of several island groups continues (e.g., Irwin, 1981; Kirch, 1986; Walter, 1996; Anderson, 2001, 2003; Wilmshurst et al., 2011). A meta-analysis of ^{14}C dates by Wilmshurst et al. (2011) suggested Polynesian arrival in the Society

Islands ~1025–1120 CE followed by dispersal to most remaining islands of East Polynesia from ~1200–1290 CE; however, AMS ^{14}C dates for Mangareva (Kirch et al., 2010), the Marquesas (Allen, 2014; Allen and Morrison, 2013; Conte and Molle, 2014), and Hawai'i (Athens et al., 2014; Dye and Pantaleo, 2010; Kirch, 2011) suggest somewhat earlier settlement of Eastern Polynesia c. 900–1100 CE. The southern Cook Islands have played a pivotal role in this debate because they are the nearest island group to the east of the earliest documented Polynesian settlements in Tonga and Samoa (Burley et al., 2015; Nunn and Petchey, 2013; Petchey et al., 2015), and southern Cook Islands sites such as Ureia (Allen and Wallace, 2007) and Tangatatau Rockshelter (Kirch et al., 2017a) record early Polynesian presence in the region. Even ideal AMS ^{14}C samples may not resolve the timing of earliest settlement in Eastern Polynesia because large fluctuations in the ^{14}C calibration curve during the past two millennia result in multi-modal probability distribution functions for calibrated ^{14}C dates and consequently large uncertainties ranging from 50 to >250 years (Taylor, 1997). Bayesian modeling of large ^{14}C data sets such as Tatangatau have substantially refined Polynesian settlement chronologies, but a better understanding of the timing and sequence of colonization of the archipelagoes of Eastern Polynesia would benefit from dates more precise than the ^{14}C technique can provide.

Recent work utilizing chronometric hygiene protocols with AMS ^{14}C dating in Western Polynesia reveal the oldest settlements occurring c. 3–2.7 ka (Burley et al., 2015; Nunn and Petchey, 2013; Petchey et al., 2015), and some sequences have been further refined by U-Th dates of coral abraders in agreement with ^{14}C dates (Burley et al., 2015, 2012; Clark et al., 2016). Polynesians used corals in several distinct contexts, and dating via the ^{238}U-^{234}U-^{230}Th system (hereafter ^{230}Th dating) applied to corals is inherently capable of producing high precision dates in the interval of East Polynesian exploration and settlement (e.g., Cobb et al., 2003; Kirch and Sharp, 2005). For example, ^{230}Th coral ages with precisions of circa 1% or better are readily attainable for suitable samples, yielding absolute uncertainties of 5-10 years for ~1000-year-old corals (all errors 2σ). ^{230}Th dating of archaeological corals has resolved the age and tempo of temple construction in East Polynesia (Kirch and Sharp, 2005; Sharp et al., 2010) and construction of monumental architecture in Eastern Micronesia (McCoy et al., 2016; Richards et al., 2015). Where suitable samples can be identified, ^{230}Th dating of coral abraders from stratified contexts, which are abundant in many Polynesian stratified sequences (Kirch, 2017a), may provide precise constraints not only on the timing of initial settlement but also on the tempo of subsequent cultural and environmental changes.

Here we characterize and date *Acropora* and *Porites* coral abraders from a carefully excavated, stratified occupation sequence at Tangatatau Rockshelter, Mangaia. We develop criteria for suitable ^{230}Th dating samples and reliable ^{230}Th coral dates, contrast behavior of the U-Th system in buried corals with that of more widely studied subaerial corals, compare the ^{230}Th dates on abraders to a well constrained age model from AMS ^{14}C ages of short-lived plant materials (Kirch, 2017b), and discuss implications of the new ^{230}Th dates for Polynesian settlement and occupation of Mangaia and the southern Cook Islands.

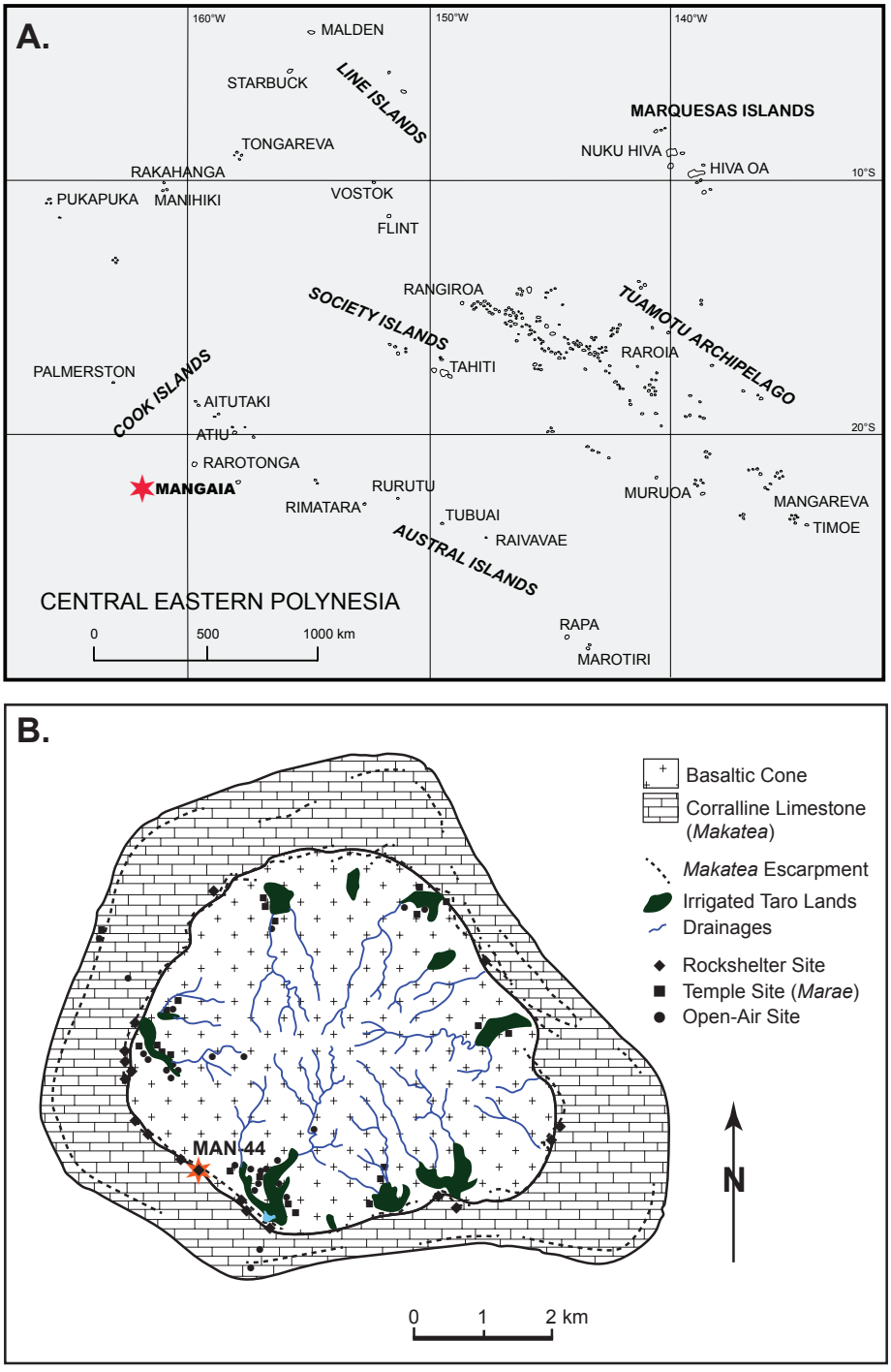

Figure 3.1: Maps of A. central Eastern Polynesia showing Mangaia Island (red star), and B. Mangaia Island with the location of Tangatatau Rockshelter (MAN-44, orange star).

1.1: Mangaia Island and MAN-44 excavations at Tangatatau Rockshelter

Mangaia is the southernmost of the Cook Islands in Eastern Polynesia (21°55' S, 157°55' W; Figure 3.1). K-Ar ages on ankaramite of the island's volcanic core reveal Mangaia formed ~18.9–16.6 Ma from hot spot volcanism now centered underneath the southeastern MacDonald Seamount, indicating it is among the oldest islands in the Cook-Austral island chains (Dalrymple et al., 1975). Fringing reefs grown upon an older limestone platform (Yonekura et al., 1988) surrounding the extinct volcanic center at Mangaia were later uplifted due to lithostatic rebound from plate flexure centered around the Rarotonga volcano, active c. 1.83-1.19 Ma (Dalrymple et al., 1975; Mcnutt and Menard, 1978). These uplifted reefs form a nearly concentric perimeter of Pleistocene coralline carbonate elevated up to ~70 m above sea level, called *makatea* in Polynesian (Kirch, 2017c; Marshall, 1927). Two periods of sea level stability during uplift resulted in marine-cut terraces forming in the uplifted limestone platform (Ellison, 1994). The inward-facing edge of the *makatea* forms cliff faces where chemical weathering and erosion have formed radial-concentric drainages directing meteoric waters from the central volcanogenic area out to the ocean. Karstic topography within the *makatea* leaves overhangs, caves, and caverns used as places of refuge, burial, defense, and habitation by pre-European contact Polynesians (Kirch, 2017c). These include Tangatatau Rockshelter, which faces toward the island's center and was formed by localized *makatea* collapse on the southeastern side of Mangaia. Tangatatau is the site of the MAN-44 excavations where coral abraders dated in this study were recovered (Figure 3.1) (Kirch, 2017c).

Model Groups	Parameter	95% HPD Interval, cal. BCE/CE
SZ-1A	α	9138-6277 BCE
	β	850-1136 CE
SZ-1B	α	850-1136 CE
	β	1315-1386 CE
SZ-2	α	1315-1386 CE
	β	1365-1405 CE
SZ-3	α	1365-1405 CE
	β	1395-1446 CE
SZ-5	α	1416-1483 CE
	β	1460-1492 CE
SZ-6 and SZ-7	α	1460-1492 CE
	β	1468-1509 CE
SZ-8	α	1468-1509 CE
	β	1500-1611 CE
SZ-9	α	1485-1512 CE, 1515-1610 CE
	β	1493-1525 CE, 1570-1720 CE
SZ-15	α	1512-1579 CE, 1589-1634 CE
	β	1527-1610 CE, 1618-1713 CE
SZ-17	α	1641-1792 CE
	β	1742-1949 CE

Table 3.1: Highest Posterior Density (HPD) estimates for Bayesian calibration model parameters in the main excavation block of MAN-44. Data are after (Kirch, 2017b).

Lab No. (MAN-44-U-Th#-)	STRATIGRAPHIC ZONE (SZ)	TAXON	SITE	UNIT	LEVEL	OBJECT NO.	WEIGHT (g)
9	2	*Acropora*	M44	D34	9	14	7.0
15	2	*Acropora*	M44	E33	11	10	1.0
25	2	*Porites*	M44	E36	8	2	27.4
8*	3	*Acropora*	M44	D34	7	5	15.1
17	3	*Acropora*	M44	E35	5	10	4.1
20	3	*Porites*	M44	D35	5	5	73.8
24	3	*Porites*	M44	E36	6	8	53.2
10	5	*Acropora*	M44	E30	8	3	5.7
11✚*	5	*Acropora*	M44	E30	8	4	11.5
22	5	*Porites*	M44	E30	8	1	2.2
3	6	*Acropora*	M44	D32	7	2	0.6
4*	6	*Acropora*	M44	D32	7	4	34.0
23	6	*Porites*	M44	E36	3	3	5.8
1✚*	7	*Acropora*	M44	C30	6	3	14.3
12	7	*Acropora*	M44	E31	6	3	3.3
13	7	*Acropora*	M44	E31	6	10	4.9
2	8	*Acropora*	M44	D32	3	7	19.1
7*	8	*Acropora*	M44	D34	3	1	4.6
14	8	*Acropora*	M44	E32	4	1	5.9
16✚	8	*Acropora*	M44	E34	3	3	13.7
18	8	*Porites*	M44	D31	5	8	2.8
19	10	*Porites*	M44	D33	3	8	35.6
5✚*	15	*Acropora*	M44	D33	2	1	8.5
6	15	*Acropora*	M44	D34	2	2	28.7
21	15	*Porites*	M44	E30	3	21	387.8

✚: Dated in duplicate; *: analyzed with laser ablation ICP-MS for ^{238}U, ^{232}Th, and ^{43}Ca

Table 3.2: Coral abraders analyzed in this study with their stratigraphic information.

The ^{14}C chronology at MAN-44 derives from a stratified sequence at the MAN-44 site excavated in natural layers during field seasons in 1989 and 1991 (Kirch, 2017d). These cross-correlated layers, connected by visibly continuous excavation wall stratigraphy across multiple excavation units, were later grouped into 17 stratigraphic zones (SZ). SZ were defined on the basis of sedimentological-stratigraphic relationships and chronologically constrained on the basis of a series of AMS ^{14}C dates (completed in 1992, 2011, and after 2013; Kirch, 2017b) obtained from short-live plant species, mostly from taxonomically identified carbonized macrobotanical remains (Kirch, 2017b). Ages were input to a Bayesian model to predict the maximum (oldest, α) and minimum (youngest, β) highest probability density (HPD) age intervals bracketing the top and bottom of each SZ, respectively (Table 1), and to produce highest probability ("Bayesian Posterior Probability Age Estimate", θ) age ranges for each ^{14}C date within these SZ. Kirch (2017b) describes the parameterization of the α and β intervals with arbitrary strata: "If stratum *k* directly overlies another stratum *j,* with abutting stratigraphic contacts and no indication of a hiatus in deposition, then the relationship between those two strata would be specified in [Equation 3.1]:"

$$\alpha_j > \theta_{j(1\ldots n)} > \beta_j = \alpha_k > \theta_{k(1\ldots n)} > \beta_k, \quad (3.1)$$

where θ values are the Bayesian Posterior Probability age estimates for each AMS ^{14}C dates associated with a given stratum. The age estimates have been calculated based on 38 of 41 AMS ^{14}C dates and the stratigraphic relationship (referred to as prior probabilities) between strata with ^{14}C dates to yield age ranges for each SZ, with SZ-1 at the base and SZ-17 at the top of the excavations.

The ^{14}C chronology at MAN-44 is extremely robust as it represents the results of meticulous screening for sample quality, filtering from a total of 71 ^{14}C dates obtained from Tangatatau (including conventional and AMS) to only 38 used in the model, all of which would be classified as "Class 1" dates by Wilmshurst et al., (2011), and it considers stratigraphic constraints from carefully described and analyzed sediments for each SZ. The model indicates that earliest human presence begins between 850–1136 CE, placing it among the oldest settlements of Eastern Polynesia (Kirch, 2017b). Among other notable findings from MAN-44, the excavations indicate human introduction to Mangaia of the Pacific rat (*R. exulans*) ~900–1180 CE, human-introduced flora, including *Morinda citrifolia* ~1050–1230 CE, and the sweet potato (*Ipomoea batatas*) before 1416–1483 CE, abundant stone tools and *debitage*, 58 discrete archaeological sedimentary features, and diverse varieties of fish hooks and other shell and bone artifacts manufactured at the site using coral abraders distributed throughout most of the sequence (Kirch et al., 2017a).

Previous studies that reported ^{230}Th dates for coral abraders from Pacific Island stratified sequences used macroscopic appearance and concordance of dates for sub-samples to assess the reliability of ^{230}Th dates (Burley et al., 2015, 2012). However, other analytical screening tests, including testing for preservation of primary mineralogy and U-series isotopic systematics, are commonly applied to ^{230}Th coral dates from subaerial contexts, such as in uplifted reefs widely exploited for paleoceanographic and paleoenvironmental studies (e.g., Cobb et al., 2003; Stirling and Andersen, 2009; McGregor et al., 2011; Hibbert et al., 2016; Muhs et al., 2017). Here, we apply these screening criteria to corals from buried contexts.

2: Samples and Methods

Twenty-five coral abraders spanning most of the Tangatatau sequence from SZ-2 to SZ-15 were selected for ^{230}Th dating, including eight *Porites* and seventeen *Acropora* (Table 2). Where available, multiple corals from the same SZ were dated to assess the reproducibility of ^{230}Th dates. Corals from the lower SZ were dated to help evaluate the timing of initial human occupation of Mangaia Island which, based on the ^{14}C dates, is older than expected based on a recent meta-analysis of Polynesian radiocarbon dates by Wilmshurst et al. (2011).

Samples were assigned Berkeley Geochronology Center (BGC) lab numbers (Table 2), prepared for analysis, and dated in BGC's U-Daughter Lab using a Thermo-Fisher NEPTUNE *Plus* multi-collector inductively coupled plasma mass spectrometer (ICP-MS). Selected corals were profiled for U and common Th (^{232}Th) via laser ablation (LA) ICP-MS. X-ray diffraction (XRD) analyses were performed at Attard's Minerals, San Diego, CA. Analytical methods are described in detail in the Appendix C.

Sample Name (MAN-44-U-Th#-)	SZ	Taxon: Acropora or Porites	U (ppb)	(^{230}Th /^{232}Th)	Uncorrected Date (CE), Error (2σ, yr.)		Corrected Date (CE), Error (2σ, yr.)		Initial (^{234}U/^{238}U)		% Calcite	Color
9	2	A	2911	30.0	1144	±4.4	1167	±12	1.1433	±0.0016	100	light to medium gray
15	2	A	2545	3.15	731.6	±5.1	1064	±170	1.1465	±0.0017	100	gray
25	2	P	2629	82.34	1003.2	±4.0	1011.6	±5.8	1.1442	±0.0034	0	white to off white
8	3	A	3116	3.63	934.9	±6.8	1179	±125	1.1432	±0.0022	>> 5	brownish gray
17	3	A	3088	12.64	1340.8	±4.2	1382	±21	1.1443	±0.0017	100	gray
10	5	A	2821	33.67	1421.7	±4.7	1434.7	±8.1	1.1415	±0.0022	> 95	light gray
11A	5	A	3299	67.58	1453.3	±4.8	1458.3	±5.4	1.1305	±0.0022	0	off white
11B	5	A	3182	57.55	1452.7	±6.7	1458.8	±7.4	1.1328	±0.0019	0	off white
22	5	P	2519	68.16	1431.8	±2.7	1437.3	±3.8	1.1416	±0.0030	0	white to off white
3	6	A	3427	35.97	1440.1	±3.0	1452.1	±6.8	1.1372	±0.0018	0	off white
4	6	A	2534	4.81	1092.5	±4.0	1249	±80	1.1438	±0.0022	100	brownish gray
23	6	P	2194	2.82	930.5	±4.8	1243	±160	1.1467	±0.0014	100	medium gray
1A	7	A	3328	45.31	1451.2	±7.7	1459.2	±8.8	1.1391	±0.0020	>> 5	off white
1B	7	A	3432	52.67	1456.1	±6.2	1462.8	±7.1	1.1394	±0.0021	>> 5	off white
12	7	A	2971	109.81	1454.3	±3.4	1457.4	±3.7	1.1419	±0.0027	100	light to medium gray
13	7	A	3110	9.22	1302.8	±7.0	1363	±32	1.1443	±0.0013	100	light gray
2	8	A	3208	6.60	1341.2	±4.2	1424	±43	1.1439	±0.0026	100	light gray
7	8	A	3579	132.80	1502.5	±3.4	1504.7	±3.6	1.1274	±0.0022	0	white
14	8	A	3263	45.35	1457.9	±4.1	1465.9	±5.8	1.1398	±0.0020	100	medium gray
16A	8	A	2977	218.94	1520.8	±7.8	1521.6	±7.8	1.1448	±0.0023	0	off white
16B	8	A	3018	301.51	1537.5	±6.7	1538.0	±6.7	1.1424	±0.0022	0	off white
18	8	P	2715	71.83	1461.3	±2.7	1466.2	±3.7	1.1451	±0.0027	0	white
5A	15	A	3405	39.66	1444.2	±6.7	1453.9	±8.4	1.1402	±0.0017	0	light yellowish gray
5B	15	A	3532	35.65	1450.0	±5.4	1461.2	±7.9	1.1411	±0.0021	0	light yellowish gray
6	15	A	2736	7.01	1321.8	±4.6	1402	±41	1.1392	±0.0018	>> 5	light gray

Table 3.3: Summary of ^{230}Th dates of Holocene coral abraders from site MAN-44 listed by stratigraphic zone. All isotope ratios are activity ratios. Uncertainties are 2 standard deviations (2σ). Uncorrected dates are calculated from measured ratios. Corrected dates were corrected for U and Th from detritus using (^{232}Th/^{238}U) = 1.21 ± 0.50, (^{230}Th/^{238}U) = 1.0 ± 0.1, and (^{234}U/^{238}U) = 1.0 ± 0.1. Decay constants are from Jaffey et al. (1971) for ^{238}U and Cheng et al. (2013) for ^{230}Th and ^{234}U. Initial (^{234}U/^{238}U) ratios are calculated from the measured ratio and the corrected date. Colors were assigned by the authors during sample preparation without use of a color palette.

Sample Name (MAN-44-U-Th#-)	SZ	Taxon: *Acropora* or *Porites*	U (ppb)	(^{230}Th /^{232}Th)	Uncorrected Age (ka), Error (2σ, ka)		Corrected Age (ka), Error (2σ, ka)		Initial (^{234}U/^{238}U)		% Calcite	Color
19	10	P	2291	420	174.7	±0.8	174.5	±0.8	1.2012	±0.0023	1	yellowish white
20	3	P	2616	13960	146.1	±1.4	146.1	±1.4	1.1701	±0.0038	0	white to off white
21	15	P	2765	28452	129.0	±1.1	129.0	±1.1	1.1520	±0.0040	0	white to off white
24	3	P	2552	5810	133.8	±0.7	133.8	±0.7	1.1582	±0.0025	< 1	yellowish white

Table 3.4: ^{230}Th ages for Pleistocene coral abraders from MAN-44, Mangaia.

3: Results

3.1: Overview

Twenty-one corals yielded Holocene dates between 1012 ± 5.8 and 1538 ± 6.7 CE (Table 3). Four corals yielded Pleistocene apparent ages of ~130 ka or greater (Table 4). Six corals were also analyzed by LA-ICP-MS to characterize the spatial distribution of U and common Th, three of which are highlighted here. Comprehensive solution, laser ablation, and XRD results are found in Appendix C and Supplementary File 3.1.

Replicate analyses of sub-samples of four Holocene *Acropora* abraders were performed to examine analytical reproducibility and sample homogeneity (Figure 3.2). Three of four corals yielded ^{230}Th dates in good agreement; their mean dates are shown on Figure 3.3. Dates of sample 16 differed slightly outside of their analytical errors. We take the weighted mean of the two dates of this coral and expand the error due to excess scatter by multiplying the standard deviation by the square root of the mean square of weighted deviates (MSWD), resulting in a ^{230}Th date of 1531± 15.9 CE, shown on Figure 3.3.

3.2: Pleistocene corals

Four of eight *Porites* corals dated are much older than the others, with apparent ^{230}Th ages ranging from ~174 to ~129 ka and with measured (^{234}U/^{238}U) ratios below the seawater value (range 1.106 to 1.123; see Table 4 and Appendix C. These likely come from the *makatea* forming the perimeter of Mangaia and Tangatatau Rockshelter. One coral appears to preserve primary U composition, with $(^{234}U/^{238}U)_0 = (^{234}U/^{238}U)_{SW}$ and an apparent age of 129 ka. These corals may be derived from a reef formed during the last interglacial sea level high stand, but only one has an intact U isotopic system from which to determine a reliable apparent age. The other corals have likely lost U, as indicated by elevated $(^{234}U/^{238}U)_0$ ratios, making their apparent ages unreliable. Nevertheless, these coral abraders are clearly much older than the site's occupation interval, making them readily recognizable as outliers. Archaeologically, this is the first demonstration that Polynesians at times utilized ancient corals from *makatea* formations for use as abraders.

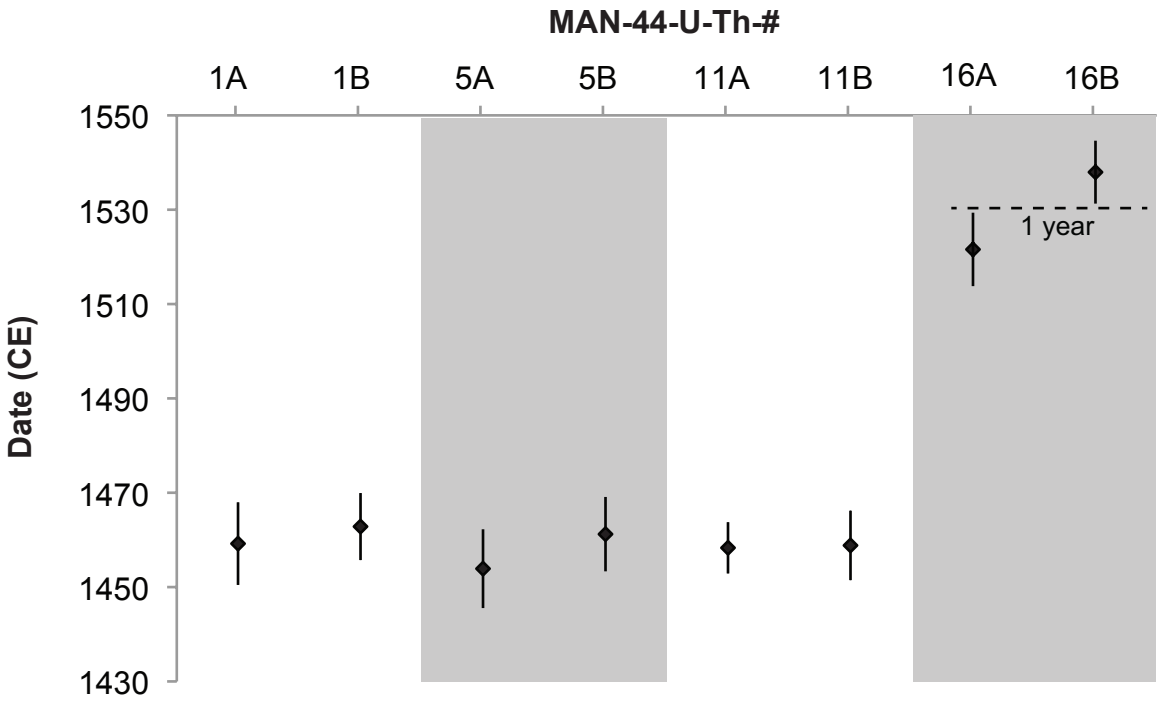

Figure 3.2: Replicate analyses of four *Acropora* coral abraders from MAN-44. The difference between replicates of sample 16 is ~1 year at 2σ. The reported date of this sample is calculated from the mean age of the two replicates, accounting for excess scatter in the final uncertainty.

3.3: Identifying reliable coral ^{230}Th dates

^{230}Th dating requires two main assumptions, namely that: 1) the sample has remained closed to U and Th exchange since formation, and 2) ^{230}Th in the sample has formed by *in situ* decay of ^{234}U, or if not, that ^{230}Th from other sources can be accurately subtracted. While shallow water corals can be highly suitable for ^{230}Th dating (e.g., Edwards et al., 2003), they can be subject to diagenesis or contamination by detritus, thereby violating one or both of the above assumptions and causing their ^{230}Th ages to be biased. The U concentration, (^{234}U/^{238}U) ratio, (^{230}Th/^{232}Th) ratio, and mineralogy of corals have been widely used to assess corals for ^{230}Th dating (e.g., Hibbert et al., 2016); however, most studies have focused on subaerially exposed corals rather than those from buried contexts, where corals are subject to prolonged contact with both vadose waters and terrigenous sediments, and reducing conditions may exist. We assess the geochemical and mineralogical properties of the dated corals and then assess the relationship of each property to physical and visual characteristics that may aid sample selection criteria. We also examine the spatial distribution of ^{238}U and ^{232}Th in six *Acropora* corals analyzed via laser ablation ICP-MS. We develop and apply selection criteria appropriate for buried corals from MAN-44, which may have implications for ^{230}Th dating of corals from other buried contexts. We then compare screened ^{230}Th coral dates to the ^{14}C chronology at MAN-44.

3.3.1: Geochemical and Mineralogical properties of corals

3.3.1.1: (^{230}Th/^{232}Th) ratios, indicators of detrital and diagenetic Th

The Th isotopic composition of corals can be used to evaluate the degree to which extraneous ^{230}Th (i.e., ^{230}Th not produced by *in situ* decay) is present, and at what levels it can be accurately subtracted using a model correction. Shallow water corals tend to have near-zero initial ^{230}Th because Th is highly insoluble in seawater and ^{230}Th produced in the water column by U decay is effectively removed by adsorption onto settling particles. Nonetheless, some modern corals have been found to contain up to ~1000 ppb of ^{232}Th (Cobb et al., 2003; Shen et al., 2008), possibly due to growth in a cloudy (detritus-rich) water column or inclusion during diagenesis, so it is important to evaluate possible contributions of extraneous ^{230}Th associated with detritus.

The majority of MAN-44 samples have (^{230}Th/^{232}Th) > 10 (note: all isotope ratios herein are expressed as activity ratios) and so the model detrital correction that we apply has little impact on the detritus-corrected age (compare detritus corrected ages with uncorrected ages in Table 3; cf., Ludwig and Paces, 2002). Such corals yield clustered ^{230}Th ages within a single SZ (where available), they generally agree with the corresponding ^{14}C model ages, and they preserve stratigraphic order (see Figure 3.3). This chronostratigraphic agreement supports our Th model correction for samples with (^{230}Th/^{232}Th) > 10. Seven samples have (^{230}Th/^{232}Th) < 10 and yield systematically older apparent ages than those of corals in the same layer with (^{230}Th/^{232}Th) >10, showing that the model correction does not quantitatively remove extraneous ^{230}Th in highly contaminated corals. Ages of corals with low (^{230}Th/^{232}Th) are inherently quite imprecise (median uncertainty = 136 years) due to error propagation associated with the large detritus correction, so no attempt was made to further refine the model detritus correction applied to them. Hence, corals with (^{230}Th/^{232}Th) < 10 fail this screening test and are not considered to yield reliable dates.

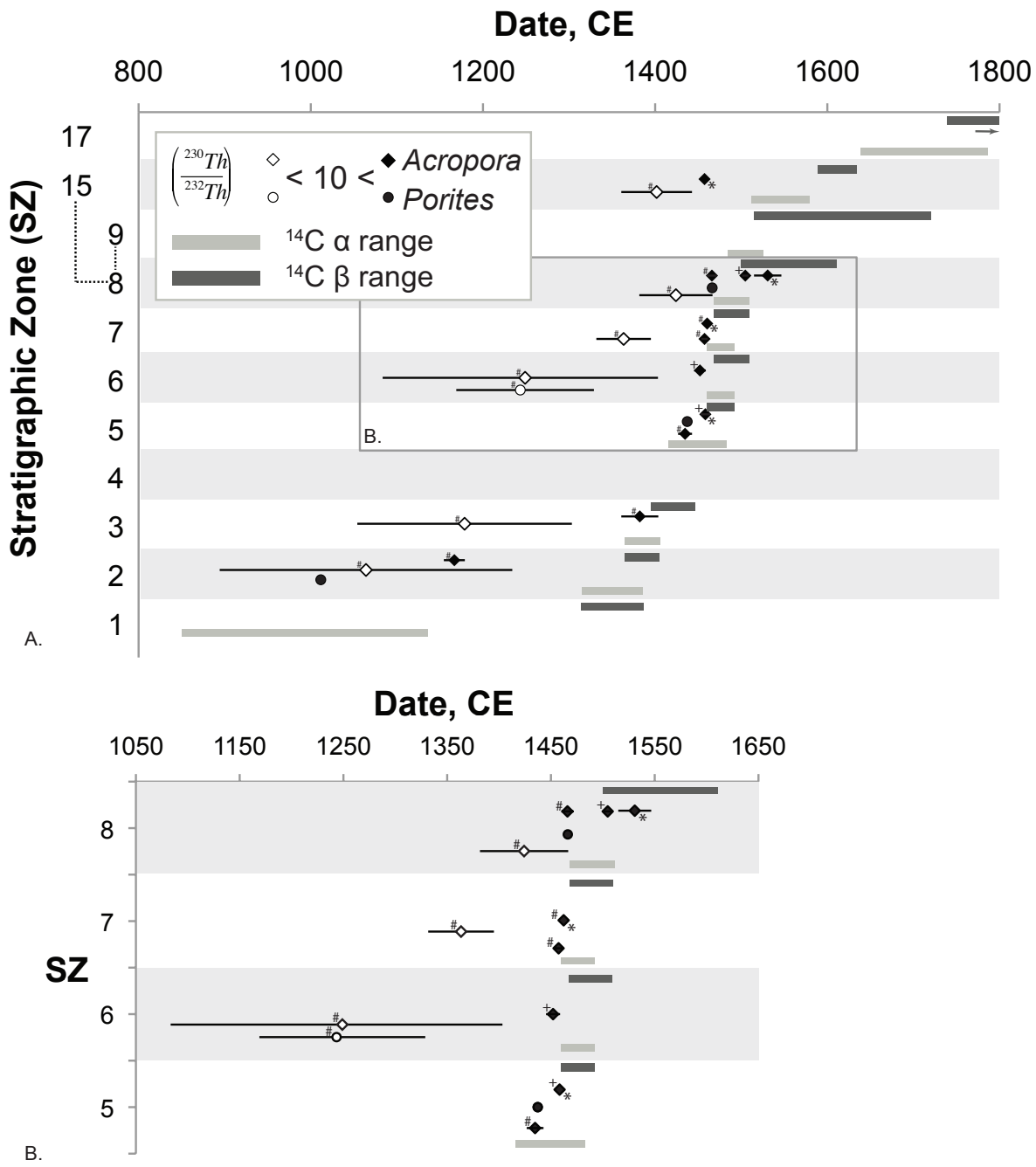

Figure 3.3: Summary of ^{14}C age model and ^{230}Th dates from MAN-44. A. Plot of Alpha (α) and Beta (β) 95% HPD Intervals from Bayesian analysis of AMS ^{14}C dates on short-lived plant materials (Kirch, 2017b) compared with ^{230}Th dates of coral abraders. ^{230}Th dates for corals with ($^{230}Th/^{232}Th$) >10 are shown with filled symbols. Asterisks (*) to the lower right of data points indicate dates that are mean values of replicate analyses. (+) and (#) symbols to the upper left of data points indicate, respectively, corals with $(^{234}U/^{238}U)_0 < (^{234}U/^{238}U)_{SW}$ and > 5% calcite. B. Enlarged view of SZ 5 through SZ 8. Note: SZ-9 and 15 locally overlie SZ-8; errors are not visible if 2σ uncertainties are smaller than the symbols. ^{230}Th dates in SZ-2 and SZ-15 that are discordant with their respective ^{14}C HPD intervals are discussed in text.

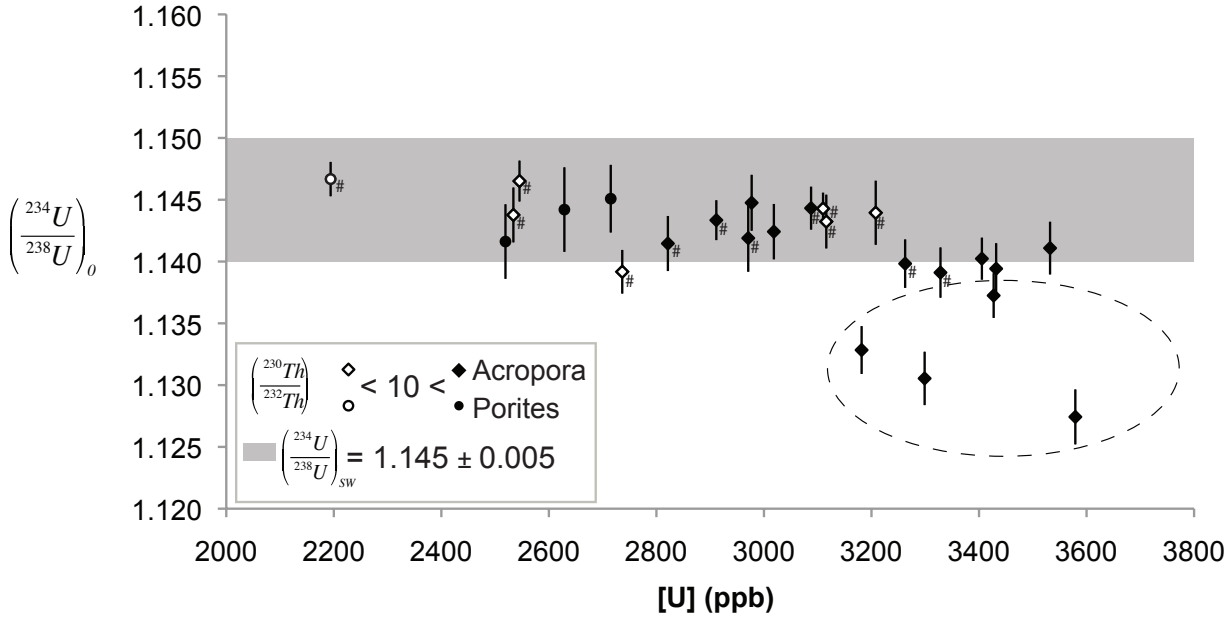

Figure 3.4: Back-calculated $(^{234}U/^{238}U)_0$ for Holocene coral abraders from MAN-44, Mangaia. Seawater ratio (shaded band) is after (Chutcharavan et al., 2018). (#) symbol indicates samples with >5 % calcite. Dashed circle surrounds corals with $(^{234}U/^{238}U)_0$ below seawater values.

3.3.1.2: [U] and initial ($^{234}U/^{238}U$)

U concentrations and $^{234}U/^{238}U$ ratios provide other reliability criteria widely applied to shallow water corals. We expect *Porites* to have bulk U concentrations of ~1.3–4.2 ppm and *Acropora* to have ~1.3–4ppm U (e.g., Cross and Cross, 1983; Bar-Matthews et al., 1993; Shen and Dunbar, 1995; Hibbert et al., 2016). All *Porites* from MAN-44 have c. 2.1-2.7 ppm U and *Acropora* have c. 2.5–3.6 ppm, within range of expectations.

Corals grow in U isotopic equilibrium with seawater and their initial ($^{234}U/^{238}U$) ratio, hereafter $(^{234}U/^{238}U)_0$, may be calculated from the ^{230}Th age and present day (measured) ($^{234}U/^{238}U$) ratio of a dated coral. Globally, open ocean seawater ($^{234}U/^{238}U$) ratios are relatively uniform at a given time, and although variable on the glacial-interglacial timescale, they may be considered constant on the timescale of the Holocene corals dated herein. Unaltered corals that grew in open ocean waters therefore have $(^{234}U/^{238}U)_0$ ratios equal to that of contemporaneous seawater (hereafter $(^{234}U/^{238}U)_{SW}$; Edwards et al., 2003). A mean value of modern and near-modern $(^{234}U/^{238}U)_{SW} = 1.145 \pm 0.0015$ was obtained in a recent comprehensive review by Chutcharavan et al. (2018); for screening MAN-44 coral abraders, we adopt a range of $(^{234}U/^{238}U) = 1.145 \pm 0.005$, which encompasses 95% of modern corals screened for diagenesis. Eighteen of 21 Holocene samples from MAN-44 have $(^{234}U/^{238}U)_0$ within this range of $(^{234}U/^{238}U)_{SW}$ (Figure 3.4), and three *Acropora* have $(^{234}U/^{238}U)_0 < (^{234}U/^{238}U)_{SW}$, one of which was measured in duplicate analyses. While corals with $(^{234}U/^{238}U)_0 < (^{234}U/^{238}U)_{SW}$ would have failed a screening test in a subaerial context, we note that the corals with depressed $(^{234}U/^{238}U)_0$ produce ages concordant with stratigraphically associated corals with $(^{234}U/^{238}U)_0 = (^{234}U/^{238}U)_{SW}$ (see Figure 3.3B). Most samples with $(^{230}Th/^{232}Th) < 10$ have $(^{234}U/^{238}U)_0 = (^{234}U/^{238}U)_{SW}$, so no correlation is apparent between low $(^{230}Th/^{232}Th)$ and low $(^{234}U/^{238}U)_0$. Furthermore, the low $(^{234}U/^{238}U)_0$ coral abraders retain their primary aragonite mineralogy (Table 3), rendering a diagenetic origin for the low $(^{234}U/^{238}U)_0$ ratios unlikely. Sample 11, a coral with a low $(^{234}U/^{238}U)$ ratio from SZ-5, yielded concordant dates in replicate analyses (Table 3), and the resulting mean date compares favorably with two other ^{230}Th dates from the same SZ (Figure 3.3B). Two further sub-samples of sample 11, which were analyzed at sub per mil precision using a distinct measurement protocol to test for possible bias in our $^{234}U/^{238}U$ measurements yielded a U isotopic composition identical to the original measurements (see Appendix C). Thus, neither sample heterogeneity nor measurement error explain its low $(^{234}U/^{238}U)_0$.

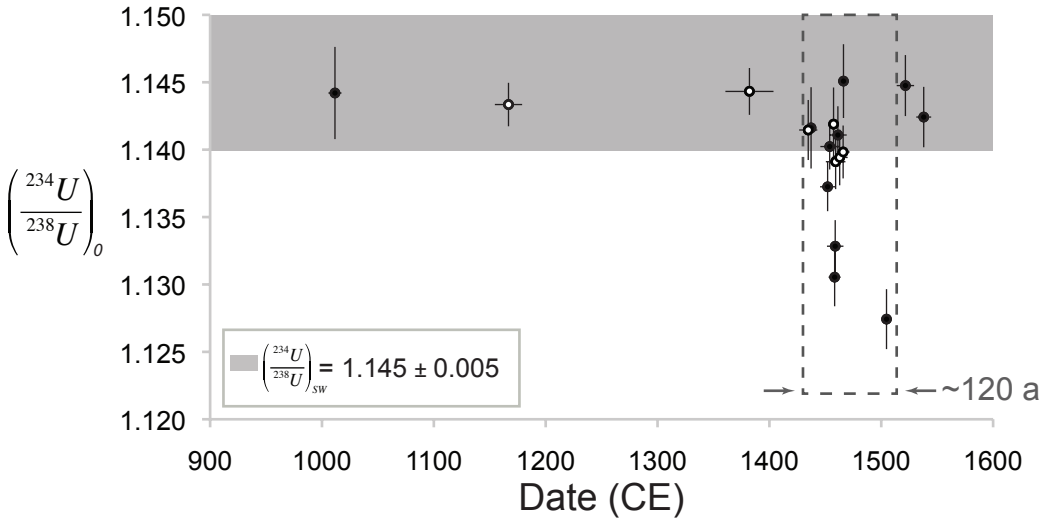

Figure 3.5: Back-calculated $(^{234}U/^{238}U)_0$ for Holocene coral abraders at MAN-44, Mangaia, compared to U-Th ages. White symbols denote samples that have > 5% calcite. The most variability in $(^{234}U/^{238}U)_0$ occurs over ~120 years.

The low $(^{234}U/^{238}U)_0$ ratios may be primary if the waters in which some of the corals grew had low $(^{234}U/^{238}U)$ ratios relative to open ocean seawater. This could occur from mixing of local terrestrial runoff, which may carry a signal of $(^{234}U/^{238}U) < (^{234}U/^{238}U)_{SW}$ if influenced by *makatea* corals with low U (see section 3.4 and Appendix C), or if groundwater interacting in the soil environment has $(^{234}U/^{238}U) < (^{234}U/^{238}U)_{SW}$, which can occur if meteoric waters are not accessing the saprolite depth (e.g., Banner et al., 1991; Suhr et al., 2018). Kirch (2017c) describes the terrain at Mangaia as "deeply laterized" and the treacherous nature of getting up and down the cliff-side slopes of the *makatea* terraces: discrete channels drain runoff where it is also easiest to climb the *makatea* to and from the shore. If ancient occupants of MAN-44 were taking corals from the shore near these *makatea* entry points to MAN-44, it is more likely that freshwater runoff, carrying a low $(^{234}U/^{238}U)$ relative to seawater, would interact at these mixing points in the sea, and corals growing there may reflect a depressed $(^{234}U/^{238}U)$ ratio expected of brackish seawater. Figure 3.5 shows that samples with low $(^{234}U/^{238}U)_0$ derive from only ~120 years of elapsed time in coral growth. Coral growth in this brief period may have coincided with a period of increased freshwater input from land, which could have been driven by changes in climate or increased human activity. Because corals with low $(^{234}U/^{238}U)_0$ agree in age with stratigraphically-related corals with $(^{234}U/^{238}U)_0 = (^{234}U/^{238}U)_{SW}$, and they are aragonitic, we conclude that they were likely to have grown in brackish water and preserve primary geochemical signatures. We consider these corals with low $(^{234}U/^{238}U)_0$ to have acceptable ^{230}Th dates at MAN-44.

3.3.1.3: Calcite content

X-ray diffraction (XRD) is commonly used to detect secondary calcite in corals that grow primary aragonite skeletons such as the *Acropora* and *Porites* corals of this study. The presence of calcite is widely considered to render corals unsuitable for ^{230}Th dating because coral U-Th systems may fail to remain closed as primary aragonite is replaced, because secondary calcite cements can bias ages, or both (e.g., Hibbert et al., 2016; Chutcharavan et al., 2018). Although recent reviews of coral ^{230}Th ages by Hibbert et al. (2016) and Chutcharavan et al. (2018) adopted >2% calcite as a rejection criterion, we found that 1% calcite was readily detectable in standards prepared using known weights of calcite and aragonite (see Appendix C).

XRF results show that more than half of Holocene corals from MAN-44 have > 5% calcite (Tables 3 and 4). In order to examine how isotopic screening criteria described above correlate with calcite alteration, Figure 3.6 shows the comparison of U and Th isotopic ratios of corals with and without detectable calcite. There is a clear association between low $(^{230}Th/^{232}Th)$ ratios and the presence of calcite, suggesting that the high common Th in such samples results from diagenetic recrystallization. Since Th is insoluble, it is likely that extraneous Th was translocated into corals with low $(^{230}Th/^{232}Th)$ ratios on fine particles with adsorbed Th during recrystallization. However, samples with high $(^{230}Th/^{232}Th)$ ratios, and hence low common Th, range from 100% aragonite (that is, they have no detectable calcite) to 100% calcite, suggesting that some corals were fully replaced by calcite without introducing significant common Th. If radiogenic ^{230}Th formed *in situ* remains immobile due to the low solubility of Th, it is possible that some recrystallized corals may retain their Th isotopic compositions. Similarly, samples

with $(^{234}U/^{238}U)_0 = (^{234}U/^{238}U)_{SW}$ range from 100% aragonite to 100% calcite. This suggests that U may also have been immobile during recrystallization. Surprisingly, corals that retain primary U isotopic compositions and high $(^{230}Th/^{232}Th)$ ratios, even if fully replaced by calcite, can yield ^{230}Th dates in close agreement with co-occurring aragonitic corals with high $(^{230}Th/^{232}Th)$ ratios and associated ^{14}C model ages. For example, four corals that have >> 5% calcite, but high $(^{230}Th/^{232}Th)$ ratios and $(^{234}U/^{238}U)_0 = (^{234}U/^{238}U)_{SW}$, yield ages consistent with ^{230}Th dates of unaltered corals and associated ^{14}C model ages (see samples marked with (#) symbols in Figure 3.3 in SZ-5, SZ-7, and SZ-8.)

We suggest that if recrystallization occurred in a reducing environment, U may have become reduced to the immobile, insoluble U(IV) state, allowing primary U to remain fixed in the coral. Reducing conditions in the organic-rich strata of the MAN-44 sequence seem likely and we suggest that this may be a critical difference between behavior of the U-Th system in buried versus subaerially exposed corals.

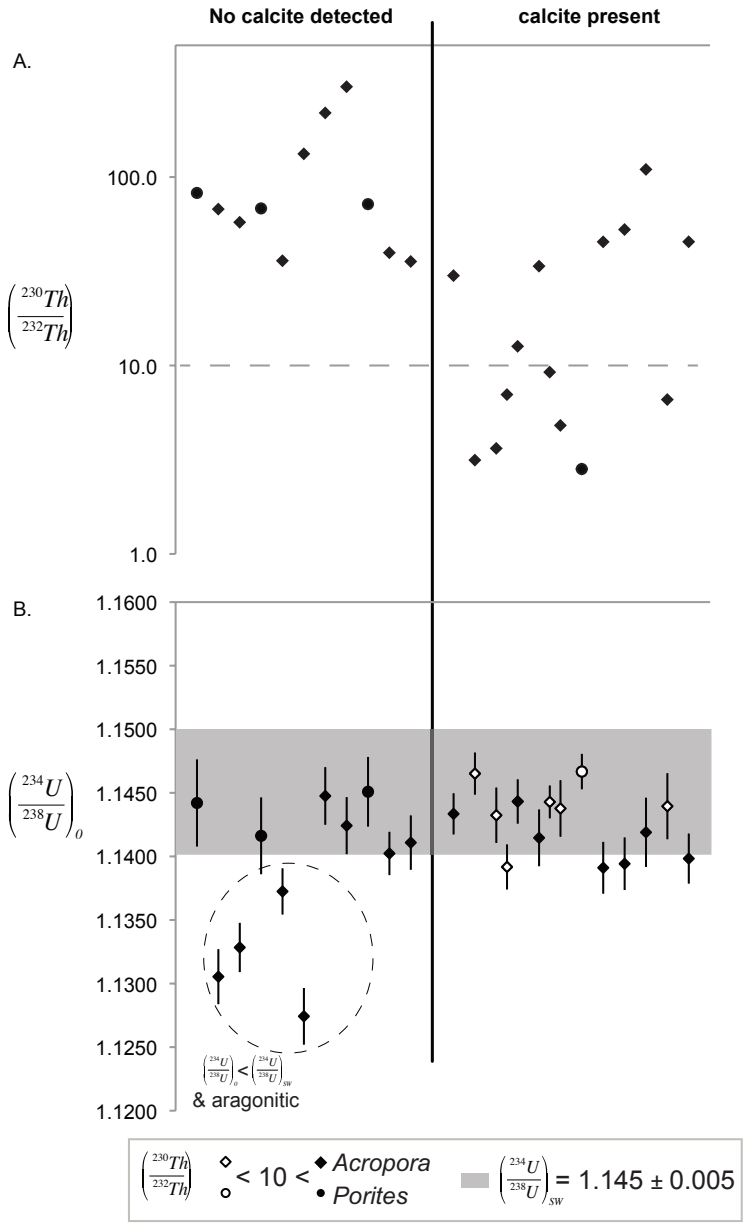

Figure 3.6: Effects of alteration to calcite on Th and U isotopic ratios of Holocene corals. A. In some corals, alteration to calcite is associated with high levels of common Th leading to low ($^{230}Th/^{232}Th$) values. Lower panel: Shaded band shows expected primary values of $(^{234}U/^{238}U)_{SW}$. No trend in $(^{234}U/^{238}U)_0$ ratios with alteration is apparent, suggesting that alteration to calcite does not alter U isotopic compositions. Samples with $(^{234}U/^{238}U)_0 < (^{234}U/^{238}U)_{SW}$ have no detectable calcite, consistent with low primary values.

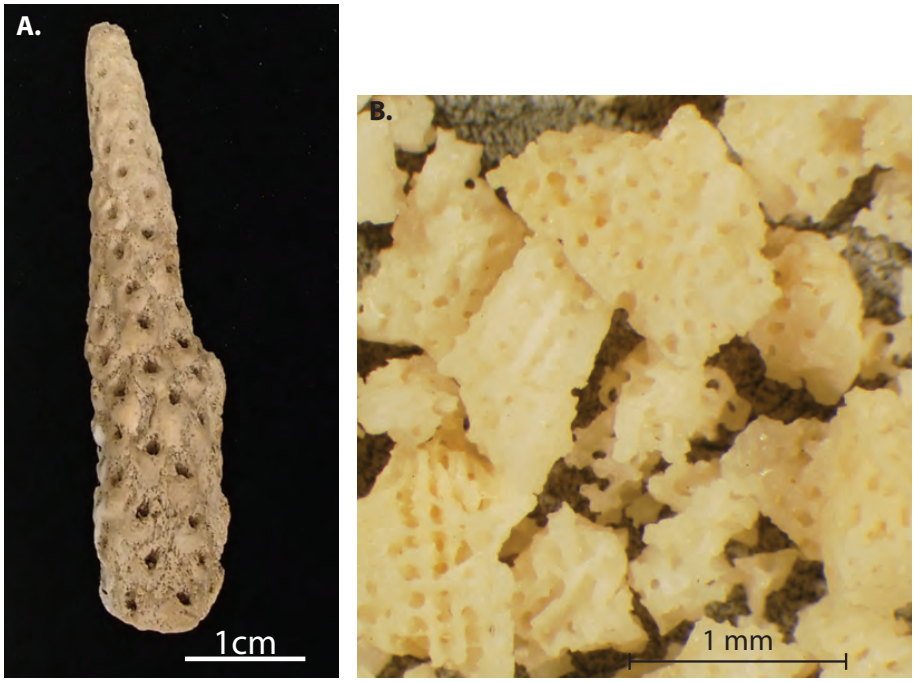

Figure 3.7: *Acropora* coral abrader MAN-44-U-Th#-7. A. Coral abrader before sample preparation; B. subsample after cleaning is porcellaneous and translucent, and it is 100% aragonite.

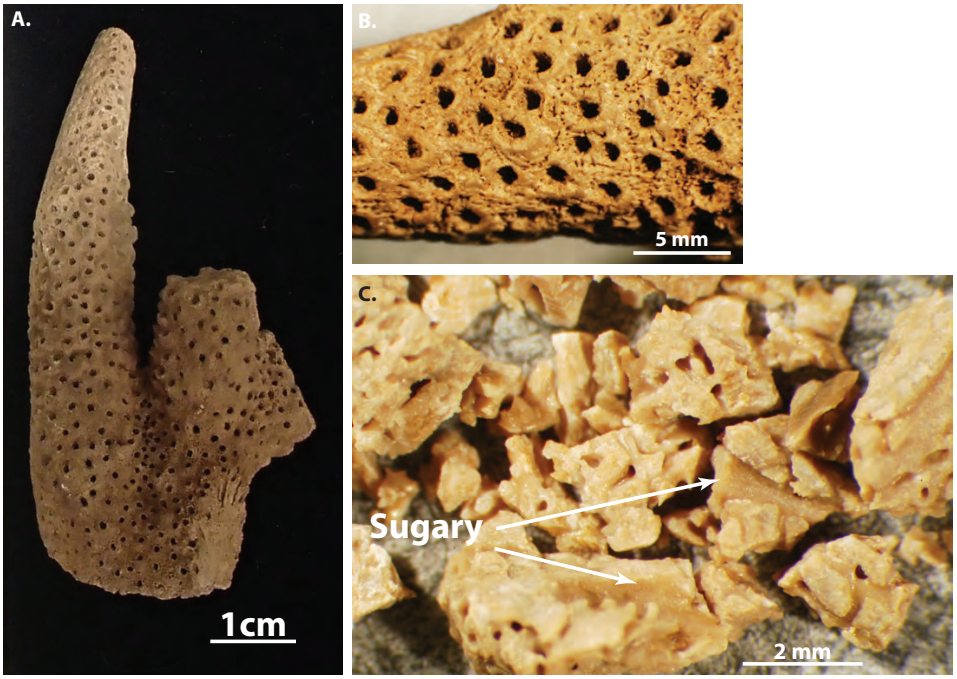

Figure 3.8: *Acropora* coral abrader MAN-44-U-Th#-6. A. Coral abrader before sample preparation; B. tip of surface, worn from abrasion by Polynesians, after sonicating in isopropranol. Coral skeletal structure is intact; despite primary macroscropic morphological preservation, this sample is 100% calcite. C. crushed, cleaned sample has sugary texture in septa channels, reflecting recrystallization to calcite.

3.3.1.4: Visual characteristics

Instead of using XRD or other analytical assessments of mineralogy to screen for recrystallization of buried corals, some studies have utilized macroscopic visual criteria, such as color and skeletal morphological preservation, to evaluate the primary preservation of archaeological coral materials in addition to agreement with co-occurring ^{14}C dates (e.g., Burley et al., 2012, 2015). Now that we have carefully screened the MAN-44 corals data using geochemical and mineralogical characteristics, we can assess the utility of visual criteria in comparison with the other screening tools. All samples with ($^{230}Th/^{232}Th$) < 10 were recrystallized and gray, as well as some samples with ($^{230}Th/^{232}Th$) > 10, but the latter group yielded ages in agreement with the other chronological constraints. Some fully aragonitic corals with precise, accurate ^{230}Th dates were light gray, and most aragonitic corals with reliable dates were white to off-white (Figures 3.7 and 3.8). In sum, light colored corals preserve primary aragonite and yield accurate ^{230}Th dates, but gray corals can also yield acceptable dates. Macroscopic skeletal morphological preservation has been previously used as a screening tool (Burley et al., 2012), but even fully recrystallized samples will retain their macroscopic morphology, as many fossils do during recrystallization. A more effective visual assessment was made with microscopic observations of coral abraders at MAN-44 (Appendix C): every sample that was characterized as having "sugary" texture in its septa channels was shown by XRD to have calcite present, while samples described as waxy, translucent, or porcellaneous were calcite free. Though indistinguishable to the naked eye, a low-power microscope is sufficient to identify these textures. In the MAN-44 coral data set, many (but not all) corals that were both gray and had microscopic sugary texture were found to be unsuitable dating materials, so we would not consider these characteristics diagnostic of the suitability of a coral for ^{230}Th dating. These visual characters thus provide a more conservative screening tool in the field than is necessary, possibly eliminating some suitable samples, but samples lacking sugary texture and darker gray-brown colors are more likely suitable for dating.

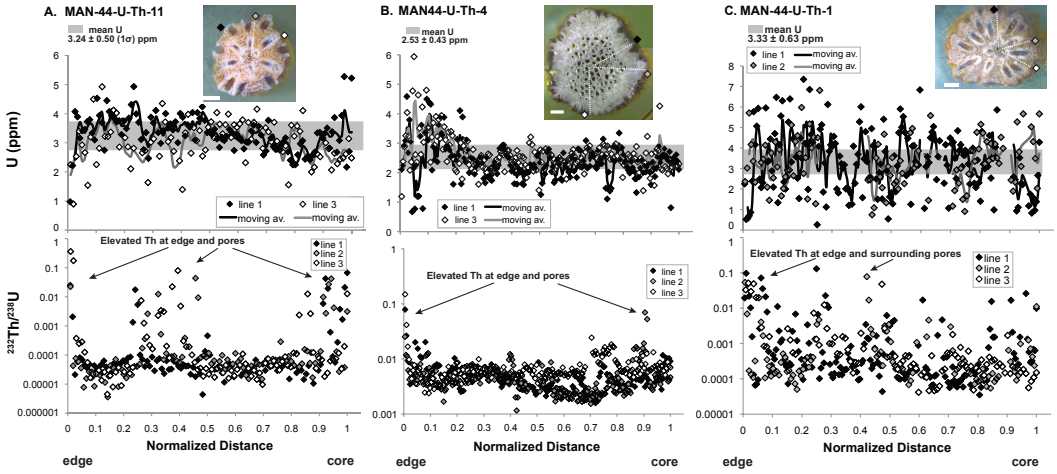

Figure 3.9: Spatial variation of [U] and $^{232}Th/^{238}U$ values in pristine and altered corals determined via laser ablation. Photos on each panel show locations of laser ablation traverses on cut and polished corals. White scale bars in photos are 1 cm long. U concentrations are plotted as moving averages (n=3). For clarity, only two lines of [U] data are shown in each plot and data points within pores were omitted. All samples show similar oscillating U concentrations consistent with seasonal variability, implying that U may have remained relatively immobile even in samples partially or fully recrystallized to calcite. A. Sample 11 is aragonitic, has high ($^{230}Th/^{232}Th$), and yields a reliable ^{230}Th date. B. Sample 4 is 100% calcite, has low ($^{230}Th/^{232}Th$), and yields an anomalously old apparent ^{230}Th date. Highly variable [U] near the outer surface suggests secondary alteration, but oscillatory variation at normalized distance >0.3 is apparent despite complete recrystallization. The $^{232}Th/^{238}U$ ratios of ~0.01-0.001 are 1-2 orders of magnitude higher than samples with high ($^{230}Th/^{232}Th$), showing that high ^{232}Th (and by inference, extraneous ^{230}Th) are pervasive in the sample. C. Sample 1 is partly recrystallized to calcite, has high ($^{230}Th/^{232}Th$), and yields a reliable ^{230}Th date. Oscillatory U is apparent despite partial recrystallization. Laser ablation analyses of more corals are available in Appendix C.

				[U] profile			$^{232}Th/^{238}U$		
Lab No. (MAN-44-U-Th#-)	($^{230}Th/^{232}Th$) > 10?	$(^{234}U/^{238}U)_0 = (^{234}U/^{238}U)_{SW}$?	% Calcite	mean ± 1σ (1σ %), ppm	original outer surface (not used in dating samples)	interior to surface (used in dating samples)	original outer surface (not used in dating samples)	interior to surface (used in dating samples)	near pores
1	yes	yes	>> 5	3.33 ± 0.63 (18.9%)	scattered; does not exceed variation seen throughout sample	2.7 - 4 ppm	sample maximum, ~0.1	~0.0001 - 0.01	sample maximum, ~0.1
4	no	yes	100	2.53 ± 0.43 (17.0%)	U minimum (~1 ppm) followed by a maximum (~5 ppm)	2-3ppm	sample maximum, ~0.1	~0.01	sample maximum, ~0.1
5	yes	yes	0	3.41 ± 0.63 (18.4%)	within variation of sample	3-4 ppm	within variation	~0.0001 - 0.001	sample maximum, ~0.1
7	yes	no	0	3.58 ± 0.62 (17.3%)	near-minimum values but not outside of sample variation	3-4 ppm	maxima ~0.01 - 0.1	highly variable, ~0.00001 - 0.001	sample maximum, ~0.1
8	no	yes	>> 5	3.12 ± 0.61 (19.6%)	within variation of sample	2.5 - 3.7 ppm	within variation	0.01 - 0.1	within variation
11	yes	no	0	3.24 ± 0.50 (15.4%)	minimum at outermost edge, ~1 ppm	2.7 - 3.7 ppm	maxima, ~0.05 - 0.5	0.00001 - 0.0001	higher values, 0.0001 - 0.1

Table 3.5: General characteristics of the spatial distribution of U and Th in samples analyzed by laser ablation ICP-MS. $^{232}Th/^{238}U$ values are isotope ratios.

3.4: Laser ablation ICP-MS

As mentioned above, some corals fully replaced by calcite (but with high ($^{230}Th/^{232}Th$) ratios) yield reliable ^{230}Th dates. Using laser ablation ICP-MS, we characterized the spatial distribution of U and ^{232}Th in aragonitic and calcitic corals with reliable dates and in calcitic corals with low ($^{230}Th/^{232}Th$) and spuriously old apparent ^{230}Th dates. Samples were cut orthogonally to their growth axes and traversed with the laser beam from the exterior surfaces to the branch cores. Average growth rates of *Acropora* are ~1–10 cm/year but can vary widely (up to 18 cm/year) depending on the environmental conditions in the reef (e.g., Dullo, 2005; Anderson et al., 2017). Traverses across the *Acropora* abraders should thus encompass a few seasonal growth bands. Table 5 provides a summary of ablated samples, their geochemical characteristics, and general observations about laser ablation results. In Figure 3.9, U concentrations and $^{232}Th/^{238}U$ ratios along radial profiles are shown for three corals: 1) a pristine aragonitic coral with a reliable ^{230}Th age, 2) a fully recrystallized coral with ($^{230}Th/^{232}Th$) < 10 and an anomalously old ^{230}Th age, and 3) a partly recrystallized coral with ($^{230}Th/^{232}Th$) > 10 and a reliable ^{230}Th age. In all three samples (Table 3.5), U concentrations show similar patterns, i.e., broad oscillations from surface to core about a mean U value with a standard deviation of ~ 15–20%. These likely reflect seasonal or longer-term changes in $[U]_{SW}$ and/or temperature-dependent coral-seawater fractionation, as first recognized in modern corals by Shen and Dunbar (1995), and later confirmed in many other studies (e.g., Min et al., 1995; Eggins et al., 2005; Potter et al., 2005; Hoffmann et al., 2009).

Since all samples have similar [U] (2–4ppm), the $^{232}Th/^{238}U$ ratio provides an indicator of common Th content. In samples with ($^{230}Th/^{232}Th$) < 10, $^{232}Th/^{238}U$ ratios are spatially rather uniform and elevated ~10–100 times those of corals with higher ($^{230}Th/^{232}Th$) ratios and reliable ^{230}Th dates. The high and relatively homogeneous $^{232}Th/^{238}U$ in calcitic corals with low ($^{230}Th/^{232}Th$) ratios suggests that the enrichment in common Th may have occurred during recrystallization to calcite, perhaps by translocation of fine grained Th-rich detritus. All corals show relative enrichment in ^{232}Th at their outer surfaces and near the edges of large pores where detritus acquired during burial could adhere to the coral. Such detritus was reduced during preparation of dating samples by abrading external surfaces and hand cleaning of crushed corals under low magnification.

Sample 1, with >> 5% calcite, appeared geochemically unaltered with respect to U and Th isotopic ratios, and returned a ^{230}Th date concordant with associated aragonitic corals. Its [U] and $^{232}Th/^{238}U$ profiles are similar to those of pristine sample 11, consistent with the interpretation that some recrystallized samples have retained primary U and Th distributions. Detailed figures and values of the [U] and $^{232}Th/^{238}U$ for all ablated samples are found in the Appendix C.

3.5: Suitability of *Porites* versus *Acropora* for ^{230}Th dating

Both *Porites* and *Acropora* coral abraders found at MAN-44 can yield precise ^{230}Th dates in agreement with ^{14}C model ages and each other. There are three cases where abraders of both types coexist in close stratigraphic association. In SZ-5 and SZ-8, the co-occurring *Porites* and *Acropora* abraders produce ^{230}Th dates in excellent agreement and they are concordant with the Bayesian model ages (Figure 3.3). In SZ-2, the ^{230}Th dates from one coral of each genus are

older than the Bayesian model ages but overlap with the model age ranges for SZ-1b below, where the first evidence of Polynesian presence (but not occupation) is found (Kirch, 2017d). However, in-built age from an interval between growth of the dated part of a coral and subsequent use of it as a coral abrader must also be considered. Probably because branch tips of *Acropora* are morphologically well suited to their use as abraders for making fish hooks, *Acropora* abraders typically preserve growth surfaces, while *Porites* abraders commonly do not. Accordingly, the in-built ages of *Acropora* abraders can often be directly ascertained and are commonly no more than a few years (within uncertainty of reliable ^{230}Th ages), while those of *Porites* abraders are subject to more uncertainty. At MAN-44, four dated *Porites* from MAN-44 have Pleistocene apparent ages; such highly anomalous ages are readily recognizable but, it is possible to find spuriously old corals on islands with *makatea*.

3.6: Modified screening criteria for ^{230}Th dating of corals from buried contexts

Integrating the geochemical, compositional, and visual criteria with the apparent ^{230}Th dates, and investigating relationships between those criteria and available chronostratigraphic constraints, we can define the most effective screening tools and criteria for assessing ^{230}Th coral dates at MAN-44. We conclude that, at MAN-44, calcite alteration is less diagnostic of unreliable ages than simply evaluating the $(^{234}U/^{238}U)_0$ and $(^{230}Th/^{232}Th)$ ratios. While many studies reject ^{230}Th dates from samples with >1–2% calcite (e.g., Hibbert et al., 2016; Chutcharavan et al., 2018), other studies in addition to this one (Bloom et al., 1974) have shown that samples with detectable calcite can yield ^{230}Th ages in agreement with closely associated aragonitic corals, implying that the presence of calcite may not be a universally applicable screening tool.

Studies of the effects of diagenetic processes on fossil corals suggest that $(^{234}U/^{238}U)$ ratios do not respond to all diagenetic processes, and diverse environmental conditions may impact the response to different diagenetic processes (e.g., Gallup et al., 1994; Thompson et al., 2003; Edwards et al., 2003). For example, $(^{234}U/^{238}U)$ ratios of altered corals in subaerial contexts may be modified by adsorption from vadose water of ^{234}U or ^{234}Th (the short-lived, immediate parent of ^{234}U; Gallup et al., 1994; Thompson et al., 2003). Loss of ^{234}U by recoil or leaching from sites damaged during ^{238}U decay may lead to sub-seawater $(^{234}U/^{238}U)$ ratios (Stirling and Andersen, 2009), but this would have a negligible effect on the ^{234}U budget of Holocene MAN-44 corals, since only ~0.2% of ^{234}U in ~1 ka corals would have formed by *in situ* decay of ^{238}U. Primary $(^{234}U/^{238}U)$ ratios lower than open ocean values in corals could occur if they are interacting with meteoric waters with below-secular equilibrium $(^{234}U/^{238}U)$ ratios, such as in tropical soils where mean annual precipitation is high (Short et al., 1988; Yanase et al., 1995), or if influenced by terrestrial runoff influenced by the Pleistocene *makatea* coralline limestone.

In their review of globally distributed Pleistocene corals, Hibbert et al. (2016) utilize similar geochemical and mineralogical screening criteria to those we examine above, concluding that site-specific factors, including the age of the coral itself, may impact the effects of calcite presence on the apparent ^{230}Th age of the coral. At MAN-44, it appears that calcite alteration does not always impact the primary ^{230}Th age. While we do not know the redox conditions that a given coral has encountered, redox conditions of the soil depositional environment could affect the redox state of U in coral abraders unlike what is seen in subaerial contexts. If this impacts U

mobility, recrystallization may not necessarily imply open system isotopic exchange during fluid-rock interaction. ^{230}Th dates of buried corals in reducing contexts would then preserve primary isotopic compositions, even if recrystallized. This may be a distinction from screening of subaerial fossil corals, since these are expected to remain in oxidative ambient conditions where U would remain in the mobile U(VI) state (e.g., Porcelli and Swarzenski, 2003). Finally, both *Porites* and *Acropora* coral abraders found at MAN-44 are geochemically suitable for ^{230}Th dating.

It is clear that no single criterion is sufficient to predict the reliability of a coral age when the *post-mortem* environmental history of fossil corals can vary greatly and variably impact the veracity of the ^{230}Th chronometer. At MAN-44, screening using a threshold (^{230}Th/^{232}Th) ratio, under which samples are considered "unreliable", appears to be sufficient without discarding otherwise acceptable results. We thus consider all samples with $(^{234}U/^{238}U)_0 = (^{234}U/^{238}U)_{SW}$ and (^{230}Th/^{232}Th) >10 to yield reliable dates. We also consider three corals with $(^{234}U/^{238}U)_0 < (^{234}U/^{238}U)_{SW}$ reliable and include them in the following discussion, as these corals are fully aragonitic and appear to have grown in seawater with low (^{234}U/^{238}U) ratios.

3.7: Stratigraphic relations of Holocene coral abrader ^{230}Th dates and ^{14}C model ages

^{230}Th ages of Holocene corals with (^{230}Th/^{232}Th) >10 at MAN-44 range from 1012 ± 5.8 and 1538 ± 6.7 CE (Figure 3.3, black symbols). Overall, these ^{230}Th coral ages preserve stratigraphic order; i.e., they become younger upward from one SZ layer to the next, as expected. Now that we have defined independent reliability criteria to identify reliable ^{230}Th coral dates, we can assess the results compared to the Bayesian model age ranges for each SZ.

There is good agreement between reliable ^{230}Th dates and ^{14}C model ages with two notable exceptions. Two ^{230}Th dates from SZ-2, 1011.6±5.8 and 1167±12 CE, are much older than the α interval (maximum age) of 1315–1386 CE for that layer determined from the Bayesian model of ^{14}C dates (Kirch, 2017b). These ^{230}Th dates do, however, fall in the range of ^{14}C dates from the underlying layer, SZ-1b, suggesting they may have been re-worked from here; as discussed below, even if these are reworked into SZ-2 from the underlying layer, their dates have archaeological significance. The other case in which the ^{230}Th dates disagree with the ^{14}C model ages is highest in the section, where the mean ^{230}Th date from SZ-15 is significantly older than its ^{14}C α range (Kirch, 2017b). While an older coral date in isolation may indicate use of a coral long after its death (that is, a result of inbuilt age), it is unlikely that this sample died many years before its use, as it has intact surficial coral rasp-like structures at its base, indicating it was likely living when it was plucked from the sea for use. This coral was likely displaced from settling or cultural site activity, perhaps from digging of a fire pit, a feature found in SZ-15.

Aside from these exceptions, there is very close agreement between the ^{230}Th coral dates and the Bayesian model ages. SZ-3 has one ^{230}Th date within the ^{14}C model ages. ^{230}Th dates from SZ-5, SZ-6, SZ-7, and SZ-8 agree well with their respective ^{14}C model ages. We can also assess the reproducibility of ^{230}Th dates where multiple samples were dated in the same layer. For example, reliable dates in SZ-5 partially overlap at 2σ, ranging in age from 1422–1453 CE with uncertainties between 2.7 and 6.7 years. Dates in SZ-7 agree and overlap. SZ-8 has four independent coral abrader ^{230}Th dates that tightly cluster (Figure 3.3). A remarkable chronostratigraphic sequence is revealed by the ^{230}Th dates within the most tightly bracketed SZ: the youngest ages of SZ-5 overlap precisely with the reliable date of SZ-6, and this date is concordant with the oldest dates of SZ-7, whose youngest ages agree with the oldest dates in SZ-

8. No stratigraphic reversals were resolved despite 1–2% relative precision in individual ages. Rather, the precision of each ^{230}Th coral age implies rapid deposition and short occupation intervals for SZ-6 and 7. The maximum dates of layers SZ-5, 6, 7, and 8 yield a tight sequence of 1434.7 ± 8.1, 1452.1 ± 6.8, 1457.4 ± 3.7, and 1465.9 ± 5.8 CE, respectively; the youngest ^{230}Th date in SZ-8 (1538 ± 6.7 CE), indicates ~50 cm of deposition and shelter occupancy over ~100 years (Kirch, 2017d).

In sum, the ^{230}Th dates of coral abraders are consistent with stratigraphic relations except in two cases, where reworking seems likely. They broadly agree with the ^{14}C chronology in the basal SZ and agree precisely from SZ-3 to SZ-8.

4: Discussion

With appropriate screening criteria for the MAN-44 corals, we can discuss implications of the ^{230}Th coral dates for other archaeological materials at MAN-44. Since ultimately, the preservation of closed system U-series geochemistry was the predominant screening tool used, the same dates presented in the comparison with ^{14}C model ages (in black symbols in Figure 3.3) are now discussed in the context of the archaeology.

4.1: Archaeological Implications of ^{230}Th chronology at MAN-44

Reliable ^{230}Th ages at MAN-44 range from c.1000–1540 CE and fall within range of the α and β ranges of each SZ, even where the ranges are quite large, as in SZ-2 (Figure 3.3). SZ-2 is defined as the earliest layer of true "occupation", and it is also the first layer with coral abraders (Kirch, 2017b). SZ-1 is a mixed layer consisting of pre-human contact bone debris (SZ-1A) and a rapid accumulation of bird bones SZ-1B) presumably due to human habitat disturbance and alteration. SZ-1B includes the first layer with rat bones *(Rattus exulans*) and charcoal from *Morinda citrifolia,* both species known to be introduced to Mangaia by Polynesians (Kirch, 2017b). SZ-1B thus represents the first layer with evidence of human presence on Mangaia, and 95% HPD intervals of the Bayesian model this initial human presence between 850-1136 CE. The oldest ^{230}Th coral age in SZ-2 dates to 1011.6 ± 5.8 CE, at least ~300 years older than the α range of SZ-2 (1315 – 1386 CE) but within the age range of SZ-1B. This sample is a *Porites,* requiring us to consider whether inbuilt age could affect the interpretation that this age truly dates Polynesian activity. However, the other reliable ^{230}Th coral age from SZ-2 is from an *Acropora,* and it also indicates an older age for SZ-2 (1167 ± 12 CE) than the Bayesian model age range, also pushing occupation back into the range of SZ-1B. Given that all other reliable ^{230}Th ages from *Porites* in the sequence closely overlap with the ages of *Acropora* samples, it is reasonable to consider the *Porites* date reliable. It is also plausible that these two abraders were deposited in the MAN-44 shelter during very short visits by Polynesians, prior to the establishment of permanent residence within the site. In this case, they may be reworked from SZ-1B, but in either case, they were indisputably brought to Tangatatau rockshelter by humans. While these dates may extend the timing of human occupation at MAN-44 if they are truly derivative of SZ-2, they do imply humans were present on Mangaia by 1012 CE, contradicting the conclusions of Wilmshurst et al. (2011) that Polynesians had not dispersed beyond the Society Islands in Eastern Polynesia until ~1190 CE. This, along with the recent ^{14}C data and

resultant model ages, suggests that the criteria adopted by Wilmshurst et al. (2011) may be overly restrictive.

Significant ecological changes followed the arrival of the earliest Polynesians: the first evidence of a larger-fruited coconut (*Cocos nucifera)* is also found in SZ-2 (Kirch et al., 2017b), indicating earlier introduction of agricultural plants. Sugarcane (*Saccharum officinarum*) and *Cordyline fruticosa* are other Polynesian-introduced plants, both found in layer SZ-3 (Kirch et al., 2017b); the ^{230}Th coral date (1382 ± 21 CE) agrees well with the α range of this layer. ^{230}Th coral dates also refine the arrival of the sweet potato (*Ipomoea batatas*) at MAN-44, a plant indigenous to South America and indicative of return voyaging to Mangaia (Hather and Kirch, 1991). Carbonized *I. batatas* remains were AMS ^{14}C-dated from SZ-8 to 1448-1616 CE (95% confidence; Kirch et al., 2017b). The stratigraphically deepest evidence of *I. batatas* is found in SZ-4A, a layer that cuts into SZ-3 and is overlain by SZ-5 and SZ-6; thus, SZ-3 provides a maximum age for SZ-4A, and SZ-6 would conservatively represent a minimum age. SZ-3 yielded one reliable ^{230}Th date, 1382 ± 21 CE, agreeing with the SZ-3 α interval (1365–1405 CE). Coral abrader ^{230}Th dates in SZ-5 and SZ-6 agree with each other and are within range of the α and β intervals, albeit more tightly, ranging from 1434.7 ± 8.1 CE to 1458.8 ± 7.4 CE. While disputes remain about the spread of the sweet potato into Polynesia being human or naturally driven (Montenegro et al., 2008; Muñoz-Rodríguez et al., 2018; Roullier et al., 2013), the absence of *I. batatas* in older layers implies that if sweet potatoes were native to Mangaia prior to Polynesian arrival, the Polynesians were not utilizing it until late in the occupation of MAN-44, which we find unlikely. Incorporating uncertainties on the ^{230}Th dates, we constrain the timing of introduction of the sweet potato to Mangaia, and potentially the return voyaging of Polynesians from South America, between 1361–1466 CE.

To constrain the age of the top of the MAN-44 sequence, since the ^{230}Th-dated coral in SZ-15 likely was reworked from a deeper layer, we rely on the youngest ^{230}Th coral dates in SZ-8 prior to the recovery of historical period artifacts found in SZ-17. SZ-16 is mainly comprised of firing features and may correspond to pre-contact occupation, but no corals were available in this layer. If SZ-8 is the best representation of a minimum occupation age for MAN-44 prior to European contact, the oldest ^{230}Th date (1538.0 ± 6.7 CE) would suggest a more restricted pre-contact occupation interval that does not overlap with the α range of SZ-17 (1641–1792 CE). Based on the ^{230}Th coral dates, it is unclear whether there was a hiatus in occupation between pre-contact layers and Historic period use of MAN-44, but the ^{14}C model ages indicate continuous occupation through SZ-17 is possible.

From SZ-3 to SZ-15, ^{230}Th ages indicate a compressed chronology spanning ~140–180 years. The ^{14}C chronology which suggests a potentially much wider range of elapsed time from these SZ, for up to many hundreds of years (Kirch, 2017b). Including the earlier occupation of SZ-2, however, the occupation interval from ^{230}Th ages is longer than what the ^{14}C model ages predict, but earlier, suggesting occupation from ~1000–1540 CE. Where there are discrepancies between the ^{230}Th and ^{14}C chronologies, the ^{230}Th ages tend to pre-date the ^{14}C chronology, as in the bracketing layers with dated corals.

It is notable that the two cases where the ^{230}Th coral dates disagree most with the ^{14}C-based Bayesian model are at the top and the bottom of the sequence. This may be partly due to their positions nearly bracketing the sequence (i.e., there is only one layer below SZ-2, and only one dated layer above SZ-15), as these loci have fewer stratigraphic constraints to provide maximum and minimum age restrictions on the Bayesian age models for SZ-2 and SZ-15, respectively. In both SZ-2 and SZ-15, the ^{230}Th coral dates also indicate older dates than those of

the ^{14}C model ages. In the layers between SZ-2 and SZ-15, where we have multiple ^{230}Th coral dates in mutual agreement and supporting the ^{14}C model, the ^{230}Th coral dates never reach the youngest end of the β age range; rather, they tend to be couched within the α range, and only in SZ-8 do they reach as far as the mid-point of the β range. If the prior constraints on the Bayesian model require that layers moving up in the sequence must be equal to or younger than the layer below it, then if the input dates are imprecise, a Bayesian approach might superficially impose younger estimates for the likelihood probabilities resulting from the actual ^{14}C measurements used to produce the posterior probabilities (α and β age ranges). This could in theory lead to systematically younger results for likelihood probability ages deduced from each ^{14}C measurement, which could produce a "younging effect" on the stratigraphic sequence in order to satisfy the prior probabilities (i.e., the preservation of stratigraphic order).

5. Conclusions

At MAN-44, where suitable corals were available, ^{230}Th dating of coral abraders has refined the chronology obtained from AMS ^{14}C dating of short-lived, species-identified plant remains and resultant model ages. Preservation of stratigraphic principles (e.g., superposition, intra-layer ^{230}Th age agreement) demonstrate internal consistency of reliable ^{230}Th dates of coral abraders. We also find general agreement of ^{230}Th ages of coral abraders with the ^{14}C chronology at MAN-44 when simply using geochemical criteria typically applied for ^{230}Th geochronology (i.e., evaluation of detritus correction to Th; evidence of closed system U-series systematics). Some corals clearly derived from the older *makatea,* but they are readily distinguished from the younger corals. However, multiple coral abraders should be sampled from layers, where possible, to better constrain populations of ^{230}Th ages and to better detect outliers. The precision and accuracy of ^{230}Th dates of Holocene coral abraders from the first layer of *in situ* occupation, SZ-2, pushes human presence at Tangatatau rockshelter ~300 years older than the ^{14}C chronology implied, and corroborating the ^{14}C model dates of SZ-1b indicating human arrival to Mangaia by at least ~1000 CE. These dates further refine the timing and tempo of environmental modification on Mangaia as Polynesians introduced agricultural practices and non-native plant species. The introduction of the sweet potato revealed by ^{230}Th coral dates also refines the timing of the return voyaging of Polynesians to Eastern Polynesia from South America.

At MAN-44, samples with $(^{234}U/^{238}U)_0 = (^{234}U/^{238}U)_{SW}$ and $(^{230}Th/^{232}Th) >10$ show strong agreement with the ^{14}C model ages and other ^{230}Th dates from the same layer, even in cases where samples have partly or completely recrystallized to calcite. Discoloration is correlated with the presence of calcite as is the presence of microscopic sugary textures, but some samples with primary geochemical composition (that hence retain a primary ^{230}Th age) were also discolored. Hence, pre-screening in the field for sugary texture with a low-power microscope and color assessment may lead to discarding some reliable samples, but it is also likely to ensure that screened samples are indeed reliable for U-series analyses. Samples with $(^{230}Th/^{232}Th) <10$ were all recrystallized to calcite, but the ^{230}Th dates of these samples would have been discarded anyway due to the effects of the model correction on the apparent ^{230}Th age. Localized brief shifts in $(^{234}U/^{238}U)_{SW}$ likely explain the primary U composition of some coral abraders. Furthermore, the retention of primary U and Th isotopic compositions in fully recrystallized samples implies that the presence of calcite may not require exclusion of a ^{230}Th date. Burial conditions may influence mineralogical preservation, the retention of primary U and

Th isotopic compositions, and the model correction for detrital ^{230}Th in Th-rich samples. The authors acknowledge that without the ^{14}C model dates and other ^{230}Th dates demonstrating good agreement, the reliability of calcitized corals could not be robustly tested. Hence, it is not our intent to advise future workers to trust all coral dates regardless of degree of remineralization; rather, in the presence of formidable independent agreement with other ages, it is possible to find calcitized corals in chronological agreement with pristine corals and ^{14}C dates. Further work examining the mobility of U in aragonite under diverse redox conditions would augment our understanding of these data.

Preservation of suitable samples, and modes of failure of the ^{238}U-^{234}U-^{230}Th system in buried corals, may be distinct from subaerially exposed fossil corals. Quality criteria of samples and isotopic measurements inherent to ^{230}Th geochronology may vary from site to site, but with proper screening criteria, ^{230}Th dating of corals are capable of producing robust and meaningful independent chronologies or enhancing existing chronologies. Site-specific environmental conditions may be important considerations of ^{230}Th data sets, if results are scrutinized with stratigraphically-related intercomparable ^{230}Th coral ages or other chronometric techniques. Where suitable samples are available, ^{230}Th dating of coral abraders has the potential to refine the chronology of settlement throughout Polynesian and other Pacific archipelagoes by determining the timing of initial settlements to semi-decadal precision and expanding the number of sites included in the greater understanding of the expansion of humans into and across the Oceanic world.

Re-printed with permission from: Niespolo, E.M., Sharp, W.D., & Kirch, P.V., 2019, ^{230}Th dating of coral abraders from stratified deposits at Tangatatau Rockshelter, Mangaia, Cook Islands: Implications for building precise chronologies in Polynesia. Journal of Archaeological Science v. 101, 21-33, doi: 10.1016/j.jas.2018.11.001

Conclusion

The techniques used in this thesis demonstrate the power of integrative research in isotope geochemistry to answer questions about geological processes and human evolution. Without precise and accurate geochronometers, correlations cannot be made either between disparate localities hosting fossils and archaeology or between climate and paleoanthropological archives. Each chapter has refined or presented novel approaches on the use of different isotopic methods. The updated calibration of Alder Creek sanidine in chapter 1 has implications not only for calibrating $^{40}Ar/^{39}Ar$ ages of tephra and other geologic materials, but it invokes assessment of other chronological signals thought to be globally isochronous. This includes the evaluation of the leads and lags in the deposition of orbitally-tuned sequences whose sediments record near-instantaneous atmospheric climate changes, and magnetic field behavior on earth as records by paleomagnetic rock record. As radioisotopic dating, astronomical tuning, and paleomagnetic reversal matching have all been utilized to date climatic and paleoanthropological archives, it is important to understand how differences in these chronometers may impact correlations (or the interpretation of causation) between climatic and evolutionary changes.

Dates and paleoenvironmental information deriving from strata associated with a paleoanthropological site represent the best-case scenario. For example, Light stable isotope records and geochronology derived directly from paleoanthropological sites eliminate ambiguities of temporal and stratigraphic correlations, and they provide local paleoenvironmental context not resolvable by conventional core-based records. This is exemplified in chapters 2 and 3, where materials derived from stratified archaeological sequences allow for direct assessment of the associated material culture within a chronological and/or environmental context. As dating techniques diversify, we must exercise caution in establishing the reliability of new approaches and characterize the precision and accuracy of each chronometer with great care to avoid the prescription of spurious age data.

The complexity of terrestrial climate records, and our ability to date them, are fields of continuous growth. With ongoing work to refine and diversify available geochronometers, and to pair precise and accurate dating approaches with paleoclimate archives, we may continue to learn about the complex relationship between humans and our environments.

Bibliography

Adams, W.M., Goudie, A.S., Orme, A.R. (Eds.), 1996. The Physical Geography of Africa. Oxford University Press, Oxford.

Akazawa, T., Aoki, K., Bar-Yosef, O. (Eds.), 2002. Neandertals and Modern Humans in Western Asia. Kluwer, New York.

Albert, P.G., Giaccio, B., Isaia, R., Costa, A., Niespolo, E.M., Nomade, S., Pereira, A., Renne, P.R., Hinchliffe, A., Mark, D.F., Brown, R., Smith, V.C., 2019. Evidence for a large magnitude eruption from Campi Flegrei caldera (Italy) at 29 ka. Geology. https://doi.org/10 .1130 /G45805.1

Aldrich, L.T., Nier, A.O., 1948. Argon 40 in potassium minerals. Phys. Rev. 74, 876–877. https://doi.org/10.1103/PhysRev.74.876

Allen, M.S., 2014. Marquesan colonisation chronologies and post-colonisation interaction: Implications for Hawaiian origins and the 'Marquesan Homeland' hypothesis. J. Pacific Archaeol. 5.

Allen, M.S., Morrison, A.E., 2013. Modelling site formation dynamics: Geoarchaeological, chronometric and statistical approaches to a stratified rockshelter sequence, Polynesia. J. Archaeol. Sci. 40, 4560–4575. https://doi.org/10.1016/j.jas.2013.06.008

Allen, M.S., Wallace, R., 2007. New Evidence From the East Polynesian Gateway : Substantive and 49, 1163–1179.

Ambrose, S., DeNiro, M., 1986. The Isotopic ecology of East African Mammals. Oecologia 69, 395–406. https://doi.org/10.1007/BF00377062

Ambrose, S.H., 2001. Middle and Later Stone Age Settlement Patterns in the Central Rift Valley, Kenya: Comparisons and Contrasts, in: Conard, N.J. (Ed.), Settlement Dynamics of the Middle Paleolithic and Middle Stone Age. Kerns Verlag, Tiibingen, pp. 21–43. https://doi.org/10.1016/j.quaint.2017.03.027

Ambrose, S.H., 1998. Chronology of the Later Stone Age and Food Production in East Africa. J. Archaeol. Sci. 25, 377–392. https://doi.org/10.1006/jasc.1997.0277

Ambrose, S.H., 1990. Preparation and Characterization of Bone and Tooth Collagen for Isotopic Analysis. J. Archaeol. Sci. 17, 431–451.

Amundson, R., Austin, A.T., Schuur, E.A.G., Yoo, K., Matzek, V., Kendall, C., Uebersax, A., Brenner, D., Baisden, W.T., 2003. Global patterns of the isotopic composition of soil and plant nitrogen. Global Biogeochem. Cycles 17. https://doi.org/10.1029/2002GB001903

Anderson, A., 2003. Initial human dispersal in Remote Oceania: Pattern and explanation, in: Sand, C. (Ed.), Pacific Archaeology: Assessments and Prospects. Le Cahirs de l'Archeologie, pp. 71–84.

Anderson, A., 2001. The chronology of prehistoric colonization in French Polynesia, in: Stevenson, C.M., Lee, G., Morin, M.J. (Eds.), Proceedings of the Fifth International Conference on Easter Island and the Pacific. Easter Island Foundation, Los Osos, pp. 247–52.

Anderson, K.D., Cantin, N.E., Heron, S.F., Pisapia, C., Pratchett, M.S., 2017. Variation in growth rates of branching corals along Australia's Great Barrier Reef. Sci. Rep. 7, 1–13. https://doi.org/10.1038/s41598-017-03085-1

Athens, J.S., Rieth, T.M., Dye, T.S., 2014. A Paleoenvironmental and Archaeological Model-Based Age Estimate for the Colonization of Hawai'l. Am. Antiq. 79, 144–155.

https://doi.org/10.7183/0002-7316.79.1.144
Austin, A.T., Sala, O.E., 1999. Foliar $\delta^{15}N$ is negatively correlated with rainfall along the IGBP transet in Australia. Aust. J. Plant Physiol. 26, 293–295. https://doi.org/10.1071/PP97167
Bachofer, F., Queneherve, G., Hertler, C., Giemsch, L., Hochschild, V., Maerker, M., 2018. Paleoenvironmental Research in the Semiarid Lake Manyara Area, Northern Tanzania: A Synopsis, in: Digital Geoarchaeology. pp. 123–138. https://doi.org/10.1007/978-3-319-25316-9
Banner, J.L., Wasserburg, G.J., Chen, J.H., Humphrey, J.D., 1991. Uranium-series evidence on diagenesis and hydrology in Pleistocene carbonates of Barbados, West Indies. Earth Planet. Sci. Lett. 107, 129–137. https://doi.org/10.1016/0012-821X(91)90049-N
Bar-Matthews, M., Wasserburg, G.J., Chen, J.H., 1993. Diagenesis of fossil coral skeletons: Correlation between trace elements, textures, and234U238U. Geochim. Cosmochim. Acta 57, 257–276. https://doi.org/10.1016/0016-7037(93)90429-Z
Barbour, M.M., Roden, J.S., Farquhar, G.D., Ehleringer, J.R., 2004. Expressing Leaf Water and Cellulose Oxygen Isotope Ratios as Enrichment above Source Water Reveals Evidence of a Péclet Effect. Oecologia 138, 426–435. https://doi.org/10.1007/s00442-003-
Bird, M.I., Turney, C.S.M., Fifield, L.K., Smith, M.A., Miller, G.H., Roberts, R.G., Magee, J.W., 2003. Radiocarbon dating of organic- and carbonate-carbon in Genyornis and Dromaius eggshell using stepped combustion and stepped acidification. Quat. Sci. Rev. 22, 1805–1812. https://doi.org/10.1016/S0277-3791(03)00151-3
Blegen, N., 2017. The earliest long-distance obsidian transport: Evidence from the ~200 ka Middle Stone Age Sibilo School Road Site, Baringo, Kenya. J. Hum. Evol. 103, 1–19. https://doi.org/10.1016/j.jhevol.2016.11.002
Blome, M.W., Cohen, A.S., Tryon, C.A., Brooks, A.S., Russell, J., 2012. The environmental context for the origins of modern human diversity: A synthesis of regional variability in African climate 150,000-30,000 years ago. J. Hum. Evol. 62, 563–592. https://doi.org/10.1016/j.jhevol.2012.01.011
Bloom, A.L., Broecker, W.S., Chappell, J.M.A., Matthews, R.K., Mesolella, K.J., 1974. Quaternary sea level fluctuations on a tectonic coast: New dates from the Huon Peninsula, New Guinea. Quat. Res. 4, 185–205. https://doi.org/10.1016/0033-5894(74)90007-6
Bourdon, B., Henderson, G.M., Lundstrom, C.C., Turner, S.P. (Eds.), 2003. Reviews in MIneralogy and Geochemistry, Volume 52: Uranium-Series Geochemistry. Geochemical Society, Washington, D.C.
Bronk-Ramsey, C., 2001. OxCal [WWW Document]. URL https://c14.arch.ox.ac.uk/oxcal.html
Bronk Ramsey, C., 2016. Development of the Radiocarbon Calibration Program. Radiocarbon 43, 355–363. https://doi.org/10.1017/s0033822200038212
Brooks, A.S., Hare, P.E., Kokis, J.E., Miller, G.H., Ernst, R.D., Wendorf, F., 1990. Dating pleistocene archeological sites by protein diagenesis in ostrich eggshell. Science. 248, 60–64. https://doi.org/10.1126/science.248.4951.60
Burley, D., Edinborough, K., Weisler, M., Zhao, J.X., 2015. Bayesian modeling and chronological precision for Polynesian settlement of Tonga. PLoS One 10, 1–14. https://doi.org/10.1371/journal.pone.0120795
Burley, D., Weisler, M.I., Zhao, J. xin, 2012. High Precision U/Th Dating of First Polynesian Settlement. PLoS One 7, 1–6. https://doi.org/10.1371/journal.pone.0048769
Casanova, J., Hillaire-Marcel, C., 1992. Chronology and Paleohydrology of Late Quaternary High Lake Levels in the Manyara Basin (Tanzania) from Isotopic Data (^{18}O, ^{13}C, ^{14}C, Th/U)

on Fossil Stromatolites. Quat. Res. 38, 205–226.
Channell, J.E.T., Hodell, D.A., Singer, B.S., Xuan, C., 2010. Reconciling astrochronological and 40 Ar/ 39 Ar ages for the Matuyama-Brunhes boundary and late Matuyama Chron . Geochemistry, Geophys. Geosystems 11, n/a-n/a. https://doi.org/10.1029/2010gc003203
Cheng, H., Adkins, J., Edwards, R.L., Boyle, E.A., 2000. U-Th dating of deep-sea corals. Geochimica et Cosmochimica Acta 64, 2401–2416. https://doi.org/10.1016/S0016-7037(99)00422-6
Cheng, H., Edwards, R.L., Southon, J., Matsumoto, K., Feinberg, J.M., Sinha, A., Zhou, W., Li, H., Li, X., Xu, Y., Chen, S., Tan, M., Wang, Q., Wang, Y., Ning, Y., 2018. Atmospheric 14C/ 12C changes during the last glacial period from Hulu Cave. Science. 362, 1293–1297. https://doi.org/10.1126/science.aau0747
Cheng, H., Lawrence Edwards, R., Shen, C.C., Polyak, V.J., Asmerom, Y., Woodhead, J., Hellstrom, J., Wang, Y., Kong, X., Spötl, C., Wang, X., Calvin Alexander, E., 2013. Improvements in ^{230}Th dating, ^{230}Th and ^{234}U half-life values, and U-Th isotopic measurements by multi-collector inductively coupled plasma mass spectrometry. Earth Planet. Sci. Lett. 371–372, 82–91. https://doi.org/10.1016/j.epsl.2013.04.006
Chisholm, B.S., Nelson, D.E., Hobson, K.A., Knyfb, M., 1983. Carbon Isotope Measurement Techniques for Bone Collagen : Notes for the Archaeologist. J. Archaeol. Sci. 10, 355–360.
Chutcharavan, P.M., Dutton, A., Ellwood, M.J., 2018. Seawater ^{234}U/^{238}U recorded by modern and fossil corals. Geochim. Cosmochim. Acta 224, 1–17. https://doi.org/10.1016/j.gca.2017.12.017
Clark, J.T., Quintus, S., Weisler, M., St Pierre, E., Nothdurft, L., Feng, Y., 2016. Refining the chronology for west polynesian colonization: New data from the Samoan archipelago. J. Archaeol. Sci. Reports 6, 266–274. https://doi.org/10.1016/j.jasrep.2016.02.011
Clark, P.U., Dyke, A.S., Shakun, J.D., Carlson, A.E., Clark, J., Wohlfarth, B., Mitrovica, J.X., Hostetler, S.W., McCabe, A.M., 2009. The Last Glacial Maximum. Science (80-.). 325, 710–714. https://doi.org/10.1126/science.1172873
Cobb, K.M., Charles, C.D., Cheng, H., Kastner, M., Edwards, R.L., 2003. U/Th-dating living and young fossil corals from the central tropical Pacific. Earth Planet. Sci. Lett. 210, 91–103. https://doi.org/10.1016/S0012-821X(03)00138-9
Coble, M.A., Grove, M., Calvert, A.T., 2011. Calibration of Nu-Instrumnets Noblesse multicollector mass spectrometers for argon isotopic measurements using a newly developed reference gas. Chem. Geol. 290, 75–87.
Conte, E., Molle, G., 2014. Reinvestigating a key site for Polynesian prehistory: New results from the Hane dune site, Ua Huka (Marquesas). Archaeol. Ocean. 49, 121–136. https://doi.org/10.1002/arco.5037
Cooper, A., Turney, C., Hughen, K.A., Brook, B.W., McDonald, H.G., Bradshaw, C.J.A., 2015. Abrupt warming events drove Late Pleistocene Holarctic megafaunal turnover. Science. 349, 602–606. https://doi.org/10.1126/science.aac4315
Coplen, T.B., 1996. New guidelines for reporting stable hydrogen, carbon, and oxygen isotope-ratio data. Geochim. Cosmochim. Acta 60, 3359–3360.
Cornwell, W.K., Wright, I., Turner, J., Maire, V., Barbour, M., Cernusak, L., Dawson, T., Ellsworth, D., Farquhar, G., Griffiths, H., Keitel, C., Knohl, A., Reich, P., Williams, D., Bhaskar, R., Cornelissen, J.H.C., Richards, A., Schmidt, S., Valladares, F., Körner, C., Schulze, E.D., Buchmann, N., Santiago, L., 2016. A global dataset of leaf delta ^{13}C values. Sci. Data.

Cornwell, W.K., Wright, I.J., Turner, J., Maire, V., Barbour, M.M., Cernusak, L.A., Dawson, T., Ellsworth, D., Farquhar, G.D., Griffiths, H., Keitel, C., Knohl, A., Reich, P.B., Williams, D.G., Bhaskar, R., Cornelissen, J.H.C., Richards, A., Schmidt, S., Valladares, F., Körner, C., Schulze, E.D., Buchmann, N., Santiago, L.S., 2018. Climate and soils together regulate photosynthetic carbon isotope discrimination within C_3 plants worldwide. Glob. Ecol. Biogeogr. 27, 1056–1067. https://doi.org/10.1111/geb.12764

Craine, J., Craine, J.M., Elmore, A.J., Aidar, M.P.M., Bustamante, M., Dawson, T.E., Hobbie, E.A., Kahmen, A., Mack, M.C., Mclauchlan, K.K., Michelsen, A., Nardoto, G.B., Pardo, L.H., 2009. Global patterns of foliar nitrogen isotopes and their relationships with climate , mycorrhizal fungi , 980–992. https://doi.org/10.1111/j.1469-8137.2009.02917.x

Crawford, E.C., Schmidt-Nielsen, K., 1967. Temperature regulation and evaporative cooling in the ostrich. Am. J. Physiol. 212, 347–353.

Crisp, M., Demarchi, B., Collins, M., Morgan-williams, M., Pilgrim, E., 2013. Quaternary Geochronology Isolation of the intra-crystalline proteins and kinetic studies in Struthio camelus (ostrich) eggshell for amino acid geochronology. Quat. Geochronol. 16, 110–128. https://doi.org/10.1016/j.quageo.2012.09.002

Cross, T.S., Cross, B.W., 1983. U, Sr, and Mg in Holocene and Pleistocene Corals A. Palmata and M. Annularis. SEPM J. Sediment. Res. Vol. 53, 587–594. https://doi.org/10.1306/212F823D-2B24-11D7-8648000102C1865D

Dalrymple, G.B., Jarrard, R.D., Clague, D.A., 1975. K-Ar Ages of Some Volcanic-Rocks From Cook and Austral Islands. Geol. Soc. Am. Bull. 86, 1463–1467. https://doi.org/10.1130/0016-7606(1975)86<1463:kaosvr>2.0.co;2

Dauphin, Y., Senut, B., 1998. Diagenetic changes in the mineral and organic phases of fossil avian eggshells from Namibia 13, 243–256.

Dawson, T.E., Mambelli, S., Plamboeck, A.H., Templer, P.H., Tu, K.P., 2002. Stable Isotopes in Plant Ecology. Annu. Rev. Ecol. Syst. 33, 507–559. https://doi.org/10.1146/annurev.ecolsys.33.020602.095451

Deino, A.L., Behrensmeyer, A.K., Brooks, A.S., Yellen, J.E., Sharp, W.D., Potts, R., 2018. Chronology of the Acheulean to Middle Stone Age transition in Eastern Africa. Science. 360, 95–98. https://doi.org/10.13140/2.1.3744.0649

Deino, A.L., Dommain, R., Keller, C.B., Potts, R., Behrensmeyer, A.K., Beverly, E.J., King, J., Heil, C.W., Stockhecke, M., Brown, E.T., Moerman, J., deMenocal, P., 2019. Chronostratigraphic model of a high-resolution drill core record of the past million years from the Koora Basin, south Kenya Rift: Overcoming the difficulties of variable sedimentation rate and hiatuses. Quat. Sci. Rev. 215, 213–231. https://doi.org/10.1016/j.quascirev.2019.05.009

Deino, A.L., Scott, G.R., Saylor, B., Alene, M., Angelini, J.D., Haile-Selassie, Y., 2010. 40Ar/39Ar dating, paleomagnetism, and tephrochemistry of Pliocene strata of the hominid-bearing Woranso-Mille area, west-central Afar Rift, Ethiopia. J. Hum. Evol. 58, 111–126. https://doi.org/10.1016/j.jhevol.2009.11.001

Demarchi, B., Hall, S., Roncal-Herrero, T., Freeman, C.L., Woolley, J., Crisp, M.K., Wilson, J., Fotakis, A., Fischer, R., Kessler, B.M., Jersie-Christensen, R.R., Olsen, J. V., Haile, J., Thomas, J., Marean, C.W., Parkington, J., Presslee, S., Lee-Thorp, J., Ditchfield, P., Hamilton, J.F., Ward, M.W., Wang, C.M., Shaw, M.D., Harrison, T., Domínguez-Rodrigo, M., Macphee, R.D.E., Kwekason, A., Ecker, M., Horwitz, L.K., Chazan, M., Kroger, R., Thomas-Oates, J., Harding, J.H., Cappellini, E., Penkman, K., Collins, M.J., 2016. Protein

sequences bound to mineral surfaces persist into deep time. Elife 5. https://doi.org/10.7554/eLife.17092
Demenocal, P., Ortiz, J., Guilderson, T., Adkins, J., Sarnthein, M., Baker, L., Yarusinsky, M., 2000. Abrupt onset and termination of the African Humid Period: Rapid climate responses to gradual insolation forcing. Quat. Sci. Rev. 19, 347–361. https://doi.org/10.1016/S0277-3791(99)00081-5
DeMenocal, P.B., 2011. Climate and human evolution. Science. 331, 540–542. https://doi.org/10.1126/science.1190683
DeNiro, M.J., 1985. Postmortem preservation and alteration of in vivo bone collagen isotope ratios in relation to palaeodietary reconstruction. Nature 317, 806–809.
DeNiro, M.J., Epstein, S., 1981. Influence of diet on the distribution of nitrogen isotopes in animals. Geochim. Cosmochim. Acta 45, 341–351. https://doi.org/10.1016/0016-7037(81)90244-1
Deniro, M.J., Schoeniger, M.J., 1983. Stable Carbon and Nitrogen Isotope Ratios of Bone Collagen: Variations within Individuals, Between Sexes , and Within Populations Raised on Monotonous Diets. J. Archaeol. Sci. 10, 199–203.
Deniro, M.J., Weiner, S., 1988. Chemical , enzymatic and spectroscopic characterization of "collagen" and other organic fractions from prehistoric bones. Geochim. Cosmochim. Acta 52, 2197–2206.
Diamond, J., 2017. Archaeology: Of rats and resilience. Nature 545, 32–33. https://doi.org/10.1038/545032a
Diamond, J., 2005. Collapse: How Societies Choose to Fail or Succeed. Viking, New York.
Dickin, A.P., 1995. Radiogenic Isotope Geology, 2nd ed. Cambridge University Press, Cambridge.
Domínguez-Rodrigo, M., Díez-Martín, F., Mabulla, A., Luque, L., Alcalá, L., Tarriño, A., López-Sáez, J.A., Barba, R., Bushozi, P., 2007. The archaeology of the Middle Pleistocene deposits of Lake Eyasi, Tanzania. J. African Archaeol. 5, 47–75. https://doi.org/10.3213/1612-1651-10085
Dullo, W.C., 2005. Coral growth and reef growth: A brief review. Facies 51, 33–48. https://doi.org/10.1007/s10347-005-0060-y
Dutton, A., Rubin, K., McLean, N., Bowring, J., Bard, E., Edwards, R.L., Henderson, G.M., Reid, M.R., Richards, D.A., Sims, K.W.W., Walker, J.D., Yokoyama, Y., 2017. Data reporting standards for publication of U-series data for geochronology and timescale assessment in the earth sciences. Quat. Geochronol. 39, 142–149. https://doi.org/10.1016/j.quageo.2017.03.001
Dye, T.S., Pantaleo, J., 2010. Age of the O18 site, Hawai'i. Archaeol. Ocean. 45, 113–119. https://doi.org/10.1002/j.1834-4453.2010.tb00087.x
Eagle, R.A., Enriquez, M., Grellet-Tinner, G., Pérez-Huerta, A., Hu, D., Tütken, T., Montanari, S., Loyd, S.J., Ramirez, P., Tripati, A.K., Kohn, M.J., Cerling, T.E., Chiappe, L.M., Eiler, J.M., 2015. Isotopic ordering in eggshells reflects body temperatures and suggests differing thermophysiology in two Cretaceous dinosaurs. Nat. Commun. 6, 1–11. https://doi.org/10.1038/ncomms9296
Edwards, R.L., Gallup, C.D., Cheng, H., 2003. U-Series dating of marine and lactustrine carbonates, in: Bourdon, B., Henderson, G.M., Lundstrom, C.C., Turner, S.P. (Eds.), Uranium-Series Geochemistry. Mineralogical Society of America, Washington, D.C., pp. 363–405.

Eggins, S.M., Grün, R., McCulloch, M.T., Pike, A.W.G., Chappell, J., Kinsley, L., Mortimer, G., Shelley, M., Murray-Wallace, C. V., Spötl, C., Taylor, L., 2005. In situ U-series dating by laser-ablation multi-collector ICPMS: New prospects for Quaternary geochronology. Quat. Sci. Rev. 24, 2523–2538. https://doi.org/10.1016/j.quascirev.2005.07.006

Ehleringer, J.R., Cerling, T.E., 2002. C 3 and C 4 Photosynthesis. Encycl. Glob. Environ. Chang.

Ehleringer, J.R., Cerling, T.E., Helliker, B.R., 1997. C_4 photosynthesis, atmospheric CO_2 , and climate. Oecologia 112, 285–299. https://doi.org/10.1007/s004420050311

Ellison, J.C., 1994. Caves and speleogenesis of Mangaia, Cook Islands.

Epstein, S., Thompson, P., Yapp, C.J., 1977. Oxygen and Hydrogen Isotopic Ratios in Plant Cellulose. Science. 198, 1209–1215.

Faith, J.T., 2018. Paleodietary change and its implications for aridity indices derived from δ18O of herbivore tooth enamel. Palaeogeogr. Palaeoclimatol. Palaeoecol. 490, 571–578. https://doi.org/10.1016/j.palaeo.2017.11.045

Faith, J.T., Tryon, C.A., Peppe, D.J., Fox, D.L., 2013. The fossil history of Grévy's zebra (Equus grevyi) in equatorial East Africa. J. Biogeogr. 40, 359–369. https://doi.org/10.1111/j.1365-2699.2012.02796.x

Farquhar, G.D., Ehleringer, J.R., Hubick, K.T., 1989. Discrimination and Photosynthesis. Annu. Rev. Plant Physiol. Plant Mol. Biol. 40, 503–537.

Feng, Q.L., Zhu, X., Li, H.D., Kim, T.N., 2001. Crystal orientation regulation in ostrich eggshells. J. Cryst. Growth 233, 548–554. https://doi.org/10.1016/S0022-0248(01)01611-6

Fry, B., 2006. Stable Isotope Ecology. Springer.

Gallup, C.D., Edwards, R.L., Johnson, R.G., 1994. The Timing of High Sea Levels Over the Past 200,000 Years. Adv. Sci. 263, 796–800.

Giaccio, B., Hajdas, I., Isaia, R., Deino, A., Nomade, S., 2017. High-precision ^{14}C and $^{40}Ar/^{39}Ar$ dating of the Campanian Ignimbrite (Y-5) reconciles the time-scales of climatic-cultural processes at 40 ka. Sci. Rep. 7, 1–10. https://doi.org/10.1038/srep45940

Gliganic, L.A., Jacobs, Z., Roberts, R.G., Domínguez-Rodrigo, M., Mabulla, A.Z.P., 2012. New ages for Middle and Later Stone Age deposits at Mumba rockshelter, Tanzania: Optically stimulated luminescence dating of quartz and feldspar grains. J. Hum. Evol. 62, 533–547. https://doi.org/10.1016/j.jhevol.2012.02.004

Gramly, R.M., 1976. Upper Pleistocene Archaeological Occurrences at Site GvJm/22, Lukenya Hill, Kenya. Man 11, 319–344.

Grove, M., Burke, A., 2015. Environmental variability and hominin dispersal. J. Hum. Evol. 87, 1–4. https://doi.org/10.1016/j.jhevol.2015.07.006

Hall, C.M., 2014. Direct measurement of recoil effects on $^{40}Ar/^{39}Ar$ standards. Adv. $^{40}Ar/^{39}Ar$ Dating From Archaeol. to Planet. Sci. 378, 53–62.

Hartman, A.T., 2018. An analysis of the effects of temperatures and circulations on the strength of the low-level jet in the Turkana Channel in East Africa. Theor. Appl. Climatol. 132, 1003–1017. https://doi.org/10.1007/s00704-017-2121-x

Hather, J., Kirch, P.V., 1991. Prehistoric sweet potato (*Ipomoea batatas*) from Mangaia Island, Central Polynesia. Antiquity 65, 887–893. https://doi.org/10.1017/S0003598X00080613

Hellstrom, J., 2006. U-Th dating of speleothems with high initial ^{230}Th using stratigraphical constraint. Quat. Geochronol. 1, 289–295. https://doi.org/10.1016/j.quageo.2007.01.004

Henderson, G.M., Anderson, R.F., 2003. The U-series Toolbox for Paleoceanography. Rev. Mineral. geochemistry 52, 493–531. https://doi.org/10.2113/0520493

Henn, B.M., Steele, T.E., Weaver, T.D., 2018. Clarifying distinct models of modern human

origins in Africa. Curr. Opin. Genet. Dev. 53, 148–156. https://doi.org/10.1016/j.gde.2018.10.003
Henshilwood, C.S., van Niekerk, K.L., Wurz, S., Delagnes, A., Armitage, S.J., Rifkin, R.F., Douze, K., Keene, P., Haaland, M.M., Reynard, J., Discamps, E., Mienies, S.S., 2014. Klipdrift Shelter, southern cape, south africa: Preliminary report on the howiesons poort layers. J. Archaeol. Sci. 45, 284–303. https://doi.org/10.1016/j.jas.2014.01.033
Hibbert, F.D., Rohling, E.J., Dutton, A., Williams, F.H., Chutcharavan, P.M., Zhao, C., Tamisiea, M.E., 2016. Coral indicators of past sea-level change: A global repository of U-series dated benchmarks. Quat. Sci. Rev. 145, 1–56. https://doi.org/10.1016/j.quascirev.2016.04.019
Hincke, M.T., Tsang, C.P.W., Courtney, M., Hill, V., Narbaitz, R., 1995. Purification and Immunochemistry of a Soluble Matrix Protein of the Chicken Eggshell (Ovocleidin 17). Calcif. Tissue Int. 56, 578–583.
Hoffmann, D.L., Spötl, C., Mangini, A., 2009. Micromill and in situ laser ablation sampling techniques for high spatial resolution MC-ICPMS U-Th dating of carbonates. Chem. Geol. 259, 253–261. https://doi.org/10.1016/j.chemgeo.2008.11.015
Högberg, P., 1997. Tansley Review No . 95: ^{15}N natural abundance in soil – plant systems. New Phytol. 137, 179–203. https://doi.org/10.1046/j.1469-8137.1997.00808.x
Hogg, A.G., Hua, Q., Blackwell, P.G., Niu, M., Buck, C.E., Guilderson, T.P., Heaton, T.J., Palmer, J.G., Reimer, P.J., Reimer, R.W., Turney, C.S.M., Zimmerman, S.R.H., 2013. SHCal13 Southern Hemisphere Calibration, 0–50,000 Years cal BP. Radiocarbon 55, 1889–1903. https://doi.org/10.2458/azu_js_rc.55.16783
Holden, N.E., 1990. Total half-lives for selected nuclides 62, 941–958.
Hunt, T.L., Lipo, C.P., 2012. The Statues that Walked: Unraveling the Mystery of Easter Island. Counterpoint, Berkeley.
Hut, G., 1987. Consultants' group meting on stable isotope reference samples for geochemical and hydrological investigations. Vienna, Austria.
Ickert, R.B., Mundil, R., Magee, C.W., J., Mulcahy, S.R., 2015. The U-Th-Pb systematics of zircon from Bishop Tuff: A case study in challenges to high-precision Pb/U geochronology at the millenial scale. Geochim. Cosmochim. Acta 268, 88–110.
Inskeep, R.R., 1962. The age of the Kondoa rock paintings in light of recent excavations at Kisese II rock shelter, in: Mortelmans, G., Nenquin, J. (Eds.), Actes Du IVe Congres Panafrican de Prehistorie et de l'ectude Du Quaternaire. Tervuren, pp. 249–256.
Irwin, G., 1981. How Lapita lost its pots: The question of continuity in the colonisation of Oceania. J. Polyn. Soc. 90, 481–484.
Jaffey, A.H., Flynn, K.F., Glendenin, L.E., Bentley, W.C., Essling, A.M., 1971. Precision measurement of half-lives and specific activities of U235 and U238. Phys. Rev. C 4, 1889–1906. https://doi.org/10.1103/PhysRevC.4.1889
Jicha, B.R., Singer, B.S., Sobol, P., 2016. Re-evaluation of the ages of ^{40}Ar/^{39}Ar sanidine standards and supereruptions in the western U.S. using a Noblesse multi-collector mass spectrometer. Chem. Geol. 431, 54–66. https://doi.org/10.1016/j.chemgeo.2016.03.024
Johnson, B.J., Fogel, M.L., Miller, G.H., 1998. Stable isotopes in modern ostrich eggshell: A calibration for paleoenviromental applications in semi-arid regions of southern africa. Geochim. Cosmochim. Acta 62, 2451–2461.
Johnson, B.J., Miller, G.H., Fogel, M.L., Beaumont, P.B., 1997. The determination of late Quaternary palaeoenvironments at Equus Cave, South Africa, using stable isotopes and

amino acid racemization in ostrich eggshell. Palaeogeogr. Palaeoclimatol. Palaeoecol. 136, 121–137. https://doi.org/10.1016/S0031-0182(97)00043-6
Johnson, T.C., 2017. Quaternary Climate Variation in Eastern Africa 1, 1–26. https://doi.org/10.1093/acrefore/9780190228620.013.525
Johnson, T.C., Werne, J.P., Brown, E.T., Abbott, A., Berke, M., Steinman, B.A., Halbur, J., Contreras, S., Grosshuesch, S., Deino, A., Lyons, R.P., Scholz, C.A., Schouten, S., Damsté, J.S.S., 2016. A progressively wetter climate in southern East Africa over the past 1.3 million years. Nature 537, 220–224. https://doi.org/10.1038/nature19065
Jones, S.C., Brian A Stewart (Eds.), 2016. Africa from MIS 6-2. Springer. https://doi.org/10.1007/978-94-017-7520-5
Jørkov, M.L.S., Heinemeier, J., Lynnerup, N., 2007. Evaluating bone collagen extraction methods for stable isotope analysis in dietary studies 34, 1824–1829. https://doi.org/10.1016/j.jas.2006.12.020
Kahmen, A., Sachse, D., Arndt, S.K., Tu, K.P., Farrington, H., Vitousek, P.M., Dawson, T.E., 2011. Cellulose $\delta^{18}O$ is an index of leaf-to-air vapor pressure difference (VPD) in tropical plants. Proc. Natl. Acad. Sci. 108, 1981–1986. https://doi.org/10.1073/pnas.1018906108
Keeling, C.D., 1979. The Suess effect: 13Carbon-14Carbon interrelations. Environ. Int. 2, 229–300. https://doi.org/10.1016/0160-4120(79)90005-9
Keeling, R.F., Graven, H.D., Welp, L.R., Resplandy, L., Bi, J., Piper, S.C., Sun, Y., Bollenbacher, A., Meijer, H.A.J., 2017. Atmospheric evidence for a global secular increase in carbon isotopic discrimination of land photosynthesis. Proc. Natl. Acad. Sci. 114, 10361–10366. https://doi.org/10.1073/pnas.1619240114
Kelly, R.L., 2013. The Lifeways of Hunter-Gatherers: The Foraging Spectrum. Cambridge University Press, Cambridge.
Kirch, P.V., 2017a. On the road of the winds: An archaeological history of the Pacific Islands before European contact. University of California Press.
Kirch, P.V., 2017b. Radiocarbon Dating and Bayesian Modeling of the Chronology of Tangatatau Rockshelter, in: Kirch, P.V. (Ed.), Tangatatau Rockshelter: The Evolution of an Eastern Polynesian Socio-Ecosystem. UCLA Cotsen Institute of Archaeology Press, p. 326.
Kirch, P.V., 2017c. The Mangaia Socio-Ecosystem: Environmental and Ethnohistoric Perspectives, in: Kirch, P.V. (Ed.), Tangatatau Rockshelter: The Evolution of an Eastern Polynesian Socio-Ecosystem. UCLA Cotsen Institute of Archaeology Press, p. 326.
Kirch, P.V., 2017d. Excavations at Tangatatau Rockshelter (Site MAN-44), in: Kirch, P.V. (Ed.), Tangatatau Rockshelter: The Evolution of an Eastern Polynesian Socio-Ecosystem. UCLA Cotsen Institute of Archaeology Press, p. 326.
Kirch, P.V., Butler, V.L., Carlier, C., Gonzalez, M.N., Hather, J.G., Horrocks, M., Kahn, J.G., Kirch, P. V., Plourde, A.M., Taomia, J.M.E., 2017a. Tangatatau Rockshelter: The Evolution of an Eastern Polynesian Socio-Ecosystem. UCLA Cotsen Institute of Archaeology Press.
Kirch, P.V., Hather, J.G., Horrocks, M., 2017b. Archaeobotanical Assemblages from Tangatatau Rockshelter, in: Kirch, P.V. (Ed.), Tangatatau Rockshelter: The Evolution of an Eastern Polynesian Socio-Ecosystem. UCLA Cotsen Institute of Archaeology Press, p. 326.
Kirch, P. V., 2011. When Did the Polynesians Settle Hawai'i? A Review of 150 Years of Scholarly Inquiry and a Tentative Answer. Hawaiian Archaeol. 12, 3–26.
Kirch, P. V., Conte, E., Sharp, W., Nickelsen, C., 2010. The Onemea site (Taravai Island, Mangareva) and the human colonization of Southeastern Polynesia. Archaeol. Ocean. 45, 66–79. https://doi.org/10.1002/j.1834-4453.2010.tb00081.x

Kirch, P. V., Sharp, W.D., 2005. Coral 230Th dating of the imposition of ritual control hierarchy in precontact Hawaii. Sci. Reports 307, 102–104.
Kirch, P. V, 1986. Rethinking East Polynesian Prehistory. J. Polyn. Soc. 95, 9–40.
Klein, R.G., 2008. Out of Africa and the evolution of human behavior. Evol. Anthropol. 17, 267–281. https://doi.org/10.1002/evan.20181
Koch, P.L., 1998. Isotopic Reconstruction of Past Continental Environments. Annu. Rev. Earth Planet. Sci. 26, 573–613. https://doi.org/10.1146/annurev.earth.26.1.573
Kohn, M.J., 2010. Carbon isotope compositions of terrestrial C_3 plants as indicators of (paleo)ecology and (paleo)climate. Proc. Natl. Acad. Sci. 107, 19691–19695. https://doi.org/10.1073/pnas.1004933107
Kohn, M.J., 1996. Predicting animal $\delta^{18}O$: Accounting for diet and physiological adaptation. Geochim. Cosmochim. Acta 60, 4811–4829.
Kuiper, K.F., Deino, A., Hilgen, F.J., Krijgsman, W., Renne, P.R., Wijbrans, J.R., 2008. Synchronizing rock clocks of earth history. Science. 320, 500–504. https://doi.org/10.1126/science.1154339
Kuiper, K.F., Hilgen, F.J., Steenbrink, J., Wijbrans, J.R., 2004. $^{40}Ar/^{39}Ar$ ages of tephras intercalated in astronomically tuned Neogene sedimentary sequences in the eastern Mediterranean. Earth Planet. Sci. Lett. 222, 583–597. https://doi.org/10.1016/j.epsl.2004.03.005
Landais, A., Barkan, E., Yakir, D., Luz, B., 2006. The triple isotopic composition of oxygen in leaf water. Geochim. Cosmochim. Acta 70, 4105–4115. https://doi.org/10.1016/j.gca.2006.06.1545
Lee-Thorp, J.A., Ecker, M., 2015. Holocene Environmental Change at Wonderwerk Cave, South Africa: Insights from Stable Light Isotopes in Ostrich Eggshell. African Archaeol. Rev. 32, 793–811. https://doi.org/10.1007/s10437-015-9202-y
Lee, J.Y., Marti, K., Severinghaus, J.P., Kawamura, K., Yoo, H.S., Lee, J.B., Kim, J.S., 2006. A redetermination of the isotopic abundances of atmospheric Ar. Geochim. Cosmochim. Acta 70, 4507–4512. https://doi.org/10.1016/j.gca.2006.06.1563
Leuthold, W., 1976. Notes on the Breeding Biology of the Ostrich *Struthio Camelus* in Tsavo East National Park, Kenya. Ibis (Lond. 1859). 541–544.
Levin, N.E., Cerling, T.E., Passey, B.H., Harris, J.M., Ehleringer, J.R., 2006. A stable isotope aridity index for terrestrial environments. Proc. Natl. Acad. Sci. 103, 11201–11205. https://doi.org/10.1073/pnas.0604719103
Lind, E.M., Morrison, M.E.S., 1974. East African Vegetation. London.
Ludwig, K.R., 2012. User's Manual for Isoplot 3.75, a geochronological toolkit for Microsoft Excel. Berkeley Geochronol. Cent. Spec. Publ. 5, 1–72.
Ludwig, K.R., Paces, J.B., 2002. Uranium-series dating of pedogenic silica and carbonate, Crater Flat, Nevada. Geochim. Cosmochim. Acta 66, 487–506. https://doi.org/10.1016/S0016-7037(01)00786-4
Ludwig, K.R., Wallace, A.R., Simmons, K.R., 1985. The Schwartzwalder uranium deposit, II: Age of uranium mineralization and lead isotope constraints on genesis. Econ. Geol. 80, 1858–1871. https://doi.org/10.2113/gsecongeo.80.7.1858
Luz, B., Barkan, E., 2011. The isotopic composition of atmospheric oxygen. Global Biogeochem. Cycles 25, 1–14. https://doi.org/10.1029/2010GB003883
Luz, B., Kolodny, Y., Horowitz, M., 1984. Fractionation of oxygen isotopes between mammalian bone-phosphate and environmental drinking water. Geochim. Cosmochim.

Acta 48, 1689–1693.
Mallick, S., Li, H., Lipson, M., Mathieson, I., Gymrek, M., Racimo, F., Zhao, M., Chennagiri, N., Nordenfelt, S., Tandon, A., Skoglund, P., Lazaridis, I., Sankararaman, S., Fu, Q., Rohland, N., Renaud, G., Erlich, Y., Willems, T., Gallo, C., Spence, J.P., Song, Y.S., Poletti, G., Balloux, F., van Driem, G., de Knijff, P., Gallego Romero, I., Jha, A.R., Behar, D.M., Bravi, C.M., Capelli, C., Hervig, T., Moreno-Estrada, A., Posukh, O.L., Balanovska, E., Balanovsky, O., Karachanak-Yankova, S., Sahakyan, H., Toncheva, D., Yepiskoposyan, L., Tyler-Smith, C., Xue, Y., Abdullah, M.S., Ruiz-Linares, A., Beall, C.M., Di Rienzo, A., Jeong, C., Starikovskaya, E.B., Metspalu, E., Parik, J., Villems, R., Henn, B.M., Hodoglugil, U., Mahley, R., Sajantila, A., Stamatoyannopoulos, G., Wee, J.T.S., Khusainova, R., Khusnutdinova, E., Litvinov, S., Ayodo, G., Comas, D., Hammer, M.F., Kivisild, T., Klitz, W., Winkler, C.A., Labuda, D., Bamshad, M., Jorde, L.B., Tishkoff, S.A., Watkins, W.S., Metspalu, M., Dryomov, S., Sukernik, R., Singh, L., Thangaraj, K., Pääbo, S., Kelso, J., Patterson, N., Reich, D., 2016. The Simons Genome Diversity Project: 300 genomes from 142 diverse populations. Nature 538, 201–206. https://doi.org/10.1038/nature18964
Marean, C.W., 1992. Implications of Late Quaternary Mammalian Fauna from Lukenya Hill (South-Central Kenya) for Paleoenvironmental Change and Fauna1 Extinctions Kenya. Quat. Res. 255, 239–255.
Marean, C.W., 1991. Late Quaternary Paleoenvironments and Faunal Exploitation in East Africa. University of California Berkeley.
Mark, D.F., Renne, P.R., Dymock, R., Smith, V.C., Simon, J.I., Morgan, L.E., Staff, R.A., Ellis, B.S., 2017. High-precision $^{40}Ar/^{39}Ar$ dating of pleistocene tuffs and temporal anchoring of the Matuyama-Brunhes boundary. Quat. Geochronol. 39, 1–23. https://doi.org/10.1016/j.quageo.2017.01.002
Marshall, P., 1927. Geology of Mangaia. Bernice P. Bish. Museum Bull. 36.
McBrearty, S., Brooks, A.S., 2000. The revolution that wasn't : A new interpretation of the origin of modern human behavior. J. Hum. Evol. 39, 453–563. https://doi.org/10.1006/jhev.2000.0435
McCoy, M.D., Alderson, H.A., Hemi, R., Cheng, H., Edwards, R.L., 2016. Earliest direct evidence of monument building at the archaeological site of Nan Madol (Pohnpei, Micronesia) identified using $^{230}Th/U$ coral dating and geochemical sourcing of megalithic architectural stone. Quat. Res. (United States) 86, 295–303. https://doi.org/10.1016/j.yqres.2016.08.002
McDougall, I., Brown, F.H., Vasconcelos, P.M., Cohen, B.E., Thiede, D.S., Buchanan, M.J., 2012. New single crystal $^{40}Ar/^{39}Ar$ ages improve time scale for deposition of the Omo Group, Omo–Turkana Basin, East Africa . J. Geol. Soc. London. 169, 213–226. https://doi.org/10.1144/0016-76492010-188
McDougall, I., Harrison, T.M., 1999. Geochronology and Thermochronology by the $^{40}Ar/^{39}Ar$ Method, 2nd ed. Oxford University Press, New York.
McGregor, H. V., Hellstrom, J., Fink, D., Hua, Q., Woodroffe, C.D., 2011. Rapid U-series dating of young fossil corals by laser ablation MC-ICPMS. Quat. Geochronol. 6, 195–206. https://doi.org/10.1016/j.quageo.2010.10.002
Mcnutt, M., Menard, H.W., 1978. Lithospheric flexure and uplifted atolls. J. Geophys. Res. 83, 1206–1212.
Mcsweeney, C., New, M., Lizcano, G., 2012. UNDP Climate Change Country Profiles:

Tanzania, UNDP Climate Change Country ProfilesCountry Profiles.
McSweeney, C., New, M., Lizcano, G., 2012. UNDP Climate Change Country Profiles: Kenya, UNDP Climate Change Country Profiles.
Merrihue, C., Turner, G., 1966. Potassium-Argon dating by activation with fast neutrons. J. Geophys. Res. 71, 2852–2857.
Mertz-Kraus, R., Jochum, K.P., Sharp, W.D., Stoll, B., Weis, U., Andreae, M.O., 2010. In situ ^{230}Th–^{232}Th–^{234}U–^{238}U analysis of silicate glasses and carbonates using laser ablation single-collector sector-field ICP-MS. J. Anal. At. Spectrom. 25, 1895. https://doi.org/10.1039/c0ja00004c
Mikhailov, K.E., 1997. Fossil and recent eggshell in amniotic vertebrates: fine structure, comparative morphology and classification. Spec. Pap. Palaeontol. 56, 1–80.
Miller, G., Magee, J., Smith, M., Spooner, N., Baynes, A., Lehman, S., Fogel, M., Johnston, H., Williams, D., Clark, P., Florian, C., Holst, R., DeVogel, S., 2016. Human predation contributed to the extinction of the Australian megafaunal bird Genyornis newtoni ∼47 ka. Nat. Commun. 7, 1–7. https://doi.org/10.1038/ncomms10496
Miller, G.H., Brigham-Grette, J., 1989. Amino acid geochronology: Resolution and precision in carbonate fossils. Quat. Int. 1, 111–128.
Miller, G.H., Fogel, M.L., 2016. Calibrating δ18O in Dromaius novaehollandiae (emu) eggshell calcite as a paleo-aridity proxy for the Quaternary of Australia. Geochim. Cosmochim. Acta 193, 1–13. https://doi.org/10.1016/j.gca.2016.08.004
Milton, S.. J., Dean, R.J., Siegfried, W.R., 1994. Food Selection by Ostrich in Southern Africa. J. Wildl. Manage. 58, 234–248.
Min, G.R., Edwards, R.L., Taylor, F.W., Recy, J., Gallup, C.D., Warren Beck, J., 1995. Annual cycles of U/Ca in coral skeletons and U/Ca thermometry. Geochim. Cosmochim. Acta 59, 2025–2042. https://doi.org/10.1016/0016-7037(95)00124-7
Min, K., Mundil, R., Renne, P.R., Ludwig, K.R., 2000. A test for systematic errors in ^{40}Ar/^{39}Ar geochronology. Geochim. Cosmochim. Acta 64, 73–98.
Montenegro, Á., Avis, C., Weaver, A., 2008. Modeling the prehistoric arrival of the sweet potato in Polynesia. J. Archaeol. Sci. 35, 355–367. https://doi.org/10.1016/j.jas.2007.04.004
Moran, V., Hoffmann, J., Donnelly, D., van Wilgen, B., Zimmermann, H., 2000. Biological Control of Alien, Invasive Pine Trees (*Pinus* species) in South Africa. Proc. X Int. Symp. Biol. Control Weeds. Mont. State Univ. Bozeman, Mont. USA. 953, 941–953.
Moreau, R.E., 1950. the Breeding Seasons of African Birds. Int. J. Avian Sci. 223–267.
Muhs, D.R., Schweig, E.S., Simmons, K.R., Halley, R.B., 2017. Late Quaternary uplift along the North America-Caribbean plate boundary: Evidence from the sea level record of Guantanamo Bay, Cuba. Quat. Sci. Rev. 178, 54–76. https://doi.org/10.1016/j.quascirev.2017.10.024
Muñoz-Rodríguez, P., Carruthers, T., Wood, J.R.I., Williams, B.R.M., Weitemier, K., Kronmiller, B., Ellis, D., Anglin, N.L., Longway, L., Harris, S.A., Rausher, M.D., Kelly, S., Liston, A., Scotland, R.W., 2018. Reconciling Conflicting Phylogenies in the Origin of Sweet Potato and Dispersal to Polynesia. Curr. Biol. 28, 1246–1256.e12. https://doi.org/10.1016/j.cub.2018.03.020
National Institute of Standards and Technology, 2012. Certificate of Analysis Standard Reference Material ® 612 Trace Elements in Glass 612.
Newsome, S.D., Miller, G.H., Magee, J.W., Fogel, M.L., 2011. Quaternary record of aridity and mean annual precipitation based on δ15N in ratite and dromornithid eggshells from Lake

Eyre, Australia. Oecologia 167, 1151–1162. https://doi.org/10.1007/s00442-011-2046-5
Nicholson, S., 2016. The Turkana low-level jet: Mean climatology and association with regional aridity. Int. J. Climatol. 36, 2598–2614. https://doi.org/10.1002/joc.4515
Nicholson, S.E., 2017. Climate and climatic variability of rainfall over eastern Africa. Rev. Geophys. 55, 590–635. https://doi.org/10.1002/2016RG000544
Niespolo, E.M., Renne, P.R., Hart, W.K., White, T.D., WoldeGabriel, G., 2018a. Toward a chronostratigraphic framework for the last million years of environmental and human evolution in the Middle Awash, Ethiopia: $^{40}Ar/^{39}Ar$ geochronology and tephra chemistry, in: Geological Society of America Annual Meeting. Indianapolis, IN.
Niespolo, E.M., Sharp, W.D., Fylstra, N.D., Aguirre-Palafox, L.E., Avery, G., Klein, R.G., 2018b. U-Th burial dating of ostrich eggshells from Ysterfontein 1 Middle Stone Age Rock Shelter, South Africa, in: African Quaternary Congress. Nairobi, Kenya.
Niespolo, E.M., Sharp, W.D., Fylstra, N.D., Avery, G., Blegen, N., Faith, J.T., Henshilwood, C.S., Klein, R., Van Niekerk, K., Weisz, D.G., Tryon, C.A., 2018c. U-Th burial dating of ostrich eggshell beyond the 14 C limit. Geochemical Society, Boston, MA.
Niespolo, E.M., Sharp, W.D., Fylstra, N.D., Tryon, C.A., Tripathy-Lang, A., Weisz, D.G., Blegen, N., Faith, J.T., Henshilwood, C.S., Lewise, J., Mackay, A., Steele, T., Van Niekerk, K., WoldeGabriel, G., 2017. U-Th burial dating of ostrich eggshells : a novel approach to dating African archaeological sequences beyond the 14 C limit, in: Geological Society of America Annual Meeting. Seattle, WA.
Niespolo, E.M., Sharp, W.D., Fylstra, N.D., Tryon, C.A., Weisz, D.G., Faith, J.T., Henshilwood, C.S., Lewis, J., Mackay, A., Steele, T.E., Van Niekerk, K.L., 2017. Patterns of Secondary U in ostrich eggshell: Applicaiton to U-Th dating of Quaternay terrestrial strata, in: American Geochemical Society. Paris.
Niespolo, E.M., Sharp, W.D., Tryon, C.A., Faith, J.T., Miller, M.J., Dawson, T.E., 2015. C and N Isotopes in Ostrich Eggshell as Proxies of Paleovegetation and Paleoprecipitation: Extraction, Preservation, and Application to Pleistocene Archaeological Samples.
Nomade, S., Renne, P.R., Vogel, N., Deino, A.L., Sharp, W.D., Becker, T.A., Jaouni, A.R., Mundil, R., 2005. Alder Creek sanidine (ACs-2): A Quaternary $^{40}Ar/^{39}Ar$ dating standard tied to the Cobb Mountain geomagnetic event. Chem. Geol. 218, 315–338. https://doi.org/10.1016/j.chemgeo.2005.01.005
Nunn, P.D., Petchey, F., 2013. Bayesian Re-evaluation of Lapita Settlement in Fiji: Radiocarbon analysis of the Lapita occupation at Bourewa and nearby sites on the Rove Peninsula, Viti Levu Island. J. Pacific Arcaheology 4, 21–34. https://doi.org/10.1038/2091178c0
Nys, Y., Gautron, J., Garcia-Ruiz, J.M., Hincke, M.T., 2004. Avian eggshell mineralization: Biochemical and functional characterization of matrix proteins. Comptes Rendus - Palevol 3, 549–562. https://doi.org/10.1016/j.crpv.2004.08.002
Nys, Y., Hincke, M.T., Arias, J.L., Garcia-Ruiz, J.M., Solomon, S.E., 1999. Avian eggshell mineralization. Poult. Avian Biol. Rev. 10, 143–166.
Owen, B.R., Renaut, R.W., Muiruri, V.M., Rabideaux, N.M., Lowenstein, T.K., McNulty, E.P., Leet, K., Deocampo, D., Luo, S., Deino, A.L., Cohen, A., Sier, M.J., Campisano, C., Shen, C.-C., Billingsley, A., Mbuthia, A., Stockhecke, M., 2019. Quaternary history of the Lake Magadi Basin, southern Kenya Rift: Tectonic and climatic controls. Palaeogeogr. Palaeoclimatol. Palaeoecol. 518, 97–118. https://doi.org/10.1016/j.palaeo.2019.01.017
Owen, R.B., Muiruri, V.M., Lowenstein, T.K., Renaut, R.W., Rabideaux, N., Luo, S., Deino, A.L., Sier, M.J., Dupont-Nivet, G., McNulty, E.P., Leet, K., Cohen, A., Campisano, C.,

Deocampo, D., Shen, C.-C., Billingsley, A., Mbuthia, A., 2018. Progressive aridification in East Africa over the last half million years and implications for human evolution. Proc. Natl. Acad. Sci. 115, 11174–11179. https://doi.org/10.1073/pnas.1801357115
Passey, B.H., Hu, H., Ji, H., Montanari, S., Li, S., Henkes, G.A., Levin, N.E., 2014. Triple oxygen isotopes in biogenic and sedimentary carbonates. Geochim. Cosmochim. Acta 141, 1–25. https://doi.org/10.1016/j.gca.2014.06.006
Petchey, F., Spriggs, M., Bedford, S., Valentin, F., 2015. The chronology of occupation at Teouma, Vanuatu: Use of a modified chronometric hygiene protocol and Bayesian modeling to evaluate midden remains. J. Archaeol. Sci. Reports 4, 95–105. https://doi.org/10.1016/j.jasrep.2015.08.024
Petit, J.R., Jouzel, J., Raynaud, D., Barkov, N.I., Barnola, J.-M., Bassile, I., Bender, M., Chappellaz, J., Davis, M., Delaygue, G., Delmotte, M., Kotlyakov, V.M., Legrand, M., Lipenkov, V.Y., Lorius, C., Ritz, L.P.C., Saltzman, E., Stievenard, M., 1999. Climate and atmospheric history of the past 420,000 years from the Vostock ice core, Antarctica. Nature 399, 429–439.
Phillips, D., Matchan, E.L., 2013. Ultra-high precision $^{40}Ar/^{39}Ar$ ages for Fish Canyon Tuff and Alder Creek Rhyolite sanidine: New dating standards required? Geochim. Cosmochim. Acta 121, 229–239. https://doi.org/10.1016/j.gca.2013.07.003
Pires, M.M., Koch, P.L., Fariña, R.A., de Aguiar, M.A.M., dos Reis, S.F., Guimarães, P.R., 2015. Pleistocene megafaunal interaction networks became more vulnerable after human arrival. Proc. R. Soc. B Biol. Sci. 282. https://doi.org/10.1098/rspb.2015.1367
Porcelli, D., Swarzenski, P., 2003. The Behavior of U- and Th-series Nuclides in Groundwater. Rev. Mineral. Geochemistry 52, 317–361. https://doi.org/10.2113/0520317
Potter, E.K., Stirling, C.H., Wiechert, U.H., Halliday, A.N., Spötl, C., 2005. Uranium-series dating of corals in situ using laser-ablation MC-ICPMS. Int. J. Mass Spectrom. 240, 27–35. https://doi.org/10.1016/j.ijms.2004.10.007
Potts, R., 1998. Variability selection in hominid evolution. Evol. Anthropol. 7, 81–96. https://doi.org/10.1002/(SICI)1520-6505(1998)7:3<81::AID-EVAN3>3.0.CO;2-A
Potts, R., Behrensmeyer, A.K., Faith, J.T., Tryon, C. a, Brooks, A.S., Yellen, J.E., Deino, A.L., Kinyanjui, R., Clark, J.B., Haradon, C.M., Levin, N.E., Meijer, H.J.M., Veatch, E.G., Owen, R.B., Renaut, R.W., 2018. Environmental dynamics during the onset of the Middle Stone Age in eastern Africa. Science (80-.). 90, 86–90. https://doi.org/10.1177/0160017606296731
R Core Team, 2018. R: A language and environment for statistical computing.
Ranhorn, K., Tryon, C.A., 2018. New Radiocarbon Dates from Nasera Rockshelter (Tanzania): Implications for Studying Spatial Patterns in Late Pleistocene Technology. J. African Archaeol. 16, 1–12. https://doi.org/10.1163/21915784-20180011
Reimer, P.J., Bard, E., Bayliss, A., Beck, J.W., Blackwell, P.G., Ramsey, C.B., Buck, C.E., Cheng, H., Edwards, R.L., Friedrich, M., Grootes, P.M., Guilderson, T.P., Haflidason, H., Hajdas, I., Hatté, C., Heaton, T.J., Hoffmann, D.L., Hogg, A.G., Hughen, K.A., Kaiser, K.F., Kromer, B., Manning, S.W., Niu, M., Reimer, R.W., Richards, D.A., Scott, E.M., Southon, J.R., Staff, R.A., Turney, C.S.M., van der Plicht, J., 2013. IntCal13 and Marine13 Radiocarbon Age Calibration Curves 0–50,000 Years cal BP. Radiocarbon 55, 1869–1887. https://doi.org/10.2458/azu_js_rc.55.16947
Renne, P.R., Balco, G., Ludwig, K.R., Mundil, R., Min, K., 2011. Response to the comment by W.H. Schwarz et al. on " Joint determination of ^{40}K decay constants and ^{40}Ar */ ^{40}K for the

Fish Canyon sanidine standard, and improved accuracy for $^{40}Ar/^{39}Ar$ geochronology" by P.R. Renne et al. (2010). Geochim. Cosmochim. Acta 75, 5097–5100. https://doi.org/10.1016/j.gca.2011.06.021
Renne, P.R., Cassata, W.S., Morgan, L.E., 2009. The isotopic composition of atmospheric argon and $^{40}Ar/^{39}Ar$ geochronology: Time for a change? Quat. Geochronol. 4, 288–298. https://doi.org/10.1016/j.quageo.2009.02.015
Renne, P.R., Swisher, C.C., Deino, A.L., Karner, D.B., Owens, T.L., DePaolo, D.J., 1998. Intercalibration of standards, absolute ages and uncertainties in Ar-40/Ar-39 dating (vol 145, pg 117, 1998). Chem. Geol. 149, 259.
Renne, P.R., WoldeGabriel, G., Hart, W.K., Heiken, G., White, T.D., 1999. Chronostratigraphy of the Miocene-Pliocene Sagantole formation, Middle Awash Valley, Afar rift, Ethiopia. Bull. Geol. Soc. Am. 111, 869–885. https://doi.org/10.1130/0016-7606(1999)111<0869:COTMPS>2.3.CO;2
Richards, D.A., Dorale, J.A., 2003. Uranium-Series Chronology and Environmental Applications of Speleothems, in: Bourdon, B., Henderson, G.M., Lundstrom, C., Turner, S. (Eds.), Reviews in Mineralogy and Geochemistry v. 52: Uranium-Series Geochemistry. Washington, D.C., pp. 407–460.
Richards, Z.T., Shen, C.C., Hobbs, J.P.A., Wu, C.C., Jiang, X., Beardsley, F., 2015. New precise dates for the ancient and sacred coral pyramidal tombs of Leluh (Kosrae, Micronesia). Sci. Adv. 1, 1–6. https://doi.org/10.1126/sciadv.1400060
Rivera, T.A., Storey, M., Schmitz, M.D., Crowley, J.L., 2013. Age intercalibration of $^{40}Ar/^{39}Ar$ sanidine and chemically distinct U/Pb zircon populations from the Alder Creek Rhyolite Quaternary geochronology standard. Chem. Geol. 345, 87–98. https://doi.org/10.1016/j.chemgeo.2013.02.021
Rivera, T.A., Storey, M., Zeeden, C., Hilgen, F.J., Kuiper, K., 2011. A refined astronomically calibrated $^{40}Ar/^{39}Ar$ age for Fish Canyon sanidine. Earth Planet. Sci. Lett. 311, 420–426. https://doi.org/10.1016/j.epsl.2011.09.017
Roberts, P., Henshilwood, C.S., Van Niekerk, K.L., Keene, P., Gledhill, A., Reynard, J., Badenhorst, S., Lee-Thorp, J., 2016. Climate, environment and early human innovation: Stable isotope and faunal proxy evidence from archaeological sites (98-59ka) in the southern Cape, South Africa. PLoS One 11, 1–20. https://doi.org/10.1371/journal.pone.0157408
Robinson, J.R., 2017. Thinking locally: Environmental reconstruction of Middle and Later Stone Age archaeological sites in Ethiopia, Kenya, and Zambia based on ungulate stable isotopes. J. Hum. Evol. 106, 19–37. https://doi.org/10.1016/j.jhevol.2017.01.013
Roden, J.S., Ehleringer, J.R., 1999. Observations of Hydrogen and Oxygen Isotopes in Leaf Water Confirm the Craig-Gordon Model under Wide-Ranging Environmental Conditions. Plant Physiol. 120, 1165–1174. https://doi.org/10.1104/pp.120.4.1165
Roullier, C., Benoit, L., McKey, D.B., Lebot, V., 2013. From the Cover: Cozzarelli Prize Winner: Historical collections reveal patterns of diffusion of sweet potato in Oceania obscured by modern plant movements and recombination. Proc. Natl. Acad. Sci. 110, 2205–2210. https://doi.org/10.1073/pnas.1211049110
Sagnotti, L., Scardia, G., Giaccio, B., Liddicoat, J.C., Nomade, S., Renne, P.R., Sprain, C.J., 2014. Extremely rapid directional change during Matuyama-Brunhes geomagnetic polarity reversal. Geophys. J. Int. 199, 1110–1124. https://doi.org/10.1093/gji/ggu287
Schefuß, E., Schouten, S., Schneider, R.R., 2005. Climatic controls on central African hydrology

during the past 20,000 years. Nature 437, 1003–1006. https://doi.org/10.1038/nature03945
Schmidt-Nielsen, K., Kanwisher, J., Lasiewski, R.C., Cohn, J.E., Bretz, W.L., 1969. Temperature regulation and respiration in the ostrich. Condor 71, 341–352.
Sealy, J., Johnson, M., Richards, M., Nehlich, O., 2014. Comparison of two methods of extracting bone collagen for stable carbon and nitrogen isotope analysis : comparing whole bone demineralization with gelatinization and ultra filtration. J. Archaeol. Sci. 47, 64–69. https://doi.org/10.1016/j.jas.2014.04.011
Ségalen, L., Lee-Thorp, J.A., 2009. Palaeoecology of late Early Miocene fauna in the Namib based on $^{13}C/^{12}C$ and $^{18}O/^{16}O$ ratios of tooth enamel and ratite eggshell carbonate. Palaeogeogr. Palaeoclimatol. Palaeoecol. 277, 191–198. https://doi.org/10.1016/j.palaeo.2009.03.018
Segalen, L., Renard, M., Pickford, M., Senut, B., Cojan, I., Le Callonnec, L., Rognon, P., 2002. Environmental and climatic evolution of the Namib Desert since the Middle Miocene: the contribution of carbon isotope ratios in ratite eggshells. Comptes Rendus Geosci. 334, 917–924. https://doi.org/10.1016/S1631-0713(02)01837-0
Shanahan, T.M., Mckay, N.P., Hughen, K.A., Overpeck, J.T., Otto-Bliesner, B., Heil, C.W., King, J., Scholz, C.A., Peck, J., 2015. The time-transgressive termination of the African humid period. Nat. Geosci. 8, 140–144. https://doi.org/10.1038/ngeo2329
Sharp, W., Fylstra, N.D., Tryon, C.A., Faith, J.T., Peppe, D.J., 2016. U-Th burial dating of ostrich eggshell: A new geochronometer for African archaeological sites. Quat. Int. 404, 198–199. https://doi.org/10.1016/j.quaint.2015.08.171
Sharp, W.D., Fylstra, N.D., Tryon, C.A., Faith, T., Peppe, D.J., 2015. U -Th Burial Dates on Ostrich Eggshell, in: American Geophysical Union. San Francisco.
Sharp, W.D., Kahn, J.G., Polito, C.M., Kirch, P. V., 2010. Rapid evolution of ritual architecture in central Polynesia indicated by precise 230Th/U coral dating. Proc. Natl. Acad. Sci. 107, 13234–13239. https://doi.org/10.1073/pnas.1005063107
Sharp, W.D., Tryon, C.A., Niespolo, E.M., Fylstra, N.D., Tripathy-Lang, A., Faith, J.T., n.d. ^{230}Th/U Burial Dating of Ostrich Eggshell. Quat. Sci. Rev.
Sharp, Z., 2007. Principles of Stable Isotope Geochemistry, Pearson Prentice Hal.
Shen, C.C., Li, K.S., Sieh, K., Natawidjaja, D., Cheng, H., Wang, X., Edwards, R.L., Lam, D.D., Hsieh, Y. Te, Fan, T.Y., Meltzner, A.J., Taylor, F.W., Quinn, T.M., Chiang, H.W., Kilbourne, K.H., 2008. Variation of initial 230Th/232Th and limits of high precision U-Th dating of shallow-water corals. Geochim. Cosmochim. Acta 72, 4201–4223. https://doi.org/10.1016/j.gca.2008.06.011
Shen, G.T., Dunbar, R.B., 1995. Environmental controls on uranium in reef corals. Geochim. Cosmochim. Acta 59, 2009–2024. https://doi.org/10.1016/0016-7037(95)00123-9
Shorrocks, B., 2007. The biology of African Savannahs. Oxford.
Short, S.A., Lowson, R.T., Ellis, J., 1988. 234U-238U and ^{230}Th-^{234}U activity ratios in the colloidal phases of aquifers in lateritic weathered zones. Geochim. Cosmochim. Acta 52, 2555–2563. https://doi.org/10.1016/0016-7037(88)90026-9
Simon, J.L., Renne, P.R., Mundil, R., 2008. Implications of pre-eruptive magmatic histories of zircons for U-Pb geochronology of silicic extrusions. Earth Planet. Sci. Lett. 266.
Sinclair, A.R.E., 1978. Factors Affecting the Food Supply and Breeding Season of Resident Birds and Movements of Palaearctic Migrants in a Tropical African Savannah. Ibis (Lond. 1859). 480–497. https://doi.org/10.1016/j.brainres.2015.10.018
Singer, B.S., 2014. A Quaternary geomagnetic instability time scale. Quat. Geochronol. 21, 29–

52.
Steiger, R.H., Jäger, E., 1977. Subcommission on geochronology: Convention on the use of decay constants in geo- and cosmochronology. Earth Planet. Sci. Lett. 36, 359–362. https://doi.org/10.1016/0012-821X(77)90060-7
Stern, L.A., Johnson, G.D., Chamberlain, C.P., 1994. Carbon isotope signature of environmental change found in fossil ratite eggshells from a South Asian Neogene sequence. Geology 22, 419–422.
Sternberg, L.O., Deniro, M.J., Johnson, H.B., 1984. Isotope ratios of cellulose from plants having different photosynthetic pathways. Plant Physiol. 74, 557–61. https://doi.org/10.1104/pp.74.3.557
Sternberg, L.S.L., 1989. Oxygen and hydrogren isotope ratios in plant cellulose: mechanisms and applications, in: Rundel, P.W. (Ed.), Stable Isotopes in Ecological Research. University of California Press, pp. 124–141.
Stirling, C.H., Andersen, M.B., 2009. Uranium-series dating of fossil coral reefs: Extending the sea-level record beyond the last glacial cycle. Earth Planet. Sci. Lett. 284, 269–283. https://doi.org/10.1016/j.epsl.2009.04.045
Suhr, N., Widdowson, M., McDermott, F., Kamber, B.S., 2018. Th/U and U series systematics of saprolite: importance for the oceanic 234U excess. Geochemical Perspect. Lett. 1, 17–22. https://doi.org/10.7185/geochemlet.1803
Taylor, R.E., 1997. Radiocarbon Dating, in: Taylor, R.., Aitken, M.J. (Eds.), Chronometric Dating in Archaeology. Plenum Press, New York, pp. 65–96.
Texier, P.J., Porraz, G., Parkington, J., Rigaud, J.P., Poggenpoel, C., Tribolo, C., 2013. The context, form and significance of the MSA engraved ostrich eggshell collection from Diepkloof Rock Shelter, Western Cape, South Africa. J. Archaeol. Sci. 40, 3412–3431. https://doi.org/10.1016/j.jas.2013.02.021
Thompson, W.G., Spiegelman, M.W., Goldstein, S.L., Speed, R.C., 2003. An open-system model for U-series age determinations of fossil corals. Earth Planet. Sci. Lett. 210, 365–381. https://doi.org/10.1016/S0012-821X(03)00121-3
Tierney, J.E., deMenocal, P.B., Zander, P.D., 2017. A climatic context for the out-of-Africa migration. Geology 45, 1023–1026. https://doi.org/10.1130/G39457.1
Tierney, J.E., Lewis, S.C., Cook, B.I., LeGrande, A.N., Schmidt, G.A., 2011a. Model, proxy and isotopic perspectives on the East African Humid Period. Earth Planet. Sci. Lett. 307, 103–112. https://doi.org/10.1016/j.epsl.2011.04.038
Tierney, J.E., Russell, J.M., Sinninghe Damsté, J.S., Huang, Y., Verschuren, D., 2011b. Late Quaternary behavior of the East African monsoon and the importance of the Congo Air Boundary. Quat. Sci. Rev. 30, 798–807. https://doi.org/10.1016/j.quascirev.2011.01.017
Timmermann, A., Friedrich, T., 2016. Late Pleistocene climate drivers of early human migration. Nature 538, 92–95. https://doi.org/10.1038/nature19365
Tribolo, C., Asrat, A., Bahain, J.-J., Chapon, C., Douville, E., Fragnol, C., Hernandez, M., Hovers, E., Leplongeon, A., Martin, L., Pleurdeau, D., Pearson, O., Puaud, S., Assefa, Z., 2017. Across the Gap: Geochronological and Sedimentological Analyses from the Late Pleistocene-Holocene Sequence of Goda Buticha, Southeastern Ethiopia, Plos One. https://doi.org/10.1371/journal.pone.0169418
Tryon, C.A., n.d. The East African Middle/Later Stone Age transition and cultural dynamics of the Late Pleistocene, Evolutionary Anthropology.
Tryon, C.A., Crevecoeur, I., Faith, J.T., Ekshtain, R., Nivens, J., Patterson, D., Mbua, E.N.,

Spoor, F., 2015. Late Pleistocene age and archaeological context for the hominin calvaria from GvJm-22 (Lukenya Hill, Kenya). Proc. Natl. Acad. Sci. 112, 2682–2687. https://doi.org/10.1073/pnas.1417909112
Tryon, C.A., Faith, J.T., 2016. A demographic perspective on the middle to later stone age transition from nasera rockshelter, Tanzania. Philos. Trans. R. Soc. B Biol. Sci. 371. https://doi.org/10.1098/rstb.2015.0238
Tryon, C.A., Faith, J.T., 2013. Variability in the Middle Stone Age of Eastern Africa. Curr. Anthropol. 54, S234–S254. https://doi.org/10.1023/A:1008961314500
Tryon, C.A., Lewis, J.E., Ranhorn, K., 2019. Excavating the archives: The 1956 excavation of the Late Pleistocene-Holocene sequence at Kisese II (Tanzania), in: Sahle, Y., Reyes-Centeno, H., Bentz., C. (Eds.), Modern Human Origins and Dispersal. Kerns Verlag, Tubingen, pp. 215–238.
Tryon, C.A., Lewis, J.E., Ranhorn, K.L., Kwekason, A., Alex, B., Laird, M.F., Marean, C.W., Niespolo, E., Nivens, J., Mabulla, A.Z.P., 2018. Middle and later stone age chronology of kisese II rockshelter (UNESCO World Heritage Kondoa Rock-Art Sites), Tanzania. PLoS One 13. https://doi.org/10.1371/journal.pone.0192029
Turrin, B.D., Donnelly-Nolan, J.M., Hearn, B.C., 1994. $^{40}Ar/^{39}Ar$ ages from the rhyolite of Alder Creek, California: age of the Cobb Mountain normal-polarity subchron revisited. Geology 22, 251–254. https://doi.org/10.1130/0091-7613(1994)022<0251:AAAFTR>2.3.CO;2
van Breugel, P., Kindt, R., Lillesø, J., Bingham, M., Demissew, S., Dudely, C., Friis, I., Gachathi, F., Kalema, J., Mbago, F., Moshi, H., Muluma, J., Namaganda, M., Ndangalasi, H., Ruffo, C., Vedaste, M., Jamnadass, R., L, G., 2015. Potential Natural Vegetation Map of Eastern Africa (Burundi, Ethiopia, Kenya, Malawi, Rwanda, Tanzania, Uganda and Zambia). Version 2.0. [WWW Document]. For. Landsc. World Agrofor. Cent. (ICRAF).
Verschuren, D., Sinninghe Damsté, J.S., Moernaut, J., Kristen, I., Blaauw, M., Fagot, M., Haug, G.H., 2009. Half-precessional dynamics of monsoon rainfall near the East African Equator. Nature 462, 637–641. https://doi.org/10.1038/nature08520
Vogel, J.C., 1983. Isotopic evidence for the past climates and vegetation of southern Africa. Bothalia 14, 391–394. https://doi.org/10.4102/abc.v14i3/4.1183
Von Schirnding, Y., Van der Merwe, N.J., Vogel, J.C., 1982. Influence of diet and age on carbon isotope ratios in ostrich eggshell 24, 3–20.
Vrba, E.S., 1985. Environment and evolution: alternative cuases of the temporal distribution of evolutionary events. S. Afr. J. Sci. 81, 229–236.
Walter, R., 1996. What is the East Polynesian “Archaic”? A view from the Cook Islands, in: Davidson, J., Irwin, G., Leach, F., Pawley, A., Brown, D. (Eds.), Oceanic Culture History: Essays in Honour of Roger Green. New Zealand Journal of Archaeolgy Special Publication, Dunedin, pp. 513–529.
West, J.B., Sobek, A., Ehleringer, J.R., 2008. A simplified GIS approach to modeling global leaf water isoscapes. PLoS One 3. https://doi.org/10.1371/journal.pone.0002447
Whedon, G.D., Proulx Heaney, R., 2018. Bone. Encycl. Br.
White, F., 1983. The Vegetation of Africa, A Descriptive Memoir to Accompany the UNESCO/AETFAT/UNSO Vegetation Map of Africa. UNESCO, Paris.
Williams, J.B., Siegfried, W.R., Milton, S.J., Adams, N.J., Dean, W.R.J., du Plessis, M.A., Jackson, S., 1993. Field Metabolism , Water Requirements , and Foraging Behavior of Wild Ostriches in the Namib. Ecology 74, 390–404.
Wilmsen, E.N., 2015. Ostrich Eggshells and their beads. South African Archaeol. Bull. 70, 89–

105.
Wilmshurst, J.M., Hunt, T.L., Lipo, C.P., Anderson, A.J., 2011. High-precision radiocarbon dating shows recent and rapid initial human colonization of East Polynesia. Proc. Natl. Acad. Sci. 108, 1815–1820. https://doi.org/10.1073/pnas.1015876108
WoldeGabriel, G., Haile-Selassie, Y., Renne, P.R., Hart, W.K., Ambrose, S.H., Asfaw, B., Heiken, G., White, T., 2001. Geology and palaeontology of the Late Miocene Middle Awash valley, Afar rift, Ethiopia. Nature 412, 175–178. https://doi.org/10.1038/35084058
Wotzlaw, J.F., Hüsing, S.K., Hilgen, F.J., Schaltegger, U., 2014. High-precision zircon U-Pb geochronology of astronomically dated volcanic ash beds from the Mediterranean Miocene. Earth Planet. Sci. Lett. 407, 19–34. https://doi.org/10.1016/j.epsl.2014.09.025
Yanase, N., Sekine, K., Payne, T.E., 1995. Groundwater geochemistry in the Koongarra ore deposit, Australia (II): Activity ratios and migration mechanisms of uranium series radionuclides. Geochem. J. 29, 31–54. https://doi.org/10.2343/geochemj.29.31
Yonekura, N., Ishii, T., Saito, Y., Maeda, Y., Matsushima, Y., Matsumoto, E., Kayanne, H., 1988. Holocene fringing reefs and sea-level change in Mangaia Island, Southern Cook Islands. Palaeogeogr. Palaeoclimatol. Palaeoecol. 68, 177–188. https://doi.org/10.1016/0031-0182(88)90038-7
Ziegler, M., Simon, M.H., Hall, I.R., Barker, S., Stringer, C., Zahn, R., 2013. Development of Middle Stone Age innovation linked to rapid climate change. Nat. Commun. 4, 1905–1909. https://doi.org/10.1038/ncomms2897

Appendix A: Supplementary Figures for Chapter 1

Supplementary Tables

Supplementary Table 1.1. Table of all $^{40}Ar/^{39}Ar$ data. Provided as Supplementary File 1.1

Supplementary Figures

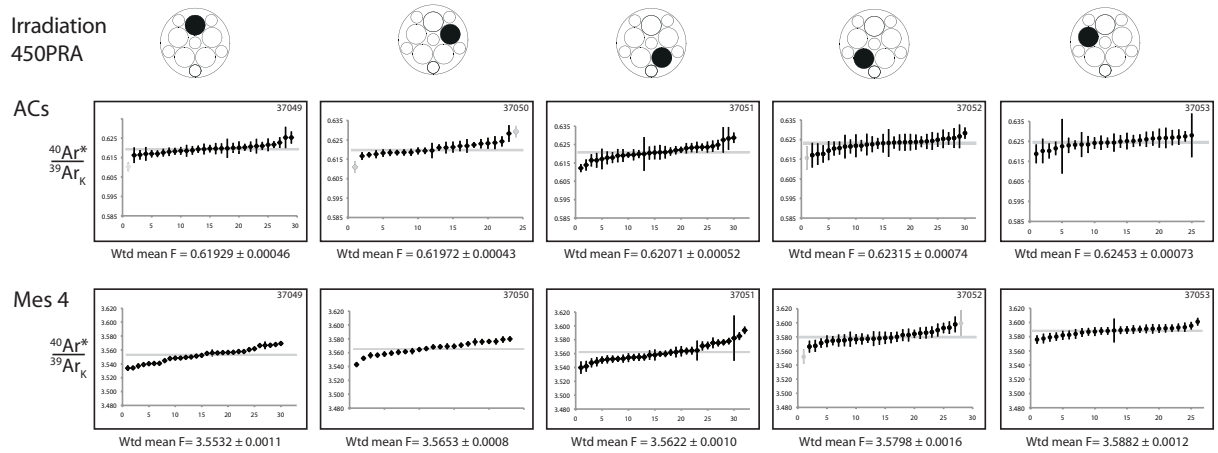

Figure A.1. F-values of all samples included in the weighted mean F-value for each pit (highlighted in black above its respective column) from irradiation 450PRA. Samples displayed in light gray were excluded from the weighted mean due to nMAD>3.

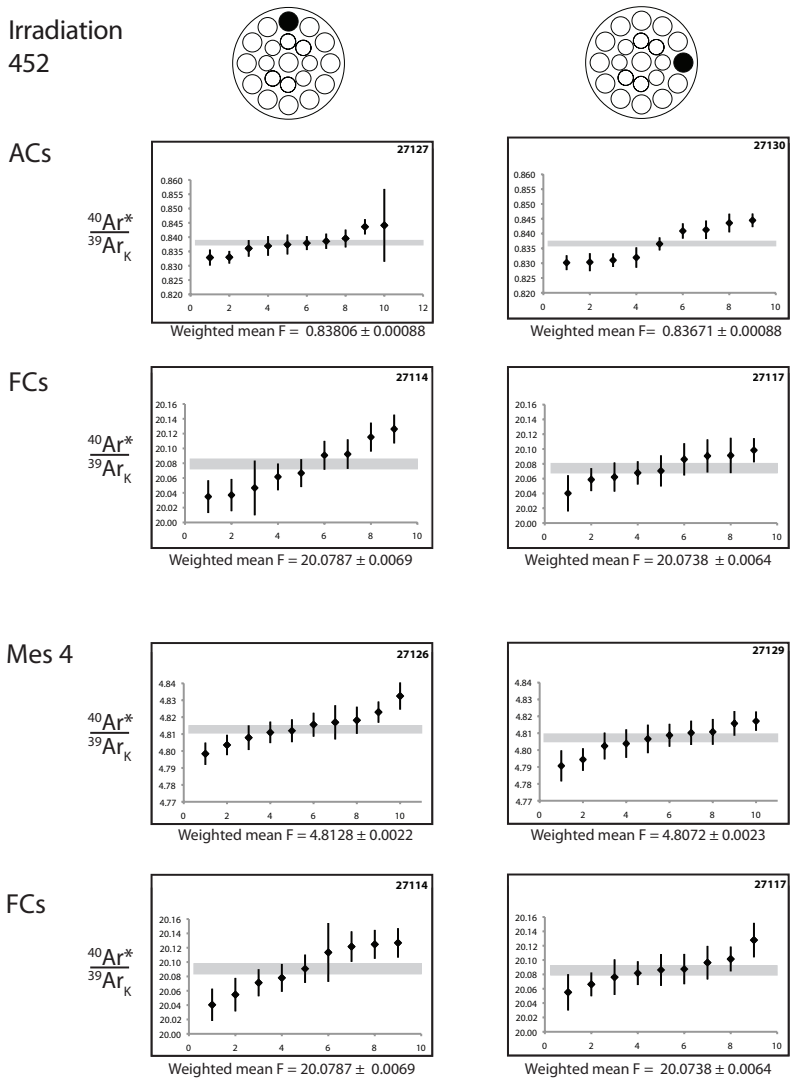

Figure A.2. F-values for samples from irradiation 452A. FCs results are plotted twice to show reduction of FCs with respect to the paired unknown displayed above it. Weighted mean F values for FCs from this irradiation reported in Table 1.3 are based on the reduction of FCs compared with ACs.

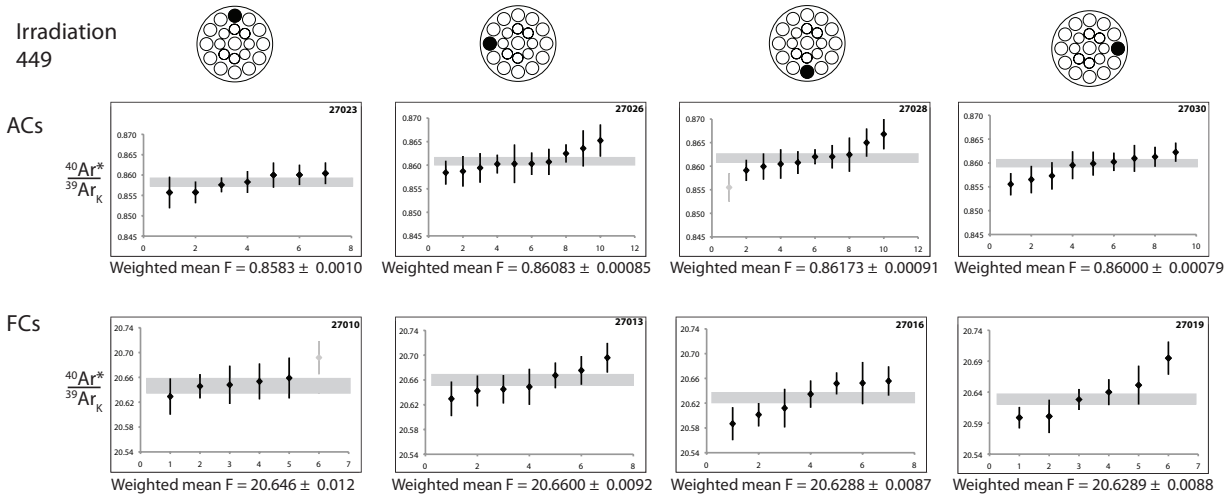

Figure A.3. F-values for samples from irradiation 449. Samples displayed in light gray were excluded from the weighted mean due to nMAD>3.

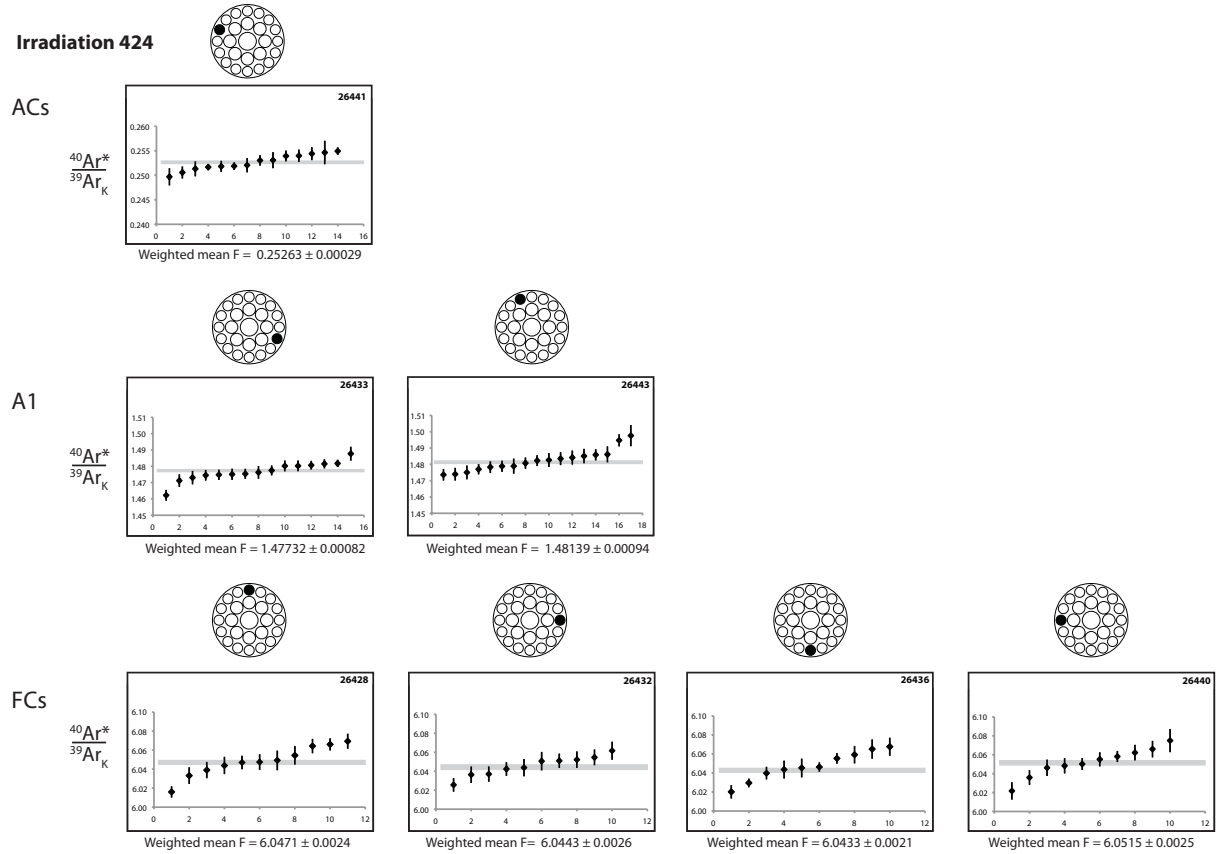

Figure A.4. F-values for samples from irradiation 424 plotted with the appropriate FCs reduction. Weighted mean F values for FCs from this irradiation reported in Table 1.3 are based on the reduction of FCs compared with ACs and A1.

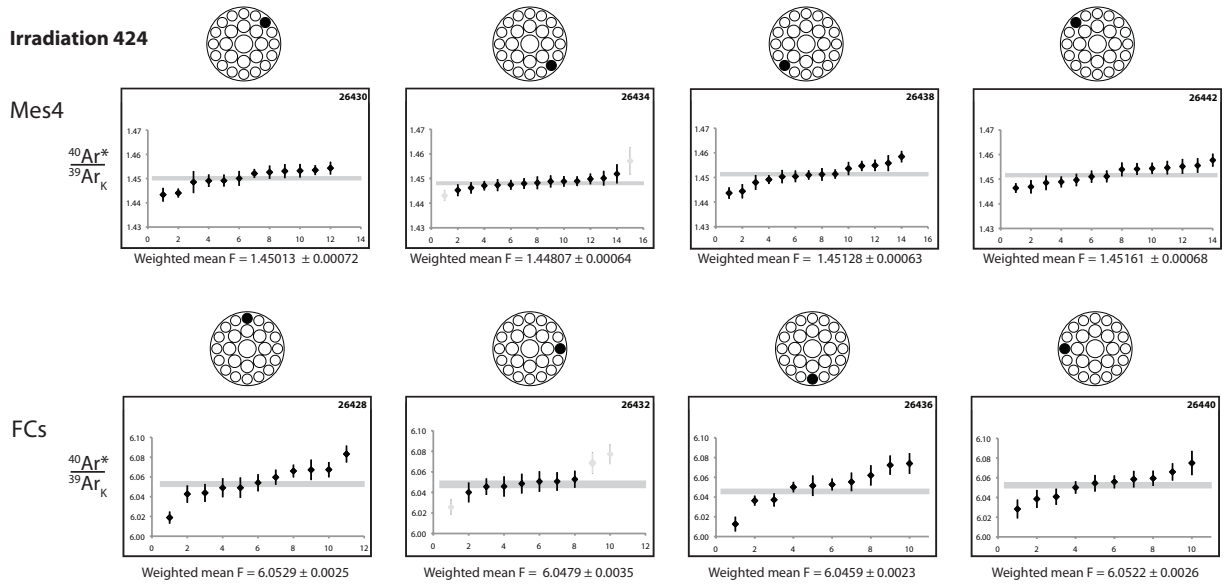

Figure A.5. F-values for Mes4 and FCs samples from irradiation 424 plotted with the appropriate FCs reduction.

a.

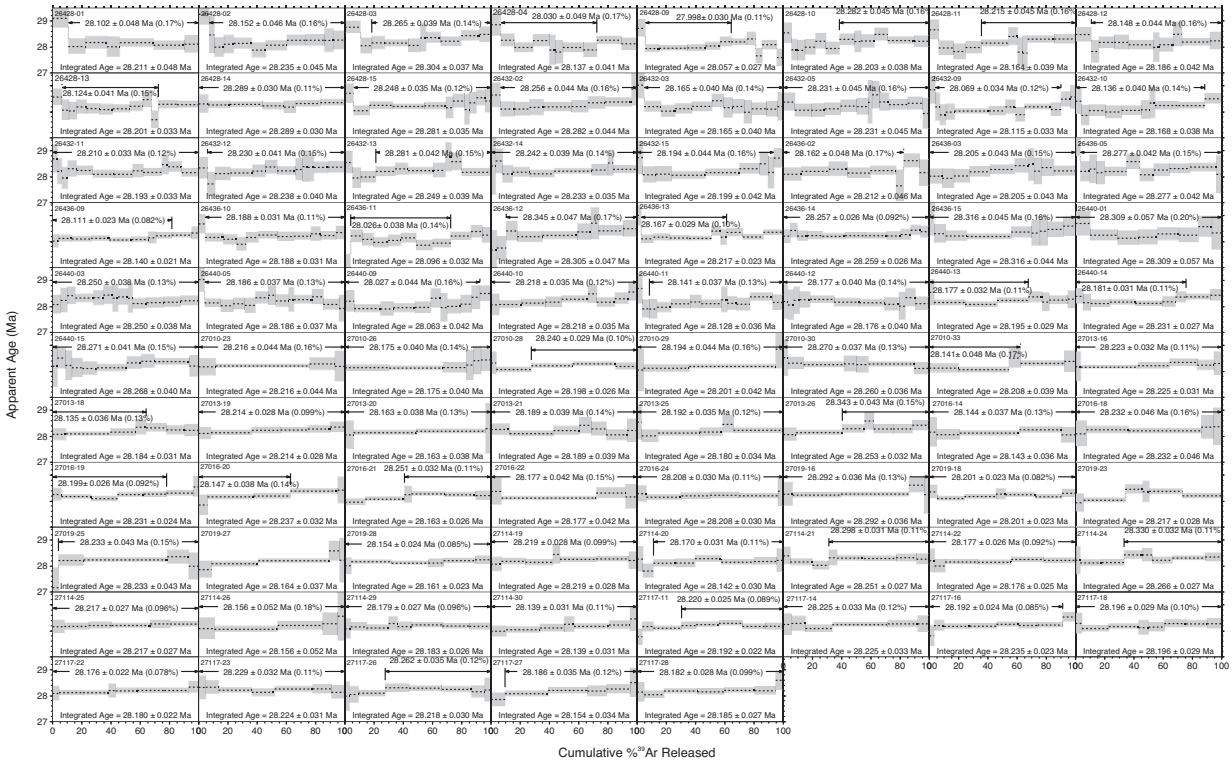

b.

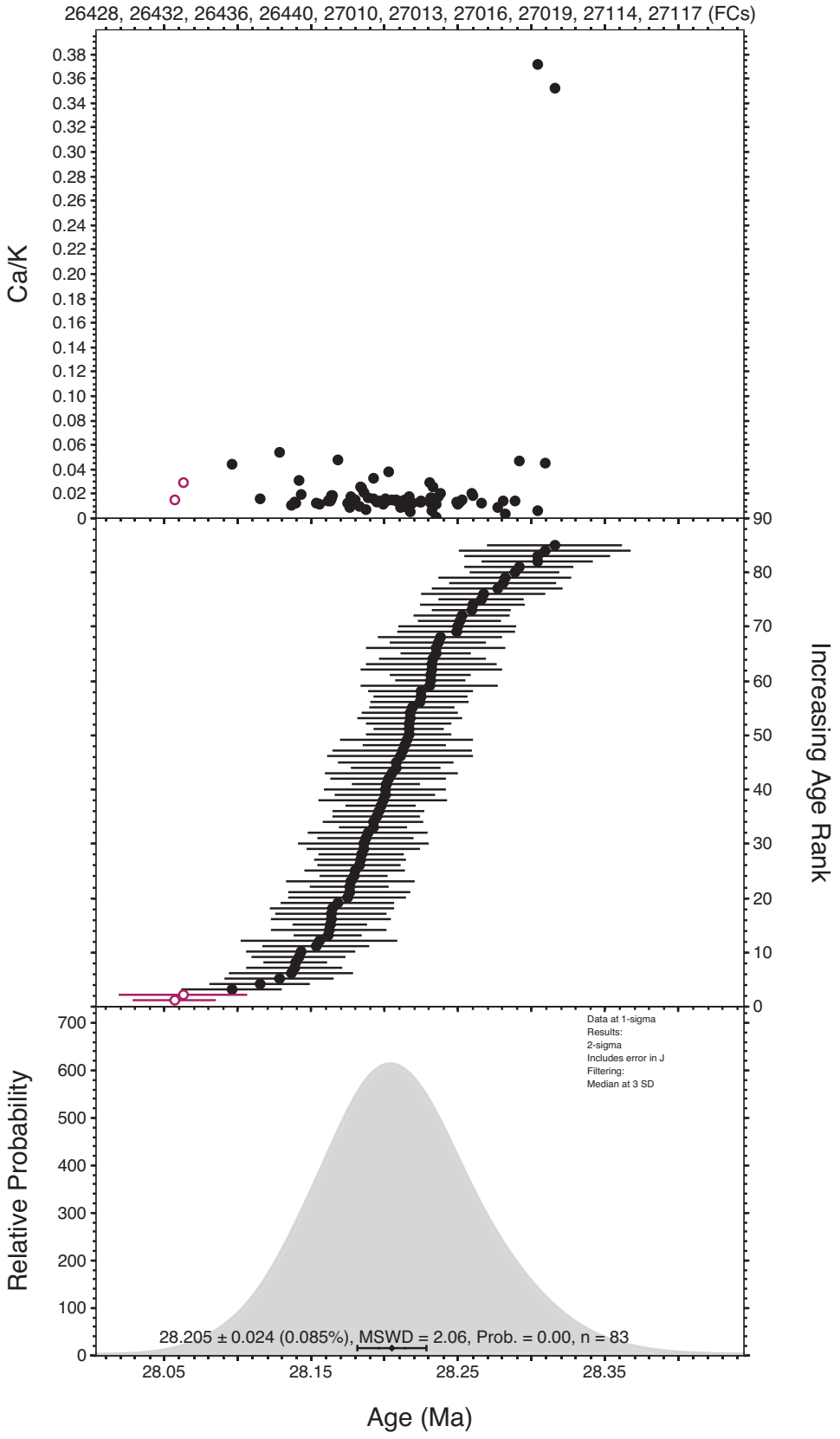
26428, 26432, 26436, 26440, 27010, 27013, 27016, 27019, 27114, 27117 (FCs)
Ca/K
Increasing Age Rank
Relative Probability
Data at 1-sigma
Results:
2-sigma
Includes error in J
Filtering:
Median at 3 SD
28.205 ± 0.024 (0.085%), MSWD = 2.06, Prob. = 0.00, n = 83
Age (Ma)

c.

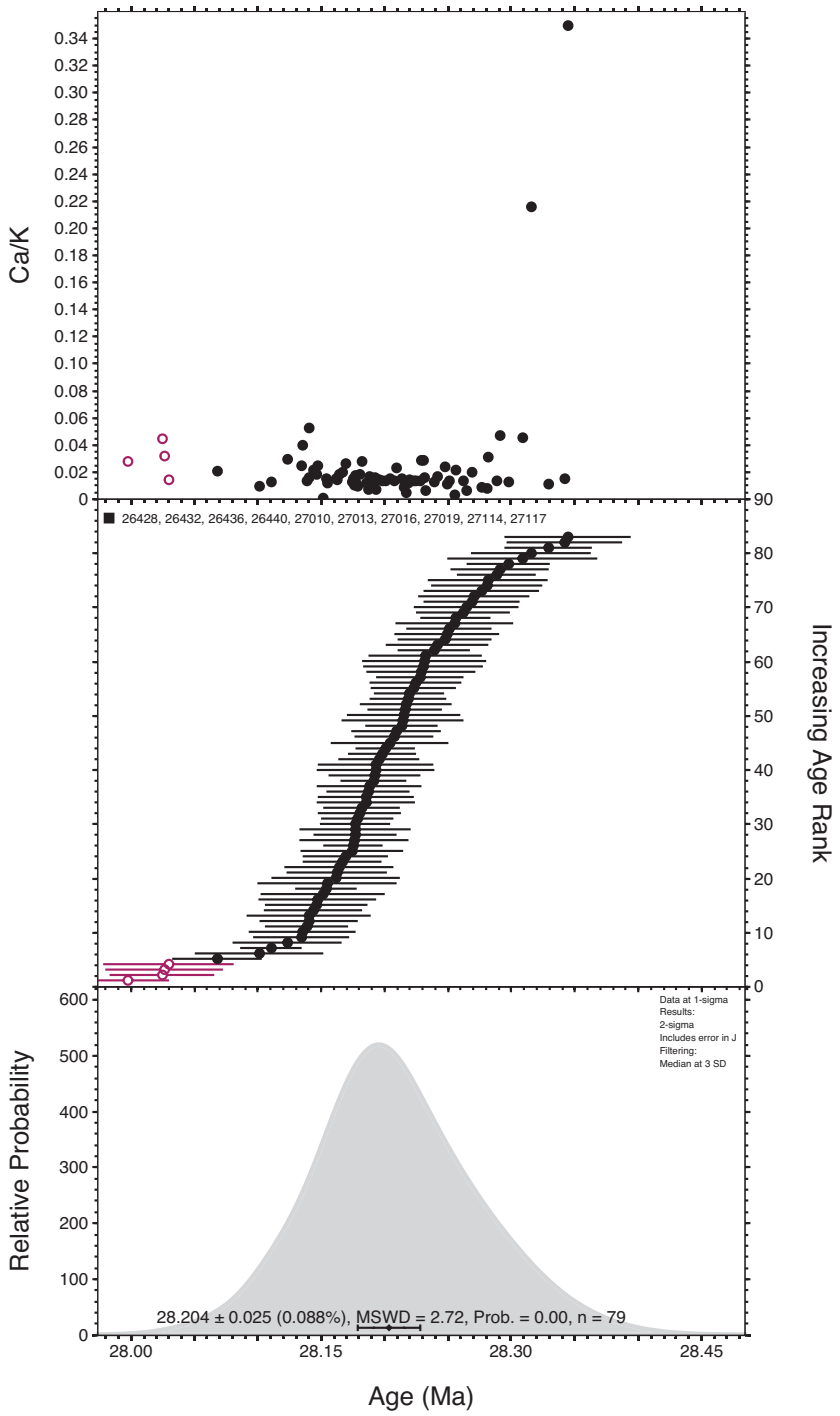

Figure A.6. Age results for FCs analyses on Noblesse. a) Step heating spectra for FCs analyses on Noblesse; b) probability distribution function of integrated ages of FC; c) probability distribution function of plateau ages of FCs yielding the same weighted mean age of FCs as the integrated ages. Figures b) and c) show results in the center plot at 2σ uncertainty, while the weighted mean of the probability distribution function in the lowest plot is presented with ±1σ uncertainty. Outliers (in red) were omitted based on nMAD > 3 filter.

a.

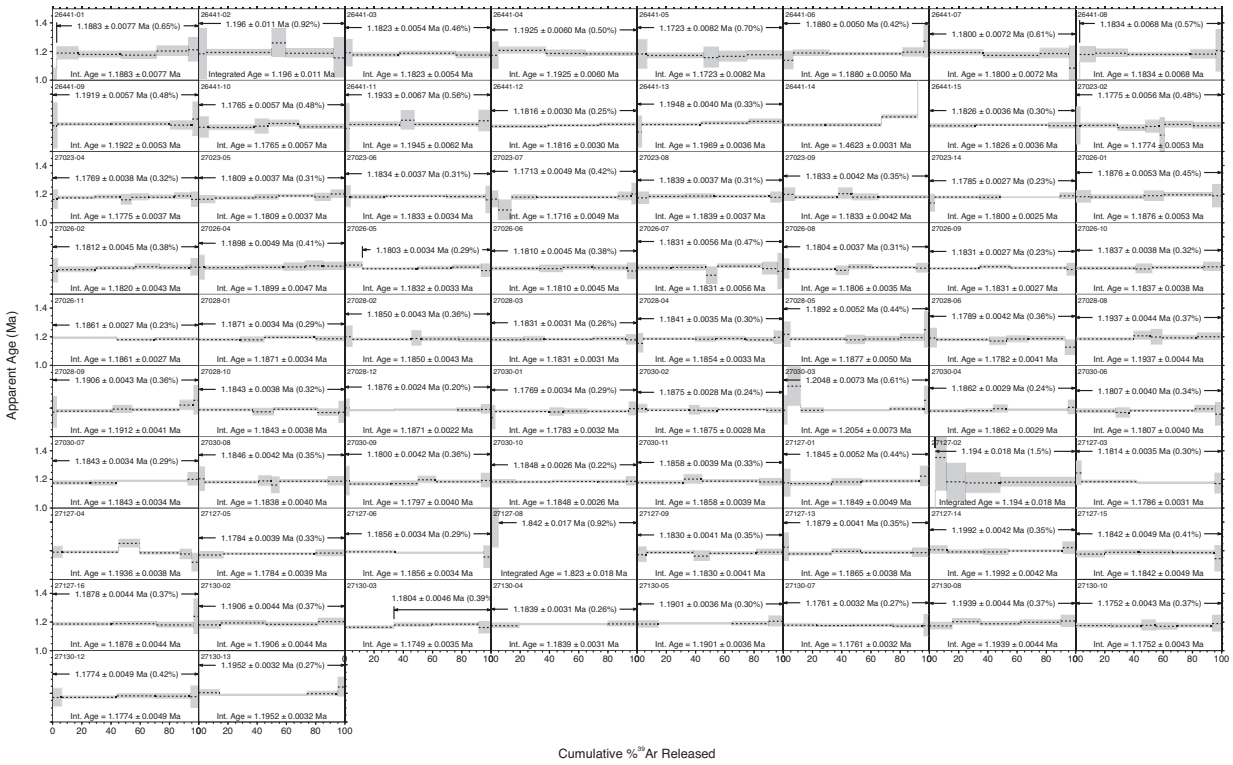
26441-01
1.1883 ± 0.0077 Ma (0.65%)
Int. Age = 1.1883 ± 0.0077 Ma
26441-02
1.196 ± 0.011 Ma (0.92%)
Integrated Age = 1.196 ± 0.011 Ma
26441-03
1.1823 ± 0.0054 Ma (0.46%)
Int. Age = 1.1823 ± 0.0054 Ma
26441-04
1.1925 ± 0.0060 Ma (0.50%)
Int. Age = 1.1925 ± 0.0060 Ma
26441-05
1.1723 ± 0.0082 Ma (0.70%)
Int. Age = 1.1723 ± 0.0082 Ma
26441-06
1.1880 ± 0.0050 Ma (0.42%)
Int. Age = 1.1880 ± 0.0050 Ma
26441-07
1.1800 ± 0.0072 Ma (0.61%)
Int. Age = 1.1800 ± 0.0072 Ma
26441-08
1.1834 ± 0.0068 Ma (0.57%)
Int. Age = 1.1834 ± 0.0068 Ma
26441-09
1.1919 ± 0.0057 Ma (0.48%)
Int. Age = 1.1922 ± 0.0053 Ma
26441-10
1.1765 ± 0.0057 Ma (0.48%)
Int. Age = 1.1765 ± 0.0057 Ma
26441-11
1.1933 ± 0.0067 Ma (0.56%)
Int. Age = 1.1945 ± 0.0062 Ma
26441-12
1.1816 ± 0.0030 Ma (0.25%)
Int. Age = 1.1816 ± 0.0030 Ma
26441-13
1.1948 ± 0.0040 Ma (0.33%)
Int. Age = 1.1969 ± 0.0036 Ma
26441-14
Int. Age = 1.4623 ± 0.0031 Ma
26441-15
1.1826 ± 0.0036 Ma (0.30%)
Int. Age = 1.1826 ± 0.0036 Ma
27023-02
1.1775 ± 0.0056 Ma (0.48%)
Int. Age = 1.1774 ± 0.0053 Ma
27023-04
1.1769 ± 0.0038 Ma (0.32%)
Int. Age = 1.1775 ± 0.0037 Ma
27023-05
1.1809 ± 0.0037 Ma (0.31%)
Int. Age = 1.1809 ± 0.0037 Ma
27023-06
1.1834 ± 0.0037 Ma (0.31%)
Int. Age = 1.1833 ± 0.0034 Ma
27023-07
1.1713 ± 0.0049 Ma (0.42%)
Int. Age = 1.1716 ± 0.0049 Ma
27023-08
1.1839 ± 0.0037 Ma (0.31%)
Int. Age = 1.1839 ± 0.0037 Ma
27023-09
1.1833 ± 0.0042 Ma (0.35%)
Int. Age = 1.1833 ± 0.0042 Ma
27023-14
1.1785 ± 0.0027 Ma (0.23%)
Int. Age = 1.1800 ± 0.0025 Ma
27026-01
1.1876 ± 0.0053 Ma (0.45%)
Int. Age = 1.1876 ± 0.0053 Ma
27026-02
1.1812 ± 0.0045 Ma (0.38%)
Int. Age = 1.1820 ± 0.0043 Ma
27026-04
1.1898 ± 0.0049 Ma (0.41%)
Int. Age = 1.1899 ± 0.0047 Ma
27026-05
1.1803 ± 0.0034 Ma (0.29%)
Int. Age = 1.1832 ± 0.0033 Ma
27026-06
1.1810 ± 0.0045 Ma (0.38%)
Int. Age = 1.1810 ± 0.0045 Ma
27026-07
1.1831 ± 0.0056 Ma (0.47%)
Int. Age = 1.1831 ± 0.0056 Ma
27026-08
1.1804 ± 0.0037 Ma (0.31%)
Int. Age = 1.1806 ± 0.0035 Ma
27026-09
1.1831 ± 0.0027 Ma (0.23%)
Int. Age = 1.1831 ± 0.0027 Ma
27026-10
1.1837 ± 0.0038 Ma (0.32%)
Int. Age = 1.1837 ± 0.0038 Ma
27026-11
1.1861 ± 0.0027 Ma (0.23%)
Int. Age = 1.1861 ± 0.0027 Ma
27028-01
1.1871 ± 0.0034 Ma (0.29%)
Int. Age = 1.1871 ± 0.0034 Ma
27028-02
1.1850 ± 0.0043 Ma (0.36%)
Int. Age = 1.1850 ± 0.0043 Ma
27028-03
1.1831 ± 0.0031 Ma (0.26%)
Int. Age = 1.1831 ± 0.0031 Ma
27028-04
1.1841 ± 0.0035 Ma (0.30%)
Int. Age = 1.1854 ± 0.0033 Ma
27028-05
1.1892 ± 0.0052 Ma (0.44%)
Int. Age = 1.1877 ± 0.0050 Ma
27028-06
1.1789 ± 0.0042 Ma (0.36%)
Int. Age = 1.1782 ± 0.0041 Ma
27028-08
1.1937 ± 0.0044 Ma (0.37%)
Int. Age = 1.1937 ± 0.0044 Ma
27028-09
1.1906 ± 0.0043 Ma (0.36%)
Int. Age = 1.1912 ± 0.0041 Ma
27028-10
1.1843 ± 0.0038 Ma (0.32%)
Int. Age = 1.1843 ± 0.0038 Ma
27028-12
1.1876 ± 0.0024 Ma (0.20%)
Int. Age = 1.1871 ± 0.0022 Ma
27030-01
1.1769 ± 0.0034 Ma (0.29%)
Int. Age = 1.1783 ± 0.0032 Ma
27030-02
1.1875 ± 0.0028 Ma (0.24%)
Int. Age = 1.1875 ± 0.0028 Ma
27030-03
1.2048 ± 0.0073 Ma (0.61%)
Int. Age = 1.2054 ± 0.0073 Ma
27030-04
1.1862 ± 0.0029 Ma (0.24%)
Int. Age = 1.1862 ± 0.0029 Ma
27030-06
1.1807 ± 0.0040 Ma (0.34%)
Int. Age = 1.1807 ± 0.0040 Ma
27030-07
1.1843 ± 0.0034 Ma (0.29%)
Int. Age = 1.1843 ± 0.0034 Ma
27030-08
1.1846 ± 0.0042 Ma (0.35%)
Int. Age = 1.1838 ± 0.0040 Ma
27030-09
1.1800 ± 0.0042 Ma (0.36%)
Int. Age = 1.1797 ± 0.0040 Ma
27030-10
1.1848 ± 0.0026 Ma (0.22%)
Int. Age = 1.1848 ± 0.0026 Ma
27030-11
1.1858 ± 0.0039 Ma (0.33%)
Int. Age = 1.1858 ± 0.0039 Ma
27127-01
1.1845 ± 0.0052 Ma (0.44%)
Int. Age = 1.1849 ± 0.0049 Ma
27127-02
1.194 ± 0.018 Ma (1.5%)
Integrated Age = 1.194 ± 0.018 Ma
27127-03
1.1814 ± 0.0035 Ma (0.30%)
Int. Age = 1.1786 ± 0.0031 Ma
27127-04
Int. Age = 1.1936 ± 0.0038 Ma
27127-05
1.1784 ± 0.0039 Ma (0.33%)
Int. Age = 1.1784 ± 0.0039 Ma
27127-06
1.1856 ± 0.0034 Ma (0.29%)
Int. Age = 1.1856 ± 0.0034 Ma
27127-08
1.842 ± 0.017 Ma (0.92%)
Integrated Age = 1.823 ± 0.018 Ma
27127-09
1.1830 ± 0.0041 Ma (0.35%)
Int. Age = 1.1830 ± 0.0041 Ma
27127-13
1.1879 ± 0.0041 Ma (0.35%)
Int. Age = 1.1865 ± 0.0038 Ma
27127-14
1.1992 ± 0.0042 Ma (0.35%)
Int. Age = 1.1992 ± 0.0042 Ma
27127-15
1.1842 ± 0.0049 Ma (0.41%)
Int. Age = 1.1842 ± 0.0049 Ma
27127-16
1.1878 ± 0.0044 Ma (0.37%)
Int. Age = 1.1878 ± 0.0044 Ma
27130-02
1.1906 ± 0.0044 Ma (0.37%)
Int. Age = 1.1906 ± 0.0044 Ma
27130-03
1.1804 ± 0.0046 Ma (0.39%)
Int. Age = 1.1749 ± 0.0035 Ma
27130-04
1.1839 ± 0.0031 Ma (0.26%)
Int. Age = 1.1839 ± 0.0031 Ma
27130-05
1.1901 ± 0.0036 Ma (0.30%)
Int. Age = 1.1901 ± 0.0036 Ma
27130-07
1.1761 ± 0.0032 Ma (0.27%)
Int. Age = 1.1761 ± 0.0032 Ma
27130-08
1.1939 ± 0.0044 Ma (0.37%)
Int. Age = 1.1939 ± 0.0044 Ma
27130-10
1.1752 ± 0.0043 Ma (0.37%)
Int. Age = 1.1752 ± 0.0043 Ma
27130-12
1.1774 ± 0.0049 Ma (0.42%)
Int. Age = 1.1774 ± 0.0049 Ma
27130-13
1.1952 ± 0.0032 Ma (0.27%)
Int. Age = 1.1952 ± 0.0032 Ma
Apparent Age (Ma)
Cumulative %39Ar Released

b.

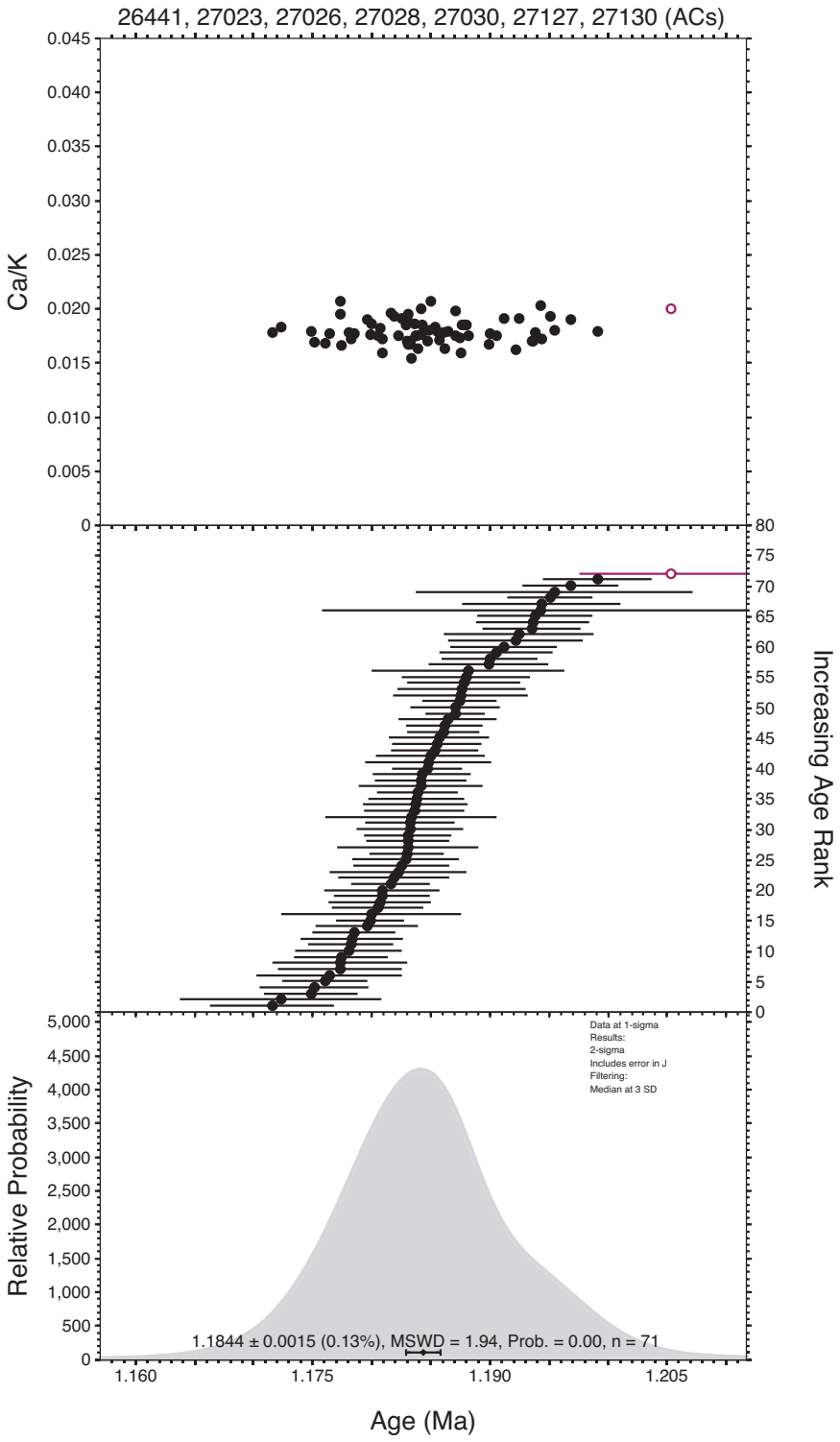
26441, 27023, 27026, 27028, 27030, 27127, 27130 (ACs)
Ca/K
Increasing Age Rank
Relative Probability
Data at 1-sigma
Results:
2-sigma
Includes error in J
Filtering:
Median at 3 SD
1.1844 ± 0.0015 (0.13%), MSWD = 1.94, Prob. = 0.00, n = 71
Age (Ma)

c.

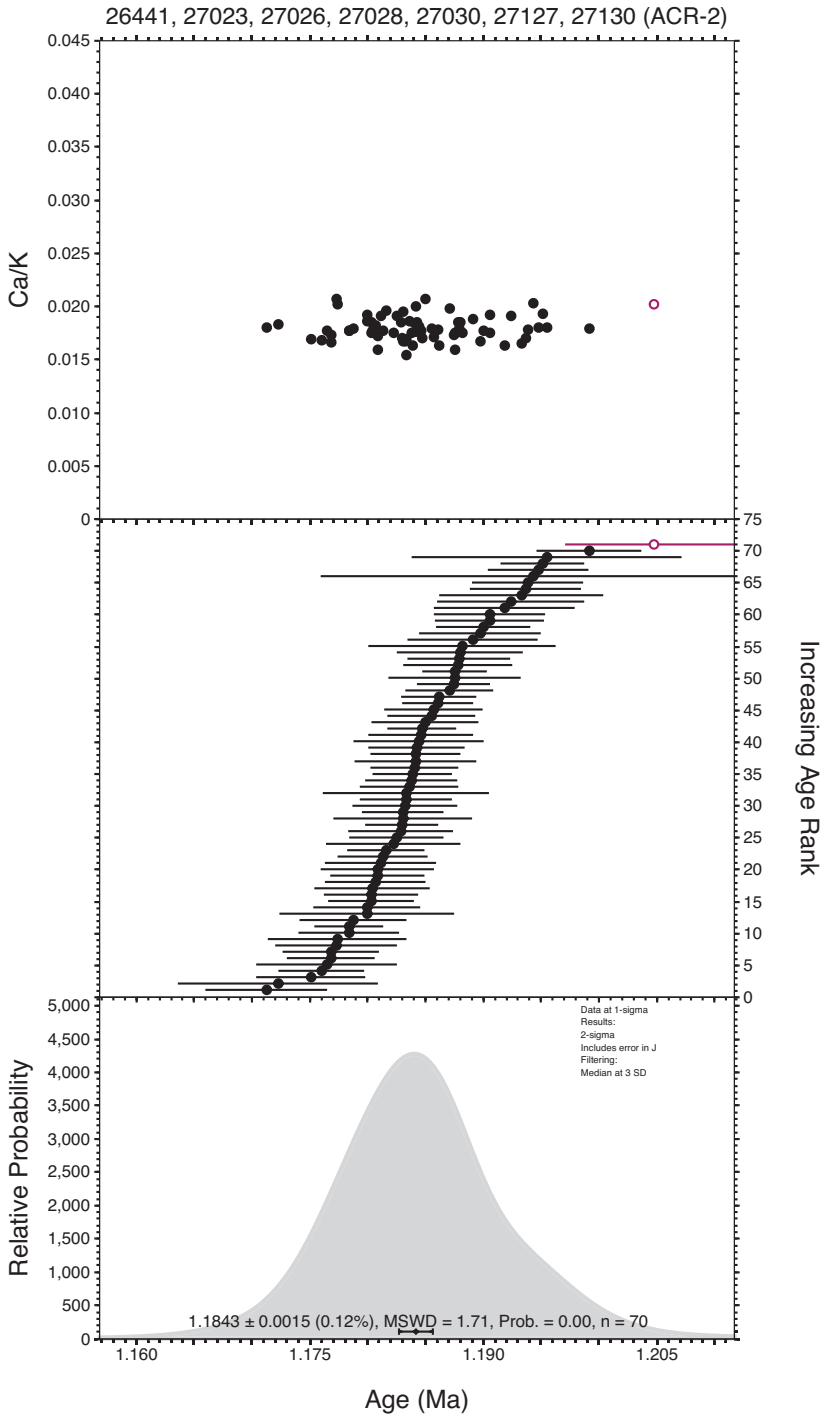

Figure A.7. Age results for ACs analyses on Noblesse. a) Step heating spectra for ACs analyses on Noblesse; b) probability distribution function of integrated ages of ACs with omitted points in red (gray in grayscale); c) probability distribution function of plateau ages of ACs yielding the same weighted mean age of ACs as the integrated ages. Figures b) and c) show results in the center plot at 2σ uncertainty, while the weighted mean of the probability distribution function in the lowest plot is presented with ±1σ uncertainty. Outliers (in red) were omitted based on nMAD > 3 filter.

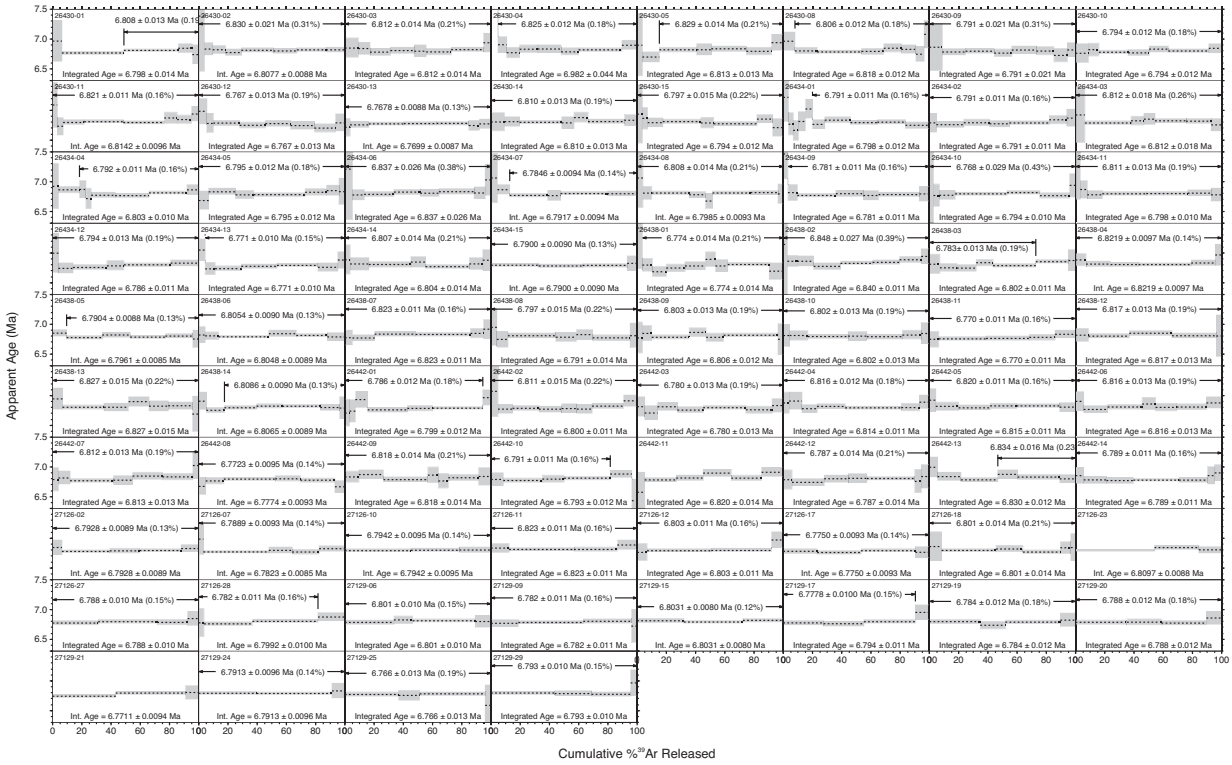

A.8. Step heating spectra for Mes4 analyses on Noblesse.

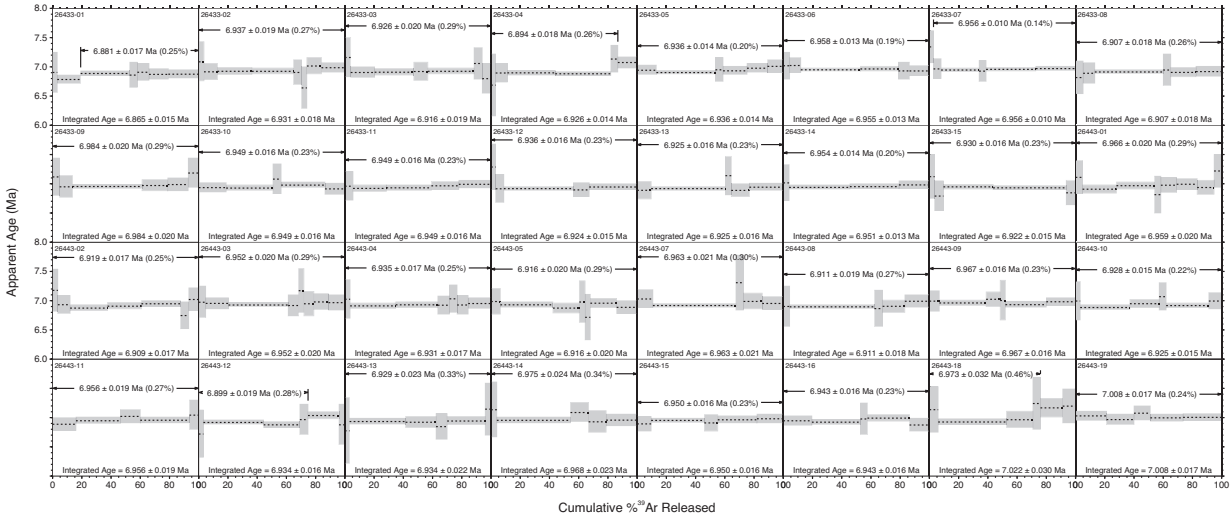

Figure A.9. Step heating spectra for A1 analyses on Noblesse.

Appendix B: Supplementary Materials for Chapter 2

B.1: Background: Formation of eggshell and preservation of OES structures in deep time

Unlike bone, eggshell is extremely stable in the semi-arid to arid climates for ~10^6 years because of their composition and structure and they are unlikely to undergo diagenesis (i.e., fossilization) under many geologic conditions. During eggshell mineralization, Organic cores (also called mammillary knobs) aggregate to coat the albumen surfaces to provide the framework for calcite mineral nucleation; calcite growth continues around and upon organic proteinaceous hexagonal-web structures to create the mammillary cone and palisade crystal layers of the eggshell internal to OES surfaces (e.g., Mikhailov, 1997; Nys et al., 1999). In the crystalline (calcite) layers, the total organic fraction is composed mainly of the glycoproteins and proteoglycans (Nys et al., 1999, and references therein) and is referred to here as the total organic fraction (TOF) extracted from the calcite matrix for C and N isotopic analysis. Resultant intra-crystalline organics remain protected by calcite crystals in deep time (Crisp et al., 2013; Dauphin and Senut, 1998; Demarchi et al., 2016; Mikhailov, 1997; Miller and Fogel, 2016; Nys et al., 2004), and petrographic study has revealed OES ranging from ~30 to > 300 ka preserve primary calcite mineral structures formed during biomineralization, including samples from this study (Figure B.1; Niespolo et al., 2017a; Niespolo et al., 2017b; Niespolo et al., 2018). Decalcified modern OES fragments preserve a completely intact organic pseudomorph (also called a protein ghost) demonstrating these intra-crystalline organic web structures (Miller and Fogel, 2016). The outer ~50 μm thick vertical crystal layer is mineralized last with only a nanocrystalline film of hydroxyapatite covering the outer surface of the OES, possibly linked to cessation of eggshell mineralization in the avian oviduct (Hincke et al., 1995; Nys et al., 2004). During sample preparation, some the surface layers are removed as they are contaminated with detritus upon deposition. Below is the protocol recommended for sampling both the calcite and TOF of ostrich eggshell for online mass spectrometric analysis.

B.2: Methods: Sample Preparation Protocol

~300 mg OES shell fragments are mechanically abraded on all surfaces with a Dremel hand drill and then cleaned under sonication in millipore water. Samples are dried and weighed, and then 20-30 wt.% of the sample is leached in 1N HCl. The remaining sample is rinsed in millipore water and dried. In early tests of the protocol, on the first modern OES tests and the Lukenya Hill samples, the remaining leached OES sample was crushed, and any remaining visibly dirty particles associated with detritus-filled pores (serving as oxygen pathways for incubating chicks; (Mikhailov, 1997) were picked out with forceps. A small fraction (~μg) of the clean crushed fraction was sampled to analyze the C isotope composition of calcite. In attempting to yield more organic material from each sample, we modified the protocol such that additional modern OES samples and all Kisese II samples are instead left intact after leaching, and visibly detritus-rich pores were drilled out with a steel bur Dremel bit. A ~sub-mg size sample is also drilled out in cross section of the leached OES fragment for isotopic analysis of the calcite fraction, ensuring that the sampled calcite represented a homogenized sample of the

eggshell after leaching, primarily derived from the palisade layer crystals. On modern OES, 0.25 to 1N HCl acid baths were tested based on different bone collagen extraction protocols (Sealy et al., 2014), where gentle acid cleaning has been recommended to preserve collagen structures in bone organic matrix. After modern OES study, we determined that the remaining leached fraction of ancient OES would be immersed in 1N HCl until all calcite is removed. After dissolution, the TOF is rinsed and centrifruged repeatedly to reduce the pH to near-neutral levels and then freeze-dried. The TOF is then weighed and packed in tin capsules for mass spectrometric analysis.

B.3: Results: Protocol testing on Modern OES

Results from the modern OES TOF extraction protocol tests are presented in Table Z. We expect pristine OES collagen to have C:N ratios of ~2.9 – 3.6 (Ambrose, 1990; DeNiro, 1985; Deniro and Weiner, 1988). Yields of OES collagen ranged from ~ 0.1-1.3 wt.% of TOF (Supplementary Table 1) with C:N ratios ranging from ~3.3 – 3.5 for samples not treated with NaOH (Table B.1). This is partially due to the heterogeneous distribution of collagen in OES. A disproportionate amount of collagen forms the organic cores, inner and outer membranes, and an outer cuticle layer all which quickly degrade in a soil environment. All of these components would nevertheless be removed during the 30wt.% chemical leaching. We did not assess TOF preservation with wt% C and N yields because bone collagen studies have demonstrated that this is not a significant quality criterion compared to compositional and isotopic preservation indicators and preservation of C:N (Sealy et al., 2014).

After full dissolution of the calcite matrix, a few of the modern OES test samples were also rinsed with 0.1N NaOH, which is commonly used in some bone collagen extraction protocols in order to remove humic acids acquired during the burial lifetime of a sample (Ambrose, 1990; Chisholm et al., 1983; Sealy et al., 2014). We don't expect to have any humic acids in the modern OES since they have never been buried, so this procedure tests if NaOH affects the C:N and isotopic composition of TOF significantly; indeed, we find significant differences in TOF yields and composition (Figure B.2) in modern OES treated with NaOH compared to those not treated with NaOH, with elevated C:N ratios reflecting N loss. One NaOH-treated sample (OES 7, C:N ratio = 92.45) demonstrated isotopic fractionation outside of the expected range between the average $\delta^{13}C_{calcite}$ value of the modern OES and its $\delta^{13}C_{TOF}$ value ($\Delta^{13}C_{calcite\text{-}TOF}$ = 19.81), and its N content was so depleted that there was not enough TOF left to measure N isotopes in the IRMS. The other NaOH-treated samples had to be combined with their most similarly-treated replicates to have enough TOF to measure; one of these returned a $\delta^{15}N$ value ~2‰ lower than all other analyses (OES2/3, C:N ratio = 4.86, $\Delta^{13}C_{calcite\text{-}TOF}$ = 13.82), which is considered to be even outside of the ~1‰ range considered as acceptable variation for different samples from animals feeding on the same controlled diet (e.g., Deniro and Schoeniger, 1983). OES 9/10 (C:N ratio = 3.67, $\Delta^{13}C_{calcite\text{-}TOF}$ = 14.02) was combined because OES 9 had almost no remaining TOF, even though they were treated with the exact same protocol; hence, this combined sample is mostly representative of OES10, and while the combined sample returned seemingly reproducible isotope data, these two samples nevertheless demonstrate the lack of reproducibility of TOF yields in samples treated with NaOH. (Jørkov et al., 2007) saw similarly disparate results between bone collagen extraction protocols that differed by the use of NaOH or other additional steps such as ultra-filtration, which separates organic molecules by weight in order to measure only the heaviest molecules from gelatinized bone collagen and is

commonly applied to AMS ^{14}C dating samples (Sealy et al., 2014). Many experiments testing the use of NaOH on bone collagen have shown that with well-preserved samples, protocol differences should not greatly affect the samples' isotope ratios, but since ~30% of the dry weight of bone is organic and comprised mainly of collagen (Whedon and Proulx Heaney, 2018), perhaps small losses of material due to NaOH treatment does not significantly perturb the isotopic measurements of preserved, extracted collagen due to simple mass balance. Instead, with such little collagen (or TOF) to begin with in OES, even a small loss of TOF due to NaOH treatment appears to have a large effect on elemental and isotopic preservation. Furthermore, numerous studies employing amino acid racemization (AAR) to ostrich and other ratite eggshell demonstrate the long-term preservation of collagen (Brooks et al., 1990; Miller and Brigham-grette, 1989), especially of essential amino acids, even during prolonged heating experiments (Johnson et al., 1998; Miller et al., 2016). While OES collagen and organic matter appear to be well-protected from diagenesis over geologic timescales at least of order ~10^5 a, the low abundance of primary organic matter in OES and lower yields (relatively ~10-40%) require that large initial sample sizes (~300 mg) be used to produce sufficient collagen for measurement. The most efficient protocol producing the best yields of collagen was that conducted on OES 5 and OES 8 and so this was the protocol used on all ancient samples and further modern OES samples (Table B.1).

B.4: Discussion: assessing modeled $\delta^{18}O_{foliarH2O}$ values

Two models for $\delta^{18}O_{foliarH2O}$ values utilized different components of the observed data set. A systematic offset between modeled $\delta^{18}O_{foliarH2O}$ values was observed (Figure 2.9 of main text). The range of $\delta^{18}O_{foliarH2O}$ values for model 1 versus model 2 are [-0.42‰, 7.24‰] and [-3.20‰, 4.79‰], respectively, indicating broadly lower values in the model 2 by ~3‰. Individual sample calculations differ in $\delta^{18}O$ values in each model by as little as 0.1‰ to as much as 4.79‰. Broadly, increases in either model result correspond to increased evapotranspiration, which is climatically controlled by temperature and vapor pressure differences at the leaf surface (akin to relative humidity; Kahmen et al., 2011). Hence, high model $\delta^{18}O$ values, which vary linearly with the measured $\delta^{18}O$ values on eggshell calcite, correspond with increased temperature and/or decreased relative humidity.

There are clearly caveats to each of these modeling approaches. In the case of model 1, for ostriches, some input parameters will not be entirely accurate since Kohn's (1996) model was not designed with input parameters specific to the biology and environment of African ostrich (e.g., it describes $\delta^{18}O_{H2O}$ for obligate drinkers, with below average ostrich body size, from environments with different ambient temperature and relative humidity than those typical of Eastern Africa). The second model could be misleading if the dietary $\delta^{13}C$ values oversimplify the contribution of CAM plants, which have an intermediate mean cellulose $\delta^{18}O$ value between that of C_3 and C_4 plants (~29.7‰, Sternberg et al., 1984), or if the mean values assigned to any of the plant photosynthetic groups are inappropriate for Eastern African plants. Neither do these models nor the variability in ostrich and plant ecology over semi-annual to annual timescales account for seasonal or diurnal changes in $\delta^{18}O$ (and sometimes also $\delta^{13}C$) values that are known to exist in some plant species, or the variation in $\delta^{18}O$ values that can exist along a single leaf surface in some plants (e.g., Landais et al., 2006). There should not be significant effects through time on precipitation $\delta^{18}O$ values due to altitudinal, and continental effects, but if meteoric waters have a different source at different sites under comparison, or if meteoric source waters

change through time at a given site, this could affect the whole ecosystem $\delta^{18}O$ values integrated into $\delta^{18}O$ values of eggshell calcite.

B.5: Supplementary Figures and Tables for Chapter 2

Supplementary File B.1: Supplementary data table for Chapter 2. Provided as Supplementary File 2.1

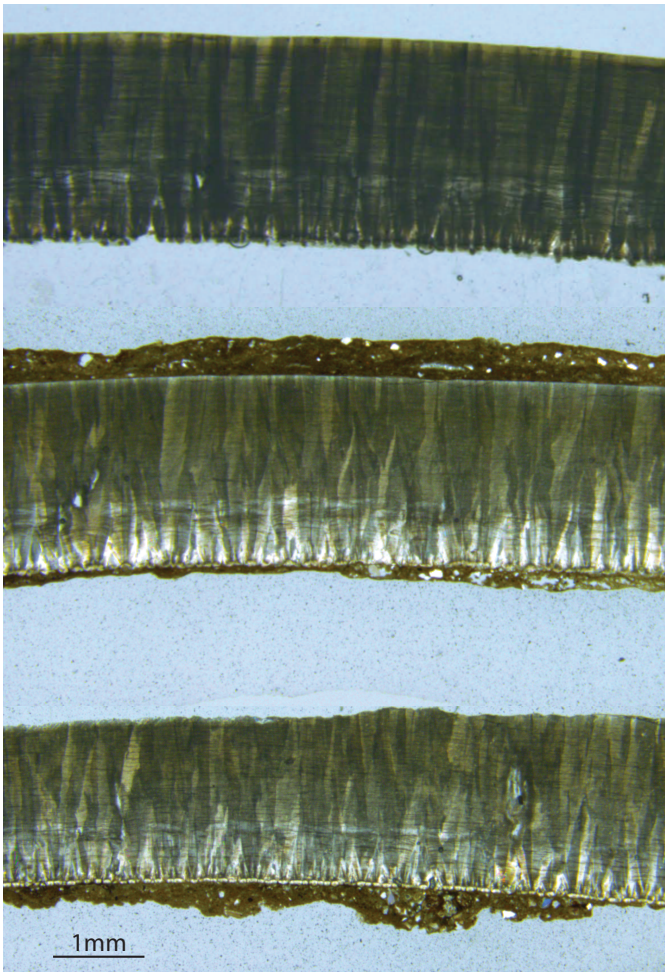

Figure B.1: Petrographic thin sections of three ostrich eggshells in cross-polarized transmitted light. Images show the preservation of structures such as the mammillary cone, palisade, and vertical crystal layers from the inner to outer surfaces of modern and ancient eggshells. Top: modern ostrich eggshell is polished to over 30 μm, hence its darker color, but calcite structures are clear; middle: 30 μm-thin section of Lukenya Hill sample 140-150D from the test pit (UBA-23935, ^{14}C age = 37,571 ± 768 calBP, 95% confidence), with detritus coating its surfaces; bottom: 30 μm-thin section of Lukenya Hill sample 140-150C from the test pit (UBA-23934, ^{14}C age = 31,985 ± 431 calBP), with detritus coating its inner surface. It has an undulating outer surface and the outer vertical crystal layer is not preserved, as a result.

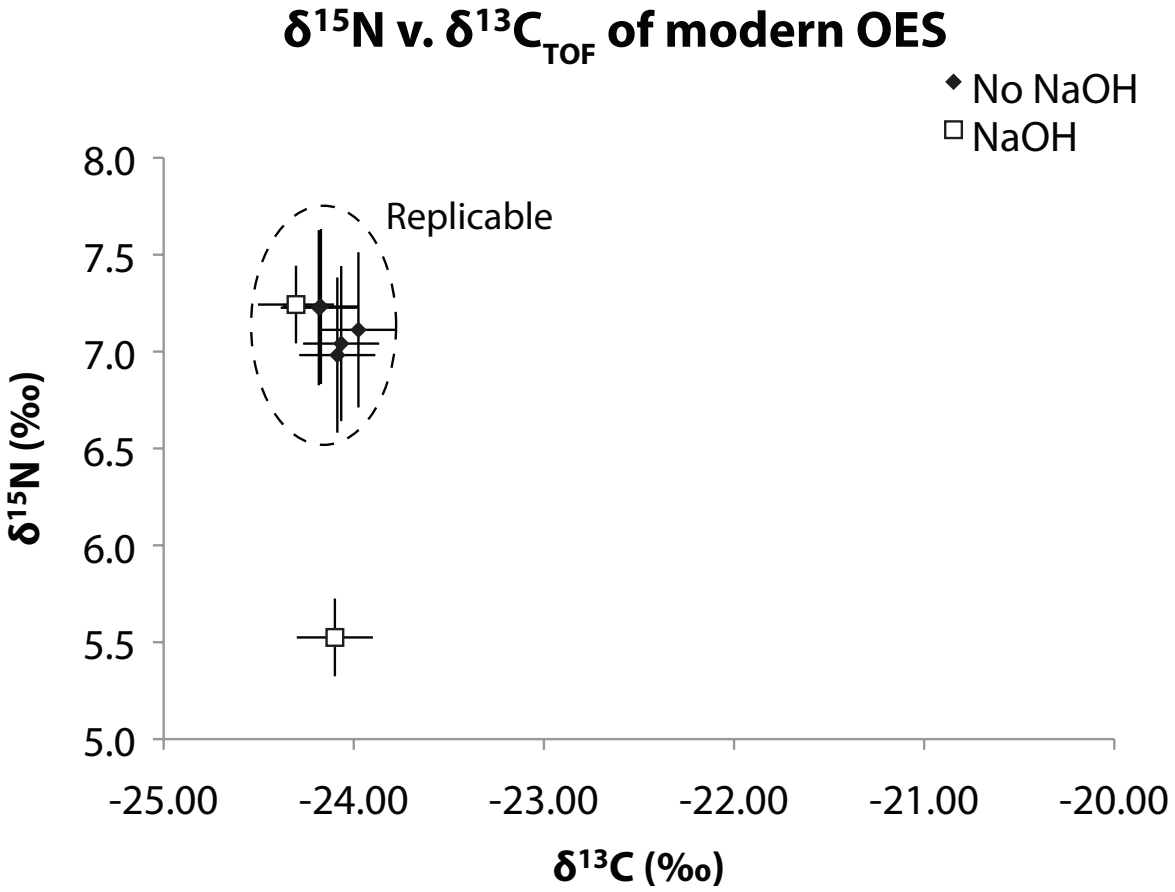

Figure B.2: Isotopic composition of the total organic fraction (TOF) in modern OES fragments from the same egg.

Sample ID	30 wt% Leach	HCl strength (N)	0.1N NaOH?	Single Acid Bath?	TOF Yield (wt%)
OES 1	No	0.5	No	No	0.23
OES 2	No	0.5	Yes	No	0.09
OES 3	No	0.25	Yes	No	0.12
OES 4	No	0.25	No	No	0.47
OES 5	**Yes**	**1**	**No**	**Yes**	**0.70**
OES 6	No	1	No	Yes	0.99
OES 7	No	1	Yes	Yes	0.25
OES 8	**Yes**	**1**	**No**	**Yes**	**1.34**
OES 9	Yes	1	Yes	Yes	0.05
OES 10	Yes	1	Yes	Yes	0.23

Table B.1: extraction protocol tests on modern OES fragments from the same egg. All aliquots were abraded and lightly crushed after leaching, where applicable. The protocol used on OES 8 (bold) is used on all ancient OES.

	Total Organic Fraction							Calcite Fraction
Sample	**% N**	**$\delta^{15}N$ (+/- 0.2)**	**% C**	**$\delta^{13}C$ (+/- 0.1)**	**C:N**	**$\delta^{13}C$ (‰ VPDB)**	**$\delta^{18}O$ (‰, VSMOW)**	**$\Delta^{13}C_{inorg-org}$**
OES1	14.2	7.2	47.7	-24.2	3.9			13.9
OES 2/3	*10.2*	*5.5*	*49.8*	*-24.1*	*5.7*			*13.8*
OES4	14.0	7.2	47.9	-24.2	4.0			13.9
OES 5	**13.4**	**7.1**	**45.4**	**-24.0**	**4.0**			**13.7**
OES 6	12.8	7.0	44.7	-24.1	4.1			13.8
OES 7	*0.7*		*61.9*	*-30.1*	*107.9*			*19.8*
OES 8	**13.5**	**7.0**	**44.7**	**-24.1**	**3.9**			**13.8**
OES 9/10	*12.1*	*7.2*	*44.3*	*-24.3*	*4.3*			*14.0*
mean composition	13.0		46.7		4.2			
2017ModOES-2	6.1	7.2	20.0	-24.1	3.9	-10.9	25.4	13.2
2017ModOES-2b	5.3	6.9	17.8	-24.1	3.9			13.2
2017ModOES-2c*	5.3	7.0	16.9	-22.8	3.7			11.9
2017ModOES-1	4.2	7.1	14.0	-22.7	3.9	-9.7	27.9	13.0
2017ModOES-1b	5.1	7.0	16.7	-24.1	3.9			14.4
mean composition	5.2		17.1		3.8			
mean δ values		7.0		-24.0		-10.3	26.7	
± (1σ)		0.5		0.4		0.8	1.8	

Supplementary Italicized samples had NaOH treatment. Some samples were combined due to extremely low sample yields after chemistry, but combined samples only differed in their protocol by the strength of NaOH used, if at all. * denotes samples whose organic fraction was entirely from the inner membrane, which is typically lost in ancient samples. Bold samples from the original tests were treated with the same protocol as the future modern OES samples (sample ID starting with 2017) and all ancient OES.

B.6: References

Ambrose, S.H., 1990. Preparation and Characterization of Bone and Tooth Collagen for Isotopic Analysis. J. Archaeol. Sci. 17, 431–451.

Brooks, A.S., Hare, P.E., Kokis, J.E., Miller, G.H., Ernst, R.D., Wendorf, F., 1990. Dating pleistocene archeological sites by protein diagenesis in ostrich eggshell. Science. 248, 60–64. https://doi.org/10.1126/science.248.4951.60

Chisholm, B.S., Nelson, D.E., Hobson, K.A., Knyfb, M., 1983. Carbon Isotope Measurement Techniques for Bone Collagen: Notes for the Archaeologist. J. Archaeol. Sci. 10, 355–360.

Crisp, M., Demarchi, B., Collins, M., Morgan-williams, M., Pilgrim, E., 2013. Quaternary Geochronology Isolation of the intra-crystalline proteins and kinetic studies in *Struthio camelus* (ostrich) eggshell for amino acid geochronology q. Quat. Geochronol. 16, 110–128. https://doi.org/10.1016/j.quageo.2012.09.002

Dauphin, Y., Senut, B., 1998. Diagenetic changes in the mineral and organic phases of fossil avian eggshells from Namibia 13, 243–256.

Demarchi, B., Hall, S., Roncal-Herrero, T., Freeman, C.L., Woolley, J., Crisp, M.K., Wilson, J., Fotakis, A., Fischer, R., Kessler, B.M., Jersie-Christensen, R.R., Olsen, J. V., Haile, J., Thomas, J., Marean, C.W., Parkington, J., Presslee, S., Lee-Thorp, J., Ditchfield, P., Hamilton, J.F., Ward, M.W., Wang, C.M., Shaw, M.D., Harrison, T., Domínguez-Rodrigo, M., Macphee, R.D.E., Kwekason, A., Ecker, M., Horwitz, L.K., Chazan, M., Kroger, R., Thomas-Oates, J., Harding, J.H., Cappellini, E., Penkman, K., Collins, M.J., 2016. Protein sequences bound to mineral surfaces persist into deep time. Elife 5. https://doi.org/10.7554/eLife.17092

DeNiro, M.J., 1985. Postmortem preservation and alteration of in vivo bone collagen isotope ratios in relation to palaeodietary reconstruction. Nature 317, 806–809.

Deniro, M.J., Schoeniger, M.J., 1983. Stable Carbon and Nitrogen Isotope Ratios of Bone Collagen: Variations within Individuals, Between Sexes, and Within Populations Raised on Monotonous Diets. J. Archaeol. Sci. 10, 199–203.

Deniro, M.J., Weiner, S., 1988. Chemical, enzymatic and spectroscopic characterization of "collagen" and other organic fractions from prehistoric bones. Geochim. Cosmochim. Acta 52, 2197–2206.

Hincke, M.T., Tsang, C.P.W., Courtney, M., Hill, V., Narbaitz, R., 1995. Purification and Immunochemistry of a Soluble Matrix Protein of the Chicken Eggshell (Ovocleidin 17). Calcif. Tissue Int. 56, 578–583.

Johnson, B.J., Fogel, M.L., Miller, G.H., 1998. Stable isotopes in modern ostrich eggshell: A calibration for paleoenviromental applications in semi-arid regions of southern Africa. Geochim. Cosmochim. Acta 62, 2451–2461.

Jørkov, M.L.S., Heinemeier, J., Lynnerup, N., 2007. Evaluating bone collagen extraction methods for stable isotope analysis in dietary studies 34, 1824–1829. https://doi.org/10.1016/j.jas.2006.12.020

Mikhailov, K.E., 1997. Fossil and recent eggshell in amniotic vertebrates: fine structure, comparative morphology and classification. Spec. Pap. Palaeontol. 56, 1–80.

Miller, G., Magee, J., Smith, M., Spooner, N., Baynes, A., Lehman, S., Fogel, M., Johnston, H., Williams, D., Clark, P., Florian, C., Holst, R., DeVogel, S., 2016. Human predation contributed to the extinction of the Australian megafaunal bird Genyornis newtoni ~47 ka. Nat. Commun. 7, 1–7. https://doi.org/10.1038/ncomms10496

Miller, G.H., Brigham-Grette, J., 1989. Amino acid geochronology: Resolution and precision in carbonate fossils. Quat. Int. 1, 111–128.
Miller, G.H., Fogel, M.L., 2016. Calibrating $\delta^{18}O$ in Dromaius novaehollandiae (emu) eggshell calcite as a paleo-aridity proxy for the Quaternary of Australia. Geochim. Cosmochim. Acta 193, 1–13. https://doi.org/10.1016/j.gca.2016.08.004
Niespolo, E.M., Sharp, W.D., Fylstra, N.D., Avery, G., Blegen, N., Faith, J.T., Henshilwood, C.S., Klein, R., Van Niekerk, K., Weisz, D.G., Tryon, C.A., 2018. U-Th burial dating of ostrich eggshell beyond the 14 C limit. Geochemical Society, Boston, MA.
Niespolo, E.M., Sharp, W.D., Fylstra, N.D., Tryon, C.A., Tripathy-Lang, A., Weisz, D.G., Blegen, N., Faith, J.T., Henshilwood, C.S., Lewise, J., Mackay, A., Steele, T., Van Niekerk, K., WoldeGabriel, G., 2017a. U-Th burial dating of ostrich eggshells : a novel approach to dating African archaeological sequences beyond the 14 C limit. Seattle, WA.
Niespolo, E.M., Sharp, W.D., Fylstra, N.D., Tryon, C.A., Weisz, D.G., Faith, J.T., Henshilwood, C.S., Lewis, J., Mackay, A., Steele, T.E., Van Niekerk, K.L., 2017b. Patterns of Secondary U in ostrich eggshell: Applicaiton to U-Th dating of Quaternay terrestrial strata, in: American Geochemical Society. Paris.
Nys, Y., Gautron, J., Garcia-Ruiz, J.M., Hincke, M.T., 2004. Avian eggshell mineralization: Biochemical and functional characterization of matrix proteins. Comptes Rendus - Palevol 3, 549–562. https://doi.org/10.1016/j.crpv.2004.08.002
Nys, Y., Hincke, M.T., Arias, J.L., Garcia-Ruiz, J.M., Solomon, S.E., 1999. Avian eggshell mineralization. Poult. Avian Biol. Rev. 10, 143–166.
Sealy, J., Johnson, M., Richards, M., Nehlich, O., 2014. Comparison of two methods of extracting bone collagen for stable carbon and nitrogen isotope analysis: comparing whole bone demineralization with gelatinization and ultra fi ltration. J. Archaeol. Sci. 47, 64–69. https://doi.org/10.1016/j.jas.2014.04.011
Whedon, G.D., Proulx Heaney, R., 2018. Bone. Encycl. Br.

Appendix C: Supplementary Materials for Chapter 3

C.1: Methods

Data acquisition methods are reported in detail here and full analytical results can be found in the Supplementary File 3.1.

C.1.1: Sample preparation

Samples were brushed to remove loose detritus and photographed. Dating samples were selected in known relation to identifiable growth surfaces whenever possible. Sample surfaces were abraded with a water-cooled saw to remove outer detritus-rich or altered material. Samples were then cleaned 3-12 hours in isopropanol in an ultrasonic bath. Samples were crushed with an agate mortar and pestle and cleaned again in isopropanol in an ultrasonic bath for 3-12 hours. 80-200 mg of the cleanest material was hand selected with steel forceps under a binocular microscope. Additional examples of intact samples and final cleaned, crushed fractions for dating can be found in the Supplementary Figures.

C.1.2: Aridus/Solutions methods

Coral samples were totally dissolved in 7N HNO_3 and equilibrated with a mixed spike containing ^{229}Th, ^{233}U, and ^{236}U. The spike was calibrated using New Brunswick National Lab CRM145 uranium solution and solutions prepared from a 69 Ma U ore from Schwartzwalder Mine, Colorado, USA that has been demonstrated to yield concordant U-Pb ages (Ludwig et al., 1985) and sample-to-sample agreement of $^{234}U/^{238}U$ and $^{230}Th/^{238}U$ ratios. U and Th were separated from sample matrix using two stages of HNO_3–HCl cation exchange chemistry followed by reaction with HNO_3 and $HClO_4$ to remove any residual organic material.

All concentration and isotopic measurements were carried out at the Berkeley Geochronology Center (BGC) on a Thermo-Fisher NEPTUNE *Plus* multi-collector inductively coupled plasma mass spectrometer (ICP-MS). Samples were introduced into the ICP-MS using an Aridus II desolvator after mixing with dilute HNO_3-HF run solution. Since young samples have low concentrations of ^{230}Th, U and Th fractions were measured separately to avoid the effect of tailing from large ^{238}U peak on ^{230}Th. Each analysis included a wash step followed by an instrumental blank, the sample measurement, and a measurement of peak tails. Sample measurements were carried out in peak-jumping mode with all masses measured on Faraday collectors during multi-collection except ^{230}Th and ^{234}U, which were measured with an ion counter. ^{234}U was also measured on a Faraday collector during replicate measurements of U isotopes on selected samples. Simultaneous collection of U and Th isotopes during respective runs included measurement of ^{238}U to normalize fluctuations in signal intensity. Instrumental backgrounds, Faraday collector baselines, and ion counter dark noise were measured at each U and Th mass while aspirating the same HNO_3-HF run solution used to dilute samples. Sample measurements incorporated within-run mass bias corrections using the known $^{233}U/^{236}U$ ratio of the spike. Ion counter yield (relative to Faraday collectors) was determined during each sample measurement by cycling ^{229}Th and ^{233}U between the ion counter and the L1 Faraday collector. Peak tails were monitored at seven half-mass positions on an ion counter from m/e = 229.5 to 241.5 while aspirating sample solution, and the sum of tails from all peaks was modeled at each U and Th mass position. Measured peak heights were corrected for Faraday baselines/ion counter dark noise, instrumental backgrounds, Faraday gains, ion counter yields, mass fractionation,

peak-tails, procedural blanks, and interfering spike isotopes. The external reproducibility of $^{234}U/^{238}U$ and $^{230}Th/^{238}U$ ratios of Schwartzwalder Mine solutions measured during analytical sessions was better than 0.4%. Procedural blanks on ^{238}U, ^{232}Th, and ^{230}Th ranged, in pg, from 257.4 to 315.9, from 29.9 to 37.4, and from 0.00044 to 0.00159, respectively. Activity ratios and ages were calculated using the half-lives of Jaffey et al. (1971) for ^{238}U, Holden (1990) for ^{232}Th, and Cheng et al. (2013) for ^{230}Th and ^{234}U.

To make a detrital Th correction, we assume Th-rich detritus integrated into the coral skeleton is at or near secular equilibrium and has a crustal Th/U ratio. ^{232}Th is not a product of U decay and its presence in a sample indicates some Th present is not the product of *in situ* decay; it has a half-life of 1.405×10^{10} a and can be treated as a stable isotope on Quaternary timescales (the timescale at which ^{230}Th dating is applicable). ^{232}Th can thus serve as an index for the amount of extraneous ^{230}Th incorporated into the corals by measuring the amount of ^{232}Th in a sample and using a model correction, typically that of bulk silicate crust, to quantify extraneous ^{230}Th (e.g., Hellstrom, 2006). Ages calculated for samples with low ($^{230}Th/^{232}Th$) ratios indicate there is more extraneous Th and will require a larger detrital correction on the corrected ^{230}Th age. This will reduce the precision of the calculated age, and may render the age inaccurate, if the ($^{230}Th/^{232}Th$) of detritus in the corals differs greatly from the modeled detrital composition. Detrital sources are commonly attributed to local parent lithologies eroding and/or providing a source of dust (e.g., Ludwig and Paces, 2002). In this case, the nearest source would likely derive from the ~18 Ma eroded volcanic material on Mangaia. We assume detritus with the $^{232}Th/^{238}U$ ratio of average silicate crust in secular equilibrium and assign and propagate the following uncertainties into the final age-errors: $(^{232}Th/^{238}U) = 1.21 \pm 0.5$; $(^{230}Th/^{238}U) = 1 \pm 0.1$; $(^{234}U/^{238}U) = 1 \pm 0.1$. Initial $(^{234}U/^{238}U)$ is back calculated from measured $(^{234}U/^{238}U)$ and the corrected date. Ages, corrected activity ratios, and uncertainties were calculated with Isoplot 3.75 (Ludwig, 2012). Uncertainties of corrected ages are reported at the 2σ level and include measurement errors, procedural ^{230}Th blanks and uncertainties associated with detritus corrections but not decay constants and data reporting follows the guidelines of Dutton et al. (2017). A comprehensive table of results can be found in the Supplementary Data Tables.

To rule out measurement error as an explanation for the low $(^{234}U/^{238}U)_0$ of some samples, we repeated solution U measurements on four samples $(^{234}U/^{238}U)_0$ within or below the range of seawater, modifying the method to measure ^{234}U using a Faraday cup instead of an ion counter. The new data are more precise and do not require correction for the relative gain of the ion counter, the single largest correction involved in $^{234}U/^{238}U$ ratio determinations. Faraday replicates on samples MAN-44-U-Th#-1, -5, -11, and -14 are within analytical uncertainty of the original measurements at 2σ in all cases. (Supplementary Table 1) shows sub-samples of corals MAN-44-U-Th#-1 and -11 in good agreement, while those from -5 overlap only slightly at 2σ, perhaps indicating some heterogeneity of $^{234}U/^{238}U$ ratios in that sample.

C.1.3: LA-ICP-MS methods

In situ concentrations of ^{238}U, ^{232}Th, and ^{43}Ca in selected *Acropora* samples were evaluated via laser ablation (LA) ICP-MS using a Photon Machines Analyte II excimer laser attached to a Thermo-Fisher NEPTUNE *Plus* ICP-MS. Magnetic field calibrations and signal intensities of ^{238}U and ^{232}Th were monitored using NIST 612 (37.38 and 37.79 ppm of U and Th, respectively; National Institute of Standards and Technology, 2012). Grand Canyon Travertine LC 190.3, a homogeneous calcite containing 2.52 ppm U (Mertz-Kraus et al., 2010), was used as

an internal standard. Based on concordant dating results between solution and *in situ* ^{230}Th dating of the same coral, Hoffmann et al. (2009) concluded that matrix differences between a secular equilibrium calcite standard and aragonitic corals would not affect reproducibility.

Coral lines were first treated with a pre-ablation step to clean and create a uniform surface at 10% laser output, 0.68 J/cm^2 fluence, 5 Hz rep rate, 65μm spot size, and 50 μm/s scan speed. The ablation step used 50% laser output, 3.4 J/cm^3 fluence, 5 Hz rep rate, 65 μm spot size, 5 μm/s scan speed, all at 4.5mJ laser energy set point. ^{238}U, ^{232}Th and ^{43}Ca were measured sequentially using magnetic field switching in cycles lasting ~7 seconds. ^{238}U and ^{232}Th were measured using an ion counter while ^{43}Ca was measured on a Faraday detector. *Acropora* samples were cut orthogonal to the growth axis, mounted in epoxy and polished, and ablation lines began in the epoxy and moved inward radially toward the approximate center of the coral. Corals are not entirely radially symmetric and so line length varies with radius; hence, data is presented with respect to normalized distance into the coral from the outer surface (normalized distance = 0) into the center of the coral (normalized distance = 1). Since corals have abundant diverse pore structures, lines crossing over pore spaces resulted in un-focused ablation. Resulting lower concentrations of ablated material and possibly fractionated elemental measurements compromise these segments of the lines and thus have been omitted from the graphical results and data tables (Supplementary tables and figures). ^{238}U, ^{232}Th, and ^{43}Ca intensities are measured separately, and [U] is calculated by taking the ratio ^{238}U/^{43}Ca and normalizing to a carbonate standard, measured identically, with a well-known U concentration (Mertz-Kraus et al., 2010). Concentrations of U are normalized to isotope dilution results for each sample and ^{232}Th/^{238}U ratios are corrected for differences in ionization efficiency of U and Th observed when analyzing spiked $CaCO_3$ solutions. Since ^{238}U and ^{43}Ca isotope intensities correlate positively, the variation in calculated [U] as oscillatory patterns seen in all samples cannot be explained by variation in the ^{238}U/^{43}Ca ratio that is used to calculate [U]. [U] and ^{232}Th/^{238}U profiles for each coral analyzed by LA-ICP-MS are provided in the Appendix C Figures and Supplementary File 3.1.

C.1.4: XRD methods

30-50 mg of each sample was crushed to a powder in a mortar & pestle. Powders were sent for analysis at Attard's Minerals (San Diego, CA) on a Philips PW1729 X-Ray Generator using PW1710 electronics and fitted with a PW 1820 Goniometer carrying a Philips proportional detector with a graphite monochromator. A Long Fine Focus Copper X-Ray tube was operated at 40kV and 30mA. Samples were run for 10 minutes and 25 seconds and measured between 10° and 60° 2θ to check for the presence of calcite and aragonite. The proportion of aragonite versus calcite was evaluated by running scans from 26° to 30° 2θ for 1 minute and 40 seconds. See the Appendix C Figures for selected diffractograms, peak positions, and peak shapes, and the Supplementary File 3.1 for all sample peak positions and intensities detected.

C.2: Supplementary Figures and Tables for Chapter 3

Sample ID (MAN-44-U-Th#-)	Detr-uncorrected ($^{234}U/^{238}U$), Faraday (2σ, %)		Detr-uncorrected ($^{234}U/^{238}U$), Ion Counter (2σ, %)	
1A	1.13836	±0.081%	1.1389	±0.18%
1B	1.13904	±0.059%	1.1392	±0.18%
5A	1.13993	±0.109%	1.1400	±0.15%
5B	1.14218	±0.092%	1.1408	±0.19%
11A	1.13079	±0.061%	1.1303	±0.19%
11B	1.13158	±0.065%	1.1326	±0.17%
14	1.13902	±0.067%	1.1396	±0.17%

Table C.1: Comparison of faraday with ion counter measurements after normalizing to CRM-145 standard.

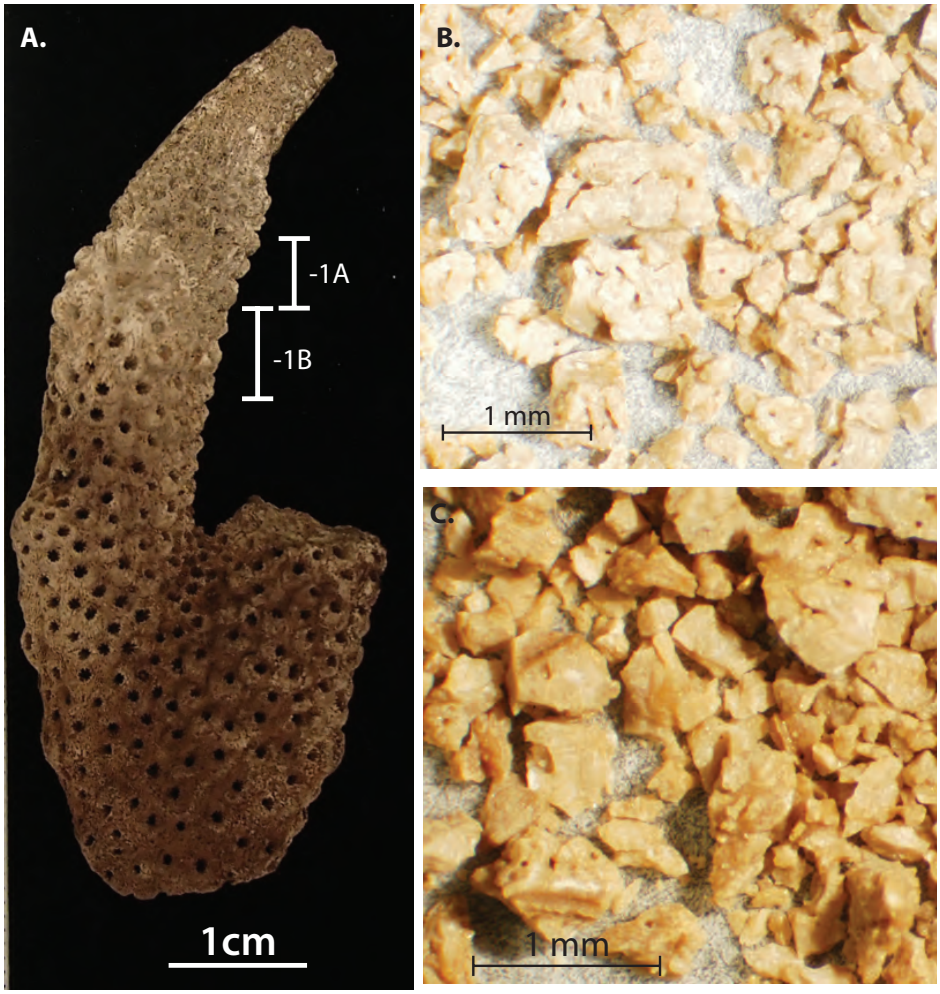

Figure C.1: *Acropora* coral abrader MAN-44-U-Th#-1. A. Sample before preparation; B. subsample -1A after cleaning; C. subsample -1B after cleaning.

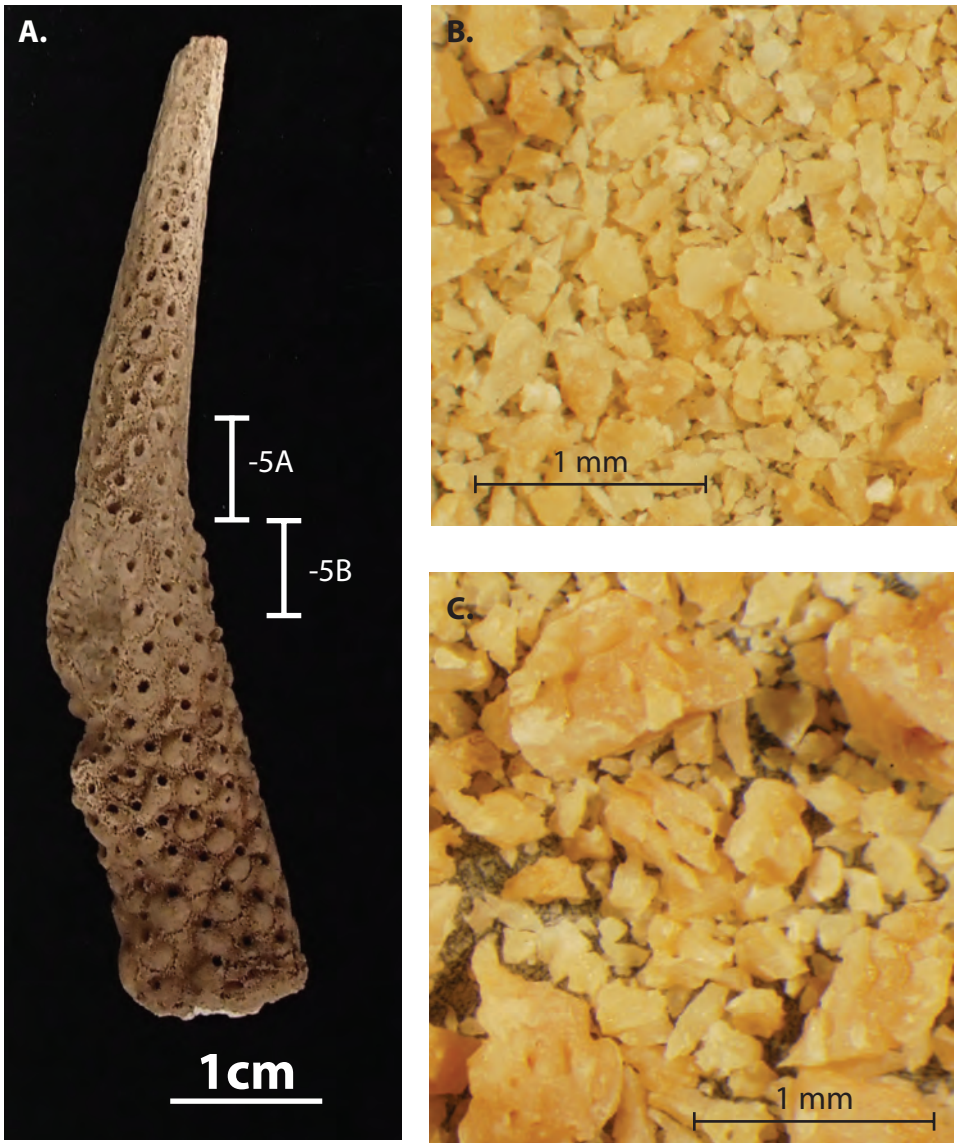

Figure C.2: *Acropora* coral abrader MAN-44-U-Th#-5. A. Sample before preparation; B. subsample -5A after cleaning; C. subsample -5B after cleaning.

Figure C.3: *Acropora* coral abrader MAN-44-U-Th#-9. A. Sample before preparation; B. subsample after cleaning.

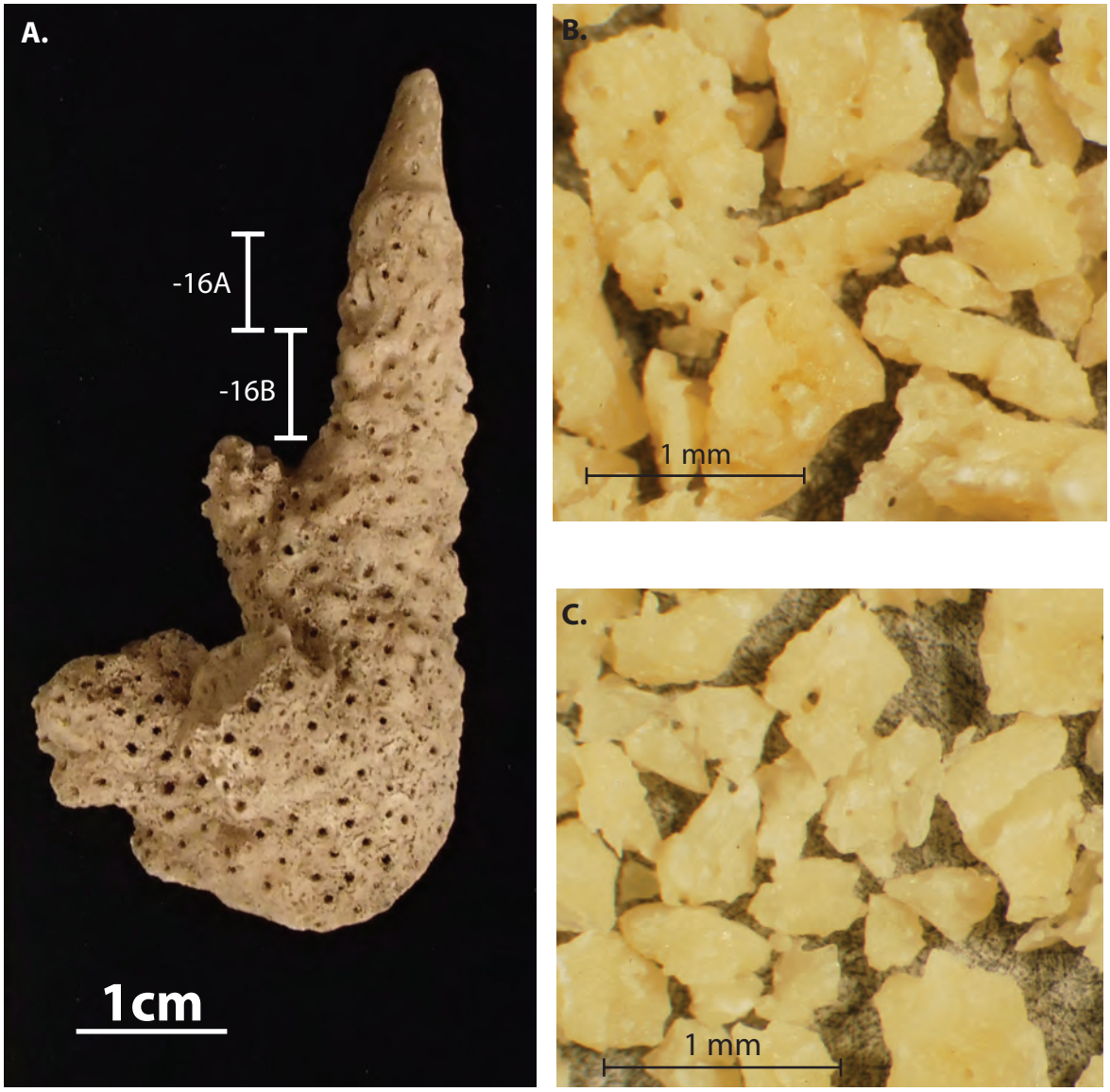

Figure C.4: *Acropora* coral abrader MAN-44-U-Th#-16. A. Sample before preparation; B. subsample -16A after cleaning; C. subsample -16B after cleaning.

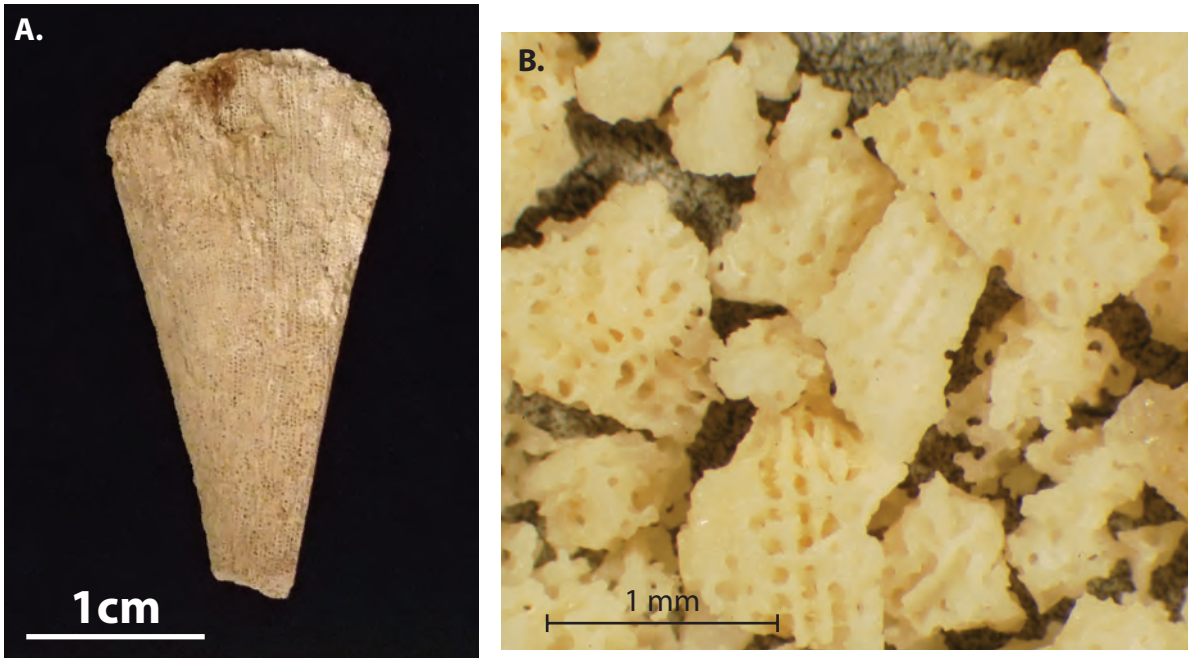

Figure C.5: *Porites* coral abrader MAN-44-U-Th#-22. A. Sample before preparation; B. subsample after cleaning.

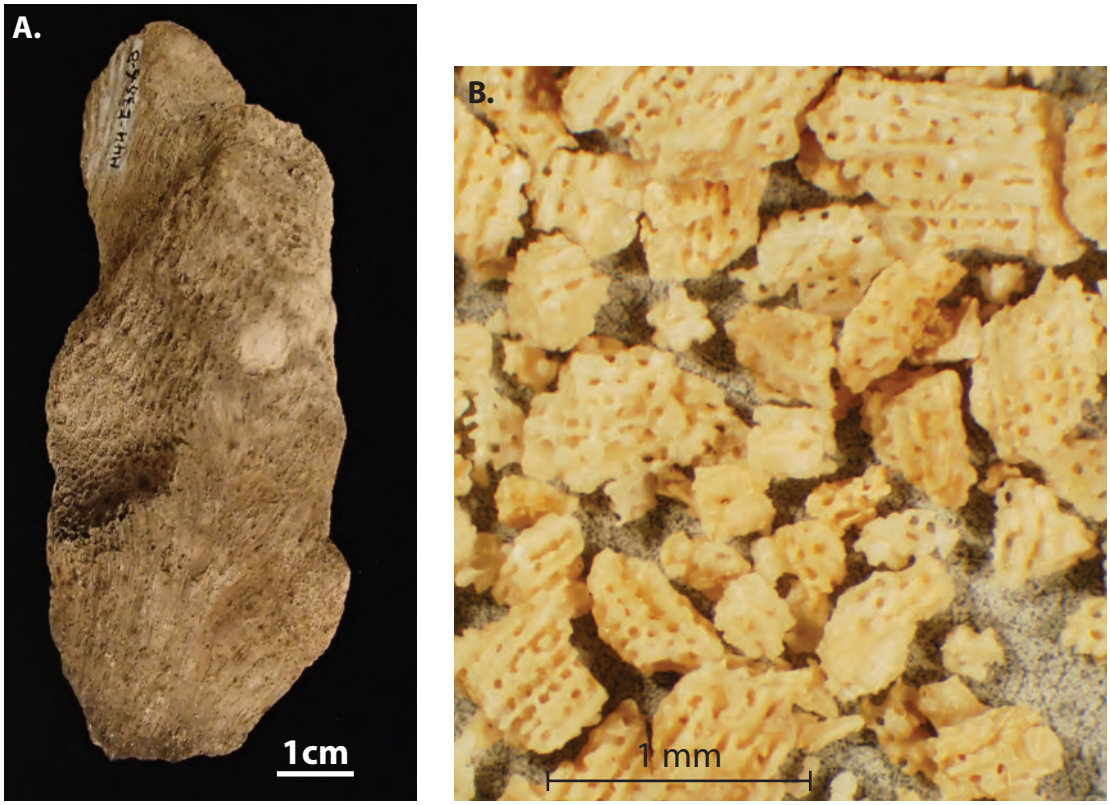

Figure C.6: *Porites* coral abrader MAN-44-U-Th#-24. A. Sample before preparation; B. subsample after cleaning.

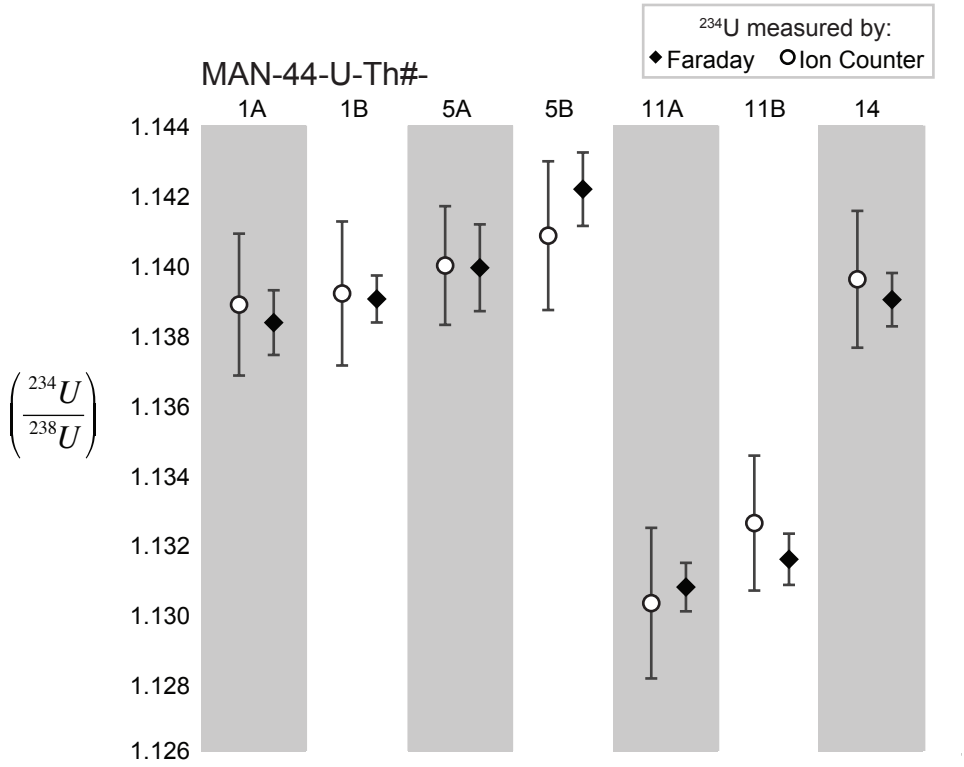

Figure C.7: Solution re-analyses of selected coral abraders. These were re-analyzed to evaluate ($^{234}U/^{238}U$) from only Faraday measurements (black diamonds) compared to those with ^{234}U measurements done on an ion counter (white circles).

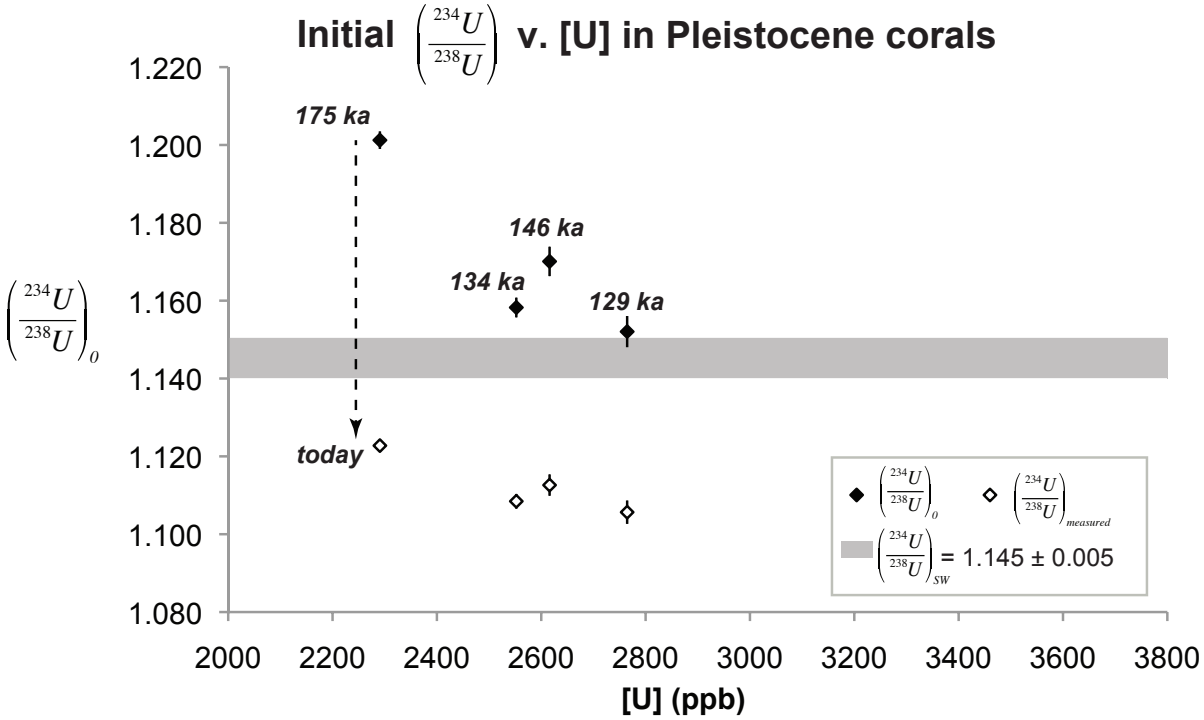

Figure C.8: Apparent ^{230}Th ages, U concentrations, and (^{234}U/^{238}U) ratios of Pleistocene coral abraders from MAN-44. These *Porites* corals were likely sourced from prominently exposed *makatea*, an older reef complex exposed by regional uplift related to hot spot volcanism now located at McDonald Seamount.

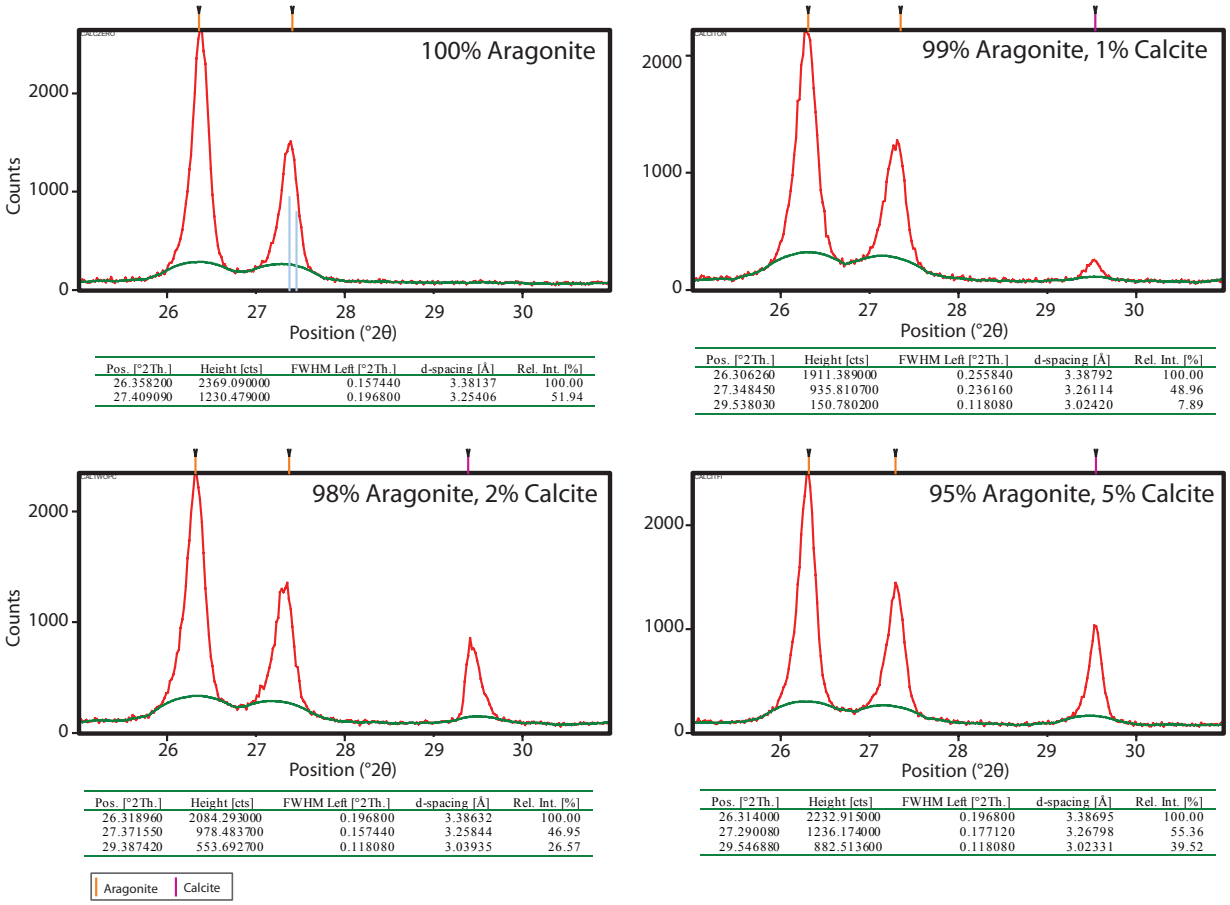

Pos. [°2Th.]	Height [cts]	FWHM Left [°2Th.]	d-spacing [Å]	Rel. Int. [%]
26.358200	2369.090000	0.157440	3.38137	100.00
27.409090	1230.479000	0.196800	3.25406	51.94

Pos. [°2Th.]	Height [cts]	FWHM Left [°2Th.]	d-spacing [Å]	Rel. Int. [%]
26.306260	1911.389000	0.255840	3.38792	100.00
27.348450	935.810700	0.236160	3.26114	48.96
29.538030	150.780200	0.118080	3.02420	7.89

Pos. [°2Th.]	Height [cts]	FWHM Left [°2Th.]	d-spacing [Å]	Rel. Int. [%]
26.318960	2084.293000	0.196800	3.38632	100.00
27.371550	978.483700	0.157440	3.25844	46.95
29.387420	553.692700	0.118080	3.03935	26.57

Pos. [°2Th.]	Height [cts]	FWHM Left [°2Th.]	d-spacing [Å]	Rel. Int. [%]
26.314000	2232.915000	0.196800	3.38695	100.00
27.290080	1236.174000	0.177120	3.26798	55.36
29.546880	882.513600	0.118080	3.02331	39.52

Figure C.9: XRD diffractograms for standards with known mixtures of aragonite and calcite.

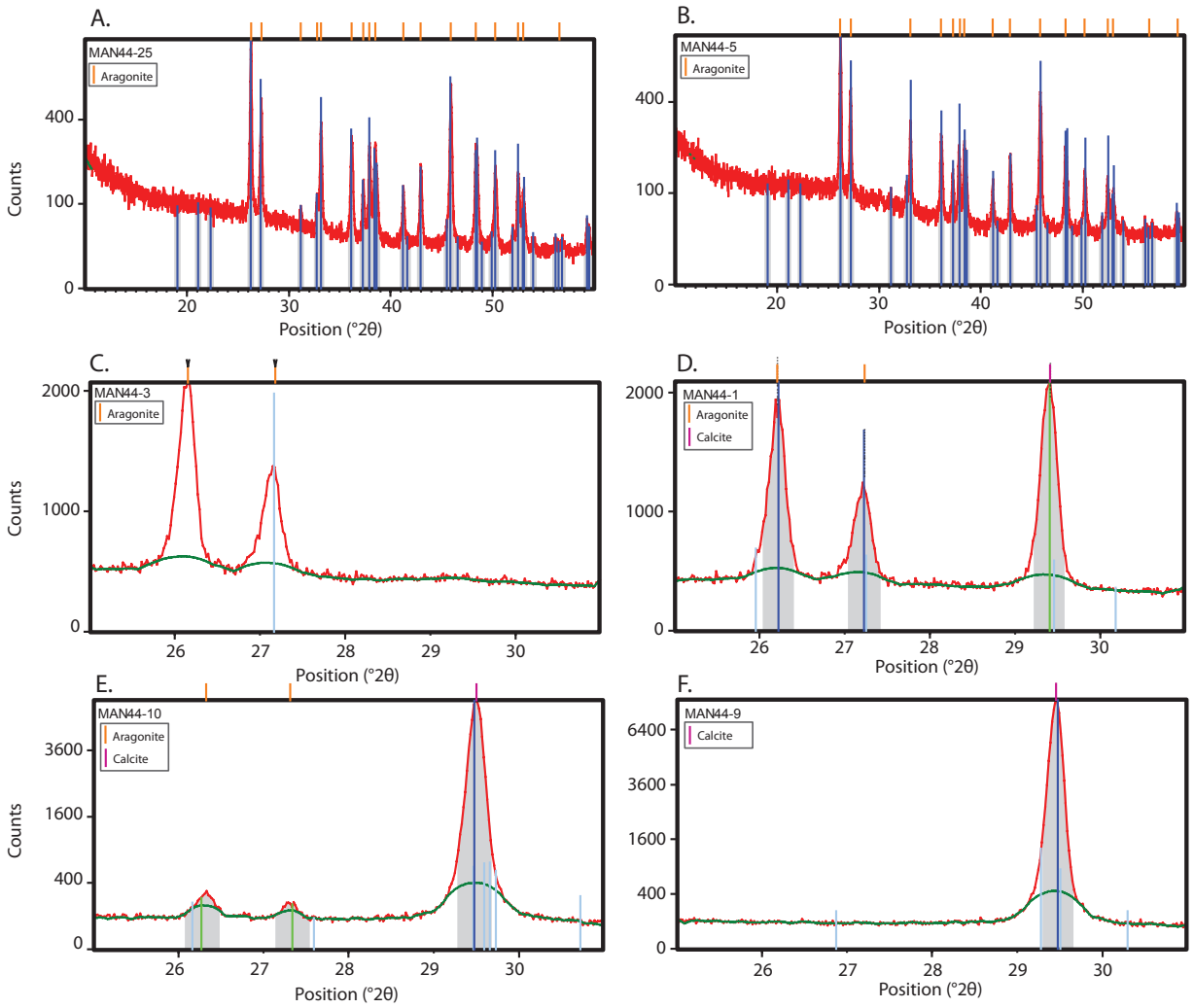

Figure C.10: X-Ray Diffractograms from selected samples from MAN-44. A. and B: 100% aragonite samples were run longer and with a wider range of 2θ to demonstrate reproducibility of briefer, shorter scans for pure aragonite samples. C., D., E., & F: main aragonite and calcite peaks are easily detected with briefer, shorter range scans, as was done for the standards. The 2θ peak positions for all MAN-44 samples are provided in the Supplementary Tables.

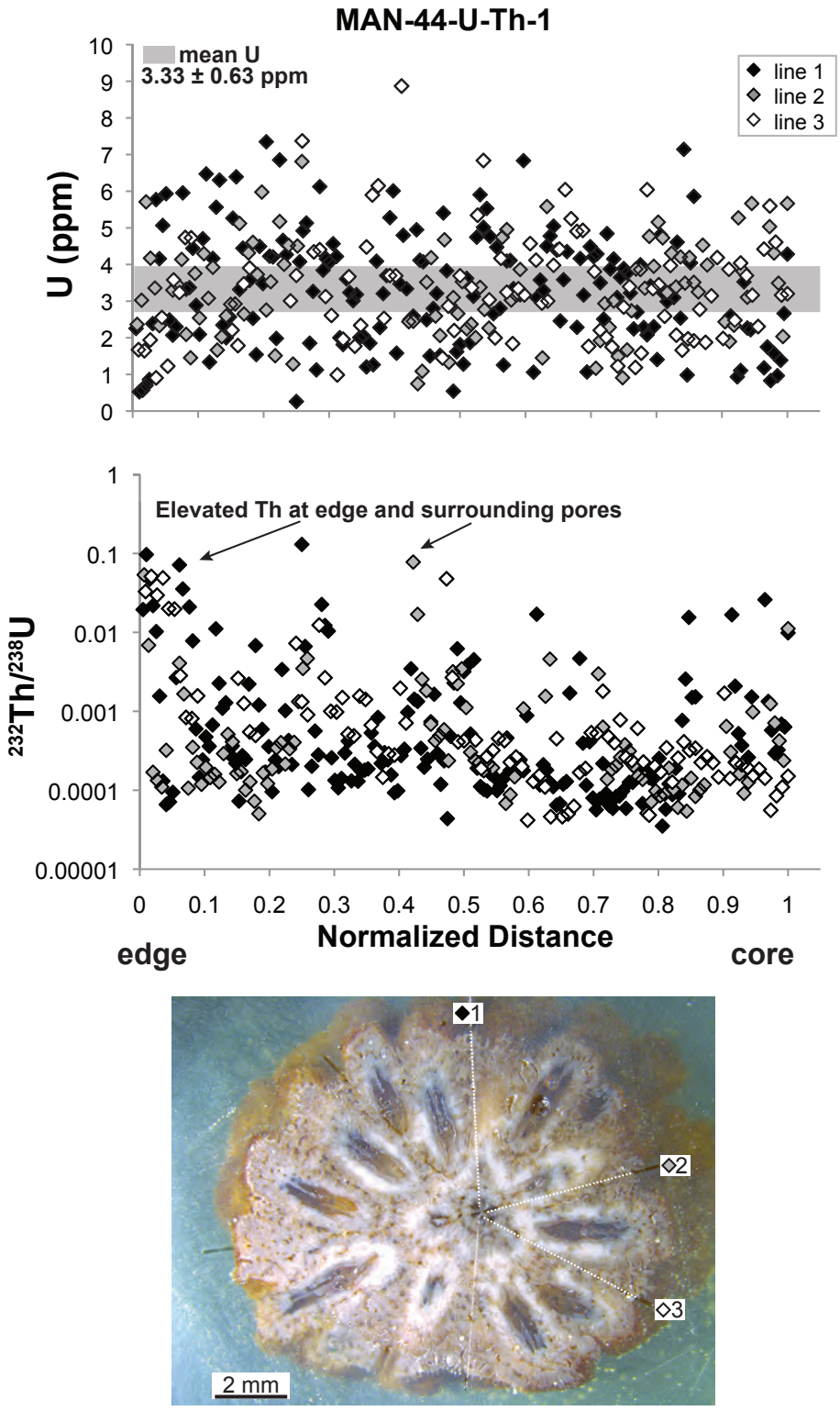

Figure C.11: [U] and $^{232}Th/^{238}U$ from LA-ICP-MS traverses of MAN-44-U-Th#-1 (>> 5% calcite). This sample was selected due to having ideal U-Th isotopic composition and being partially recrystallized.

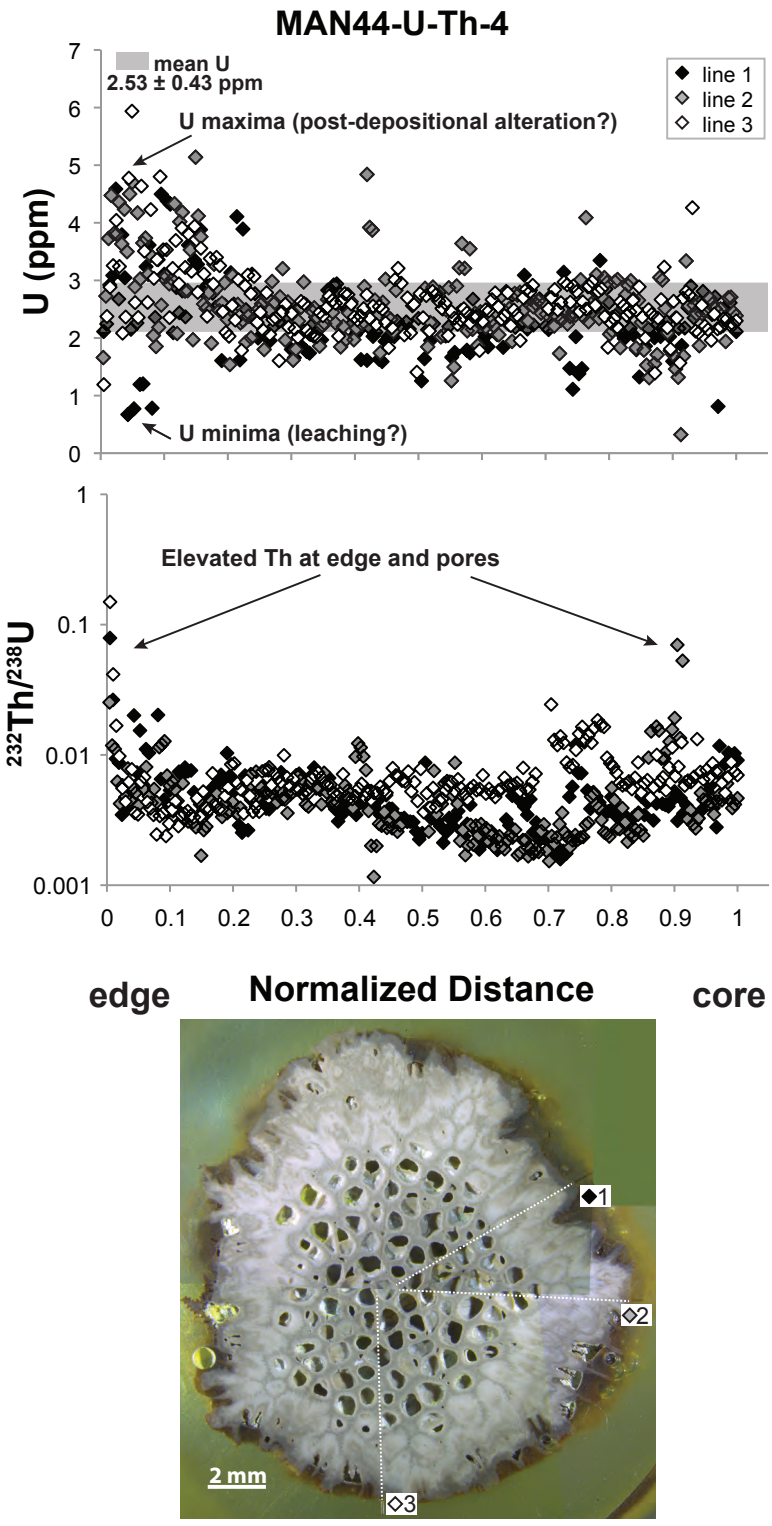

Figure C.12: [U] and $^{232}Th/^{238}U$ from LA-ICP-MS traverses of MAN-44-U-Th#-4 (100% calcite). This sample was selected due to having low ($^{230}Th/^{232}Th$) and being fully recrystallized.

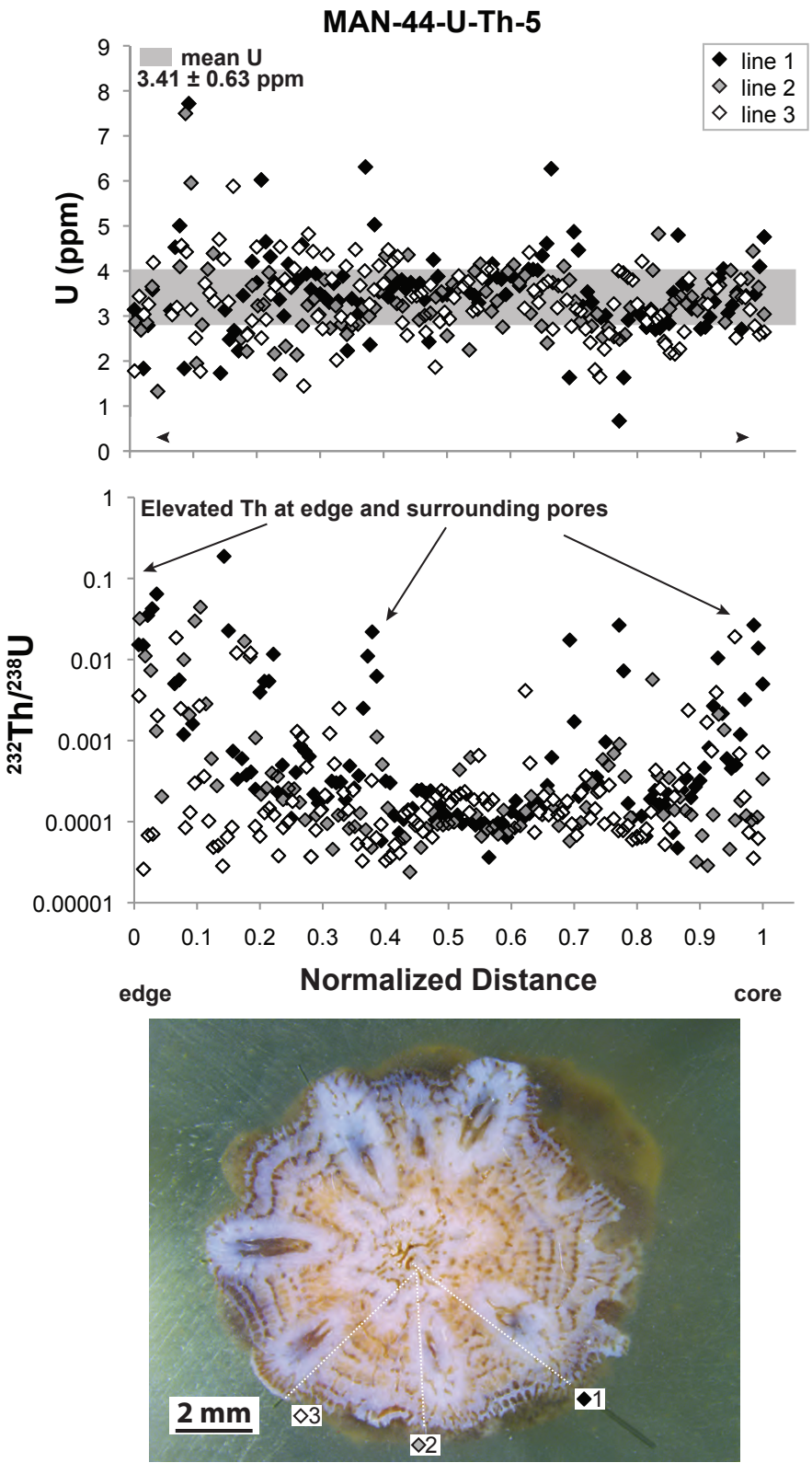

Figure C.13: [U] and $^{232}Th/^{238}U$ from LA-ICP-MS traverses of MAN-44-U-Th#-5 (100% aragonite). This was selected as an ideal sample.

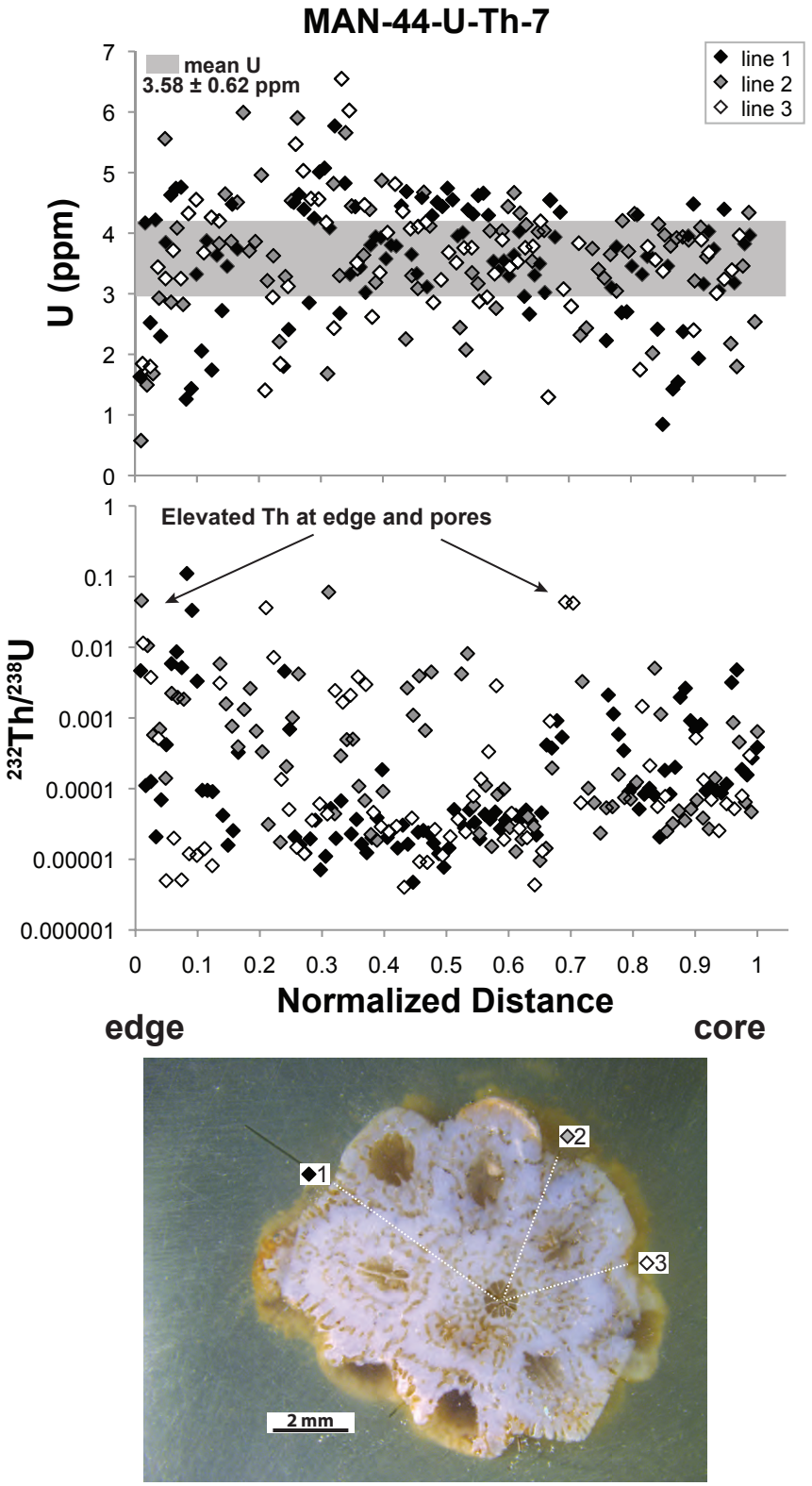

Figure C.14: [U] and $^{232}Th/^{238}U$ from LA-ICP-MS traverses of MAN-44-U-Th#-7 (100% aragonite). This sample was selected due to low ($^{234}U/^{238}U$).

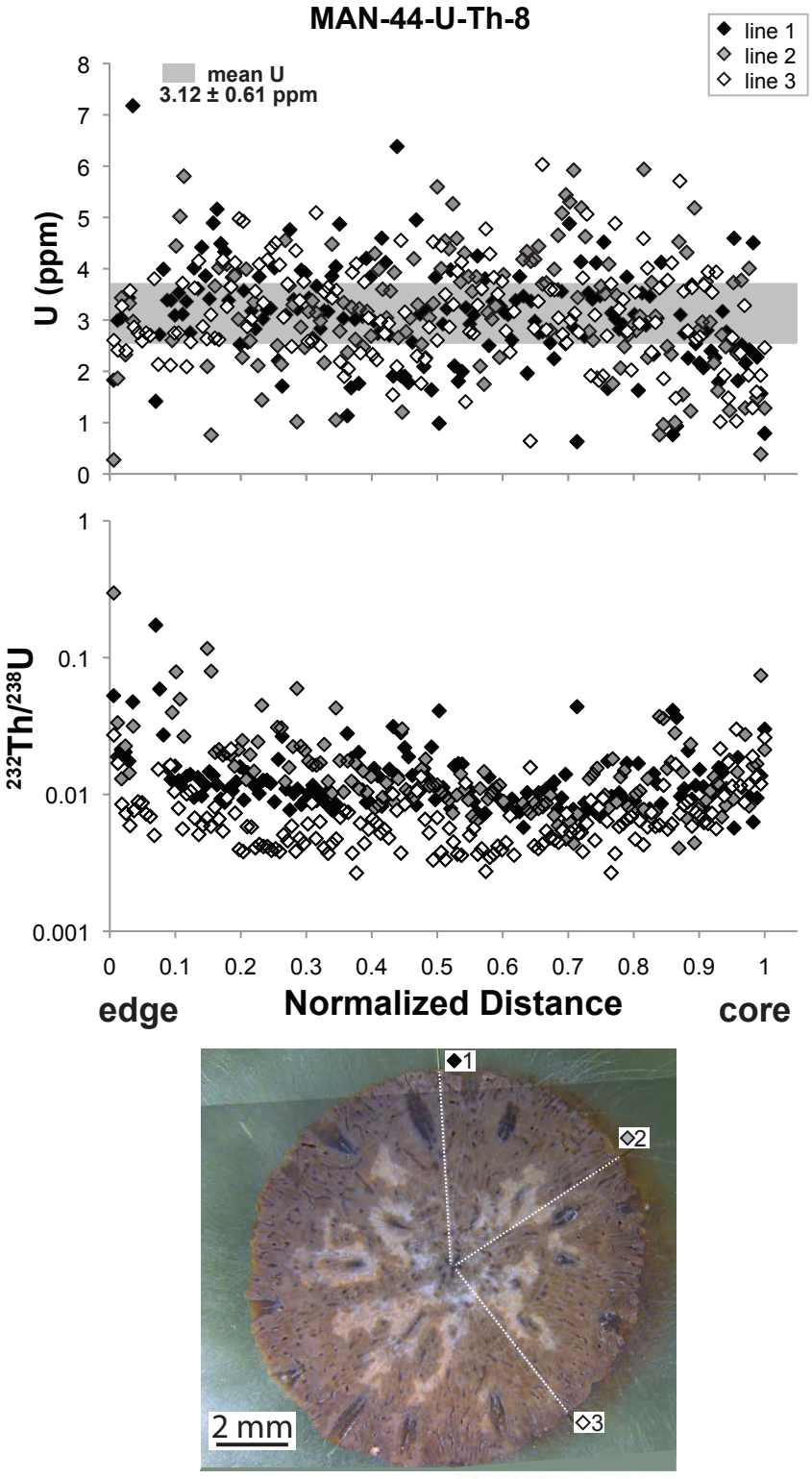

Figure C.15: [U] and $^{232}Th/^{238}U$ from LA-ICP-MS traverses of MAN-44-U-Th#-8 (>> 5% calcite). This sample was selected due to low ($^{230}Th/^{232}Th$).

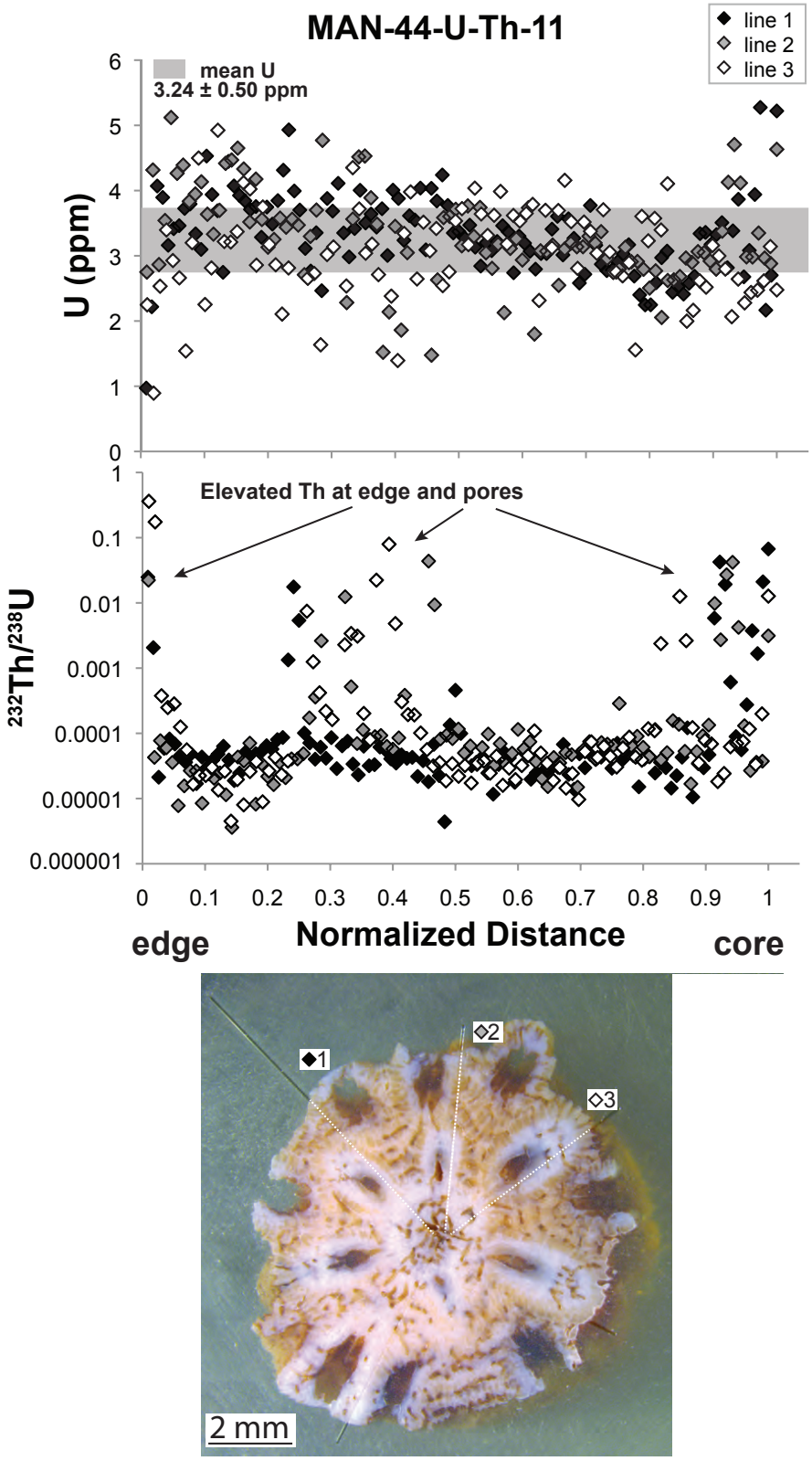

Figure C.16: [U] and $^{232}Th/^{238}U$ from LA-ICP-MS traverses of MAN-44-U-Th#-11 (100% aragonite). This sample was selected due to low $(^{234}U/^{238}U)_0$.

C.3: References

Cheng, H., Lawrence Edwards, R., Shen, C.C., Polyak, V.J., Asmerom, Y., Woodhead, J., Hellstrom, J., Wang, Y., Kong, X., Spötl, C., Wang, X., and Calvin Alexander, E., 2013, Improvements in ^{230}Th dating, ^{230}Th and ^{234}U half-life values, and U-Th isotopic measurements by multi-collector inductively coupled plasma mass spectrometry: Earth and Planetary Science Letters, v. 371–372, p. 82–91, doi: 10.1016/j.epsl.2013.04.006.

Dutton, A., Rubin, K., McLean, N., Bowring, J., Bard, E., Edwards, R.L., Henderson, G.M., Reid, M.R., Richards, D.A., Sims, K.W.W., Walker, J.D., and Yokoyama, Y., 2017, Data reporting standards for publication of U-series data for geochronology and timescale assessment in the earth sciences: Quaternary Geochronology, v. 39, p. 142–149, doi: 10.1016/j.quageo.2017.03.001.

Hellstrom, J., 2006, U-Th dating of speleothems with high initial ^{230}Th using stratigraphical constraint: Quaternary Geochronology, v. 1, p. 289–295, doi: 10.1016/j.quageo.2007.01.004.

Hoffmann, D.L., Spötl, C., and Mangini, A., 2009, Micromill and in situ laser ablation sampling techniques for high spatial resolution MC-ICPMS U-Th dating of carbonates: Chemical Geology, v. 259, p. 253–261, doi: 10.1016/j.chemgeo.2008.11.015.

Holden, N.E., 1990, Total half-lives for selected nuclides: v. 62, p. 941–958.

Jaffey, A.H., Flynn, K.F., Glendenin, L.E., Bentley, W.C., and Essling, A.M., 1971, Precision measurement of half-lives and specific activities of U235 and U238: Physical Review C, v. 4, p. 1889–1906, doi: 10.1103/PhysRevC.4.1889.

Ludwig, K.R., 2012, User's Manual for Isoplot 3.75, a geochronological toolkit for Microsoft Excel: Berkeley Geochronology Center Special Publication, v. 5, p. 1–72.

Ludwig, K.R., and Paces, J.B., 2002, Uranium-series dating of pedogenic silica and carbonate, Crater Flat, Nevada: Geochimica et Cosmochimica Acta, v. 66, p. 487–506, doi: 10.1016/S0016-7037(01)00786-4.

Ludwig, K.R., Wallace, A.R., and Simmons, K.R., 1985, The Schwartzwalder uranium deposit, II: Age of uranium mineralization and lead isotope constraints on genesis.: Economic Geology, v. 80, p. 1858–1871, doi: 10.2113/gsecongeo.80.7.1858.

Mertz-Kraus, R., Jochum, K.P., Sharp, W.D., Stoll, B., Weis, U., and Andreae, M.O., 2010, In situ 230Th–232Th–234U–238U analysis of silicate glasses and carbonates using laser ablation single-collector sector-field ICP-MS: Journal of Analytical Atomic Spectrometry, v. 25, p. 1895, doi: 10.1039/c0ja00004c.

National Institute of Standards and Technology, 2012, Certificate of Analysis Standard Reference Material ® 612 Trace Elements in Glass, p. 612, https://www-s.nist.gov/srmors/certificates/612.pdf.